Scintillation Light Transport In The Large Reactor Antineutrino Detector JUNO

Wilfried Walter Depnering
Born in Bad Schwalbach, Germany

Faculty of Physics, Mathematics, and Computer Science of
Johannes Gutenberg University
in Mainz

Dissertation submitted for the award of the title
Doctor of Natural Science

Mainz Monday, 23rd November, 2020

*"**Impossible** is a word that*
humans use far too often."
Seven of Nine

Acknowledgements

Due to data privacy, I will not mention any specific names in this acknowledgements section. However, it is an inner need for me to thank everyone who helped me to accomplish this aim of life.

These are my colleagues, my friends and my family. They helped me solving programming issues and supported me in the lab during the development and construction phase of my laser calibration system AURORA. Without these precious and adorable people my way to the finish line would not have been this pleasant and educational. In addition, they always found the perfect balance between distracting activities and constructive & motivational chats. Whenever I was close to give in, they were there for me. They knew how to encourage me with only a few words. I am very grateful for their support over the last five years. Thank you for everything!

Abstract

In low-energy neutrino physics, liquid scintillator (LS) detectors play a major role. The *Jiangmen Underground Neutrino Observatory* (JUNO) will be a multipurpose neutrino experiment and is currently under construction in South China. JUNO's main goal is the determination of the neutrino mass ordering at a 3-4σ significance within an operation time of six years. With a target mass of 20 kt, JUNO will be the largest LS detector constructed so far. A crucial requirement is to reach an energy resolution of at least 3% @ 1 MeV. Besides other aspects, this demands a sufficiently high transparency of the liquid scintillator. This transparency is expressed in terms of the attenuation length L and scattering length L_s. To fulfill the demands on the energy resolution, JUNO strives for values of $L = 20$ m and $L_s = 27$ m, respectively. To ensure that the detector performance meets these requirements for the whole operation period and does not degrade over time, the target's transparency will be continuously monitored. This is the purpose of the laser calibration system AURORA (**A U**nit for **R**esearching **O**n-line the LS t**RA**nsparency), which is installed in the water volume surrounding the JUNO central detector.

The first part of this thesis is about the design, construction, and performance tests of AURORA. A specially selected diode provides laser light at a wavelength of $\lambda = 430$ nm, which corresponds to the spectral region of the scintillator light emission. The light is distributed into an array of 100 m long fibers by an automated fiber switch. The laser light is decoupled from gradient-index (GRIN) lenses that permit to collimate the beam underwater. Full aperture angles of less than 0.25° can be achieved. To avoid any damage to the photomultiplier tubes (PMTs), piezo-electric actuators have been introduced to ensure that the beams can be remotely tilted by around 1°. Thus, even if the geometry shifted due to the detector filling, it would be possible to compensate for misalignment. Any interference with the electronic readout of the PMTs has to be avoided. The generated magnetic field of these electro-mechanical devices has been tested and found to be acceptably small.

The second part of this thesis focuses on the investigation of AURORA's potential to determine the attenuation length L and the scattering length L_s of the LS studying

statistical and systematical uncertainties. In order to evaluate the feasibility and sensitivity of the developed analysis approach, detailed studies with JUNO's official simulation framework `offline` have been conducted. It is found that a 50 s run provides sufficient statistics to reduce the relative uncertainty to the 0.1% level. Moreover, several sources of systematic uncertainties were studied. For an absolute measurement of the attenuation and scattering length, systematic uncertainties of $\Delta L = \pm 13$ cm and $\Delta L_s = \pm 23$ cm can be achieved. For a relative measurement that compares the development of the LS transparency over time, several systematic contributions do not have to be included. In this case, the systematic uncertainties are reduced to $\Delta L = \pm 7$ cm and $\Delta L_s = \pm 11$ cm, respectively.

Table of contents

List of figures

List of tables

Chapter 1

Historical Introduction

Since the mystery of the continuous energy spectrum of β decay particles and the associated alleged violation of energy, momentum and angular momentum conservation was resolved, first, by postulating, second, by detecting an additional particle – the so called neutrino ν – a completely new field in particle physics has unfolded [14, 168].

1.1 First Evidence For The Existence Of Neutrinos

The neutrino was postulated first by *Wolfgang Ernst Pauli*[1] in 1930 [14] in order to explain the results of β decay experiments carried out by *Lise Meitner*[2] and *Otto Hahn*[3] in 1911, by *Jean Danysz*[4] in 1913 and even more accurate by *James Chadwick*[5] in 1914 [36, 76]. He assumed that the β decay has to be a three-body decay satisfying the nowadays well known nuclear reaction shown in equation (1.1):

$$M(A,Z) \rightarrow D(A,Z+1) + e^- + \bar{\nu}_e \tag{1.1}$$

Here, $M(A,Z)$ stands for the mother nucleus with the mass number A and the proton number Z while $D(A,Z+1)$ is the produced daughter nucleus. The e^- and $\bar{\nu}_e$ represent the already detected electron and the newly introduced neutrino particle[6], respectively.

[1] *25$^{\text{th}}$ of April 1900, †15$^{\text{th}}$ of December 1958.
[2] *7$^{\text{th}}$ of November 1878, †27$^{\text{th}}$ of October 1968.
[3] *8$^{\text{th}}$ of March 1879, †28$^{\text{th}}$ of July 1968.
[4] *11$^{\text{th}}$ of March 1884, †4$^{\text{th}}$ of November 1914.
[5] *20$^{\text{th}}$ of October 1891, †24$^{\text{th}}$ of July 1974.
[6] From here on ν and $\bar{\nu}$ will refer to neutrinos and antineutrinos, respectively.

In the proposed three-body decay, a fraction of the nuclear transition Q-value (released energy) is used to create the electron and the electron antineutrino. The rest of the energy is distributed to the reaction products and carried away as the recoil energy of the daughter nucleus and as kinetic energy of the electron and electron antineutrino [44]. In agreement with observation, the consequence is a continuous energy spectrum of the detected electron without violating the energy conservation. With introducing the neutrino as a spin-$\frac{1}{2}$ particle [14] it was also possible to bypass the imminent violation of the angular momentum conservation. In β decays, the mother and the daughter atom always have the same spin (integer or half-integer), which can be explained by the emission of two spin-$\frac{1}{2}$ particles, the electron and the electron antineutrino [76, 168]. From the β decay, it is possible to conclude that the neutrino is a fermion (spin-$\frac{1}{2}$ particle) without any electrical charge. Furthermore, the shape of the β spectrum indicates a neutrino rest mass m_ν smaller than the electron rest mass m_e. Otherwise, the maximum energy of the electron E_{e^-} could not be so close to the maximal possible energy of the β spectrum $E_{\max}$.

In 1952, *James Sircom Allen*[7] and *George W. Rodeback*[8] found the first experimental evidence for the neutrino's existence in the electron capture (EC) reaction of ^{37}Ar:

$$^{37}\mathrm{Ar} + e^- \rightarrow ^{37}\mathrm{Cl} + \nu_e + Q \tag{1.2}$$

Here, ^{37}Ar and ^{37}Cl stand for the synthetic radioisotope of argon and the stable isotope of chlorine, respectively.

In the EC reaction there are only two particles in the final state and, therefore, the recoil energy of the chlorine nucleus should be fixed assuming momentum conservation in single neutrino processes. This is exactly what Allen and Rodeback observed. While with a Q-value of 816 keV the recoil energy of the nucleus should be 9.67 eV [168], their measurement revealed a final recoil energy of (9.63 ± 0.03) eV [113], which is in good agreement with the theoretical prediction.

1.2 The Discovery Of The Neutrino

In the end, it was *Clyde Lorrain Cowan Jr*[9] and *Frederick Reines*[10] who finally discovered the neutrino in 1956. In the *Cowan-Reines neutrino experiment*, electron

[7] *11$^{\text{th}}$ of August 1911, †15$^{\text{th}}$ of September 1983.
[8] **unknown*, †*unknown*.
[9] *6$^{\text{th}}$ of December 1919, †24$^{\text{th}}$ of May 1974.
[10] *16$^{\text{th}}$ of March 1918, †26$^{\text{th}}$ of August 1998.

antineutrinos $\bar{\nu}_e$ from the nuclear power plant (NPP) at *Savannah River* interacted with protons p in a cadmium chloride ($CdCl_2$) loaded water tank producing positrons e^+ and neutrons n via the *inverse beta decay* (IBD) reaction (see figure 1.1).

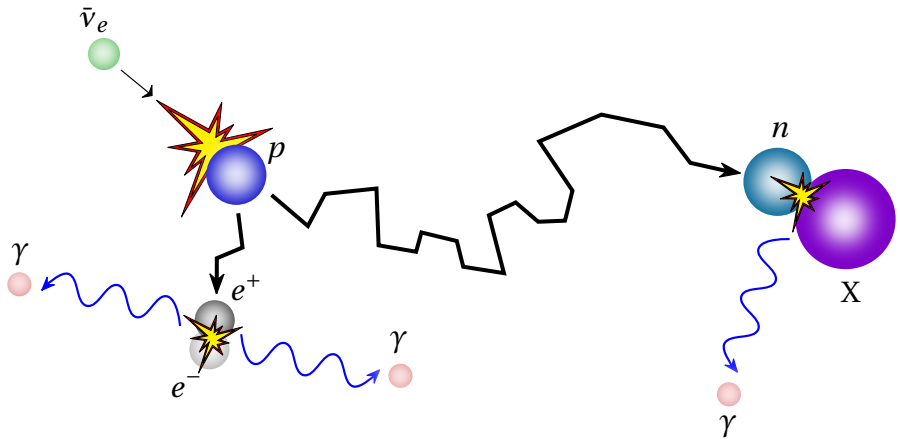

Fig. 1.1 Scheme of the inverse beta decay

*The figure shows the **inverse beta decay** and the subsequent reactions – the **positron annihilation** and the **neutron capture** – which are generating the **prompt** and the **delayed signal**, respectively.*

The IBD reaction is widely used in low-energy neutrino physics experiments. Here, an electron antineutrino reacts with a proton generating a positron and a neutron. The advantage of this detection reaction is given by the sequence of a prompt and delayed signal with characteristic energies which can be easily separated from background reactions. While the electron-positron annihilation results in the emission of two γ-particles after already a few nanoseconds with an overall energy of 1.022 MeV, the visible energy of the delayed neutron capture reaction depends on the capturing nucleus species. If in figure 1.1 the particle X is a proton[11], the emitted γ will have an energy of around 2.2 MeV [68]. In case of a ^{113}Cd or ^{157}Gd nucleus[12], several γ-particles can be emitted with an overall energy of around 9.0 MeV [99] or 7.9 MeV [122].

[11] In general, molecules of organic compounds contain a lot of protons. Therefore, in unloaded organic scintillators a proton-neutron capture reaction is most likely.

[12] Cadmium and gadolinium are often used in neutron capture reactions because of their significant higher neutron capture cross section on the one hand and the higher energies of the emitted γ-particles on the other hand leading to a greatly enhanced neutron capture signal.

1.3 Further Accomplishments In Neutrino Physics

In addition to the discovery of the electron antineutrino, many other accomplishments in neutrino physics have been made. One of those achievements was the discovery of parity violation in weak interactions (WI) and the direct measurement of the neutrino's helicity (see section 2.1.1) which finally led to the formulation of the V-A theory (see section 2.1.2). In addition to the electron neutrino ν_e, two new flavors were discovered – the myon neutrino ν_μ and the tau neutrino ν_τ (see section 2.1.1). Further experiments showed that neutrinos are changing their flavor during their propagation through space. Here, different mechanisms of flavor conversion could be identified (see section 2.2.1, 2.2.2 and 2.2.3). With the development of the electroweak theory by *Sheldon Glashow*[13], *Steven Weinberg*[14] and *Abdus Salam*[15] the existence of two further gauge bosons, the $W^\pm$ and Z^0 bosons, was predicted and later on also confirmed (see section 2.1.2). These bosons are moderating the WI. In 1987, neutrinos originating from a supernova type-II explosion could be observed by large underground neutrino detectors. The so called supernova *SN 1987A* occurred in the Large Magellanic Cloud at a distance of around 50 kpc and generated overall 25 neutrino events within a time range of 12 s [168]. To the present day, several other discoveries have been made revealing step by step the big picture. Nevertheless, new accomplishments also raise new questions, and, therefore, research in neutrino physics is indeed far from its end.

One of the remaining open questions concerns the so called *neutrino mass ordering*. In order to investigate this fascinating and important property of the neutrino, an international collaboration was founded, currently building the so called *Jiangmen Underground Neutrino Observatory* (JUNO) in China. One crucial parameter of the 20 kt liquid scintillator detector is the energy resolution which has to be at least 3% @ 1 MeV. Besides other aspects, the target mass has to be as transparent as possible in order to reach this sensitivity. Consequently, calibration units which determine and monitor the target material are mandatory. AURORA[16] will be one of those instruments measuring the scintillator transparency. This dissertation presents the design and the characterization measurements of the AURORA system. In addition, sensitivity studies, carried out with the official JUNO simulation, which investigate AURORA's uncertainties and a self-written software control are presented, too.

[13] *5$^{\text{th}}$ of December 1932.
[14] *3$^{\text{rd}}$ of May 1933.
[15] *29$^{\text{th}}$ of January 1926, †21$^{\text{st}}$ of November 1996.
[16] **A U**nit for **R**esearching **O**n-line the LS t**RA**nsparency.

This thesis is divided into several chapters following the subsequent structure: Chapter 2 focuses on theoretical basics providing the most important concepts of neutrino physics. In addition to general properties of the neutrino particle, flavor conversion processes like neutrino oscillation and the Mikheyev–Smirnov–Wolfenstein (MSW) effect are discussed in more detail presenting necessary facts to understand the problem of the neutrino mass ordering and how JUNO aims to resolve it. Afterwards, in chapter 3 the JUNO experiment itself is discussed. Here, the experiment's layout, conceptual design and physics program are presented. Especially the design of the central detector is of great importance for this thesis because it already predetermines features of the developed AURORA laser system involving specific conditions for its outline. Subsequently, chapters 4 and 5 are about liquid scintillators and fairly unknown technologies included in AURORA's set-up, respectively, in order to present the most important basics regarding hardware components. After that, chapter 6 discusses AURORA's set-up and the characterization of all single components in more detail. In addition, chapter 7 presents studies on the AURORA system carried out with the official JUNO simulation in order to investigate AURORA's sensitivity and limiting systematics. Finally, this thesis ends with a conclusion and outlook.

Chapter 2

Theoretical Background

The following chapter provides an introduction to the theoretical background of neutrino physics giving an overview of the important basics in order to establish a solid foundation on which the rest of this thesis will be built on. In section 2.1 general properties of the neutrino particle are presented drawing the *bigger picture* and referring to its place in the standard model (SM). The subsequent section 2.2 is about the phenomenon of *flavor conversion* which cannot be explained by the SM anymore. In section 2.3 the current status of neutrino physics is summarized while in section 2.4 the still unanswered question about the *neutrino mass ordering* is discussed in more detail. Here, the focus lies on JUNO's approach of determining the neutrino mass ordering by measuring distortions in the oscillation pattern of reactor antineutrino fluxes.

2.1 The Neutrino Inside The Standard Model

In order to gain a deeper understanding of the neutrino's nature on the one hand and the logical consequences for neutrino experiments on the other, this section focuses on the fundamental properties of the ν particle, its interaction with ordinary matter and the underlying *V-A theory*.

2.1.1 General Properties Of The Neutrino

In the SM neutrinos are spin-$\frac{1}{2}$ *Dirac fermions* with neither an electrical nor a color charge and a rest mass equal zero. That is why they cannot interact with their environment via electromagnetic or strong interaction. Instead, only the weak force is available resulting in typically small cross sections [121]. As an example, for reactor neutrinos the IBD has a cross section of around $\sigma_{\mathrm{IBD}} \sim 10^{-43}\,\mathrm{cm}^2$ [103, 168].

Neutrinos are produced in weak current reactions. There are different types of neutrinos, designated as *flavor*, which can be created during a WI. Similar to the three known charged leptons, the electron e^-, the muon μ^- and the tau τ^-, three different neutrino flavors are known as well, the *electron neutrino* ν_e, the *muon neutrino* ν_μ and the *tau neutrino* ν_τ (see figure 2.1).

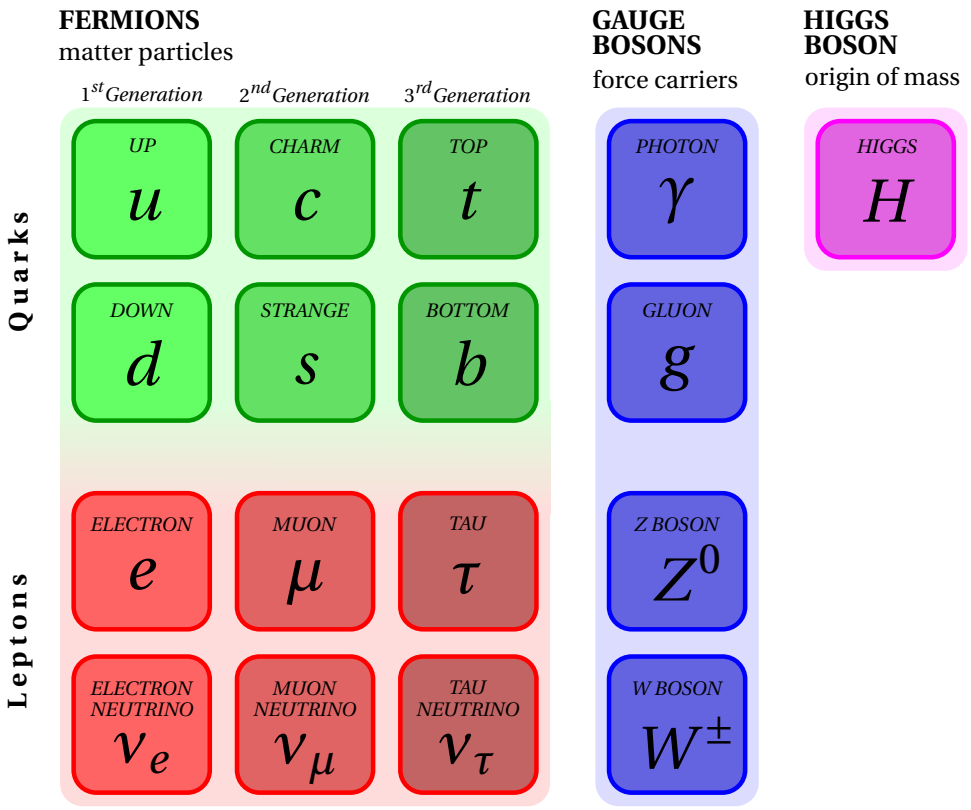

Fig. 2.1 The Standard Model of particle physics

*In the chart above the **Standard Model of elementary particles** is illustrated which already combines three of the four known fundamental forces, the electromagnetic, strong and weak interaction. The first three columns show the three generations of **elementary fermions** being the basic components of the known matter particles. These fermions can be divided into two subclasses - the **quarks** (green) and **leptons** (red). In the fourth column the **gauge bosons** (blue) are listed. These particles mediate the fundamental forces. In the fifth column the **Higgs particle** (magenta) is presented which confers mass on matter particles via the Higgs mechanism [118]. Due to their small masses neutrinos are assumed to acquire mass through a different mechanism - the so called **Seesaw mechanism** [47, 106].*

In the fourth column of figure 2.1 the force carrying gauge bosons are listed. The WI is mediated by the Z^0 boson ($m_Z = 91.1876 \pm 0.0021$ GeV [121]) and the $W^\pm$ bosons ($m_W = 80.379 \pm 0.012$ GeV [121]) being exchanged during *neutral current* (NC) and

charged current (CC) reactions, respectively. In figure 2.2 *Feynman diagrams* are shown serving as an example for each reaction type.

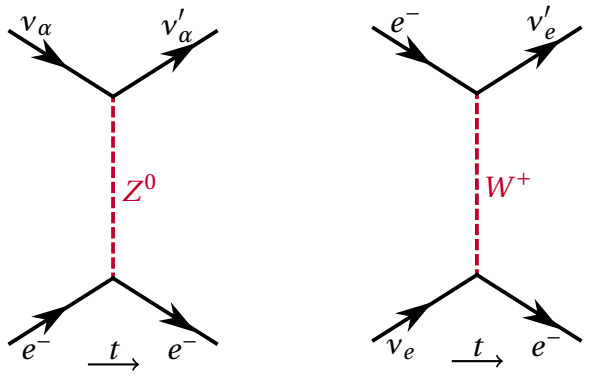

(a) Weak NC interaction (b) Weak CC interaction

Fig. 2.2 Weak current interactions

*Shown are the **elastic scattering** (ES) processes neutrinos can undergo when interacting with their environment. While all three neutrino flavors are able to interact via the **neutral current** channel being moderated by the **Z^0 gauge boson**, for ES only electron neutrinos can interact via the **charged current** reaction channel being moderated by the **W^+** and **W^- gauge bosons**.*

From the total decay width Γ_Z of the Z^0 resonance it is possible to determine the number N_ν of neutrinos which on the one hand are lighter than half of the Z^0 boson mass ($m_\nu < \frac{1}{2} m_Z$) and on the other hand are active and do interact with their environment via WI. The result of the *LEP experiment* indicates that $N_\nu = 2.9840 \pm 0.0082$ [121], and, therefore, at least three different active neutrino flavors should exist.

The helicity $\mathscr{H}$ of a particle X is the projection of its spin $\vec{s}$ onto the direction of its momentum $\vec{p}$ satisfying equation (2.1):

$$\mathscr{H} = \frac{\vec{s} \bullet \vec{p}}{|\vec{p}|} \tag{2.1}$$

In the case of a non-vanishing particle mass the eigenvalues of the helicity can range between -s, -s+1, ..., +s-1, +s only assigning discrete values because the eigenvalues of the spin $\vec{s}$ (with respect to an axis) only have discrete values as well. A particle with a mass $m_X > 0$ only propagates with a velocity $|\vec{v}| < c$. Consequently, it is always possible to boost into a reference system in which the momentum changes its sign. Due to the momentum dependency in equation (2.1), the helicity value can, therefore, differ from reference system to reference system.

For a massless particle with a velocity $|\vec{v}| = c$ only two different helicity eigenvalues can be realized (see figure 2.3).

(a) Positive helicity $\mathscr{H} = +s$ (b) Negative helicity $\mathscr{H} = -s$

Fig. 2.3 Possible helicity configurations of a massless particle X

*Shown are the two possible **helicity states** of a massless particle X. If momentum p (blue) and spin s (red) are pointing in the same direction, the helicity will have a value of $\mathscr{H} = +s$ and the particle is defined as **right-handed**. If momentum and spin are anti-parallel to each other, the helicity will have the opposite sign with $\mathscr{H} = -s$ being designated as **left-handed**.*

Here, the spin and the momentum can only be aligned parallel (positive helicity) or anti-parallel (negative helicity) to each other resulting in a right-handed or left-handed particle, respectively. Thus, for $|\vec{v}| = c$, helicity is an intrinsic particle property and, therefore, independent from the chosen reference system.

While helicity refers to one specific handedness value (left-handed *or* right-handed) of a particle in a specific reference system, *chirality* refers to the handedness components (left-handed *and* right-handed) of a particle independent from the reference system. Using *projection operators* the fraction of these chiral components (projections) of a particle wavefunction Ψ can be calculated. For a massless particle with $|\vec{v}| = c$ (like SM neutrinos) helicity and chirality are the same. In the SM neutrinos are massless particles, too. Consequently, it might be expected that for neutrinos and antineutrinos both helicity configurations would exist. However, in nature only left-handed neutrinos and right-handed antineutrinos are observed. This phenomenon lies in the fact that only the *chiral* left-handed components of particles and the *chiral* right-handed components of antiparticles have a weak charge giving them the opportunity to communicate with other weak charged particles via WI. Therefore, neutrinos and antineutrinos are always only produced as chiral left-handed and chiral right-handed fermions, respectively. A more sophisticated discussion about WI follows in section 2.1.2.

2.1.2 Weak Interaction And V-A Theory

The construction of the mathematical model which describes WI was driven by the observation of allowed β decay processes. Here, a combination of mathematical operators which transform as vectors[1] (V) and axial vectors[2] (A) was found to be able to explain sufficiently all experimental data. This is the reason why the WI describing model is also designated as a *V-A theory*[3].

Like all modern theories of elementary particles, also the V-A theory is a *gauge theory*, and, therefore, observable quantities remain invariant under specific potential transformations. The inner structure of such a *gauge transformation* is specified through a symmetry group. In case of the electroweak interaction it is the product of two groups SU(2)⊗U(1), where SU(2) belongs to the *weak isospin* and U(1) to the *hypercharge*. The SU(2)⊗U(1) based theory is also called Glashow-Weinberg-Salam (GWS) model or quantum flavor dynamics (QFD). Here, the chiral left-handed charged lepton field $l_L(x)$ and the chiral left-handed neutrino field $\nu_{lL}(x)$ are combined into a doublet of weak isospin in SU(2) while the chiral right-handed charged lepton field $l_R(x)$ forms a singlet of weak isospin in SU(2)[4]. According to the SM chiral right-handed neutrinos and chiral left-handed antineutrinos do not exist. Due to similarities between the quark and lepton sector, it is possible to organize these WI particles as shown in table 2.1.

Fermions	Quarks	Leptons
Doublets	$\begin{pmatrix} u \\ d' \end{pmatrix}_L, \begin{pmatrix} c \\ s' \end{pmatrix}_L, \begin{pmatrix} t \\ b' \end{pmatrix}_L$	$\begin{pmatrix} e^- \\ \nu_e \end{pmatrix}_L, \begin{pmatrix} \mu^- \\ \nu_\mu \end{pmatrix}_L, \begin{pmatrix} \tau^- \\ \nu_\tau \end{pmatrix}_L$
Singlets	$u_R, d_R, c_R, s_R, t_R, b_R$	e^-_R, μ^-_R, τ^-_R

Table 2.1 Elementary particles arranged as doublets and singlets [168]

*Listed are the **fermions** of the elementary particles being arranged as **doublets for chiral left-handed fields** and **singlets for chiral right-handed fields**.*

[1] A vector is represented with γ matrices by γ_μ.
[2] An axial vector is represented with γ matrices by $\gamma_\mu\gamma_5$.
[3] Successful description by the combination of a vector and an axial vector being represented with γ matrices by $\gamma_\mu(1-\gamma_5)$.
[4] Although only the left-handed component of a lepton takes part in WI, it is a combination of both components which describes the physical particle. For example, in order to acquire mass both components have to interact with the Higgs particle.

The Lagrangian which uses electromagnetic, weak charged and neutral currents and, therefore, satisfies the GWS model is given by the following equation:

$$\mathscr{L} = -e\left\{ A_\mu J^\mu_{em} + \frac{W^+_\mu \bar{\nu}_{eL}\gamma_\mu e_L + W^-_\mu \bar{e}_L \gamma_\mu \nu_{eL}}{\sqrt{2}\sin\theta_W} + \frac{Z_\mu J^\mu_{NC}}{\sin\theta_W \cos\theta_W} \right\} \tag{2.2}$$

Here, A_μ and θ_W stand for the *photon field* and the *Weinberg angle*, respectively, while J^μ_{em} and J^μ_{NC} are the corresponding currents that are defined as follows:

$$J^\mu_{em} = -\bar{e}_L\gamma_\mu e_L - \bar{e}_R\gamma_\mu e_R = -\bar{e}\gamma_\mu e \tag{2.3}$$

$$J^\mu_{NC} = \frac{1}{2}\bar{\nu}_{eL}\gamma_\mu \nu_{eL} - \frac{1}{2}\bar{e}_L\gamma_\mu e_L - \sin^2\theta_W J^\mu_{em} \tag{2.4}$$

2.2 Neutrino Flavor Oscillation

Although the neutrinos are fundamental particles and the electromagnetic neutral representatives of the lepton family within the SM, not all of their physical properties can be explained by the SM. One of these properties is a non-vanishing rest mass for at least two of the three known mass eigenstates [96]. Similar to the quark sector, the neutrino flavor eigenstates are different from the neutrino mass eigenstates leading to flavor conversion processes. In the following section the phenomenon of the so called *neutrino flavor oscillation* is discussed in more detail. While in section 2.2.1 the general formalism for neutrino mixing in vacuum is presented, section 2.2.2 is about oscillation in matter. Another flavor mixing process - the *adiabatic flavor conversion* - which neutrinos experience when they travel through a media of slowly changing matter density is discussed in section 2.2.3.

2.2.1 Neutrino Oscillation In Vacuum

It is known from oscillation experiments that neutrinos produced in a well defined flavor eigenstate can be detected as a different flavor eigenstate after covering a certain path distance. In order to understand this kind of neutrino mixing, the underlying mathematical basics are required first. The following derivations are predominantly based on references [89, 96, 103, 168].

First, n orthonormal flavor eigenstates $|\nu_\alpha\rangle$ are defined. Because of their orthonormality these eigenstates satisfy $\langle\nu_\beta|\nu_\alpha\rangle = \delta_{\alpha\beta}$. Second, n orthonormal mass eigenstates $|\nu_i\rangle$ are defined which also fulfill $\langle\nu_j|\nu_i\rangle = \delta_{ij}$. It is possible to connect these

eigenstates via an unitary mixing matrix U. This mixing matrix rotates the n eigenstates, and, therefore, the mass eigenstates can be expressed as a superposition of flavor eigenstates. Obviously, this also works the other way round following the relations in equation (2.5):

$$|\nu_\alpha\rangle = \sum_i U_{\alpha i} |\nu_i\rangle \qquad |\nu_i\rangle = \sum_\alpha \left(U^\dagger\right)_{i\alpha} |\nu_\alpha\rangle = \sum_\alpha U^*_{\alpha i} |\nu_\alpha\rangle \tag{2.5}$$

In addition, the unitary matrix U applies to the relations in equation (2.6):

$$U^\dagger U = 1 \qquad \sum_i U_{\alpha i} U^*_{\beta i} = \delta_{\alpha\beta} \qquad \sum_i U_{\alpha i} U^*_{\alpha j} = \delta_{ij} \tag{2.6}$$

For an antineutrino $U_{\alpha i}$ has to be replaced by $U^*_{\alpha i}$ satisfying relation (2.7):

$$|\bar{\nu}_\alpha\rangle = \sum_i U^*_{\alpha i} |\bar{\nu}_i\rangle \tag{2.7}$$

With $2n$ neutrino states the $n \times n$ unitary matrix U will have n^2 elements. The $2n-1$ relative phases of the neutrino states can be reduced to $(n-1)^2$ independent parameters leading to $\frac{1}{2} n\,(n-1)$ weak mixing angles and $\frac{1}{2}\,(n-1)\,(n-2)$ CP violating phases of a n-dimensional rotation matrix.

While being created and detected as flavor eigenstates, the propagation of neutrinos is described by the evolution[5] of their corresponding mass eigenstate components. A mathematical accurate derivation would require a neutrino treated as a superposition of quantum mechanical wave packets. However, due to normalization steps and valid assumptions[6] in the course of this ansatz, a mathematical object similar to a plane wave is what remains [89]. That is the reason why a so called *plane wave approximation*, given by formula (2.8), is normally used in the first place to derive the neutrino oscillation equation.

$$|\nu_i\,(x,t)\rangle = e^{-\mathbf{i}(E_i t - px)} |\nu_i\rangle \tag{2.8}$$

E_i, p and x stand for the energy of each mass eigenstate $|\nu_i\rangle$, the momentum and spatial coordinates, respectively.

[5] Evolution in space and time.

[6] Differences in velocity between the mass eigenstates are negligible, and, therefore, no spreading of the wave packet occurs. In general, this assumption is valid for neutrinos which are created and detected on Earth. For cosmic neutrinos (*e.g.* supernova neutrinos) this assumption might be wrong.

With a rest mass of less than ~1 eV [89] and normally kinetic energies in several orders of magnitude higher, neutrinos are ultrarelativistic. Consequently, it is justified to apply the relativistic approximation $p_i = E_i$ after simplifying the *energy-momentum relation* via a *Taylor expansion*. Due to small differences in rest mass and, therefore, in velocity, the energies of the single mass eigenstates can be treated as identical. Consequently, the relation $E_i = E_k = E$ is valid leading to formula (2.9):

$$E_i = \sqrt{m_i^2 + p_i^2} \simeq p_i + \frac{m_i^2}{2p_i} \simeq E + \frac{m_i^2}{2E} \tag{2.9}$$

The development of the flavor content of a neutrino produced as flavor eigenstate $|\nu_\alpha\rangle$ evolving into a state $|\nu_\beta\rangle$ can be described by equation (2.10):

$$|\nu(x,t)\rangle = \sum_{i,\beta} U_{\alpha i} U_{\beta i}^* e^{-\mathbf{i}(E_i t - px)} |\nu_\beta\rangle \tag{2.10}$$

The time-dependent transition amplitude A for a flavor conversion $\nu_\alpha \to \nu_\beta$ is then given by relation (2.11):

$$A(\alpha \to \beta)(t) = \langle \nu_\beta | \nu(x,t)\rangle = \sum_i U_{\beta i}^* U_{\alpha i} e^{-\mathbf{i}(E_i t - px)} \tag{2.11}$$

Using equation (2.9), it is possible to rewrite formula (2.11) leading to relation (2.12):

$$A(\alpha \to \beta)(t) = \langle \nu_\beta | \nu(x,t)\rangle = \sum_i U_{\beta i}^* U_{\alpha i} \exp\left(-\mathbf{i}\frac{m_i^2}{2}\frac{L}{E}\right) = A\left(\alpha \to \beta\right)(L) \tag{2.12}$$

Here, L is the distance between neutrino origin (creation point) and detector.

In the case of an antineutrino, formula (2.12) would change into equation (2.13):

$$A\left(\bar{\alpha} \to \bar{\beta}\right)(t) = \sum_i U_{\beta i} U_{\alpha i}^* e^{-\mathbf{i}E_i t} \tag{2.13}$$

Using the transition amplitude A, it is possible to calculate the transition probability P for such a flavor conversion just by squaring equation (2.12):

$$P\left(\alpha \to \beta\right)(t) = \left|A\left(\alpha \to \beta\right)\right|^2 = \sum_i \sum_j U_{\alpha i} U_{\alpha j}^* U_{\beta i}^* U_{\beta j} e^{-\mathbf{i}(E_i - E_j)t} \tag{2.14}$$

$$= \sum_i \left|U_{\alpha i} U_{\beta i}^*\right|^2 + 2\,\mathrm{Re} \sum_{j>i} U_{\alpha i} U_{\alpha j}^* U_{\beta i}^* U_{\beta j} \exp\left(-\mathbf{i}\frac{\Delta m_{ij}^2}{2}\frac{L}{E}\right) \tag{2.15}$$

In equation (2.15) the mass squared difference Δm^2_{ij} satisfies relation (2.16):

$$\Delta m^2_{ij} = m^2_i - m^2_j \tag{2.16}$$

While the second term of equation (2.15) describes the time or spatial dependent neutrino oscillation, the first term can be identified as an average transition probability. This first term can be rewritten following relation (2.17):

$$\langle P_{\alpha\to\beta}\rangle = \sum_i \left|U_{\alpha i}U^*_{\beta i}\right|^2 = \sum_i \left|U^*_{\alpha i}U_{\beta i}\right|^2 = \langle P_{\beta\to\alpha}\rangle \tag{2.17}$$

Applying CP invariance, $U_{\alpha i}$ has to be real, and, therefore, equation (2.15) simplifies to formula (2.19):

$$P\left(\alpha\to\beta\right)(t) = \sum_i U^2_{\alpha i}U^2_{\beta i} + 2\sum_{j>i} U_{\alpha i}U_{\alpha j}U_{\beta i}U_{\beta j}\cos\left(\frac{\Delta m^2_{ij}}{2}\frac{L}{E}\right) \tag{2.18}$$

$$= \delta_{\alpha\beta} - 4\sum_{j>i} U_{\alpha i}U_{\alpha j}U_{\beta i}U_{\beta j}\sin^2\left(\frac{\Delta m^2_{ij}}{4}\frac{L}{E}\right) \tag{2.19}$$

Calculating the complementary probability, the probability to find the neutrino in its original flavor eigenstate is given by equation (2.20):

$$P\left(\alpha\to\alpha\right) = 1 - \sum_{\alpha\neq\beta} P\left(\alpha\to\beta\right) \tag{2.20}$$

From equation (2.19) it is possible to conclude that neutrino oscillation can be observed as long as at least one neutrino mass eigenstate has a non-vanishing mass and the non-diagonal terms in U are not equal to zero so mixing between the flavors can occur. It can also be seen from equation (2.19) that the observation of neutrino oscillations does not tell us anything about the absolute mass of neutrinos. Instead of performing absolute neutrino mass measurements, oscillation experiments are only sensitive to the mass squared difference Δm^2 between neutrino mass eigenstates.

Up to now three different neutrino flavor eigenstates are known. Thus, in order to accurately describe neutrino oscillation in vacuum three flavors should be considered leading to the transition probability formula (2.21):

$$P(\alpha \to \beta) = \delta_{\alpha\beta} - 4 \sum_{i>j=1}^{3} \mathrm{Re}\left(K_{\alpha\beta,ij}\right) \sin^2\left(\frac{\Delta m^2_{ij}}{4}\frac{L}{E}\right) \pm 4 \sum_{i>j=1}^{3} \mathrm{Im}\left(K_{\alpha\beta,ij}\right) \sin\left(\frac{\Delta m^2_{ij}}{4}\frac{L}{E}\right) \cos\left(\frac{\Delta m^2_{ij}}{4}\frac{L}{E}\right) \tag{2.21}$$

Here, the sign of the second term is positive (+) for neutrinos and negative (-) for antineutrinos. In addition, $K_{\alpha\beta,ij}$ is an abbreviation for a product of several U-matrices satisfying the expression $U_{\alpha i} U^*_{\beta i} U^*_{\alpha j} U_{\beta j}$.

In this case the mixing matrix U is called *Pontecorvo–Maki–Nakagawa–Sakata matrix* or just U_{PMNS} and fulfills the form in equation (2.22) being named after *Bruno Pontecorvo*[7], *Ziro Maki*[8], *Masami Nakagawa*[9] and *Shoichi Sakata*[10]. While Maki, Nakagawa and Sakata introduced this matrix in order to describe the phenomenon of neutrino oscillation, Pontecorvo predicted this kind of neutrino flavor conversion in the first place.

$$U_{\mathrm{PMNS}} = \begin{bmatrix} 1 & 0 & 0 \\ 0 & c_{23} & s_{23} \\ 0 & -s_{23} & c_{23} \end{bmatrix} \begin{bmatrix} c_{13} & 0 & s_{13} e^{-\mathbf{i}\delta_{\mathrm{CP}}} \\ 0 & 1 & 0 \\ -s_{13} e^{\mathbf{i}\delta_{\mathrm{CP}}} & 0 & c_{13} \end{bmatrix} \begin{bmatrix} c_{12} & s_{12} & 0 \\ -s_{12} & c_{12} & 0 \\ 0 & 0 & 1 \end{bmatrix} \tag{2.22}$$

Here, c_{ij} and s_{ij} refer to $\cos(\theta_{ij})$ and $\sin(\theta_{ij})$, respectively. The parameter δ_{CP} stands for the CP violating phase term.

The two-flavor scheme can be used as an adequate approximation to the three-flavor oscillations in many cases [89]. With this approach the mixing matrix U_{PMNS} simplifies to an 2×2 matrix and neutrino oscillation can already be described by one mixing angle θ and one mass difference Δm^2 following formula (2.23):

$$P(\alpha \to \beta) = \delta_{\alpha\beta} - \sin^2(2\theta) \sin^2\left(\frac{\Delta m^2}{4}\frac{L}{E}\right) \tag{2.23}$$

[7] *22$^{\mathrm{nd}}$ of August 1913, †24$^{\mathrm{th}}$ of September 1993.
[8] *1929, †2005.
[9] *1932, †2001.
[10] *18$^{\mathrm{th}}$ of January 1911, †16$^{\mathrm{th}}$ of October 1970.

2.2.2 Neutrino Oscillation In Matter

If neutrinos are traversing matter, the neutrino oscillation behavior is changing due to the neutrino flavor dependent interaction abilities. While in ES processes ν_μ and ν_τ can only interact with leptons via NC reactions, ν_e are able to interact with their environment additionally via CC reactions (see figure 2.2). Taking matter effects into account, the WI Lagrangian (see equation 2.2) modifies to the following expression:

$$-\mathscr{L}_{\nu_\alpha} = \frac{G_F}{\sqrt{2}} \nu_\alpha^\dagger \left(1-\gamma_5\right) \nu_\alpha \sum_f N_f \left(\delta_{\alpha f} + I_{3f_L} - 2\sin^2\theta_W Q_f\right) \tag{2.24}$$

Here, only low-energy neutrino interactions of the flavor α with the background matter are considered. G_F is the Fermi coupling constant, θ_W is the Weinberg angle, I_{3f_L} is the eigenvalue of the fermion field f_L of the third component of the weak isospin and Q_f is the charge of f.

In the modified Lagrangian the ability of electron neutrinos to interact with matter via the CC reaction channel is realized by the Kronecker delta $\delta_{\alpha f}$. It states that there is a CC contribution if the flavor of the traversing neutrino and the flavors of the charged leptons in the surrounding material are the same.

Phenomenologically the potential which electron neutrinos are perceiving during their transit through matter has changed. Mathematically, this modification is expressed by the non-diagonal terms in the Hamiltonian[11] which are not equal to zero anymore. Consequently, the mass eigenstates of the vacuum case are no longer eigenstates in the matter case. In order to obtain the mass eigenstates in matter and the corresponding mass eigenvalues the new Hamiltonian has to be diagonalized. In the two-flavor case this leads to the following mass eigenstates:

$$m^2_{1m,2m} = \frac{1}{2}\left[(\Sigma + A) \mp \sqrt{\left(A - \Delta m^2 \cos 2\theta\right)^2 + \left(\Delta m^2\right)^2 \sin^2 2\theta}\right] \tag{2.25}$$

Here, the following expressions were used to shorten formula (2.25):

$$\Sigma = m_2^2 + m_1^2, \quad \Delta m^2 = m_2^2 - m_1^2, \quad A = 2\sqrt{2} G_F E \left(N\left(\nu_\alpha\right) - N\left(\nu_\beta\right)\right) \tag{2.26}$$

While $N\left(\nu_\alpha\right) = \delta_{\alpha e} N_e - \frac{1}{2} N_n$ stands for the matter density a neutrino of flavor α is aware of, N_e and N_n refer to the electron and neutron density, respectively.

[11] The Hamiltonian is used to derive the equation of motion.

With an mixing matrix U_m which connects the mass eigenstates in matter $m_{1m,2m}$ with the flavor eigenstates (*e.g.* ν_e, ν_μ) the corresponding mixing angle θ_m is given by the following equation:

$$\sin 2\theta_m = \frac{\sin 2\theta}{\sqrt{\left(\frac{A}{\Delta m^2} - \cos 2\theta\right)^2 + \sin^2 2\theta}} \tag{2.27}$$

Using the subsequent relation

$$\Delta m^2_m = m^2_{2m} - m^2_{1m} = \Delta m^2 \sqrt{\left(\frac{A}{\Delta m^2} - \cos 2\theta\right)^2 + \sin^2 2\theta}, \tag{2.28}$$

an expression for the neutrino oscillation probability in matter similar to the vacuum case can be derived resulting in the following equations:

$$P_m\left(\nu_e \to \nu_\mu\right) = \sin^2 2\theta_m \times \sin^2 \frac{\Delta m^2_m}{4} \frac{L_m}{E} \tag{2.29}$$

$$P_m\left(\nu_e \to \nu_e\right) = 1 - P_m\left(\nu_e \to \nu_\mu\right) \tag{2.30}$$

The corresponding oscillation length in matter is then given by the subsequent formula:

$$L_m = \frac{4\pi E}{\Delta m^2_m} = \frac{L_0}{\sqrt{\left(\frac{A}{\Delta m^2} - \cos 2\theta\right)^2 + \sin^2 2\theta}} = \frac{\sin 2\theta_m}{\sin 2\theta} L_0 \tag{2.31}$$

Due to the resonance type form, even for small $\sin\theta$ values maximal mixing in matter is possible [168]. This kind of flavor mixing, also referred to as *resonant* or *adiabatic conversion*, plays an important role in the Sun and is discussed in section 2.2.3. There are several physical consequences which can be derived from equation (2.27), (2.28) and (2.31). Firstly, if $A \to 0$, the matter corrections are negligible and θ_m, Δm^2_m and L_m convert back to θ, Δm^2 and L_0, respectively. Secondly, if the value for A becomes very large, the influence of the surrounding matter suppresses the oscillatory behavior. Thirdly, if A has an *intermediate* value, the matter corrections become very prominent. Here, the oscillatory behavior depends on whether neutrinos or antineutrinos are propagating through the material. In addition, the occurring linear term of Δm^2 in those formulas makes it possible to resolve the sign of the mass squared difference [13, 19]. This is also true for the 3 flavor scenario [19]. Consequently, the influence of matter on the oscillatory behavior of neutrinos can be used to determine the hierarchy of the neutrino mass eigenstates. A more detailed discussion can be found in section 2.4.

2.2.3 Resonant Flavor Conversion And MSW Effect

As already mentioned in the previous section, matter effects can be used to resolve the sign of the mass squared differences and, therefore, reveal which neutrino mass eigenstate is heavier or lighter than the other one. Here, a resonant process of flavor conversion, designated as the MSW effect, can be used to identify those signs [112, 168]. The MSW mechanism is based on the differing interaction behavior of different neutrino flavors with matter. While all flavor types can interact with matter via the NC channel, only electron neutrinos can interact with ordinary matter via the CC channel (see figure 2.2) leading to a modified interaction potential as already discussed in section 2.2.2. The consequence is a resonance type form for the neutrino oscillation (see equation (2.31)) [168]. Figure 2.4 illustrates the MSW effect for a two-flavor scenario.

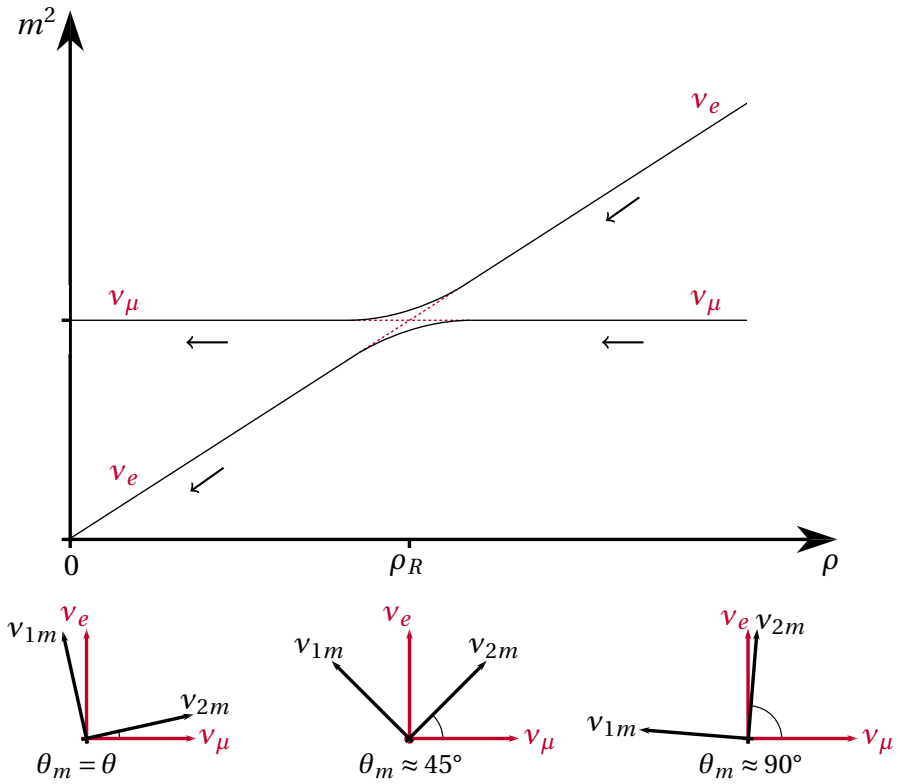

Fig. 2.4 MSW mechanism

*Shown are the three different stages of the **MSW effect** for a two-flavor scenario. At high densities the electron flavor eigenstate is similar to the second mass eigenstate. Here, θ_m is around 90° and neutrino oscillation is strongly suppressed. At lower density values ($\rho \approx \rho_R$) the **resonance region** is reached. Here, the mixing angle θ_m is around 45° and **maximal mixing between both flavor eigenstates** occurs even for small vacuum mixing angles. For a density $\rho = 0$ the mixing angle θ_m becomes θ and ordinary vacuum oscillation takes place.*

Solar neutrinos for example were used to identify the sign of Δm^2_{21}. For the sake of simplicity the following argumentation will rely on a two-flavor scenario. For an accurate analysis with more reliable results the entire three-flavor scenario has to be considered. In the Sun's interior (figure 2.4 on the right) where the fusion processes take place the matter density is so high that the flavor eigenstate of the electron neutrinos ν_e is almost identical with the second mass eigenstate ν_{2m}, and, therefore, ordinary neutrino oscillation is strongly suppressed [112]. Propagating outwards neutrinos will traverse regions where the *effective mixing angle* is around 45° (figure 2.4 in the middle), and, consequently, maximal mixing occurs even for small vacuum mixing angles. In these *resonance regions* electron neutrinos can be converted into muon neutrinos and vis versa. On their way out of the Sun (figure 2.4 on the left) the neutrino's mass eigenstates ν_m will further change their orientation relative to the flavor eigenstates ν_α reaching vacuum conditions at the Sun's surface. At this point ordinary vacuum oscillation takes place. During the resonant transition phase the following resonance condition is fulfilled and can be used to determine the sign of the mass squared difference [95, 168].

$$A = \Delta m^2 \cdot \cos 2\theta \tag{2.32}$$

In the Sun, only electron neutrinos[12] are created, and, thus, the parameter A in equation (2.32) is of positive sign. With a value for $\theta < 45°$ (θ_{12} has a value of around 33.48° [121]) the cosine function also contributes a positive sign. Consequently, the resonance condition is only fulfilled if $\Delta m^2 = m_2^2 - m_1^2$ also has a positive sign, and, therefore, the second mass eigenstate has to be heavier than the first one [95, 105].

Matter effects on Earth traversing neutrinos might be also used to resolve the sign of Δm^2_{32} or Δm^2_{31} [31, 34, 105, 168]. A more detailed discussion about determining the sign of the atmospheric mass squared difference, and with it the neutrino mass ordering itself, can be found in section 2.4.

[12] In the Sun, only fusion processes occur where protons are converted into neutrons. Consequently, only electron neutrinos and not electron antineutrinos or neutrinos of another flavor type are produced.

2.3 Current Status Of Knowledge

Since the existence of the neutrino has been confirmed by *Cowan* & *Reines* great efforts were made to reveal all the secrets which are related to this still not fully understood particle. Carrying out experiments with solar, atmospheric, reactor and accelerator neutrinos, general properties and most of the unknown parameters that describe the three-generation oscillation have been carefully measured and studied.

The mixing angle $\sin^2\theta_{12}$ and the mass squared difference Δm^2_{21} were predominantly determined by solar neutrino experiments (*e.g.* SNO[13], Borexino[14] and Super-Kamiokande[15]) and the long-baseline[16] reactor neutrino experiment KamLAND[17] which were looking for a deficit of electron neutrinos and antineutrinos in the solar and reactor neutrino flux, respectively [121].

Values for the oscillation parameters $\sin^2\theta_{23}$ and Δm^2_{32} were obtained by different kind of experiments. Besides the already mentioned Super-Kamiokande experiment, long-baseline accelerator experiments (*e.g.* MINOS[18], T2K[19] and NOνA[20]) and neutrino telescope experiments (*e.g.* ANTARES[21] and IceCube-DeepCore[22]) successfully accessed the parameter space spanned by these quantities. Predominantly, in those oscillation experiments the disappearance of muon neutrinos has been observed and studied. For a more precise measurement of $\sin^2\theta_{23}$ a combined analysis of muon neutrino (antineutrino) disappearance and electron neutrino (antineutrino) appearance is mandatory. In addition, it is also possible to strengthen the found results by conducting analyses which are looking for the appearance of tau neutrinos. Furthermore, it was also possible to derive values for the mass squared difference Δm^2_{32} from short-baseline[23] reactor neutrino measurements. The results are in good agreement with the long-baseline accelerator measurements of T2K and MINOS [121].

[13] **S**udbury **N**eutrino **O**bservatory, Canada.
[14] Italian diminutive of **BOREX** which stands for **BOR**on solar neutrino **EX**periment, Italy.
[15] **Super**-**Kamioka** **N**eutrino **D**etection **E**xperiment, Japan.
[16] Approximately 180 km.
[17] **Kam**ioka **L**iquid Scintillator **A**nti**N**eutrino **D**etector, Japan.
[18] **M**ain **I**njector **N**eutrino **O**scillation **S**earch, USA.
[19] **T**okai *to* **K**amioka, Japan.
[20] **N**uMI **O**ff-Axis ν_e **A**ppearance, USA.
[21] **A**stronomy with a **N**eutrino **T**elescope and **A**byss environmental **RES**earch project, France.
[22] Upgrade of the **IceCube** Neutrino Detector, Antarctica.
[23] In the order of 1 km.

In contrast to KamLAND, short-baseline reactor neutrino experiments have shown a high sensitivity to determine the mixing angle $\sin^2\theta_{13}$. Besides the two experiments Double Chooz[24] and RENO[25], it was the Daya Bay[26] experiment which measured $\sin^2\theta_{13}$ with the highest precision. Here, the reactor experiments were looking for the disappearance of electron antineutrinos in the neutrino flux of nuclear power plants. Alternatively, also solar and accelerator neutrino experiments had been able to obtain limits on the oscillation parameter $\sin^2\theta_{13}$ [121].

The CP violating phase δ_{CP} is also investigated by long-baseline accelerator experiments like MINOS, T2K and NOνA. Here, on the one hand the already measured oscillation parameters Δm^2_{21}, $\sin^2\theta_{12}$ and $\sin^2\theta_{13}$ are used as constraints while on the other hand electron neutrino (antineutrino) appearance and muon neutrino (antineutrino) disappearance data is obtained in order to measure δ_{CP} [121].

In table 2.2 the neutrino oscillation parameters are summarized giving an accurate overview of the current status.

Parameter	Best fit value $\pm1\sigma$ (NO)	Best fit value $\pm1\sigma$ (IO)
$\sin^2\theta_{12}$	$0.310^{+0.013}_{-0.012}$	$0.310^{+0.013}_{-0.012}$
$\sin^2\theta_{23}$	$0.582^{+0.015}_{-0.019}$	$0.582^{+0.015}_{-0.018}$
$\sin^2\theta_{13}$	$0.02240^{+0.00065}_{-0.00066}$	$0.02263^{+0.00065}_{-0.00066}$
δ_{CP}	$1.21^{+0.22}_{-0.16}$	$1.56^{+0.14}_{-0.16}$
$\Delta m^2_{21} \times 10^{-5}\,\mathrm{eV}^2$	$7.39^{+0.21}_{-0.20}$	$7.39^{+0.21}_{-0.20}$
$\Delta m^2_{32} \times 10^{-3}\,\mathrm{eV}^2$	$+2.525^{+0.033}_{-0.031}$	$+2.512^{+0.034}_{-0.031}$

Table 2.2 Best fit values of the three-flavor neutrino oscillation parameters

*Listed are the **best fit results of each oscillation parameter and the corresponding** 1σ **uncertainty range**. While the **second column** shows the best fit results for the **normal mass ordering**, the **third column** presents those for the **inverted mass ordering** scenario. Although current NOνA results show for the mixing angle θ_{23} a **preference in favor of the second octant** [9], a first octant solution is still allowed. Consequently, the so called **octant problem** remains unsolved. The parameter values are taken from the reference [52].*

However, some properties of the neutrino remain undetermined. First of all, it is still unknown whether or not the neutrino is its own antiparticle, or in other words,

[24] Neutrino Oscillation Experiment in **Chooz**, France.
[25] **R**eactor **E**xperiment for **N**eutrino **O**scillation, South Korea.
[26] Neutrino Oscillation Experiment at **Daya Bay**, China.

whether the neutrino is a *Dirac* ($\nu_x \neq \bar{\nu}_x$) or a *Majorana* ($\nu_x = \bar{\nu}_x$) fermion. One way to determine this crucial property is the search for neutrinoless double beta decay ($0\nu\beta\beta$) events. For some radioactive isotopes a single beta decay process is energetically forbidden. In order to become more stable two nucleons[27] have to decay at the same time. While for the Dirac case always two neutrinos should be emitted during the decay process, for the Majorana case this is unnecessary. Here, the released neutrinos could annihilate with each other resulting in a neutrinoless double beta decay. If such a decay is observed, the neutrino behaves like a Majorana particle and the process violates *lepton number conservation* [33, 58]. In addition, determining the neutrino's nature could also answer the question how neutrinos gain mass. In the majorana case the extremely light neutrino mass is explained via the *seesaw mechanism* also giving a possible explanation for the *baryon asymmetry* via *leptogenesis* [46, 57]. Isotopes like ^{48}Ca (*e.g.* NEMO-3[28]), ^{76}Ge (*e.g.* GERDA[29]), ^{130}Te (*e.g.* SNO+[30]) or ^{136}Xe (*e.g.* KamLAND-Zen[31]) are prominent double β emitters and used in the mentioned experiments. The decay rate of $0\nu\beta\beta$ is given by the half-time $T^{0\nu}_{1/2}$ and proportional to the square of the effective neutrino mass $\langle m_{\beta\beta}\rangle$ following equation (2.33):

$$\left(T^{0\nu}_{1/2}\right)^{-1} = G^{0\nu}\left|M^{0\nu}\right|^2 \langle m_{\beta\beta}\rangle^2 \tag{2.33}$$

Here, $\langle m_{\beta\beta}\rangle \equiv \left|\left|U^L_{e1}\right|^2 m_1 + \left|U^L_{e2}\right|^2 m_2 e^{i\phi_2} + \left|U^L_{e3}\right|^2 m_3 e^{i\phi_3}\right|$, $G^{0\nu}$ is the phase space factor, $M^{0\nu}$ is the nuclear matrix element, $e^{i\phi_{2,3}}$ are the Majorana CP phases and U^L_{ej} (with j=1-3) is the neutrino mixing matrix [58]. From equation (2.33) it is easy to conclude that the event rate in such experiments determines the mass scale of light neutrino mass. Up to now no $0\nu\beta\beta$ decays could be recorded providing only limits for the half-time and, therefore, for the effective neutrino mass. The most stringent result stems from KamLAND-Zen with an effective mass of $\langle m_{\beta\beta}\rangle < 61 - 165$ meV at 90% C.L. originating from the limit $T^{0\nu}_{1/2} > 1.07 \times 10^{26}$ years [58, 121]. Determining the neutrino mass ordering will help to improve results from $0\nu\beta\beta$ experiments (see section 2.4).

Another still undetermined parameter is the CP violating phase δ_{CP} which might provide, at least to some extent, an explanation for the observed *matter-antimatter-asymmetry* in our universe [58]. In solar and atmospheric oscillation experiments

[27] Either two protons decay into two neutrons ($p \rightarrow n + e^+ + \nu_e$) corresponding to a $\beta^+\beta^+$ event or two neutrons decay into two protons ($n \rightarrow p + e^- + \bar{\nu}_e$) corresponding to a $\beta^-\beta^-$ event.
[28] **N**eutrino **E**ttore **M**ajorana **O**bservatory, France.
[29] **Ger**manium **D**etector **A**rray, Italy.
[30] The successor experiment of **SNO**, Canada.
[31] Double Beta Decay Search using the **KamLAND** detector, Japan.

δ_{CP} shows an inferior influence on neutrino propagation. Therefore, this effect is widely masked by systematic uncertainties [4]. However, the oscillation parameter δ_{CP} could be measured in long-baseline accelerator experiments operating in appearance mode ($\nu_\mu \rightarrow \nu_e$) and taking advantage of matter effects [48]. *E.g.* an accelerator based neutrino source would have the advantage that both the neutrino flavor content and the energy spectrum of the initial state can be chosen. Because of the relatively large mixing angle $\sin^2\theta_{13}$ the T2K experiment with a baseline of around 295 km is already able to obtain limits on the CP violating phase [5]. For longer baselines (*e.g.* NOνA) the influence of matter effects is enhanced, and, therefore, the result depends stronger on the sign of Δm^2_{32}. Those accelerator experiments will benefit from experiments like JUNO, which will be able to provide constraints on the neutrino mass ordering independently from these matter effects.

Also unknown is the absolute mass scale of the neutrino. Here, three different approaches exist to answer this question – cosmological observations, the already mentioned neutrinoless double beta decay and direct neutrino mass determination methods [50]. Cosmological surveys and neutrinoless double beta decay experiments[32] rely on cosmological and nuclear[33] models, respectively. Consequently, these approaches are both model dependent. In contrast to that, direct neutrino mass determination methods like β decay experiments do not need such an input from theory models and can be considered as model independent.
The cosmological approach is based on observations of the matter distribution in the visible universe. These structures have been formed out of fluctuations in the early universe and were influenced by cosmic neutrinos[34] with high thermal velocities at that time. Below their *free streaming length* those neutrinos were damping density perturbations. The strength of this effect depends on the absolute mass of neutrinos [4, 83, 155]. Using large galaxy surveys an upper limit for the sum of neutrino masses can be obtained with $\langle m_\Sigma \rangle < 0.2\,\text{eV}$ [121]. Here, the sum of neutrino masses is defined as $\langle m_\Sigma \rangle = m_1 + m_2 + m_3$ [83].
The approach which utilizes neutrinoless double beta decay experiments in order to determine the absolute neutrino mass has already been discussed. The best result comes from KamLAND-Zen with an upper limit of $\langle m_{\beta\beta} \rangle < 0.06\,\text{eV}$ [58, 121].
In direct neutrino mass experiments kinematic relations are used to obtain the absolute mass of the neutrino. On the one hand neutrinos which are emitted during a supernova can be used to constrain upper limits for the neutrino mass

[32] For the $0\nu\beta\beta$ approach to work neutrinos have to be Majorana particles.
[33] The nuclear matrix element $M^{0\nu}$ (see equation (2.33)) is calculated using nuclear models.
[34] Today designated as relic neutrinos.

by performing a time-of-flight measurement. Such a study was carried out after the supernova SN 1987 A resulting in an upper limit of $m_\nu < 5.7\,\text{eV}$ [4, 121]. On the other hand the investigation of the endpoint region of a β spectrum can be used to obtain the neutrino mass. Here, the shape of the β spectrum close to the endpoint is directly related to the neutrino's mass. Consequently, constraints can be obtained by analyzing the shape of the β spectrum near the endpoint. In this approach the neutrino mass is given by $\langle m_\beta \rangle = \sqrt{\left|U_{e1}^L\right|^2 m_1^2 + \left|U_{e2}^L\right|^2 m_2^2 + \left|U_{e3}^L\right|^2 m_3^2}$ (see reference [83]). Besides other experiments KATRIN[35] uses this kind of approach for molecular tritium claiming to be sensitive to the neutrino mass down to 0.2 eV at 90% C.L. [162]. During the TAUP[36] conference in 2019 the KATRIN experiment released its first result of an upper limit on the neutrino mass with m_ν <1.1 eV at 90% C.L., which was later also published in Physical Review Letters [12]. Project 8 will measure the β spectrum from atomic tritium decays by detecting cyclotron radiation from individual β electrons in a magnetic field performing a so called *Cyclotron Radiation Emission Spectroscopy* (CRES) [17]. The collaboration anticipates a final sensitivity of 0.04 eV at 90% C.L. [16].

Another unknown parameter in neutrino physics is the *neutrino mass ordering* (NMO). Due to the nature of oscillation experiments only the difference between mass eigenstates can be investigated (see equation 2.21), but not the absolute mass itself. While the influence of the MSW effect on solar neutrinos revealed the sign of the mass squared difference Δm_{21}^2 to be positive, the sign of Δm_{31}^2 is still unknown. Consequently, two scenarios are possible: Either the first mass eigenstate m_1 or the third mass eigenstate m_3 is the lighter one (see figure 2.5) referring to the *normal* (NO) or *inverted mass ordering* (IO), respectively. Determining the NMO is JUNO's primary goal and will be discussed in more detail in the following section.

2.4 The Neutrino Mass Ordering

As already discussed in the previous section it is still unknown which of the two neutrino mass orderings is realized in nature. Revealing the true mass ordering would have a huge impact on neutrino physics. Firstly, it would be possible to rule out all beyond standard model (BSM) theories which are predicting the opposite mass ordering. Secondly, uncertainties of δ_{CP} measurements would be reduced significantly. Thirdly, the neutrino mass ordering also determines the scope for future

[35] **Ka**rlsruhe **Tri**tium **N**eutrino Experiment.
[36] 16^{th} International Conference on **T**opics in **A**stroparticle and **U**nderground **P**hysics, September 9-13, 2019, Toyama, Japan.

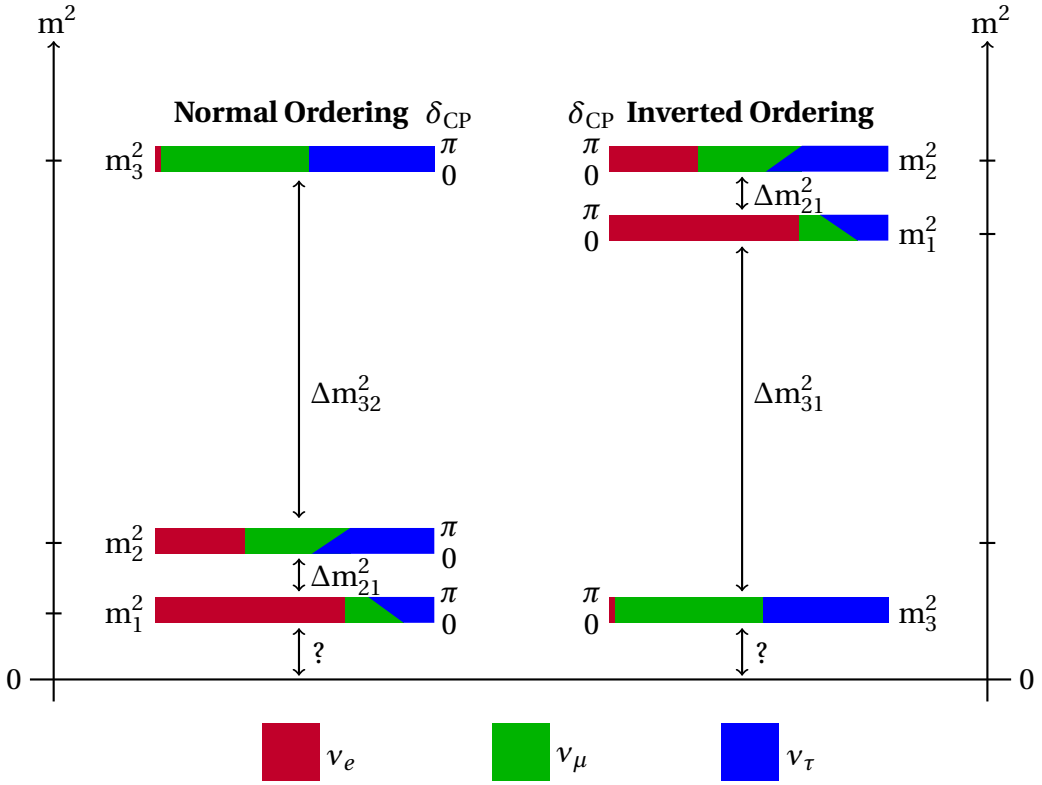

Fig. 2.5 Neutrino mass ordering

The chart illustrates both scenarios of possible ***neutrino mass orderings****. The ordering with the neutrino mass eigenstate m_1 as the lightest and m_3 as the heaviest one is called* ***normal ordering****. The scenario with m_3 as the lightest mass eigenstate and m_2 as the heaviest one is called* ***inverted ordering****. The influence of the* ***phase factor*** δ_{CP} *on the mixing is also indicated. The graph is oriented towards reference [94].*

neutrinoless double beta decay experiments by limiting the parameter space within the observation of a signal would be still possible. Fourthly, taking cosmological measurements into account the knowledge about the neutrino mass ordering could also be used to determine the absolute mass scale of neutrinos. Finally, the neutrino mass ordering can help to understand flavor transition mechanisms during a core-collapse supernovae in a more sophisticated way [18, 31]. Here, in addition to the MSW effect in less dense star regions self-induced neutrino interactions are taking place within the *neutrinosphere*[37]. Those flavor conversion processes lead to a swap between spectra of ν_e ($\bar{\nu}_e$) and spectra of ν_x ($\bar{\nu}_x$) with $x = \mu, \tau$ (*collective neutrino oscillation* [51]). For the NO these neutrino interactions do not play a significant role. For the IO the spectra of neutrinos are swapped above a characteristic energy, while for antineutrinos an almost complete flavor exchange takes place [37, 40].

[37] A region close to the star's core within a radius of $r \sim 10^3$ km.

2.4.1 Determining The NMO With Long-Baseline Experiments

While a lot of phenomena and physical quantities are influenced by the NMO, only a few experimental approaches in oscillation experiments are sensitive to unambiguously determine the true nature of the NMO.

Long-baseline experiments are one way to approach this topic. While the underlying principle is the MSW effect and its influence on the oscillatory behavior of neutrinos (see section 2.2.3), the energy scale and the achievable baselines are different to the solar case which revealed the sign of Δm^2_{21}. Here, Earth traversing neutrinos at GeV energies provided by accelerators or reactions in the Earth's atmosphere are used to resolve the sign of Δm^2_{31} [31]. Among other experiments, DUNE[38], ORCA[39] and PINGU[40] (or the smaller IceCube-Upgrade) will benefit from these matter effects.

For a long-baseline accelerator experiment like DUNE in which the muon neutrino beam crosses a distance of around 1300 km [7] through matter, the electron neutrino appearance oscillation probability $P_{\mu e}$ in a constant density approximation is given by the following equation:

$$\begin{aligned} P_{\mu e} = &+ \sin^2\theta_{23}\sin^2 2\theta_{13}\frac{\sin^2(\Delta_{31}-aL)}{(\Delta_{31}-aL)^2}\Delta^2_{31} + \cos^2\theta_{23}\sin^2 2\theta_{12}\frac{\sin^2(aL)}{(aL)^2}\Delta^2_{21} \\ &+ \sin 2\theta_{23}\sin 2\theta_{13}\sin 2\theta_{12}\frac{\sin(\Delta_{31}-aL)}{(\Delta_{31}-aL)}\Delta_{31}\frac{\sin(aL)}{(aL)}\Delta_{21}\cos(\Delta_{31}+\delta_{\mathrm{CP}}) \end{aligned} \tag{2.34}$$

Here, $\Delta_{ij} = \frac{\Delta m^2_{ij} L}{4E}$, L is the baseline, E is the neutrino energy in GeV, $a = \frac{G_F N_e}{\sqrt{2}}$, G_F is the Fermi constant and N_e is the electron number density in the Earth.

In equation (2.34) the parameters a, which is associated with the matter effect, and the CP violating phase δ_{CP} are colored red. Both switch their sign when changing the appearance channel from $\nu_\mu \to \nu_e$ to $\bar{\nu}_\mu \to \bar{\nu}_e$. The origin of asymmetry introduced by the matter effect lies in the composition of the Earth's material, or more precisely, in the presence and absence of electrons and positrons, respectively. Beyond baselines of 1200 km [7] the asymmetry caused by matter effects exceeds the maximal possible asymmetry generated by δ_{CP} and therefore the degeneracy of both effects is resolvable. Since the resonance condition for neutrinos (antineutrinos) is only met in the NO (IO) case, the NMO can be unambiguously determined [6, 7].

[38] **D**eep **U**nderground **N**eutrino **E**xperiment.
[39] **O**scillation **R**esearch with **C**osmics in the **A**byss.
[40] **P**recision **I**ceCube **N**ext **G**eneration **U**pgrade.

In a neutrino telescope experiment like PINGU the oscillation pattern of Earth traversing atmospheric muon neutrinos is analyzed. Figure 2.6 shows the survival probability of muon neutrinos for different energies and azimuth angles.

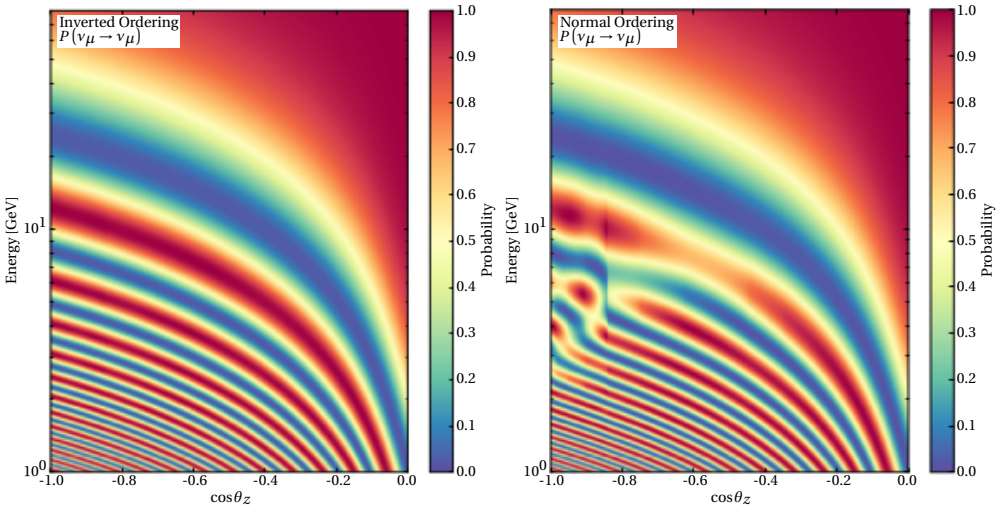

Fig. 2.6 PINGU oscillograms for muon neutrinos for both NMO scenarios

*Both graphs show the **survival probability** of **muon neutrinos** after **traveling through the Earth** as a function of the **neutrino energy** and the cosine of the true **zenith angle**. Here, the value* $\cos\theta_z = -1$ *corresponds to a path directly through the center of the Earth. While the left graph shows the oscillogram for the **IO**, the right plot illustrates the survival probability for the **NO** case. For **muon antineutrinos** the results are essentially the same as for muon neutrinos in the opposite NMO scenario. The plot is taken from reference [1].*

Figure 2.6 illustrates the difference in the oscillation pattern of atmospheric muon neutrinos between both NMO scenarios. For muon antineutrinos the patterns are swapped. Although PINGU is not capable of distinguishing between neutrinos and antineutrinos on an event-by-event level, the NMO still causes a measurable net-effect in the amplitude of the asymmetry introduced by the matter effect. This is caused by differences in the atmospheric fluxes and cross sections for neutrinos and antineutrinos [3].

While DUNE claims to measure the NMO with a significance of 5σ for all possible δ_{CP} values after only 2 years of data taking[41] [6], PINGU[42] (the smaller IceCube-Upgrade) would need in case of the NO scenario to be true at least 3 years (less than 4 years) to reach a 5σ significance. In the IO scenario both IceCube extensions will need far more than 6 years for the 5σ significance [2].

[41] Data taking is anticipated to start in 2026 [54].
[42] PINGU is proposed but not yet funded.

2.4.2 Determining The NMO With JUNO

A complementary approach is a medium-baseline reactor neutrino experiment like JUNO which is able to investigate the nature of the NMO independent from matter effects [34]. The survival probability for electron antineutrinos emitted by a nuclear reactor shows an oscillation pattern which depends on the NMO scenario (see figure 2.5). The survival probability P_{ee} is described by the following formula:

$$\begin{aligned} P_{ee} = 1 - \cos^4\theta_{13}\sin^2 2\theta_{12}\sin^2\Delta_{21} + \sin^2 2\theta_{13}\sin^2\theta_{12}\sin^2\Delta_{21}\cos 2\Delta_{31} \\ - \sin^2 2\theta_{13}\sin^2\Delta_{31} \mp \frac{\sin^2(2\theta_{13})}{2}\sin^2(\theta_{12})\sin(2\Delta_{21})\sin(2|\Delta_{31}|) \end{aligned} \tag{2.35}$$

In equation (2.35) the most important parts are highlighted in red. On the one hand the argument of the last sine function is bracketed by absolute value bars. Here, the argument Δ_{31} itself directly refers to the NMO. In case of a NO scenario the argument is defined as negative, while for the IO case the argument becomes positive. This is the reason why the sign of the last term in formula (2.35) depends on the NMO. On the other hand the sine function in red in the beginning of the last term contains the mixing angle θ_{13}, which defines the amplitude of this effect. This kind of approach to determine the NMO is only possible because of the relatively large value[43] for θ_{13}. Nevertheless, medium-baseline experiments have to achieve a relative energy resolution of at least $\Delta m^2_{21}/\Delta m^2_{31} \sim 0.03$, otherwise the two NMO scenarios cannot be distinguished from each other [15]. With an energy resolution of at least 3% at 1 MeV this limit is extremely challenging and poses high demands on the performance of a detector like JUNO [41].

Figure 2.7 shows the survival probability for reactor antineutrinos using a baseline of $L = 53.0\,\text{km}$ close to the solar oscillation maximum where the difference induced by the NMO becomes maximal. While the frequency and the amplitude of the main oscillatory behavior is determined by the solar neutrino mass splitting Δm^2_{21} and the solar mixing angle θ_{12}, respectively, the high-frequency oscillation is caused by the atmospheric splitting Δm^2_{31} which is directly related to the NMO. The black and dashed line show how the survival probability P_{ee} would look like if there were no atmospheric splitting at all. The blue and red curve show the whole survival probability referring to the normal and inverted ordering, respectively. In addition, the magenta gradient in the background indicates the relative amplitude of the

[43] Although θ_{13} is the smallest of all three mixing angles, its value is larger than originally expected.

convolution[44] between the reactor neutrino flux and the neutrino cross section. As figure 2.7 points it out, the oscillation patterns of both NMO scenarios are shifted relatively to each other. By performing a *Fourier analysis* the actual frequencies of the vacuum oscillation pattern can be extracted determining the true nature of the NMO [15].

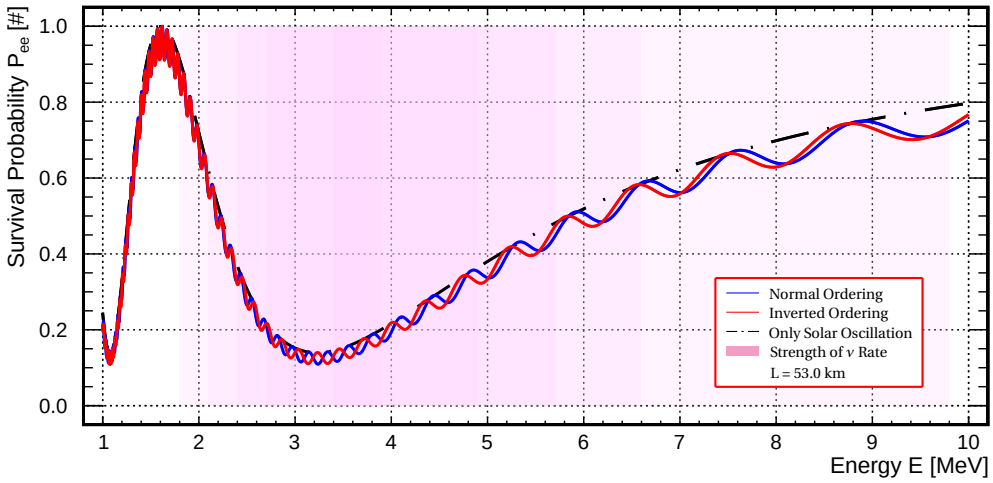

Fig. 2.7 Influence of the NMO on the oscillation pattern

*Illustrated is the **survival probability** P_{ee} for different scenarios. While the **blue** and **red curve** refer to the **normal** and **inverted ordering** case, respectively, the **dashed, black line** only shows **solar oscillation** by setting $\Delta m^2_{31} = 0$. In addition, the intensity of the **reactor neutrino event rate** is indicated in **magenta**. The graph is oriented towards reference [41].*

In contrast to previous studies, current analyses show a global preference of 3.4σ in favor of NO [41]. This result takes data from a lot of experiments into account including studies from solar, atmospheric, accelerator and reactor neutrino experiments with long and short baselines. The data input from atmospheric neutrinos obtained by the Super-Kamiokande experiment currently has the strongest influence on this trend [41]. But although global analyses about the NMO already entered the sensitivity region between 3-4σ, which the JUNO experiment claims to achieve after 6 years of data taking, an independent test of the NMO by performing an alternative approach is still extremely important. Except for DUNE, no single experiment currently under construction will be able to achieve a 5σ NMO measurement in the near future. Consequently, experiments will have to combine their individual strengths in order to exceed this discovery limit. Here, approaches with distinct experimental set-ups will generate the largest synergy effects. *E.g.* a combination between JUNO and the neutrino telescope IceCube-DeepCore or PINGU will lead

[44] The expected measurable neutrino flux.

to a 5σ significance in less than 6 years [2]. Therefore, accomplishing JUNO's main goal – besides the rest of the broad physics program – is still an absolute necessity.

While this section focused on the physical principle of JUNO's neutrino mass ordering determination method, chapter 3 will discuss the experimental realization of this approach in more detail.

Chapter 3

The Jiangmen Underground Neutrino Observatory

The Jiangmen Underground Neutrino Observatory is a 20 kt multipurpose liquid scintillator detector. Its main goal is the determination of the neutrino mass ordering at a 3-4σ significance within an operation period of six years. JUNO detects reactor antineutrinos via the IBD (see figure 1.1) operating with an aspired energy resolution[1] of 3% @ 1 MeV [15] that is required to resolve the NMO induced oscillation pattern [15, 49].

The following chapter presents the JUNO experiment. In section 3.1 the location of the JUNO detector and its geographical relation to the *Taishan Antineutrino Observatory* (TAO) – JUNO's near detector – and the NPPs is shown in more detail while section 3.2 focuses on the conceptual design of the JUNO detector itself. Afterwards in section 3.3, the physics potential and program of the JUNO experiment are discussed in more detail.

3.1 Layout Of The JUNO Experiment

With the ground-breaking ceremony in 2015 the excavation of the Jiangmen Underground Neutrino Observatory had started. The completion of the construction and readiness for data taking is scheduled for 2021. In accordance with the requirements for determining the neutrino mass ordering, the detector has been placed 53 km [15, 49] away from its neutrino sources – the Yangjiang and Taishan nuclear power plants. These reactors lie in the coastal area of South China in the *Jiangmen*

[1] And a spatial resolution of 12 cm [15].

Prefecture of the *Guangdong Province*. Figure 3.1 shows a map of the geographical relation between the JUNO experiment, the NPPs and the surrounding area.

Fig. 3.1 Location of the Jiangmen Underground Neutrino Observatory [139].

*The map shows parts of the **Guangdong province** located in South China. The brighter area indicates the **Jiangmen prefecture** – a subdivision of the Guandong province. Apart from the two cities **Jiangmen City** and **Kaiping** being highlighted by the blue dots, the location of **JUNO** and both NPPs **Yangjiang** and **Taishan** are marked being highlighted by the red dots. The distance of 53 km between the JUNO detector and the NPPs is indicated as well. JUNO's near detector **TAO** is located close to the Taishan NPP.*

As illustrated in figure 3.1, the distance between the JUNO detector and the NPPs is around 53 km. This is the optimized distance for determining the neutrino mass ordering [15, 49]. The JUNO detector is assembled in an underground laboratory between 433 m and 460 m [15] below ground. With a height of 268 m [15] the small *Dashi hill* is located on top of the underground laboratory resulting in a vertical overburden of around 700 m [49] which translates into a shielding against cosmic rays of 2000 m.w.e. [15].

JUNO's neutrino mass ordering determination method relies on an accurate measurement of distortions in the overall oscillation pattern originating from beat

effects between oscillations which correspond to the two mass squared differences Δm^2_{31} and Δm^2_{32} [15, 56]. While the amplitude of the beat is given by $\sin^2 2\theta_{13}$, the relative difference between the beat frequency and the main oscillation is in the order of magnitude of around $\Delta m^2_{21}/\Delta m^2_{31} \simeq 1/30$ [56] (see section 2.4.2). Consequently, this distortion effect in the oscillation pattern is very small and, therefore, the systematics have to be understood to an unprecedented level. Especially the uncertainties of the reactor antineutrino flux have to be known as precisely as possible. One way to minimize these uncertainties is the measurement of a reference reactor antineutrino spectrum by using a near detector with an energy resolution better than the one of the JUNO detector itself. With this approach it is possible to look for fine-structures in the reactor neutrino spectrum that might mimic the NMO signature. The Taishan Antineutrino Observatory[2] will perform such a measurement and is located close to the Taishan NPP [35, 38, 56, 152].

In the following table 3.1 the thermal power and the baseline of all nuclear power plant cores are listed.

Cores	Thermal Power [GW]	Baseline [km]
YJ-C1	2.9	52.75
YJ-C2	2.9	52.84
YJ-C3	2.9	52.42
YJ-C4	2.9	52.51
YJ-C5	2.9	52.12
YJ-C6	2.9	52.21
TS-C1	4.6	52.76
TS-C2	4.6	52.63
TS-C3	4.6	52.32
TS-C4	4.6	52.20

Table 3.1 Thermal power and baseline of the nuclear power plant cores

*Shown are the striven **thermal power** and the planned **baseline** of the six **Yangjiang (YJ)** and four **Taishan (TS) nuclear power plant cores**. While the **construction of all six Yangjiang cores will be completed when JUNO's data taking phase starts**, only **two of the Taishan cores will be ready** for operation. Therefore, in the beginning the total thermal power of the cores will be around 26.6 GW before later on the total thermal power increases up to 35.8 GW [49].*

[2] The detector's designation was determined during a collaboration-wide survey and originally suggested by Jun Wang.

3.2 Conceptual Design Of The JUNO Detector

The JUNO experiment will have two different entrances giving access to the underground lab and leading to the experimental hall – a 616 m deep vertical shaft and a 1340 m long tunnel with a slope of 42.5% [15].

Several distinct subsystems form the JUNO detector. On the one hand there are the water Cherenkov detector and the muon top tracker being used to reduce the muon and radioactive background. On the other hand there is the central detector with its main purpose to detect neutrino signals. Figure 3.2 shows a scheme of the Jiangmen Underground Neutrino Observatory.

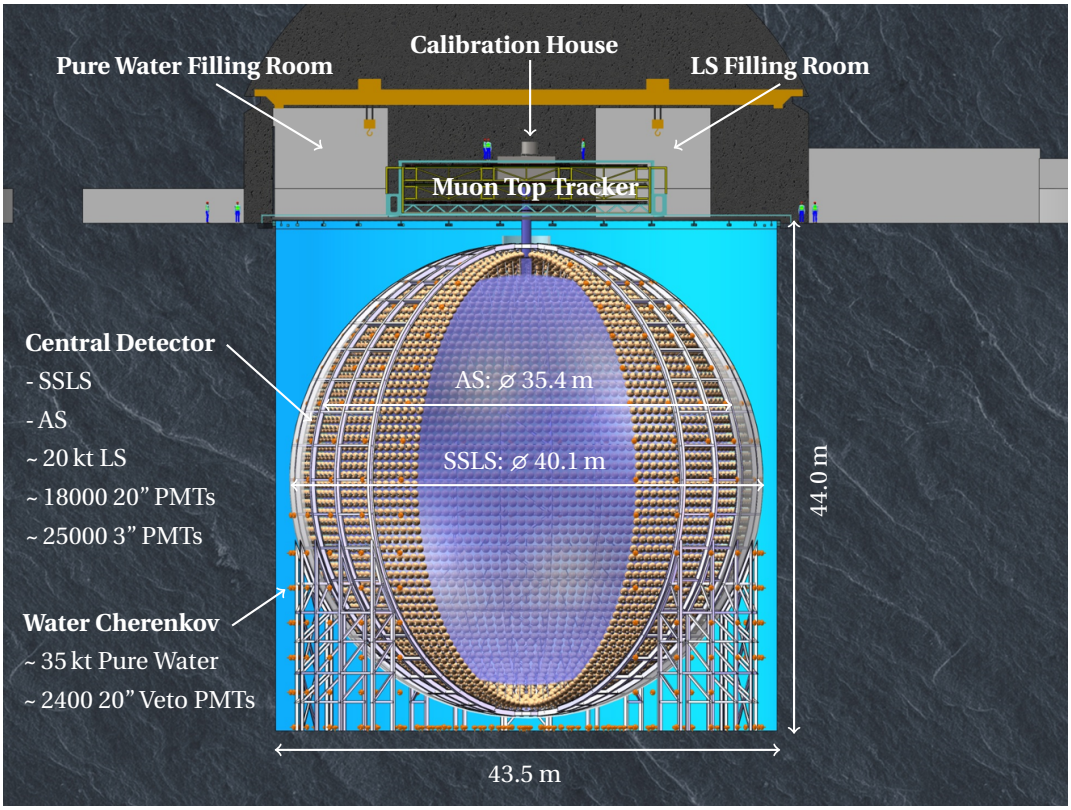

Fig. 3.2 Scheme of the Jiangmen Underground Neutrino Observatory [69].

*Highlighted are the **Acrylic Sphere** (AS) in violet with an inner diameter (ID) of 35.4m, the **Stainless Steel Latticed Shell** (SSLS) in gray with an ID of 40.1m, the **PMTs** in orange and the **Water Cherenkov Detector** in blue. In addition, the **Muon Top Tracker** (TT), the **Calibration Room**, the **Liquid Scintillator** and **Pure Water Filling Room** are illustrated as well.*

In the following subsections the single parts of the JUNO detector are discussed in more detail in order to provide a deeper understanding of the detector's structure and, therefore, of the construction of the calibration system AURORA.

3.2.1 Central Detector

The central detector (CD) is a LS detector with a fiducial mass of around 20 kt. In order to shield the CD from natural radioactivities coming from the surrounding rock and air, the whole structure is submerged in a water pool containing around 35 kt [49] of ultrapure water [15, 49]. While the acrylic sphere (AS) serves as a vessel which contains the LS, the stainless steel latticed shell (SSLS) serves as a support structure for the AS and the PMTs. A PMT coverage of around 77% and a PMT photocathode quantum efficiency of at least 35% in the wavelength range of interest are aspired in order to successfully conduct the JUNO experiment [15]. Figure 3.3 shows a scheme of the CD highlighting the AS and the SSLS.

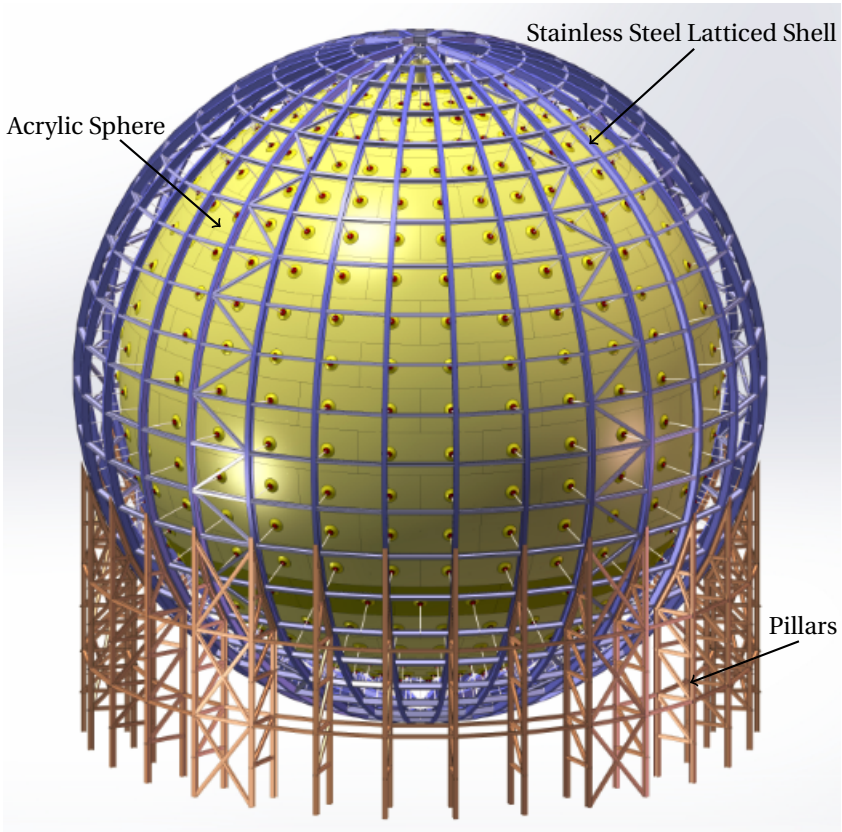

Fig. 3.3 Scheme of the central detector [69].

*Illustrated are the **Acrylic Sphere** (yellow) and the stainless steel support structure consisting of the **Stainless Steel Latticed Shell** (blue) and the **Pillars** (brown).*

Due to the intersection points with the laser calibration system AURORA, the SSLS and the AS are discussed in more detail.

Stainless Steel Latticed Shell

The SSLS is made of the stainless steel alloy `X5CrNiMo17-12-2`[3] which has a higher resistance to corrosion effects in ultrapure water due to its increased molybdenum content [133]. This improvement is a crucial requirement for the SSLS and all other metallic components inside the CD. They are all submerged in the water pool and will remain there for the whole running time of JUNO which is expected to last for at least 20 years [15]. For the same reason, all metallic components of AURORA inside the CD are made of stainless steel `X2CrNiMo17-12-2` which belongs to the same class of alloys[4].

Serving as a support structure for the acrylic sphere and the PMTs, the SSLS is designed as a spherical lattice. This offers several advantages: In contrast to a closed sphere, a lattice structure needs less material and has, therefore, less weight and production costs. In addition, a lattice structure has an increased flexibility and can redistribute mechanical stress more efficiently resulting in a diminished load for each part of the SSLS and the connecting elements [49]. Figure 3.4 shows crucial SSLS components in more detail.

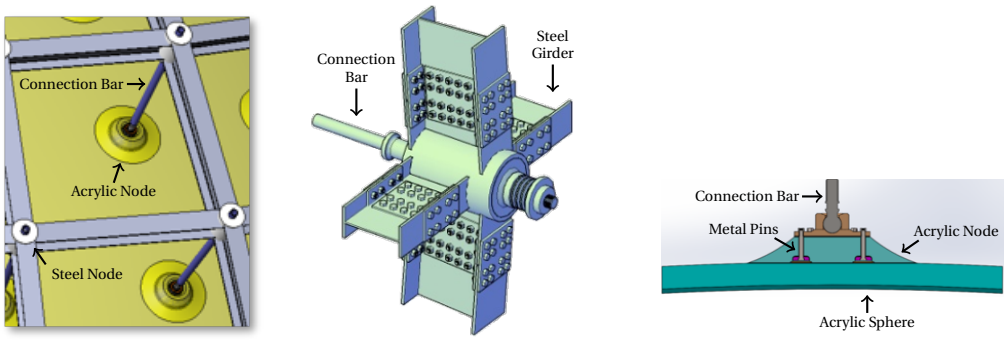

(a) Connection bars (b) Steel node (c) Acrylic node

Fig. 3.4 Support structure of the central detector [69]

The figures show the supporting elements which connect the SSLS with the acrylic sphere. Figure 3.4(a) illustrates the ***connection bars*** *which are positioning and fixing the* ***acrylic sphere*** *inside the* ***stainless steel structure****. While figure 3.4(b) shows the connection point between connection bar and SSLS, figure 3.4(c) visualizes the connection point between connection bar and acrylic sphere in more detail.*

[3] Material Number 1.4401; AISI 316.

[4] Due to the higher resistance to oxidation, the stainless steel 1.4404 has superseded the stainless steel 1.4401. That is why on the European market the stainless steel 1.4401 is barely available. As a consequence, AURORA's metallic components are made of 1.4404 (AISI 316L) which has, apart from the diminished oxidation behavior, the same physical properties like the stainless steel 1.4401.

Looking through the center of the CD targeting the opposite side of the support structure, figure 3.4 illustrates that there are several components which can obstruct the view. Especially the connection bars and the acrylic nodes (see figure 3.4(a) and 3.4(c), respectively) might constitute a real obstacle. This crucial point was taken into account during the design phase of the calibration system AURORA (see chapter 6). As a consequence AURORA's laser beams are tiltable conferring the ability to align their direction even after the filling procedure.

Acrylic Sphere

The AS is made of around 170 3 m×8 m×12 cm *polymethylmethacrylate)* (PMMA) sheets. The polymer PMMA, also known as plexiglass, is a *thermoplast* and, thus, deformable when its temperature[5] exceeds 135 °C [49, 126].

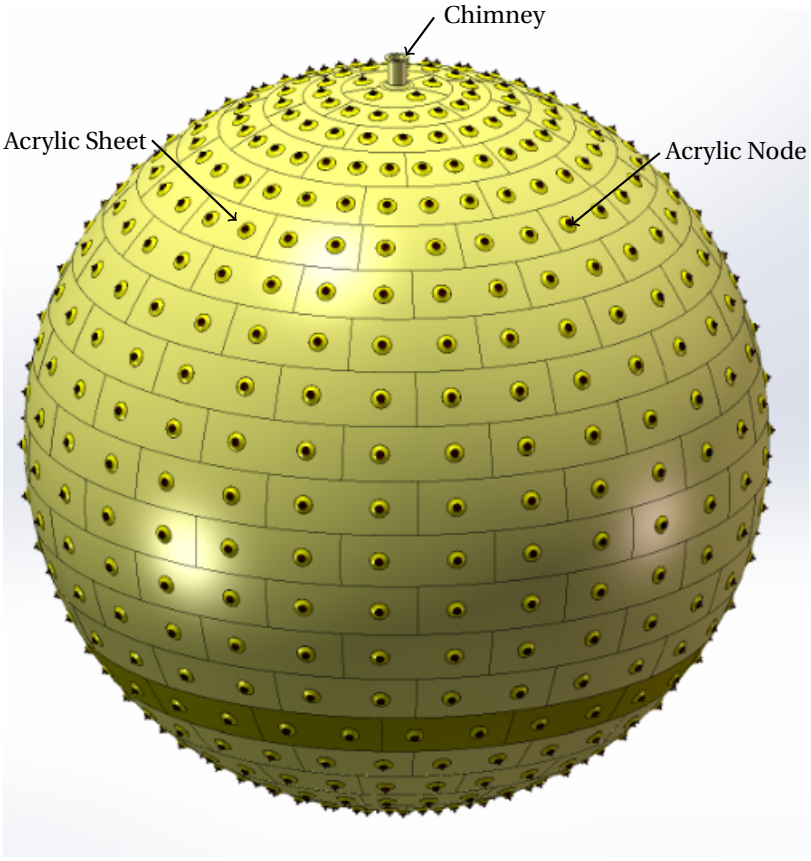

Fig. 3.5 Scheme of the acrylic sphere [69].

Visualized is the acrylic sphere – the vessel of the liquid scintillator. Indicated are also the 3 m×8 m and 12 cm thick ***acrylic sheets*** *(around 170 in total) and the* ***acrylic nodes*** *[49].*

[5] Threshold temperature may vary depending on the deformation method, the monomer additives and the sheet thickness.

Figure 3.5 shows a scheme of the acrylic sphere. After being bent, satisfying a curvature radius of 17.7 m, the acrylic panels are sticked together using the *bulk-polymerization* method [49, 153]. Here, a liquid of monomers are mixed with a radical initiator which starts the polymerization process. Consequently, for the gluing procedure the same compound (PMMA) is used leading to an almost vanishing transition zone between those acrylic sheets. Although the expected disturbance of a light beam which hits such a transition area is negligibly small, the LS calibration measurements performed with the AURORA system will also benefit from tiltable laser beams for this kind of obstacle.

The acrylic vessel is filled with 20 kt of the LS *linear alkylbenzene* (LAB), which is a straight alkyl chain of 10-13 carbon atoms connected to a benzene ring [80]. This organic scintillator is characterized by its excellent transparency and will be optimized via purification procedures striving to reach an *attenuation length*[6] L of at least 20 m at a wavelength of 430 nm [15, 49]. In addition, LAB also possesses a high *light yield* (LY) [88]. These are the two most important properties of LAB, which allow the construction of such a huge spherical detector. If the L or LY value were lower, the final number of detectable photons at the verge of the CD would be too small resulting in an insufficient energy resolution for the JUNO experiment [49].

3.2.2 Veto Detector

Although the veto detector is not directly linked to the calibration system AURORA, the importance of its function for the JUNO experiment is undeniable and, therefore, will be presented briefly in this section. With its main purpose to improve the signal-to-noise ratio, the veto detector surrounds the CD being composed of two distinct subdetectors – the water Cherenkov detector on the one hand and the muon top tracker on the other hand [15, 49].

Water Cherenkov Detector

The water Cherenkov detector is a cylindrical water pool of 44.0 m height and has a diameter of 43.5 m being filled with ultrapure water and equipped with around 2400 20” veto PMTs. The dimensions of the water pool ensure that, independent from the direction, there are always at least 2 m of water between the CD and the pool’s walls or air. This is an effective protection against radioactivity from the surrounding rock and air leading to a reduced background rate. In addition, the veto PMTs inside

[6] According to the reciprocal relation between the attenuation length L, the absorption length L_a and the scattering length L_s, the values of L_a and L_s have to be at least 60 m and 30 m, respectively.

the water pool will detect Cherenkov light, which is emitted by charged particles traversing the pool with a velocity higher than the speed of light in this medium. A valuable tool to further diminish the background rate inside the CD [15, 49].

Muon Top Tracker

On top of the water Cherenkov detector, the muon top tracker (TT) will be installed in order to accurately measure the direction of muons. This will help to improve the signal-to-noise ratio inside the CD as well. The TT was part of the OPERA[7] target tracker. For the JUNO experiment the plastic scintillator strips will be repurposed. One strip is 6.86 m long, 10.6 mm thick and 26.3 mm wide. 64 strips are forming one module being read out on both sides using wavelength shifting fibers and a 64-channel multi-anode PMT from Hamamatsu. In the end, four modules are put together in order to create a sensitive tracker plane of $6.7 \times 6.7\,\mathrm{m}^2$. With two of those planes perpendicular to each other the tracker already provides 2D track information [10]. The muon top tracker in JUNO has three of these layers stacked atop each other with a distance of 1.0 m and 1.5 m covering 25% of the upper water pool surface [15, 49].

3.2.3 Additional Important Areas On-Site

In the following section further underground locations are presented. For AURORA the most important area is the *TT bridge*, as it is the location of all components which are not submerged in the CD. In addition, without any claim to completeness, further structures are mentioned in order to paint a more sophisticated picture of the underground lab.

Underground Assembly Hall, Calibration House and TT Bridge

During the construction phase of the CD, most of the components will not be sent to the experimental hall piece by piece. Smaller elements will be assembled in the *underground assembly hall* and then transported as combined functional units to the experimental hall. The underground assembly hall is 40.0 m long and has 12.0 m and 12.5 m in width and height, respectively, being right next to the experimental hall. It is also connected to the inclined shaft via a small tunnel of 5.7 m in width and 6.5 m in height. This ensures that equipment can be sent via rail car from the surface directly to the underground assembly hall. The PMT array, also relevant

[7] **O**scillation **P**roject with **E**mulsion t**R**acking **A**pparatus – a neutrino oscillation appearance experiment which detected tau neutrinos from an originally pure muon neutrino beam.

for the fiber termination of the AURORA system, will be installed batchwise in the underground assembly hall as well. Consequently, it will be difficult to adjust the laser beam direction beforehand. This is another crucial argument for a fiber termination with the possibility of tilting the laser beams. With this feature an occurring misalignment can be compensated even after the filling procedure [49].
Although AURORA is a subunit of the detector calibration system, none of AURORA's components will be located in the *calibration house* where the other calibration devices are stored, controlled and monitored. As AURORA does not need an environment with temperature control, its components outside the CD will be installed in a rack on the TT bridge. This has the advantage that the electrical cables and the optical fibers can be guided directly into the CD without the necessity to lay these cables through the whole underground lab. Thus, especially for the fragile optical fibers a severe damage potential can be minimized [49].

3.3 Physics Potential Of JUNO

The following section deals with JUNO's physics potential giving a brief overview of the experiment's program. While in section 3.3.1 all aspects concerning neutrino oscillation physics are presented, section 3.3.2 focuses more on the low energy neutrino physics part. Section 3.3.3 is about the exotic sector of JUNO's agenda.

3.3.1 Neutrino Oscillation Physics

Besides the determination of the neutrino mass ordering which was already explained and discussed in more detail in section 2.4.2, the combination of an excellent energy resolution and a large fiducial volume will allow JUNO to perform many other important measurements in neutrino and astro-particle physics. One of these topics is the future unitarity test of the PMNS matrix supported by precision measurements of the solar oscillation parameters θ_{12}, Δm^2_{21} and the atmospheric oscillation parameter $\left|\Delta m^2_{32}\right|$ to better than 1% [107]. Those precision measurements are feasible because with a baseline of 53 km JUNO is exactly located at the oscillation maximum of Δm^2_{21}. Moreover, the atmospheric mixing angle θ_{13} is also accessible in JUNO. However, the optimized baseline for a θ_{13} measurement is around 2 km and, therefore, JUNO, with a baseline of 53 km, will be less precise in comparison to the current θ_{13} results [15, 49].

3.3.2 Low Energy Neutrino Physics

The detection of neutrinos and antineutrinos originating from extraterrestrial and terrestrial sources offers the opportunity to study several other phenomena:

Supernova Burst Neutrinos

Firstly, supernova burst neutrinos which are coming from supernovae in our galaxy. For a supernova at a galactic distance of 10 kpc with an average neutrino energy of around $\langle E_\nu \rangle \simeq 12$ MeV, JUNO already expects 5.5×10^3 [49] neutrino events in the detector. Such a high statistic would help to improve our understanding about the complex mechanisms inside a star at its end [15].

Diffuse Supernova Neutrino Background

Secondly, the diffuse supernova neutrino background (DSNB) being formed by past core-collapse events all over the visible universe. Including information about the *cosmic star-formation rate*, the *average core-collapse neutrino spectrum* and the *rate of failed supernovae*, JUNO expects that a 3σ signal is conceivable after ten years of data taking for typical DSNB assumptions [15, 49]. If no DSNB signal can be found, the new upper limit on the DSNB flux will be almost an order of magnitude better than the current result of Super-Kamiokande [15].

Solar Neutrinos

Thirdly, solar neutrinos being generated in fusion processes inside the Sun's core. On the one hand measurements on the solar neutrino flux will help to investigate the 2σ tension [70] between the values for Δm^2_{21} obtained by reactor and solar neutrino experiments. On the other hand measurements on the solar neutrino flux could increase the precision on the relative element abundances. Depending on the success in background reduction JUNO might even be able to measure the so called *CNO neutrinos*. Those are released during β decays of the isotopes ^{13}N, ^{15}O and ^{17}F (catalysts of the *CNO fusion cycle*) and directly related to the abundance of elements heavier than ^{1}H, abundance X, and ^{4}He, abundance Y, designated as *metallicity*, abundance Z [63]. Consequently, it would be possible to shed some light on the solar matter composition and the current discrepancy[8] between metallicity predictions based on measurements of the Sun's photosphere

[8] The mismatch of element abundances between standard solar model predictions based on photosphere observations and past solar neutrino flux measurements is called the solar metallicity problem.

and metallicity predictions derived from past solar neutrino flux measurements. In addition, JUNO will perform high precision measurements of the low-energy part of the ^{8}B neutrino spectrum[9]. This energy region lies between the low-energy part ($E_\nu < 1\,\text{MeV}$) of the solar spectrum for which even for high densities matter effects are negligible and therefore pure vacuum oscillation dominates and the high-energy part ($E_\nu > 10\,\text{MeV}$) for which matter effects prevail and vacuum oscillation is highly suppressed. This *transition region* between the vacuum- and the MSW-dominated neutrino oscillation is especially sensitive to non-standard interactions which might influence the transition characteristics [15, 49, 157].

Atmospheric Neutrinos

Fourthly, atmospheric neutrinos which are released during particle decays in the Earth's atmosphere. The oscillation of Earth-traversing neutrinos is influenced by matter effects. Consequently, the neutrino mass ordering can also be measured by detecting upward atmospheric neutrinos. Here, the ability to determine the neutrino mass ordering is at a 1-2σ level for ten years of data taking [49]. In addition, atmospheric neutrinos can be used to study CP violation effects on the one hand and to precisely measure the atmospheric mixing angle θ_{23} on the other hand [15].

Geoneutrinos

Finally, geoneutrinos being produced in radioactive β decay processes in the Earth's crust and mantle. By measuring the geoneutrino flux it is possible to learn more about the Earth's chemical composition, especially about the thorium and uranium abundance and distribution inside the Earth's crust and mantle. In addition, studying geoneutrinos will shed light on the power source of the geodynamo which generates the magnetosphere shielding the Earth from the dangerous cosmic ray flux [49]. JUNO expects to record around 300–500 geoneutrino events per year. Consequently, after already six months JUNO would exceed the present world sample of recorded geoneutrinos which includes around 150 events. Unfortunately, due to the same origin[10], geoneutrinos are not distinguishable from the reactor neutrino signal and as a result the separation of both signals is challenging. In JUNO's reactor spectrum analysis the geoneutrino signal will be a free fit parameter assuming a fixed Th/U ratio due to secular equilibrium [15].

[9] Down to ~ 3 MeV.
[10] Radioactive β decay of thorium and uranium.

3.3.3 Beyond Standard Model Searches

In addition to neutrino oscillation and low energy neutrino physics inside the SM, JUNO also provides opportunities to look for new physics beyond the SM. The following section summarizes these exotic searches.

Proton Decay

The JUNO detector contains 20 kt of organic scintillator and, therefore, the target mass provides around 6.75×10^{33} protons giving the perfect opportunity to look for proton decay. Here, the SUSY favored decay channel $p \rightarrow K^+ + \bar{\nu}$ would reveal if SUSY models might be realized in nature [49].

Sterile Neutrinos

Using a 60 MeV/amu cyclotron-driven ^{8}Li source as an additional neutrino source right next to the JUNO detector, the experiment can also look for short-baseline oscillations. Current studies show that this approach completely covers the allowed region of the reactor anomalies and the corresponding global analysis region for the $\bar{\nu}_e$ disappearance channel in a $3+1$ model at a 5σ C.L. after five years of data taking. In addition, based on the same considerations also the entire global analysis region of the $\bar{\nu}_e$ appearance channel would be covered at a C.L greater than 5σ. Consequently, if no oscillation signal is observed, all present anomalies (including LSND and MiniBooNE) will be excluded at a 5σ C.L. [15].

Dark Matter And Nonstandard Neutrino Interaction

Due to the detector's high sensitivity, JUNO can also look for neutrinos which are created in dark matter annihilation reactions performing so called indirect dark matter searches. In addition, JUNO will be able to test nonstandard neutrino interactions, Lorentz and CPT invariance violation. Furthermore, JUNO is able to investigate different exotic phenomena of new physics beyond the Standard Model like anomalous magnetic moments [15, 49].

Chapter 4

Photon Transport In Liquid Scintillators

As already mentioned in chapter 3, JUNO is a neutrino detector filled with around 20 kt of liquid scintillator. AURORA's purpose is to measure the transparency of the liquid by using laser beams which traverse the detector volume. The photon transport inside the scintillator is, therefore, determining fundamental characteristics of the AURORA system, like the chosen laser wavelength. Consequently, this chapter will first focus on liquid scintillators in section 4.1 and the related scintillation mechanism in section 4.2 before it deals with fluorophores, wavelength shifters and JUNO's liquid scintillator mixture in section 4.3. In the end, photon propagation inside a medium is discussed in more detail in section 4.4. Unless specifically stated, the content of this chapter is based on the references [23], [82] and [90].

4.1 Organic Liquid Scintillators

Scintillators are a widely used technology in particle physics to detect and discriminate various types of radiation. Even though there is a large range of different scintillator materials, they all share the common property to emit light – designated as *luminescence* – when charged particles are traversing their atomic, ionic or molecular structure. The luminescence photons are emitted by de-exciting electrons which were excited by the incident radiation in the first place [82]. The JUNO detector is filled with an organic liquid scintillator, and, therefore, this chapter will focus on this type of scintillator. Organic scintillators have in common that their molecular structure possesses at least one *aromatic center* also called *benzene ring*. The special orbital structure of a benzene ring is illustrated in figure 4.1. In general, carbon atoms have in total six electrons in their atomic shell. While two of them

are bound in the first $1s$-orbital[1], the remaining four outer electrons are distributed over the second $2s$-orbital and the $2p$-orbitals. In case of double bonds the orbitals of the carbon's second shell[2] are *sp^2-hybridized* forming three so called sp^2-orbitals, which are energetically identical and coplanar arranged in space (see the 120° angle between the black illustrated orbitals in figure 4.1(a)). In addition, this electron configuration creates a single p-Orbital which is perpendicularly oriented to the sp^2-orbital plane (see figure 4.1(b)). The sp^2-orbitals are forming so called σ-bonds between the carbon atoms and are responsible for the planar, hexagonal shape of the benzene structure. In σ-bonds electrons are strongly bound and do not contribute to the creation of scintillation light. In contrast to that, the remaining p-orbitals are forming a different type of intramolecular connection – so called π-bonds[3] – with less strong bound electrons. The π-electrons are *delocalized* in an electron cloud (see red band structure in figure 4.1(b)) which surrounds the benzene ring, and, therefore, they are much easier to excite. These π-electrons are responsible for the scintillation light.

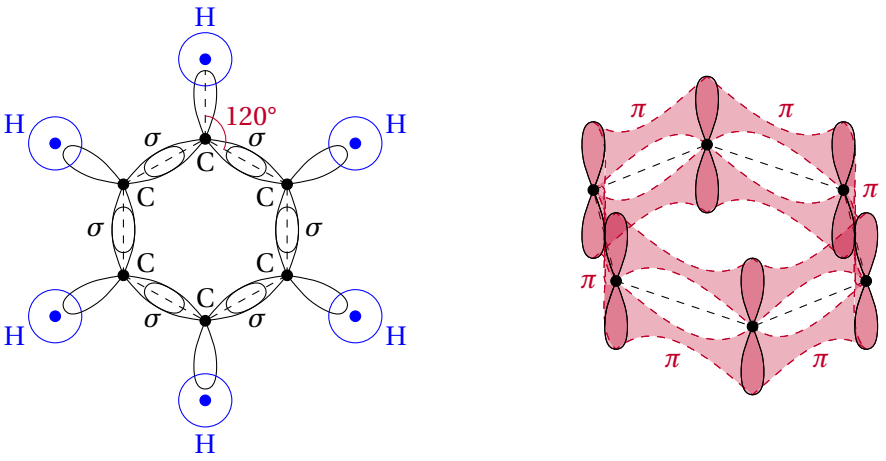

(a) σ-bonds (b) π-bonds

Fig. 4.1 Orbital structure of a benzene ring

*Shown is the **molecular** and **orbital structure** of a **benzene ring** – the **functional group of organic scintillators**. On the left side the **sp^2-orbitals** are illustrated being responsible for the strong σ-**bonds** (drawn in black) between the carbon atoms. On the right the remaining **p-orbitals** are shown creating the π-**bonds** (drawn in red) between the carbon atoms. The graph is oriented towards reference [90].*

Hence, for the scintillation mechanism π-electron systems play an important role. The following section discusses the scintillation process in more detail.

[1] The first shell consists of the $1s$-orbital only.
[2] The second shell consists of the $2s$-orbital and three $2p$-orbitals.
[3] Second bond of the double bond structure.

4.2 The Scintillation Mechanism

During an IBD event in JUNO a reactor antineutrino will interact with a proton of a scintillator molecule generating a neutron and a positron. As the positron carries a charge, it will excite π-electrons in the scintillator molecule along its way through the liquid loosing its kinetic energy, step by step, via scattering and collisions until it is annihilated with a bound electron. Depending on its initial kinetic energy, the energy deposit -$\frac{\mathrm{d}E}{\mathrm{d}x}$ is driven by several processes[4] and can be described by the *Berger-Seltzer* formula[5]:

$$-\frac{\mathrm{d}E}{\mathrm{d}x} = \eta\rho\frac{Z}{A}\frac{1}{\beta^2}\left[\ln\frac{\tau^2(\tau+2)\left(m_e c^2\right)^2}{2I^2} + F(\tau) - \delta - 2\frac{C}{Z}\right] \tag{4.1}$$

Here, the constant $\eta = 2\pi N_a r_e^2 m_e c^2 = 0.1535\,\mathrm{MeV\,cm^2/g}$ [82] with N_a, r_e, m_e and c as *Avogadro's number*, the *classical electron radius*, the *electron's rest mass* and the *speed of light*, respectively. While ρ describes the material's density, β is the ratio between particle velocity v and speed of light c. The parameters Z and A refer to the atomic number and atomic weight of the absorbing material. I stands for the mean excitation potential. The parameter τ describes the ratio between the electron's kinetic energy and its rest mass. The factors δ and C are density and shell correction terms, respectively. The correction function $F(\tau)$ is different for electrons and positrons and defined by the following equations:

$$F(\tau) = \begin{cases} 1 - \beta^2 + \dfrac{1}{8}\dfrac{\tau^2}{(\tau+1)^2} - \ln(2)\dfrac{2\tau+1}{(\tau+1)^2} & \text{for } e^- \\ 2\ln(2) - \dfrac{\beta^2}{12}\left(23 + \dfrac{14}{\tau+2} + \dfrac{10}{(\tau+2)^2} + \dfrac{4}{(\tau+2)^3}\right) & \text{for } e^+ \end{cases} \tag{4.2}$$

The incident positrons will deposit their kinetic energy in the scintillator through scattering and collisions with π-electrons which are, therefore, excited. The energy states of a π-electron in an organic molecule can be schematically illustrated as in figure 4.2 – a so called *Jabłoński diagram*. Here, S_0 refers to the ground state while S_i with $i \geq 1$ denotes electronic excited states. In contrast to the singlet spin-states S_i, the T_i energy levels stand for triplet spin-states. These T_i states cannot be populated directly by excitation. Here, an internal, radiationless transition process takes place – designated as *intersystem crossing* – which involves a spin reversal through spin-orbit coupling. Both electronic state types possess several sublevels –

[4] While for kinetic energies $E > 100\,\mathrm{MeV}$ [23] (number refers to a medium with Z similar to air or water) *bremsstrahlung* is the most dominant process, ionization and excitation are more prominent at lower energies.

[5] In principle, it is the *Bethe-Bloch* formula just modified for electrons and positrons.

so called *vibrational states*. While the gap between electronic states is in the order of a few eV, the spacing between vibrational states is in the order of a few tenths of eV [82].

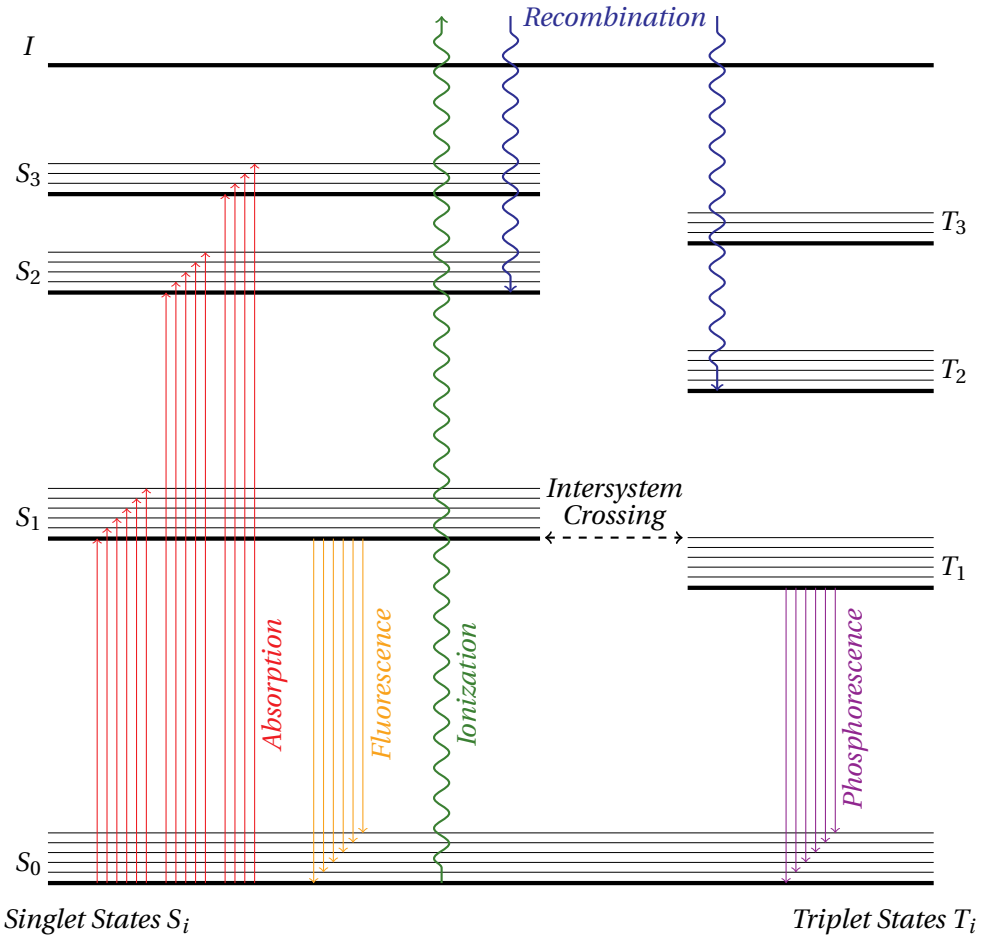

Fig. 4.2 Jabłoński diagram

*Illustrated are the energy levels of the π-electrons in an organic scintillator molecule. Here, S_0 represents the **ground state** of the molecule while the other S_i levels with $i > 0$ are **excited singlet spin-states**. Levels which are designated as T_i with $i > 0$ refer to the so called **excited triplet spin-states**. In addition to the **electronic energy levels**, **vibrational sublevels** are drawn as well. The graph is oriented towards reference [65].*

As shown in figure 4.2, all singlet spin-states and the corresponding vibrational sublevels can be populated by *absorption* (red arrows). Due to a radiationless process designated as *internal degradation*[6], the π-electrons decay into the S_1 state before they populate one of the vibrational energy levels of the ground state S_0.

[6] Due to energy losses via intermolecular collisions and energy dissipation through the emission of phonons, vibrational states normally have lifetimes in the ps range [90].

The emitted radiation from this last transition step is called *fluorescence* (yellow arrows) whereas S_1 is characterized by a typical lifetime of a few ns [82]. Similar to the singlet spin-states S_i, the energy levels T_i can also decay by internal degradation until the T_1 state is reached. The transition between T_1 and S_0 is highly forbidden by multipole selection rules, and, therefore, T_1 is characterized by much longer lifetimes of up to several milliseconds or even hours [23]. The emitted radiation during that relaxation process is called *phosphorescence* (violet arrows). A competitive reaction to the phosphorescence transitions is the interaction of two triplet spin-states T_1 creating a S_1 and S_0 state. Here, the π-electron in the S_1 state will decay into the S_0 state by emitting fluorescence light. In addition to the prompt fluorescence, this intermediate step adds a delayed component to the scintillator's light spectrum.

Due to non-radiative intermediate steps between absorption and scintillation, the re-emitted light in general has longer wavelengths, and, therefore, the scintillator becomes partly transparent for scintillation light. In case of a transparency measurement[7] with laser beams, the optical characteristics of the medium should be well-known, so that processes like absorption/reemission can be avoided or specifically triggered and collected data correctly interpreted. Hence, the following section presents JUNO's scintillator mixture and the related optical properties.

4.3 The JUNO Scintillator Mixture

Due to the size of the JUNO detector, the used liquid scintillator has to fulfill an unprecedented demand on its transparency. Fortunately, a liquid scintillator designated as LAB is characterized by large values for its attenuation length L (see section 4.4) and, hence, shows a high transparency[8]. In addition, this LS also has a high light yield [88] which makes this liquid an ideal candidate as the organic solvent for the JUNO experiment. Only because of these features it is possible to build liquid scintillator detectors as large as JUNO [49]. Thus, an LAB loaded LS will be discussed in more detail in section 4.3.1. In order to diminish self-absorption effects 2.5 g/L of a fluorophore called *2,5-diphenyloxazole* (PPO) and 1 to 4 mg/L of a wavelength shifter called *1,4-bis(2-methylstyryl)benzene* (bis-MSB) are added to the solvent LAB [8, 102]. Section 4.3.2 will focus on the working principle of these additives and their influence on the solvent's transparency.

[7] Like AURORA will perform regarding JUNO's liquid scintillator.
[8] After purification $L \geq 26\,\text{m}$ @ 430 nm [159].

4.3.1 The Organic Scintillator Linear Alkylbenzene

LAB was chosen to be the LS solvent for the JUNO experiment because of its high transparency. The molecular structure of this hydrocarbon is illustrated in figure 4.3.

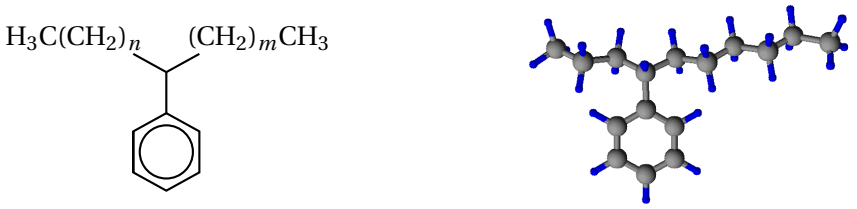

(a) Chemical structure (b) 3D model

Fig. 4.3 LAB molecule

*The figure shows the **chemical structure** of the organic scintillator **linear alkylbenzene**. As indicated on the left, LAB consists of an **aromatic center** (benzene ring) and **two carbon-hydrogen-chains** of the length $n+1$ and $m+1$. On the right a three dimensional model of the LAB molecule is drawn with $n=2$ and $m=5$. Here, the **carbon and hydrogen** atoms are colored **black and blue**, respectively.*

Like every other organic, fluorescent molecule, LAB also possesses a benzene ring in its molecular structure which is responsible for the scintillation light. The additional hydrocarbon chains can vary in their length with $n+m=7-10$ [129]. Table 4.1 presents the maxima's position of the absorption and emission spectrum.

Linear Alkylbenzene (LAB)	
Molecular Formula	$C_9H_{12}(CH_2)_{m+n}$
Absorption Peak	260 nm
Emission Peak	283 nm

Table 4.1 Physical and chemical properties of LAB [90]

*Listed are the most important **spectral properties** of the scintillator **linear alkylbenzene**.*

As listed in table 4.1, LAB absorbs and emits light in the ultraviolet range (see also figure 4.7). In order to enhance the solvent's transparency for scintillation light, so called *fluorophores* (short *fluors*) or *wavelength shifter* have to be added. This will be discussed in more detail in the following section.

4.3.2 Wavelength Shifter To Enhance The Transparency

In order to reduce self-absorption one fluor and one wavelength shifter are added to the solvent LAB. Their working mechanism is based on the *Franck-Condon principle* being illustrated in figure 4.4.

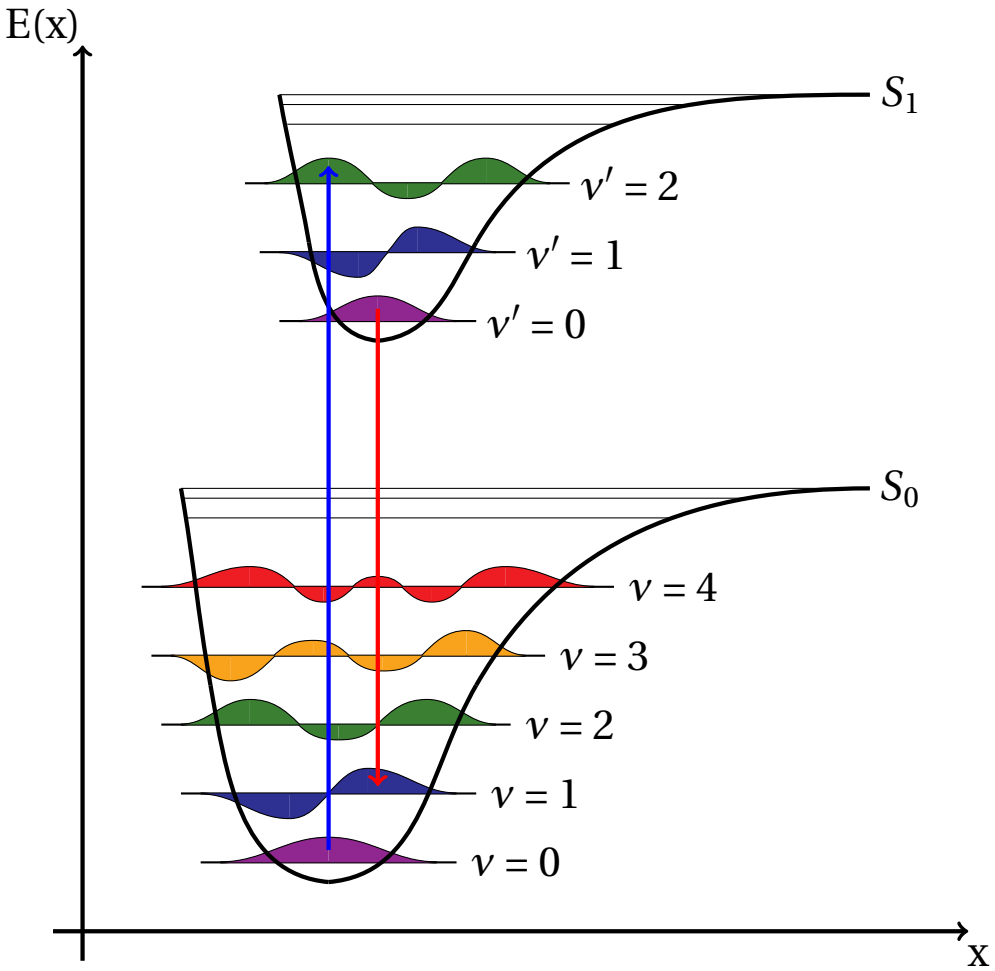

Fig. 4.4 Franck-Condon principle

*Illustrated is the **Franck-Condon principle** which is the reason for the **wavelength shift** – also known as **Stokes shift** – during **absorption** (blue arrow) and **reemission** (red arrow) processes. Besides the electronic energy level S_0 (ground state) and the electronic energy level S_1 (first excited state), several **vibrational sublevels** (ν and ν') and the related **wave functions** are drawn as well. Due to the higher accuracy, a **Morse potential** is used to illustrate the potential energy of electronic states inside a molecule instead of a rectangular quantum well. The graph is oriented towards references [23, 115].*

Figure 4.4 shows the ground state S_0 and the first excited state S_1 as *Morse potentials* of a scintillator's π-electron. In addition, the vibrational sublevels and the corresponding wave functions are illustrated. In case of an excitation, the π-electron is

only allowed to migrate from its initial state to a higher energy states when the wave functions of both sublevels are overlapping in space (see blue arrow). The spatial distribution of the sublevel's wave function changes when the electronic energy state is occupied. Consequently, the originally overlapping sublevels no longer share the same spatial coordinates, and, therefore, the electron cannot relax into the ground state S_0 via the same transition path. By emitting *phonons* the π-electron will loose a fraction of its energy until it populates the energetically lowest sublevel of the excited state S_1. During the de-excitation process the π-electron migrates between two energy states with overlapping wave functions (see red arrow). If the resulting state is not the ground state S_0 with $\nu = 0$, the π-electron will emit further phonons until the lowest energy level is reached. Due to the emission of phonons during the excitation and de-excitation cycle, the re-emitted photon has less energy in comparison to the absorbed one and, therefore, a longer wavelength[9]. Absorption and reemission spectra of such compounds are relatively displaced to each other. The difference in wavelengths between the spectra's maxima is designated as *Stokes shift* [60]. Depending on the fluor, wavelength shifts in the order of 100 nm are realizable. If the wavelength of the re-emitted photon is above the absorption spectrum of the solvent, the probability for re-absorption is already diminished[10] and, therefore, the scintillator transparency significantly increased.

In the JUNO experiment the fluor is PPO. Its spectral properties are presented in the following subsection.

The Fluor 2,5-Diphenyloxazole

Like LAB, PPO also possesses π-electron systems. Figure 4.5 shows the molecular structure of this compound. Besides two benzene rings, the central *oxazole ring* also has a conjugated double bond structure and provides further π-electrons. As it is listed in table 4.2, the absorption peak of PPO is located close to the emission peak of LAB[11], and, therefore, both spectra are widely overlapping [101]. This ensures that most of the emitted radiation undergoes a wavelength shift. In addition, table 4.2 shows that the difference between absorption and emission peak of PPO is around 60 nm [90]. Consequently, the wavelength of the radiation already reaches the UV-threshold of the optical visible range.

[9] This is the reason why these fluorophores are also called wavelength shifters.
[10] Due to small fluor concentrations, the probability for re-absorption by the wavelength shifters is also reduced.
[11] Difference is around 20 nm.

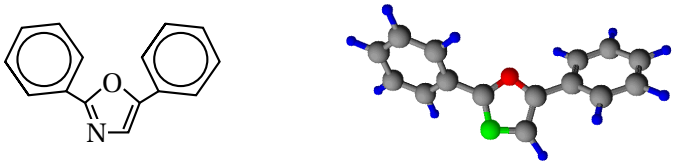

(a) Chemical structure (b) 3D model

Fig. 4.5 PPO molecule

*Illustrated is the **chemical structure** of the fluor **2,5-diphenyloxazole**. The left figure shows in detail that PPO consists of **two hexagonal benzene rings** which are connected via a **third, pentagonal ring structure**. Besides carbon and hydrogen, this third ring contains a **nitrogen and oxygen** atom as well. On the right a three dimensional model of PPO is shown. While **carbon and hydrogen** are drawn in **black and blue**, respectively, **nitrogen and oxygen** are indicated in **green and red**.*

2,5-Diphenyloxazole (PPO)	
Molecular Formula	$C_{15}H_{11}NO$
Absorption Peak	303 nm
Emission Peak	365 nm

Table 4.2 Physical and chemical properties of PPO [90]

*Shown are the most important **spectral properties** of the fluor **2,5-diphenyloxazole**.*

The wavelength shifter in JUNO's scintillation mixture is bis-MSB. The spectral properties of this compound are discussed in more detail in the following section.

The Wavelength Shifter 1,4-Bis(2-methylstyryl)benzene

Similar to LAB and PPO, bis-MSB contains several π-electron systems. In total the molecular structure exhibits three benzene rings which are connected via conjugated double bond chains (see figure 4.6). Table 4.3 provides the most important spectral information about bis-MSB. The location of bis-MSB's absorption peak is close to the emission maximum of PPO[12]. Consequently, the emission spectrum of PPO and the absorption spectrum of bis-MSB are sufficiently overlapping, resulting in an adequate energy transport between those two molecules. The Stokes shift of bis-MSB is around 75 nm [90]. With an emission peak located around 420 nm, bis-MSB emits photons in the blue range of the optical visible spectrum. Besides

[12] Difference is around 20 nm.

LAB's high transparency, the *quantum efficiency* of the light detecting PMTs is close to their maximum in this wavelength range leading to optimal conditions for light detection.

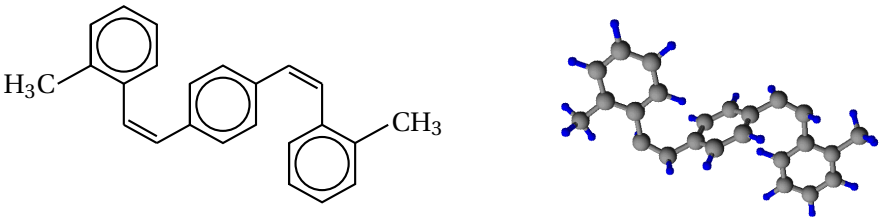

(a) Chemical structure (b) 3D model

Fig. 4.6 Bis-MSB molecule

*The figure shows the **chemical structure** of **1,4-bis(2-methylstyryl)benzene**. On the left it is visible that bis-MSB consists of **three benzene rings**. On the right a three dimensional model of bis-MSB shows the **spatial orientation** of the three rings relatively to each other. Here, the **carbon and hydrogen** atoms are illustrated in **black and blue**, respectively.*

1,4-Bis(2-methylstyryl)benzene (Bis-MSB)	
Molecular Formula	$C_{24}H_{22}$
Absorption Peak	345 nm
Emission Peak	420 nm

Table 4.3 Physical and chemical properties of bis-MSB [90]

*This table lists the most important **spectral properties** of the wavelength shifter **1,4-bis(2-methylstyryl)benzene**.*

There are different mechanisms to transport excitation energy from one molecule to another one. On the one hand energy can be transferred via direct contact. Here, two molecules collide with each other producing thermal energy. In this case no optical photon is emitted in the end and, therefore, cannot be detected by the PMTs. This process is designated as *collision quenching*. Another, rarely occurring mechanism which involves direct contact between the molecules is the process of *complex formation*. Here, a quantum donor and acceptor molecule create an excited state complex in order to transfer the energy. On the other hand the excitation energy can also be transferred without direct contact between two molecules. One possibility is the emission and re-absorption of a real photon. Another mechanism is the so called *Förster resonance energy transport* (FRET). In this case the energy is transmitted via *dipole-dipole interaction*, which is quantum

mechanically described by the exchange of a virtual photon [75]. Due to the dipole nature of this interaction, the efficiency ϵ_F of this energy transport is inversely proportional to the sixth power of the distance r_{DA} between donor and acceptor (see equation (4.3) from [74]), and, therefore, this mechanism only takes place at short ranges (less than 10 nm [39]). The interaction is radiationless, and, hence, no detectable photon is emitted [74].

$$\epsilon_F = \frac{R_0^6}{R_0^6 + r_{\mathrm{DA}}^6} \tag{4.3}$$

Here, R_0 refers to the *Förster radius*, which is defined as the value for which the energy transfer efficiency ϵ_F is 50%. R_0 depends on the donor's quantum efficiency and the size of the overlapping area between donor's emission and acceptor's absorption spectrum [81].

While normally the lifetime of excited states with subsequent fluorescence radiation[13] is in the order of a few ns, the lifetime of excited states with subsequent FRET interactions is shorter [74]. In case of LAB this is the reason why the excitation energy is predominantly transferred to the fluor PPO via the radiationless FRET mechanism. For PPO the situation looks a little bit different. Here, both FRET interactions and the emission of real photons can occur. In contrast to that, due to a missing acceptor, bis-MSB has to emit a real photon in order to de-excite. Because of the short interaction range of the FRET mechanism, it is reasonable to assume that already after a short distance most of the scintillation light is shifted to a wavelength region which is similar to the emission profile of PPO and bis-MSB (see figure 4.7). Consequently, for AURORA it makes sense to measure the liquid scintillator transparency in the same region of the optical spectrum[14].

Figure 4.7 presents the absorption[15] and emission spectra[16] of the solvent LAB, the fluor PPO and the wavelength shifter bis-MSB being colored red, orange and blue, respectively. While the absorption spectra are drawn with a solid line, the

[13] De-excitation by emitting a real photon.
[14] AURORA will perform transparency measurements at a wavelength of around 430 nm.
[15] Also designated as extinction.
[16] There is a small difference between the wavelength of PPO's emission maximum and bis-MSB's absorption maximum reported in tables 4.2 and 4.3, respectively, and the illustrated spectra in figure 4.7. These spectral shifts are caused by interactions between the solvent and solutes during the spectroscopy measurement and, therefore, primarily depend on the choice of the solvent determining to a certain point the spectrum's shape and position. Nevertheless, the derived observations and, thus, the consequences for this thesis, especially for the laser system AURORA, are still valid.

emission spectra are displayed with a dashed line. As already discussed in the previous sections, figure 4.7 also clearly points out that the absorption and emission spectrum of LAB are overlapping with each other. In this region self-absorption takes place which diminishes the scintillator's transparency. In addition, it is visualized to which extent the emission spectrum of LAB overlaps with the absorption spectrum of PPO as well as the emission spectrum of PPO overlaps with the absorption spectrum of bis-MSB. This ensures that the scintillation light is efficiently shifted to higher wavelength values reducing self-absorption and, therefore, increasing the liquid's transparency.

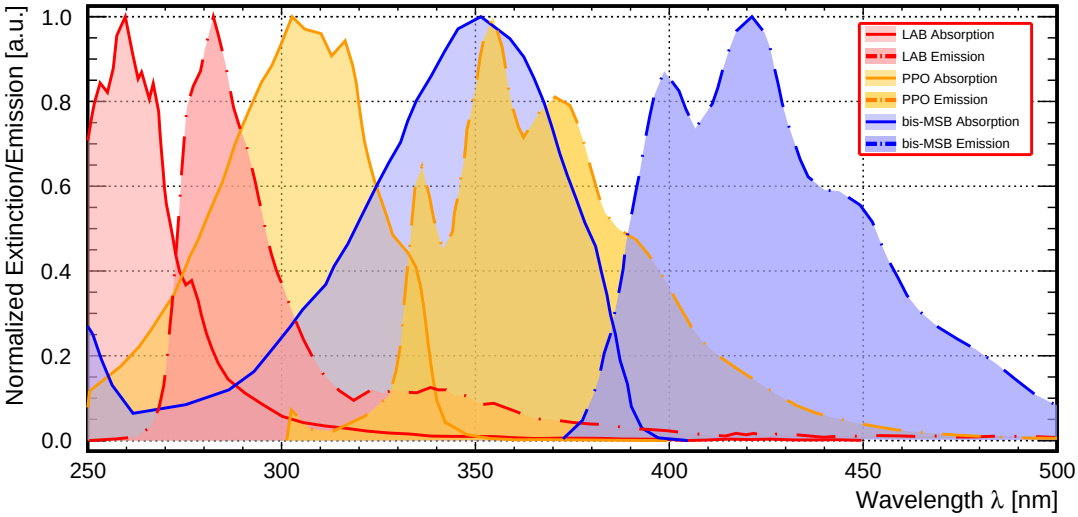

Fig. 4.7 Absorption and emission spectra of LAB, PPO and bis-MSB

*Presented are the **absorption** and **emission spectra** of **LAB**, **PPO** and **bis-MSB** colored **red**, **orange** and **blue**, respectively. While the **absorption spectrum** of a compound is indicated by a **solid line**, the corresponding **emission spectrum** is visualized by a **dashed line**. The data of the individual spectra were extracted from the references [8, 22, 26, 45, 67].*

In addition, the absorption spectrum of bis-MSB covers most of the emission spectrum of LAB. This also enhances the efficiency of the wavelength shift within the scintillator mixture. The absorption spectrum of bis-MSB ends in a wavelength region around 405 nm. While below this threshold absorption and reemission processes will dominate, optical photons will be predominantly scattered above this wavelength. Due to the fact that the fluor PPO and the wavelength shifter bis-MSB are transferring the original excitation energy[17] as real photons, the propagation of optical photons inside a medium plays an important role and, therefore, will be discussed in more detail in the following section.

[17] Scintillation light of LAB.

4.4 Photon Propagation Inside A Medium

The transparency of a medium is related to the photon absorbency of the constituent molecules. Effectively, the decreasing intensity follows an exponential decay law, the *Beer-Lambert-Law*, which is described by the following equation if multiple scattering is negligible and only 1D propagation is considered:

$$I(x) = I_0 \cdot \exp\left(-\frac{x}{L}\right) \tag{4.4}$$

The variable $I(x)$ refers to the intensity of a narrow light beam after a path length x inside a homogeneous medium. I_0 stands for the incident intensity of the light beam and the parameter L is the so called *attenuation length* which depends on the material's optical properties and is in general a function of the wavelength of the transmitted photons [166].

When light is propagating through an absorber, the single photons will be absorbed and scattered by the medium depending on the material's transparency. In case of a narrow light beam, the intensity loss is sufficiently described by the attenuation length L, see equation (4.4). Here, it makes no difference if the photons are absorbed by the material or just scattered following a direction unequal to the initial beam orientation. When dealing with a huge volume – like the liquid scintillator inside the acrylic sphere of the JUNO detector – and a photosensitive surface which covers the whole solid angle[18] the situation looks different. In this case scattered light can still be detected contributing to the overall light yield and, therefore, does not diminish the energy resolution[19] of the detector (see figure 6.1). Consequently, it makes more sense to distinguish between absorption and scattering processes. Following this ansatz, the attenuation length is described as a combination of an *absorption length* L_a and a *scattering length* L_s, which take all the absorption and scattering processes into account [166]. While during absorption the photon is converted into heat and can no longer be detected by the PMTs, in scattering processes the photon's wavelength and/or direction is just altered. The relation between the lengths satisfies the following formula:

$$\frac{1}{L} = \frac{1}{L_a} + \frac{1}{L_s} \tag{4.5}$$

[18] The PMTs are distributed over the whole solid angle of $\int_0^{\pi} \sin\theta \mathrm{d}\theta \int_0^{2\pi} \mathrm{d}\phi = 4\pi$.

[19] While scattering does not reduce the energy resolution, the spatial and time resolutions, however, are diminished due to changing propagation directions and longer travel paths.

The scattering length L_s can be split into several different scattering lengths which only consider individual scattering processes. In the optical wavelength range the most prominent processes are *absorption/reemission*, *Mie scattering* and *Rayleigh scattering* [160]. The corresponding scattering lengths are related to each other via the following equation:

$$\frac{1}{L_s} = \frac{1}{L_{ab,re}} + \frac{1}{L_{Mie}} + \frac{1}{L_{Ray}} \tag{4.6}$$

Which scattering process an optical photon undergoes depends on its wavelength and on the specific molecule it is scattering on. Figure 4.8 illustrates the features of all three scattering processes. Here, the amplitude of the differential cross section is given by the width of the colored areas. While sapphire stands for the parallel polarization component with respect to the initial light beam direction, silver illustrates the amplitude of the orthogonal polarization component.

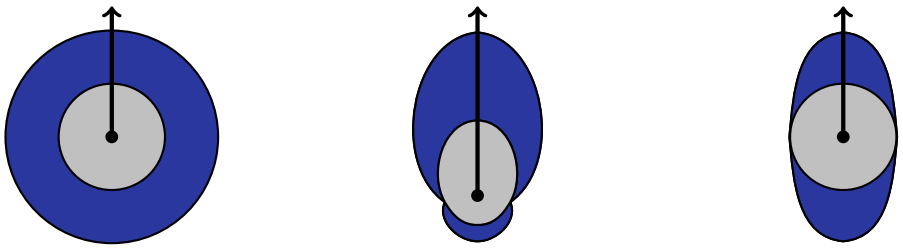

(a) Absorption/Reemission (b) Mie scattering (c) Rayleigh scattering

Fig. 4.8 Scattering processes [66]

*Illustrated is the **spatial distribution of light emission** regarding the three most prominent **scattering processes** in a medium like the liquid scintillation mixture of JUNO – **absorption/reemission** (a), **Mie scattering** (b) and **Rayleigh scattering** (c). Here, with respect to the incident light beam direction, the **orthogonal** and **parallel polarization component** are distinguished from each other by the colors **silver** and **sapphire**, respectively.*

In a liquid scintillator mixture optical photons can be absorbed and re-emitted if the wavelength of the photon lies within the absorption region of the solvent[20] or

[20] Primary the liquid scintilator LAB.

solute[21]. Here, the direction of the re-emitted photon does not follow a specific distribution and is, therefore, isotropic. The following relation applies:

$$\left(\frac{\mathrm{d}\sigma}{\mathrm{d}\Omega}\right)_{ab,re} = const. \tag{4.7}$$

Although above the absorption spectrum of bis-MSB absorption/reemission is rare, chemical reactions in the LS might generate new molecules introducing absorption bands in this wavelength region and, thus, diminish the LS's transparency. Such a chemical aging of the LS could be recognized by AURORA, as a transparency reduction directly influence the distribution of the detected photons inserted by the optical fibers.

Optical photons[22] scatter off small particulates (*e.g.* dust, gas bubbles or water drops) via Mie scattering if the particle's size ranges between the wavelength of the photon and a few millimeters [167]. Here, the emission direction of the scattered photons is strongly anisotropic and varies greatly depending on the particulates' material, shape, orientation and size relative to the photon's wavelength [25, 27]. While for photons with a wavelength similar to the obstacle's extent ($\lambda \approx d$) forward scattering is dominant, the contributions of backward scattering components are increasing with the particulates' sizes ($\lambda < d$) [167]. Due to the large effort to clean the JUNO scintillator by using different purification plants[23] and techniques, see reference [86], the LS's degree of pollution caused by dust or other impurities is expected to be insignificant [32]. Therefore, Mie scattering is expected to be negligible. However, it might be possible that adsorbed contaminants remain at the surface of some CD components (*e.g.* the stainless steel structure or the acrylic sphere). Thus, these impurities might be reintroduced in water or even in the LS by convective processes, slowly polluting those liquids over time [11]. Depending on the contamination's severity, Mie scattering might make a measurable contribution towards the overall scattering amplitude. Another scenario could be the pollution of the CD by dust, gas bubbles or water drops, which might enter the detector through supply pipes. This will additionally enhance the Mie scattering contribution. Due to the anisotropy of Mie scattering and the more distinct forward scattering component, a slowly growing Mie scattering contribution could be identified by the laser system AURORA by comparing the distribution of the scattered photons over subsequent measurements. In case of Mie scattering the relative amount of detected photons will increase on the detector's hemisphere of the exiting laser beam, while in its ab-

[21] Primary the fluor PPO and the wavelength shifter bis-MSB.
[22] In general, the wavelength of optically visible photons ranges between 380 nm and 780 nm [42].
[23] Distillation, Alumina Column, Water Extraction and Nitrogen Stripping.

sence the photon statistics in this area is less pronounced. Consequently, AURORA is a valuable tool to identify degradations in the LS transparency which are caused by the introduction of such microscopic impurities.

In addition to absorption/reemission and Mie scattering processes, photons can also scatter off bound electrons in the scintillator material. This Rayleigh scattering usually takes place when the wavelength of the photon is at least as large as the scatter particle size. Since this is an intrinsic property of the molecules making up the LS, the related Rayleigh scattering length can neither be influenced nor improved by purification and, thus, sets a natural limit to the transparency of a medium [160]. In general, the Rayleigh scattering length exhibits a λ^4 wavelength dependency. In case of an uniform liquid[24] the differential cross section of Rayleigh scattering is given by the following equation:

$$\left(\frac{\mathrm{d}\sigma}{\mathrm{d}\Omega}\right)_{Ray} = \frac{1+\cos^2(\theta)}{2} \tag{4.8}$$

As shown in figure 4.8(c), forward and backward scattering have the same probability. For an ideal Rayleigh scatterer the amplitude of the parallel polarization component becomes zero for a scattering angle $\theta = 90°$ while the differential cross section of the perpendicular polarization is isotropic. LAB, however, is neither completely uniform nor significantly small in comparison to the wavelength of optical photons and, therefore, not a perfect Rayleigh scatterer [27]. Consequently, the parallel polarization component additionally has an isotropic scattering contribution. This characteristic can be expressed by the so called *depolarization ratio* δ [85]. When the intensity $I(\theta)$ of scattered light is split into a parallel and perpendicular component $I_\parallel(\theta)$ and $I_\perp(\theta)$, respectively, their general contributions are given by the following formulas:

$$I_\parallel(\theta) = \frac{\cos^2(\theta)}{2}A + \frac{1}{2}B \quad \text{and} \quad I_\perp(\theta) = \frac{1}{2}A + \frac{1}{2}B \tag{4.9}$$

The depolarization ratio δ is then given for the scattering angle $\theta = 90°$ by the measurable fractions A and B satisfying the following equation:

$$\delta = \frac{I_\parallel(\theta = 90°)}{I_\perp(\theta = 90°)} = \frac{B}{A+B} \tag{4.10}$$

[24] A uniform liquid contains perfect spherical scattering centers and its density is not fluctuating. Here, due to destructive interference, scattering for the parallel polarization component will be eliminated except in the forward and backward direction [166].

At a wavelength $\lambda = 430\,\text{nm}$ for LAB a value of $\delta = 0.31 \pm 0.04$ was found. The Rayleigh scattering length was measured to be $L_{Ray} = 27.0 \pm 2.3\,\text{m}$ [166].

As discussed in section 4.3.2, emission and absorption via FRET interactions will predominantly take place at rather short ranges directly after the excitation of LAB molecules. Subsequently, most of the scintillation light will propagate through the JUNO detector as optical photons being emitted by the fluor PPO and the wavelength shifter bis-MSB. Consequently, it makes sense to perform AURORA's transparency measurements at a wavelength which lies within the effective emission band of the wavelength shifters that is dominated by bis-MSB over large distances. This ensures that changes in the LS's transparency that immediately affect the propagation of the scintillation light can be properly monitored over time. AURORA's laser peak maximum is at 430 nm and, therefore, lies close to the emission maximum of bis-MSB[25].

[25] Spectral maximum of bis-MSB is located at 420 nm.

Chapter 5

Technology Basics

In the course of this thesis various kinds of technologies and hardware components are mentioned. In order to achieve a better understanding for these devices and the related characteristics the following section will focus on their theoretical basics and working principles. Firstly, in section 5.1 the concept of a diode laser is described before, secondly, in section 5.2 the general working mechanism of piezoelectric crystals is discussed in more detail. Finally, in section 5.3 the characteristics of GRIN optics are presented focusing on cylindrical GRIN lenses.

5.1 Diode Lasers

One of the most important components of the developed laser system is the laser source itself. Due to the easy handling, the low costs and the high efficiency a solid state laser with an active medium based on semiconductor materials was chosen. In comparison to other laser types, these diode lasers have the advantage that they are small in size and with a large selection of materials almost every wavelength in the near UV, visible and infrared region is realizable [108, 114].

Semiconductor materials can be distinguished from *metals* and *insulators* by the size of the *gap* between the *valence band* and *conduction band*. While in the valence band electrons are still bound to their atom, the conduction band combines energy states in which electrons are already delocalized moving as free particles through the atomic lattice [108]. In a semiconductor the *gap* between those two bands is usually in the order of 1 eV [43], whereat for a temperature $T = 0\,\mathrm{K}$ the valence band is completely filled with electrons and the conduction band is entirely empty [114].

Figure 5.1 shows the three most important transition processes in a photo-active medium using a simplified two-band structure model.

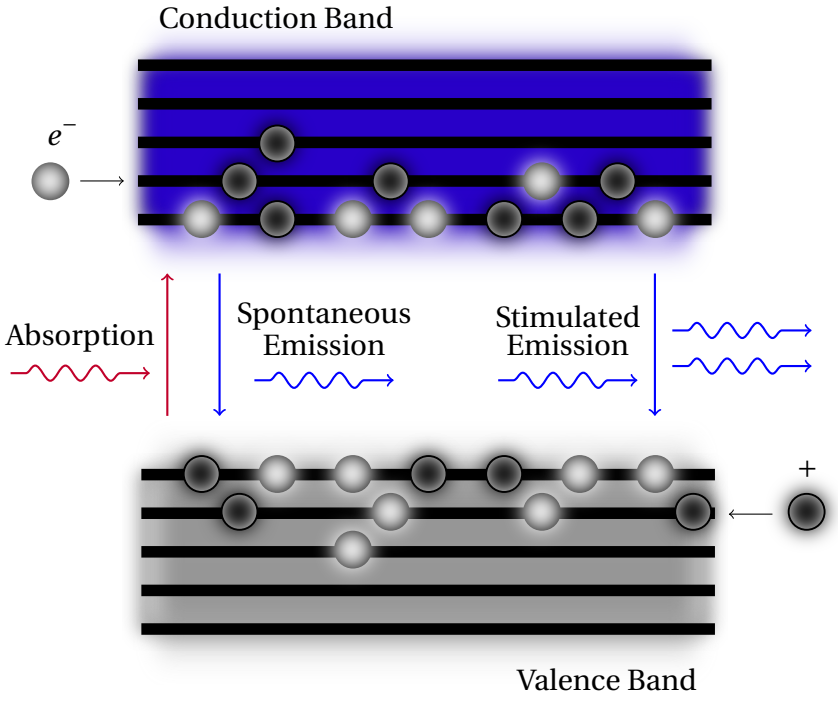

Fig. 5.1 Transition processes inside a photo-active medium

*The figure shows the simplified **two-band structure model** of a photo-active medium. While the **valence band** and the **conduction band** are indicated by the colors **silver** and **blue**, respectively, the **holes** and **electrons** are colored **black** and **white**. In a photo-active medium three important processes may occur – **absorption** (red arrow), **spontaneous emission** and **stimulated emission** of a photon. While the **recombination** of an electron-hole pair (blue arrows) spontaneously occurs after a **characteristic lifetime**, the recombination can also be triggered by an **irradiated photon** with an **energy similar to the band gap**. Here, the emitted photon has the same wavelength, direction and polarization like the irradiated photon additionally sharing a constant phase relation. The graph is oriented towards reference [114].*

For lasing media stimulated emission (third process in figure 5.1) plays an important role as this mechanism is used to generate coherent photon emission [116].

Electrons are Fermi particles and, therefore, can be described by the *Fermi-Dirac statistics*. From this statistics it follows that under standard conditions ($T \approx 300\,\mathrm{K}$) in an intrinsic semiconductor like silicon or germanium (both are elements of the fourth group of the periodic table of the elements) most of the states in the conduction band are not occupied by electrons, as the thermal energy is not sufficient to trigger a transition process [98]. In order to increase the charge carrier density in a semiconductor, its lattice can be doped by elements of the third (p-doped) or the

fifth (n-doped) group. Elements of the third (fifth) group increase the density of holes (electrons) in the valence band (conduction band) [24, 82]. In a laser diode both types of doped semiconductors are combined in order to provide enough charge carriers in the corresponding conduction band (E_c) and valence band (E_v).

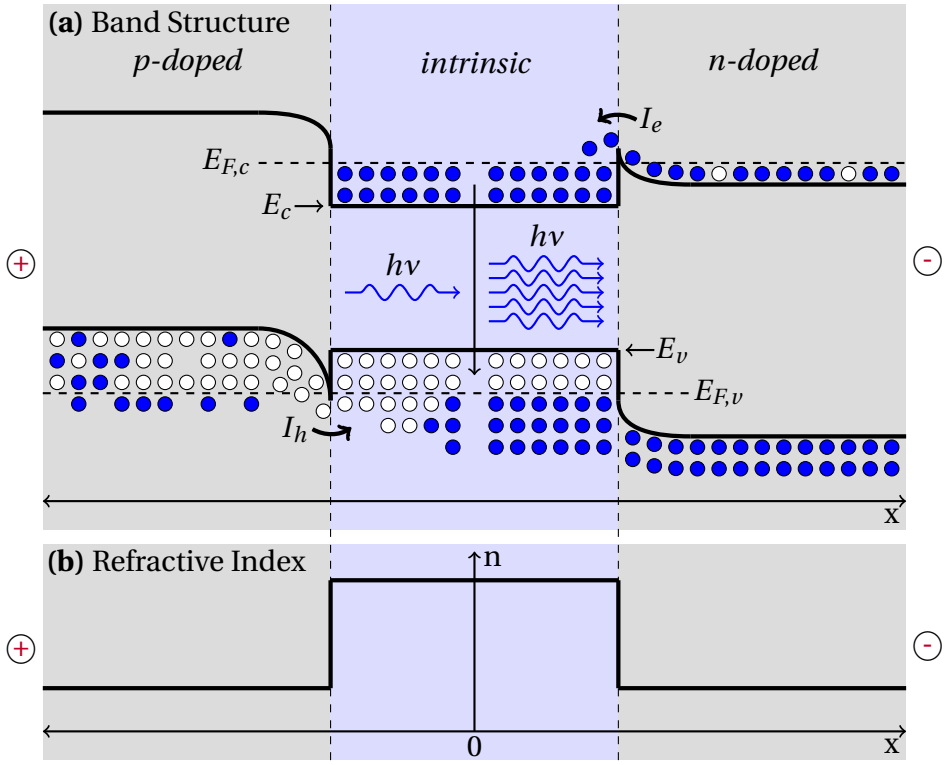

Fig. 5.2 Band structure and refractive index profile of a laser diode

*The figure illustrates the **p-i-n junction** of a laser diode. The **gray colored columns** indicate **p-doped** and **n-doped layers** in the semiconductor material, the **blue column** shows an **intrinsic (undoped) semiconductor layer** which is also designated as the **active zone**. While the **blue dots** refer to **electrons**, the **white dots** stand for **holes**. The **charges on the left and right** indicate the **polarity of the applied voltage**. On the one hand subfigure (a) shows the **band structure** of such a junction, on the other hand subfigure (b) shows its **refractive index profile**, which varies with the applied voltage. The graph is oriented towards reference [78].*

In order to emit light a semiconductor needs its conduction band and valence band populated with electrons and holes, respectively. This so called *population inversion* can be achieved by packing a p-doped, an undoped (intrinsic) and an n-doped layer together like a sandwich (see figure 5.2). By applying a voltage to this kind of configuration, holes of the p-doped layer and electrons of the n-doped layer can overcome their potential wells entering the intrinsic layer. Here, these charge carriers are trapped as the potential wells of the opposite layer are too high. While below a specific current limit only spontaneous emission takes place

(behaves like an LED), above this so called *threshold current* the diode starts to emit laser light. At this point, the above described population inversion is formed continuously injecting electrons and holes into the active zone. An irradiated photon with an energy similar to the gap then starts the stimulated emission process (see figure 5.2(a)) and coherent photon emission occurs [24, 78]. In order to increase the light output the generated photons have to traverse this intermediate layer several times before exiting the semiconductor material. This is realized by total reflection as the refractive index n abruptly decreases at the transition surface of the intrinsic layer (see figure 5.2(b)). Here, n is a function of the present currents I_e and I_h. In addition, photons are contained in the active zone by mirrors[1] at which the photons are reflected. The generated laser light is able to escape this so called *resonator* through a semi-transparent window[2] (dark blue area in figure 5.3) also designated as an edge.

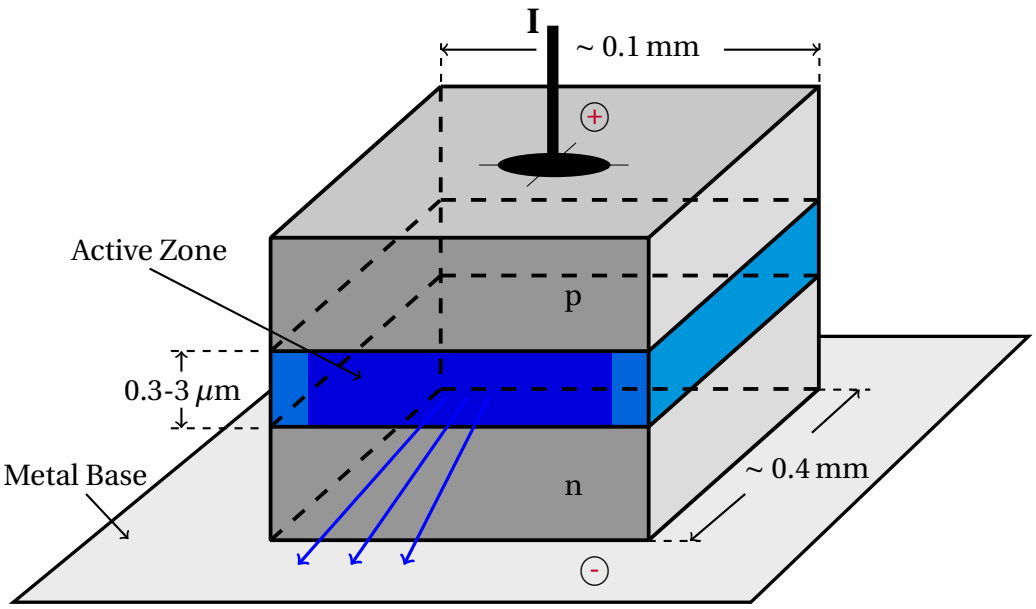

Fig. 5.3 Edge emitting laser diode

*Shown is a simplified drawing of an **edge emitting laser diode**. Illustrated are the **semiconductor crystal** with the **active zone** and the **metal base**. In addition, the typical dimensions of an edge emitting laser diode are drawn as well. An applied current will generate the required **population inversion**. The laser light (drawn as blue arrows) is then a result of the **simultaneous relaxation** of these electrons during the **stimulated emission** process. The graph is oriented towards reference [43].*

[1] In the majority of cases these mirrors are just untreated crystal surfaces which are arranged perpendicularly to the threshold surface.
[2] Chemically treated crystal surface.

Figure 5.3 presents the dimensions of a typical edge emitting laser diode. While the whole crystal structure is less than 1 mm in size, the height of the active zone is with around 1 μm even smaller. For a laser diode and, therefore, also for AURORA this has two important consequences. On the one hand with an edge width and a wavelength of the traversing photons in the same order of magnitude diffraction takes place. This is the reason why in general the beam profile of diode lasers shows characteristic diffraction circles. On the other hand the diffraction itself leads to huge aperture angles of around 6° -12° in the horizontal direction of the active layer and 15° - 40° in the vertical direction of the active zone [120]. In AURORA's case the laser beam is collimated via an aspheric lens positioned in front of the laser diode in order to collimate the beam reducing the intensity loss caused by a highly divergent beam path.

The emitted photons of a laser diode do not have all the same wavelength. Instead, the outgoing light exhibits a narrow wavelength distribution. One reason for that is the band structure of a laser diode. Here, not only one but several types of orbitals of each atom contributes to the band structure of both the valence and conduction band. These energy levels spatially and energetically overlap with each other. Consequently, the photon which triggers the stimulated emission and, therefore, determines the wavelength of the photon cascade can have various wavelengths [97]. In addition, line broadening effects slightly reshape the emission spectrum of a diode laser. On the one hand electrons and holes can interact with phonons and defects in the lattice structure, on the other hand natural broadening based on the Heisenberg uncertainty principle may occur. Nevertheless, the final distribution with a typical peak width of only a few nanometers is still narrow [114, 116]. In AURORA's case the emission spectrum (peak-shaped) has a width of around $\sigma = 4.4 \pm 0.6$ nm. A more detailed discussion about the laser diode's characterization measurements can be found in section 6.2.1.

5.2 Piezoelectric Crystals

Another important component of the laser system is the *fiber termination holder* (FTH), which is responsible for the adjustment of the laser beam direction inside the JUNO detector. This part of the system has to be mounted onto the SSLS, and, therefore, it is located close to the PMTs (see chapter 3) whose performance can be easily influenced by electromagnetic fields. In order to avoid any disturbances in the PMTs' performance it is mandatory that the controlling element of the FTH does not generate any external magnetic field which exceeds a value[3] of 5 μT [156]. Besides issues with waterproofness and high costs, this was already a reason to exclude ordinary electric devices in advance. On the contrary, piezo crystals are not conductive. Consequently, they do not generate any external fields in the static mode[4] representing an ideal candidate for the realization of a control device.

From an electronic point of view, piezo actuators can be treated as capacitors with the piezo crystal positioned between the capacitor's plates like a dielectric medium [91]. The necessary charging currents typically range from a few μA up to a few mA [110]. In case of AURORA's actuators the maximally possible current provided by the piezo driver is 75 mA [125]. With a diameter of 11 mm, the generated magnetic flux density ($|\vec{B}|$) of AURORA's piezo actuators will not exceed 3 μT on their lateral surface during the charging procedure. Thus, the magnetic field is still below the acceptable limit of 5 μT and does not pose any threat to the PMTs' performance. Measurements regarding the magnetic field of AURORA's piezo actuators are discussed in more detail in section 6.3.2.

Figure 5.4 shows the lattice structure of *lead zirconium titanate* – a common piezoelectric ceramic which is also used for the AURORA system. Lead zirconium titanate (PZT) lattices belong to the group of *perovskite structures*. As shown in figure 5.4, Pb^{2+} cations and O^{2-} anions are forming a face-centered cubic unit cell while additionally a Zr^{4+} or a Ti^{4+} cation is placed in the center of this lattice structure. If the temperature T is smaller than the *Curie temperature* T_C, the centered Zr^{4+}/Ti^{4+} ions are displaced and a dipole moment $\vec{p}$ occurs inside the unit cell. Without any external electrical field applied the orientation of the unit cells' dipoles is randomly distributed and no piezoelectric properties can be observed. On the contrary, if an external electrical field is applied, the individual dipoles are realigned orientating towards the electrical field lines. Here, the Zr^{4+}/Ti^{4+} ions are displaced along the

[3] Limit was set to 10% of the Earth's magnetic flux density ($|\vec{B}| \approx 50\,\mu$T in Central Europe).
[4] Piezoelectric elements are operating in the static mode as long as a direct voltage signal is applied.

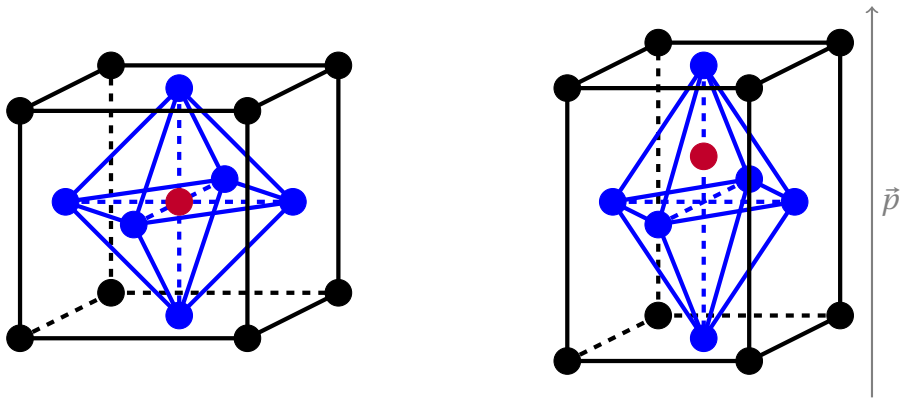

(a) Above Curie temperature $T > T_C$ (b) Below Curie temperature $T < T_C$

Fig. 5.4 Crystalline structure of lead zirconium titanate

*The figure illustrates the **lattice** of a **crystalline lead zirconium titanate structure** with the chemical formula **Pb**$[\boldsymbol{Zr}_x \boldsymbol{Ti}_{1-x}]$ **O**$_3$. While the **Pb**$^{2+}$ **cations and O**$^{2-}$ **anions** are colored **black and blue**, respectively, the **Zr**$^{4+}$ and **Ti**$^{4+}$ **ions** are colored **red**. The index x indicates the fraction of unit cells which contain a Zr^{4+} or a Ti^{4+} cation. While figure 5.4(a) shows the **lattice structure above** a material-dependent **Curie temperature** T_C, figure 5.4(b) shows the same structure **below this temperature threshold**. In this case the Zr^{4+}/Ti^{4+} ion is displaced from the center and a **dipole moment** $\vec{p}$ **occurs** (**gray arrow**). The graph is oriented towards references [53, 93].*

polar axis[5] of the octahedral structure formed by the O^{2-} anions. In the end the dipoles are all oriented in the same direction and the piezoelectric material becomes polarized. Additionally, the uniform orientation also causes a dilation[6] in the lattice structure [21]. This kind of behavior is designated as the *inverse piezoelectric effect*[7]. For PZT materials a stretching (or compression) of around 0.1% of the original crystal length is realizable [93]. In AURORA's case the piezoelectric crystals have a length of 4.3 cm with a maximal dilation of 48.0 μm [20]. This is the available stroke which can be used in order to tilt AURORA's laser beams inside the JUNO detector by at least 1.0°. A more detailed discussion about the electro-mechanical realization can be found in section 6.3.

[5] Blue, dashed lines in figures 5.4(a) and 5.4(b).
[6] If the polarity of the electrical field is reversed, the tension is turned into a compression.
[7] As the name points it out, there is also a *direct piezoelectric effect* which describes the occurrence of electrical charges on a crystal's surface if the lattice structure experiences mechanical stress.

5.3 Gradient-Index Lenses

Besides the laser diode and the piezoelectric ceramics, another important technology are GRIN lenses. They are directly mounted on the fiber termination collimating the laser beam underwater after the light is decoupled from the fiber[8]. As already mentioned in the chapters before, AURORA will measure and monitor the optical transparency of the LS inside the JUNO detector. In comparison to other laser systems, AURORA will not only determine the attenuation length L but also the scattering length L_s and the absorption length[9] L_a. One crucial aspect of disentangling those optical lengths from each other is the collimation of the laser beams. In addition, a collimated light beam offers the opportunity to perform these measurements at higher intensities, as the laser spot size fits into the area between the large PMTs protecting those from direct illumination. Consequently, the following section will focus on the working principle and the related advantages of GRIN optics components. Unless specifically stated, the content of this section is based on the reference [62].

In general, the range of angles over which an optical component, *e.g.* a fiber or lens, is able to accept or emit light is defined by the *numerical aperture* (NA). In case of an optical fiber the NA satisfies the following formula:

$$\mathrm{NA} = n \cdot \sin\varphi = \sqrt{n_{core}^2 - n_{clad}^2} \tag{5.1}$$

Here, n refers to the refractive index of the medium from which the light couples into the fiber. In this case φ is the acceptance angle of the fiber[10]. The parameters n_{core} and n_{clad} stand for the refractive indices of the fiber's core and cladding material, respectively [150].

Incorporating the refractive index in its definition, the NA remains constant for a light beam while transiting from one medium into another one. For optical fibers a wide variety of NAs are realizable ranging around NA = 0.10 – 0.55 [145, 146, 150]. In case of JUNO, if a light guiding fiber terminated at the verge of the detector having a NA = 0.50, more than 12% of the photosensitive area would be directly illuminated[11]. The recorded events in this area would be a superposition of direct illumination and scattered light diminishing AURORA's sensitivity for disentangling

[8] A more detailed discussion about AURORA can be found in chapter 6.
[9] L_a can be calculated via equation 4.5 if L and L_s are known.
[10] The refractive index n can also refer to the medium into which the light decouples after propagating through the fiber. In this case φ describes the aperture angle of the fiber.
[11] Disregarding any scattering processes.

the scattering length L_s from the absorption length L_a. This is the reason, why AURORA's light beams should be sufficiently collimated. While in air for example *aspheric lenses* with their curved surfaces are sufficient to collimate a divergent light beam, those lenses are no longer an option in media like water[12]. Here, due to the similar refractive indices between the lens' material ($n \approx 1.48$ at 430 nm [148]) and the surrounding medium ($n \approx 1.34$ at 430 nm [149]), the refraction is insufficient and collimation becomes extremely challenging. GRIN lenses do not need curved surfaces with large differences between the refractive indices at the transition surface to refract light. This is why they are a perfect alternative to ordinary lenses.

In contrast to an ordinary lens, GRIN lenses can be cylindrically shaped and consist of an inhomogeneous dielectric material with a refractive index distribution that has a maximum at the optical axis and decreases continuously from the axis to the periphery along the transverse direction. In such a medium, rays are curved towards higher refractive indices following a sinusoidal trajectory (see figure 5.5). AURORA's GRIN lenses exhibit a refractive index distribution $n\left(x,y,z\right)$ which is similar to the transverse parabolic profile expressed by relation (5.2) and, therefore, will be used for the following discussion:

$$n^2\left(x,y,z\right) = \begin{cases} n_0^2\left[1-g^2\left(z\right)\left(x^2+y^2\right)\right] & \text{for } r=\sqrt{x^2+y^2} \le a,\ 0 \le z \le d \\ 1 & \text{otherwise} \end{cases} \tag{5.2}$$

Here, n_0 refers to the refractive index at the optical axis and a and d stand for the radius and thickness (length) of the lens, respectively. The expression $g\left(z\right)$ is the so called *gradient parameter* which is a slowly varying function that describes the evolution of the refractive index along the z-axis.

While in this definition the lens is surrounded by vacuum ($n = 1$), in AURORA's case the GRIN lenses are located in the CD's buffer layer, and, therefore, they will be submerged in ultrapure water. Consequently, the refractive index outside the lens will have a value of $n = 1.3378$ [149] for the laser's wavelength of $\lambda = 430\,\text{nm}$. In contrast to ordinary lenses, GRIN optics exhibit an improved collimation performance in a medium with a higher refractive index. This behavior can be explained by the cylindrical shape, as oblique beams are refracted towards the normal if the optical density of the surrounding medium is higher than the one of the lens (*Snell's Law*).

[12] AURORA's laser light will decouple from the fibers inside the CD's buffer area which is filled with water.

Mathematically, the propagation of rays close to the optical axis[13] (aligned along the z-axis) inside inhomogeneous and dielectric media can be studied by solving the following linear second-order differential equation:

$$\ddot{x} + g^2(z)\, x = 0 \tag{5.3}$$

Assuming a cylindrical and, therefore, symmetric GRIN medium, the ray equation for the y-coordinate follows from analogy. The dots in equation (5.3) denotes derivatives with respect to z.

The solution of equation (5.3) gives the position $x(z)$ and slope $\dot{x}(z)$ of a ray trajectory's point P. Here, the solution can be expressed as a combination of two linearly independent particular solutions which are designated as an axial ray $H_a(z)$ and a field ray $H_f(z)$ [61]. With respect to a reference plane, *e.g.* the input face of a GRIN lens ($z = 0$), the axial ray is defined as the paraxial ray which originates at the optical axis ($H_a(0) = 0$) and has a slope of $\frac{\pi}{4}$ ($\dot{H}_a(0) = 1$). In contrast to that, the field ray leaves the reference plane parallel to the optical axis ($\dot{H}_f(0) = 0$) at the unit height ($H_f(0) = 1$). The general solution of equation 5.3 is given by the following relations:

$$x(z) = H_f(z)\, x_0 + H_a(z)\, \dot{x}_0 \tag{5.4}$$

$$\dot{x}(z) = \dot{H}_f(z)\, x_0 + \dot{H}_a(z)\, \dot{x}_0 \tag{5.5}$$

Here, the equations 5.4 and 5.5 give the position and slope for any z for a ray that leaves the reference plane at the position x_0 with a slope $\dot{x}_0$. The general forms of $H_a(z)$, $\dot{H}_a(z)$, $H_f(z)$ and $\dot{H}_f(z)$ are given by the following equations:

$$H_a(z) = \frac{1}{\sqrt{g_0 g(z)}} \sin\left[\int_0^z g(z')\,\mathrm{d}z'\right] \tag{5.6}$$

$$\dot{H}_a(z) = \sqrt{\frac{g(z)}{g_0}} \cos\left[\int_0^z g(z')\,\mathrm{d}z'\right] \tag{5.7}$$

$$H_f(z) = \sqrt{\frac{g_0}{g(z)}} \cos\left[\int_0^z g(z')\,\mathrm{d}z'\right] \tag{5.8}$$

$$\dot{H}_f(z) = -\sqrt{g_0 g(z)} \sin\left[\int_0^z g(z')\,\mathrm{d}z'\right] \tag{5.9}$$

The quantity g_0 refers to the value of the gradient parameter at the reference plane.

[13] Designated as paraxial rays.

As already mentioned AURORA's GRIN lenses are directly mounted on the fiber termination using an acrylic glue for the interface. The fiber itself illuminates the planar input face of the GRIN lens as an on-axis light source at a working distance $d_0 = 0.0\,\text{mm}$. Figure 5.5 illustrates a more general case for the maximally possible acceptance angle[14] φ of the GRIN lens for the working distance $d_0 \neq 0.0\,\text{mm}$.

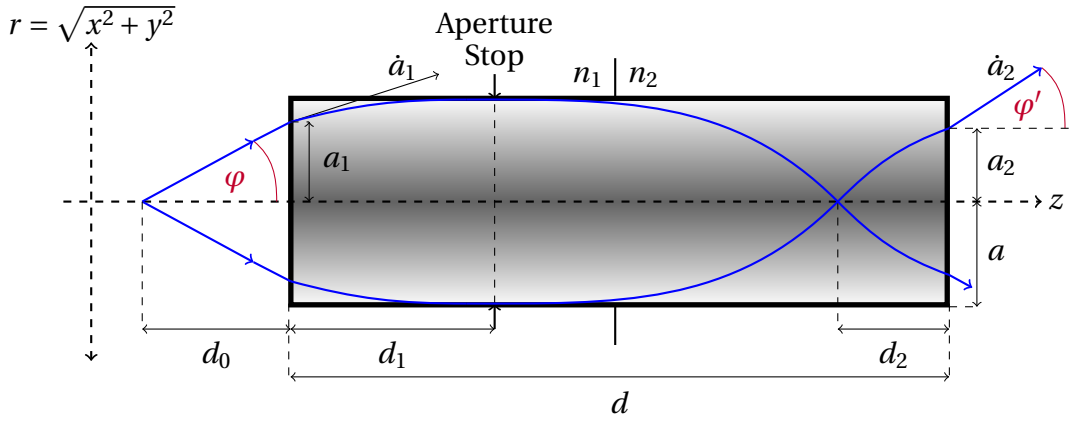

Fig. 5.5 Light propagation inside a gradient-index lens

*The figure shows the **working principle** of a **gradient-index lens**. Indicated by the **gray color**, the **refractive index** has a **maximum value** along the **optical axis** (center of the lens) and continuously decreases when going radially outwards. In such an optical medium **oblique rays** are refracted during their propagation through the lens being curved towards higher refractive indices. The result is a **sinusoidal trajectory** of the light beam (blue arrows). The graph is oriented towards reference [62].*

Here, the optical axis of the lens is aligned along the z-axis. The parameters d and a refer to the thickness (length) and radius of the GRIN lens, respectively, while φ stands for the acceptance angle. In addition, the parameters a_1 and $\dot{a}_1$ specify the maximally acceptable radius and the slope of the ray inside the lens at the transition surface. With respect to the input face, the position of the *aperture stop*[15] is given by the distance d_1. The parameters a_2 and $\dot{a}_2$ refer to the radius of the illuminated spot on the output face and the related slope of the exciting ray, respectively. The quantity d_2 stands for the distance between image plane and output surface. If d_2 is negative (positive), the image will be virtual (real) and the outgoing light beam is divergent (convergent). While the angle φ' stands for the aperture angle of the GRIN lens, the parameters n_1 and n_2 refer to the refractive indices of the surrounding media at the input and output face, respectively.

[14] Indicated in red.
[15] Defines the ray cone angle at the image point.

As shown in figure 5.5, rays inside a GRIN lens are bent following a sinusoidal trajectory. The position and slope of the ray is then given by the following two equations:

$$x(z) = R(z)\sin\left[\int_0^z g\left(z'\right)\mathrm{d}z' + \delta_0\right] \tag{5.10}$$

$$\dot{x}(z) = g(z)\,R(z)\cos\left[\int_0^z g\left(z'\right)\mathrm{d}z' + \delta_0\right] \tag{5.11}$$

Here, the amplitude $R(z)$ and phase δ_0 are given by the following formulas:

$$R(z) = \frac{\sqrt{1+\left(n_0 g_0 d_0\right)^2}}{n_0 d_0\sqrt{g_0 g(z)}} = \frac{\sqrt{\dot{x}_0^2+\left(g_0 x_0\right)^2}}{\sqrt{g_0 g(z)}} \tag{5.12}$$

$$\delta_0 = \tan^{-1}\left(n_0 g_0 d_0\right) = \tan^{-1}\left(\frac{g_0 x_0}{\dot{x}_0}\right) \tag{5.13}$$

Taking into account that only rays will be confined in the lens for which $R(z) \le a$ with $0 \le z \le d$ is fulfilled, the cone of light which reaches the input face is limited. The radius of the maximally acceptable light spot on the input face is, therefore, defined by the following equation:

$$a_1 = \frac{n_0 d_0\sqrt{g_0 g(z)}}{\sqrt{1+n_0^2 g_0^2 d_0^2}}\,a \tag{5.14}$$

Consequently, the numerical aperture of the GRIN lens for the input face is given by the following formula:

$$\mathrm{NA_{in}} = n_1\sin\varphi = \sqrt{\frac{a_1^2}{a_1^2+d_0^2}} = \frac{n_0 a\sqrt{g_0 g(z)}}{\sqrt{1+n_0^2 g_0\left(a^2 g(z)+d_0^2 g_0\right)}} \tag{5.15}$$

The evolution of the position $x_m(z)$ and the slope $\dot{x}_m(z)$ of the marginal rays inside the lens can be described by the following relations:

$$x_m(z) = a_1 F(z) \tag{5.16}$$

$$\dot{x}_m(z) = a_1\dot{F}(z) \tag{5.17}$$

Where $F(z)$ and $\dot{F}(z)$ are given by the following definitions:

$$F(z) = H_f(z) + \frac{H_a(z)}{n_0 d_0} \quad \text{and} \quad \dot{F}(z) = \dot{H}_f(z) + \frac{\dot{H}_a(z)}{n_0 d_0} \tag{5.18}$$

The distance d_1 between input face and aperture stop of the GRIN lens is defined by the following equation:

$$\tan\left[\int_0^{d_1} g\left(z'\right)\mathrm{d}z'\right] = \frac{1}{n_0 g_0 d_0} \tag{5.19}$$

While the radius a_2 of the light spot on the output face and the related slope of the marginal ray inside the lens at the transition surface is given by the equations (5.16) and (5.17) with $z = d$, the distance d_2 between output face and image plane and the numerical aperture of the outgoing light cone is given by the following formulas:

$$d_2 = -\frac{n_2\left(n_1 H_a(d) + n_0 d_0 H_f(d)\right)}{n_0\left(n_1 \dot{H}_a(d) + n_0 d_0 \dot{H}_f(d)\right)} \tag{5.20}$$

$$\mathrm{NA}_{\mathrm{out}} = n_2 \sin\varphi' = \sqrt{\frac{a_2^2}{a_2^2 + d_2^2}} = \frac{n_0 a\sqrt{g(d)\,g(z)}}{\sqrt{1 + n_0^2 g(d)\left(a^2 g(z) + d_2^2 g(d)\right)}} \tag{5.21}$$

As shown in figure 5.5, light oscillates around the axis. In case of a *self-focusing* (selfoc) GRIN lens the gradient parameter is constant along the z-axis $\left(g(z) = g_0\right)$ and the oscillation period is given by the following relation:

$$p \cdot \lambda_{\mathrm{GRIN}} = p \cdot \frac{2\pi}{g_0} = d \tag{5.22}$$

Here, the parameter p, designated as *pitch*, gives the fraction of the oscillation period λ_{GRIN} inside the GRIN lens also determining the lens' behavior (see figure 5.6). Assuming planar input and output faces, rays from a point-like on-axis light source directly positioned on the input face will be collimated if the pitch is either $p = 0.25$ or $p = 0.75$. In this case the rays will leave the lens parallel to the optical axis (see figure 5.6(a) and 5.6(c)). For a pitch value of $p = 0.5$ or $p = 1.0$ the rays are focused on the output face and the light beam is divergent (see figure 5.6(b) and 5.6(d)). Consequently, a GRIN lens' behavior depends on its length. As a consequence, in order to perform typical functions as focusing or collimation, the GRIN lenses have to be designed properly. AURORA's GRIN lenses have a pitch of $p = 0.25$ for a design wavelength[16] of $\lambda = 670\,\mathrm{nm}$ [135]. In general, due to the wavelength dependency of the refractive index n, *chromatic aberration* effects occur. Thus, light with a wavelength $\lambda \neq 670\,\mathrm{nm}$ will not be perfectly collimated if the light source is directly positioned on the input face of the GRIN lens. Fortunately, AURORA's GRIN lenses exhibit a second minimum regarding the working distance d_0 at $\lambda = 440\,\mathrm{nm}$ [119]. Using equations (5.6), (5.7), (5.20) and (5.21) and taking the chromatic aberration

[16] Unfortunately, only GRIN lenses with a design wavelength of 670 nm or higher are available.

into account, a cone angle (double aperture angle) of $\alpha^* = 0.26°$ can be calculated for AURORA's lenses ($\lambda = 430\,\text{nm}$). This result is close to the measured average value of roughly $\alpha^* \approx 0.24°$. For more details see section 6.2.11.

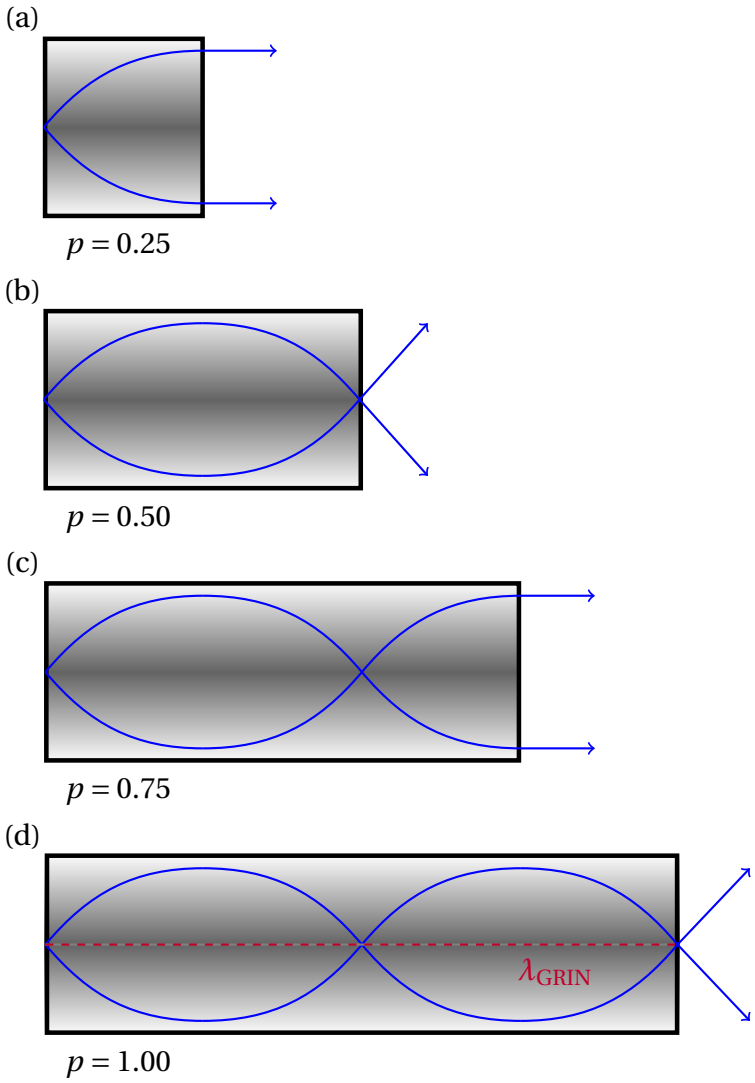

Fig. 5.6 GRIN lenses and their pitch

*The drawing illustrates the **ray trajectory** (blue arrows) inside various GRIN lenses with **different pitches**. Here, all lenses have **planar input and output faces** and the **point-like on-axis light source** is directly **positioned on the input face**. With a **pitch of p = 0.25 and p = 0.75** an exiting **light beam gets collimated** while for a **pitch p = 0.50 and p = 1.00** the **ray is focused on the output face**. In the latter two cases the outgoing **beam is divergent**. A GRIN lens with a **pitch p = 1.00** has a **length which is equal to a whole oscillation period** λ_{GRIN} (dashed, red line). The graph is oriented towards reference [62].*

Chapter 6

A U R O R A – Conceptual Design

JUNO is a multipurpose neutrino detector, which is filled with around 20 kt of liquid scintillator. To accomplish its physics goals (see chapter 3), an energy resolution of at least 3% @ 1 MeV [15] is required. According to the references [15, 49], this requirement for the energy resolution is connected via equation (6.1) with the amount of photoelectrons (PEs) which are recorded during such a low energy event.

$$\frac{\sigma_E}{E} = \frac{3\%}{\sqrt{E\,(\mathrm{MeV})}} \propto \frac{1}{\sqrt{N_{PE}}} \tag{6.1}$$

Here, the quotient $\frac{\sigma_E}{E}$ refers to the relative energy resolution. While E stands for the visible energy measured in MeV, N_{PE} indicates the total number of recorded PE hits.

From equation (6.1) a number of at least 1200 PEs can be derived to be able to reach the challenging energy resolution of 3%. On the one hand this number depends on parameters like the quantum and collection efficiency of the PMTs as well as the PMT coverage, as these quantities determine how many photons are successfully converted into photoelectrons. On the other hand the total amount of PEs depends on the number of photons which reach the PMT array in the first place. The photon statistics themselves are primarily determined by the light yield and transparency of the LS. As already mentioned in chapter 4, for a detector with a photo-active surface over the whole solid angle, the attenuation length L does not sufficiently describe the LS transparency. Here, it is more adequate to use the absorption length

L_a and the scattering length L_s because only absorbed photons cannot contribute to the overall budget of detected PEs anymore. Figure 6.1 shows the impact of the LS transparency on the total amount of detected PEs and, therefore, also its influence on JUNO's energy resolution.

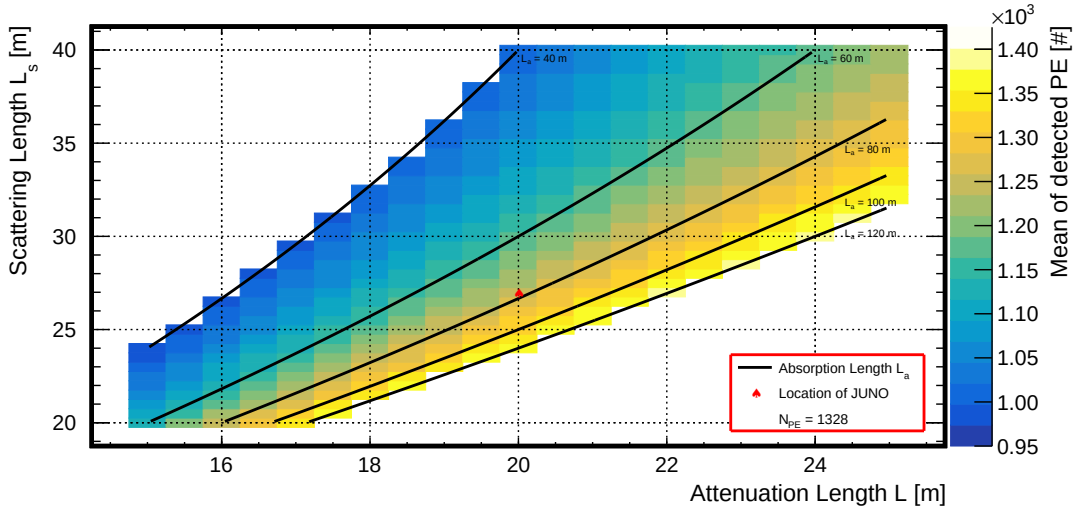

Fig. 6.1 PE statistics for various L and L_s combinations

The histogram presents the ***expected amount of recorded PEs*** *for 1 MeV neutrino events depending on the* ***attenuation length*** *L and* ***scattering length*** *L_s. Here, for each L and L_s combination* ***ten thousand electrons*** *with a* ***visible energy of 1 MeV*** *were simulated, originating* ***from the detector's center****. The* ***mean of the resulting distribution*** *was taken as an estimate for the expected amount of PEs. The error of the mean is given by the* ***RMS value of the individual distribution*** *and exhibits a* ***relative uncertainty of around 3%*** *for all entries. While* ***along the black lines*** *the value for the* ***absorption length*** *L_a* ***is constant****, the* ***red spade symbol*** *indicates the striven* ***location of the JUNO experiment****. The* ***official simulation framework*** `offline` *(version:* `J19v1r1-Pre4`*) was used to produce this plot.*

The attenuation length L was varied from 15.0 m to 25.0 m in 0.5 m steps while for the scattering length L_s values between 20.0 m and 40.0 m were considered using a step width of 0.5 m as well. Only (L,L_s) value pairs with a resulting absorption length $40.0\,\text{m} \leq L_a \leq 120.0\,\text{m}$ were taken into account. This is the reason why there are no entries in the upper left and lower right corner of figure 6.1.

From the color gradient in figure 6.1 it can be easily deduced that the amount of detected PEs predominantly depends on the absorption length L_a. In contrast to that, the scattering length L_s only plays a minor role. Here, for constant absorption lengths (along black lines) the PE yield is reduced for decreasing scattering lengths. This behavior can be explained by the effectively increasing path length. With an enlarged travel distance the chances for a photon to get absorbed by a molecule are

enhanced as well. Following a vertical line in figure 6.1 clearly shows that for a constant attenuation length L different PE yields can be expected. As a consequence, for measuring the LS transparency and, therefore, for determining one crucial aspect of the energy resolution of the JUNO detector, it is mandatory to locate the exact position of JUNO's scintillator mixture in the parameter space of figure 6.1.

Furthermore, JUNO's exact location within figure 6.1 is important for JUNO's spatial resolution as well. As an increasing scattering length corresponds to a smaller number of scattering processes, the original directions of emitted photons will less alter. Hence, the uncertainty of the reconstructed vertex is automatically improved. The value of the scattering length L_s, consequently, plays here a major role and should be monitored.

In addition, up to now the optical properties of the liquid scintillator are measured mostly in small scaled experiments like tiny cuvettes or in tubes of only a few meters. On these scales, absorption effects are difficult to measure and, therefore, might be underestimated. To get a more realistic picture, measurements in objects comparable to the size of the JUNO detector are crucial. As AURORA will measure the optical properties in the detector itself, it is a perfect opportunity to get a more clear view on those parameters.

Such advanced transparency measurements will not only provide important parameters for both JUNO's energy and spatial resolution. They will also help to identify if materials like the water of the CD, the acrylic sphere or the LS itself show temporal changes in their performance due to aging effects. This kind of degradation can have several reasons. On the one hand contaminants like water bubbles or dust could enter the detector via supply pipes, increasing the probability for Mie scattering processes inside the LS volume. In addition, products of chemical reactions could introduce new absorption bands in all kind of materials (water, acrylic and LS), diminishing the overall photon statistics (see section 4.4).

In contrast to other calibration systems which normally only measure one of the three optical lengths L, L_s or L_a, the calibration system AURORA[1,2] was invented to do exactly this – measuring and monitoring the LS transparency by determining all three optical lengths L, L_s and L_a.

[1] **A U**nit for **R**esearching **O**n-line the LS t**RA**nsparency.
[2] Logo designed by Dr. Natalie Schützler – a really good friend of mine.

In addition, the AURORA system will have the useful feature of tiltable laser beams. This will ensure that even after the filling procedure the direction of the laser beams can be corrected in order to compensate for an occurring misalignment. A useful tool in case the laser hits in its zero position (not tilted) obstacles like connection bars, acrylic nodes or the transition zone between two acrylic sheets. This feature can also be used to target an unoccupied slot of a small PMT. In this case the transparency measurement can be conducted at higher beam intensities without posing a threat to the lifetime of the primarily affected PMTs, leading to an improved signal-to-noise ratio.

This chapter will focus on the design of the calibration system AURORA and all hardware related topics. While in section 6.1 the general design is presented serving as an introduction, in the sections 6.2 and 6.3 the optical and electro-mechanical subsystems are discussed in more detail. Afterwards, section 6.4 deals with the CD interface explaining where exactly and how the AURORA system will be installed into the JUNO detector. In section 6.5, the durability and persistence of several components are shown to ensure that the system will survive the whole operation time underwater. Furthermore, several mechanical stress tests were performed. The subsequent section 6.6 presents the radioactive background contribution of those components which are located inside the CD. In the end, section 6.7 will present the self-written software control of the AURORA system.

6.1 AURORA's General Design

This section will just give a brief overview of AURORA's general design before in the subsequent sections the system is discussed in more detail. Figure 6.2 presents a scheme including all parts of the optical and electro-mechanical system (for pictures of the set-up see appendix B). Most of these components are located in a rack on the TT bridge. The rest of the components will be installed inside the CD.

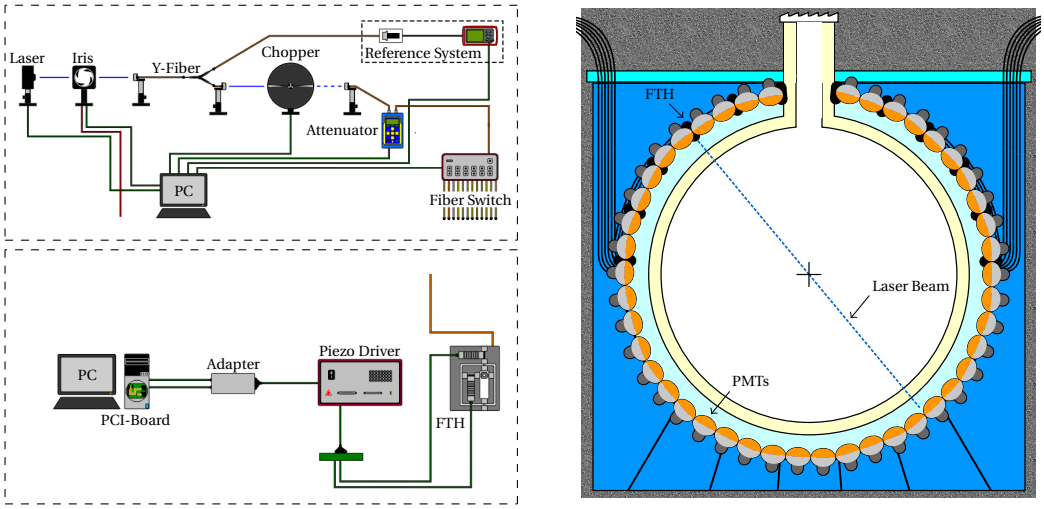

(a) Optical & electro-mechanical system

(b) CD components

Fig. 6.2 Overview of the AURORA system

On the one hand there is the optical system (detailed discussion in section 6.2). Its main purpose is to provide the laser light for the transparency measurement. In addition, it also manipulates the properties of the beam by cutting the continuous wave laser into short pulses, varying the pulse's final intensity and distributing them to one of the twelve endpoints in the CD. Most of the corresponding components are positioned in an optical enclosure.

On the other hand there is the electro-mechanical system (detailed discussion in section 6.3). Its main purpose is to provide a fiber termination which can be tilted for the transparency measurements if this is necessary.

In principle, all twelve lasers are pointing to the detector's center. Besides the cables which are routed along the pool's wall and the SSLS, the FTH devices with the mounted GRIN lenses are the only components which are installed in the CD. They are distributed over the whole northern hemisphere.

6.2 AURORA's Optical System

The following section focuses on the optical system of AURORA. It includes all optical components which are producing, shaping and guiding the laser beam in order to conduct the LS transparency measurements inside the CD. Figure 6.3 gives an overview about the optical system, showing how the single components are connected with each other.

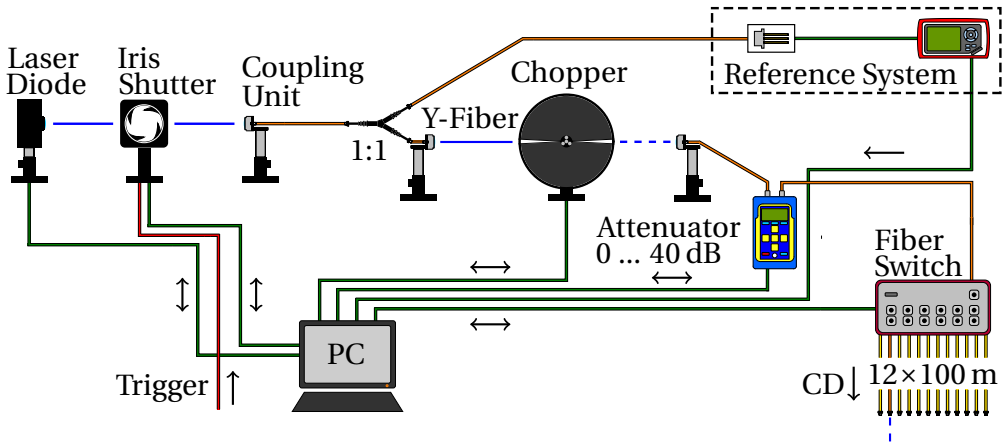

Fig. 6.3 Scheme of the optical system

*Illustrated is the scheme of **AURORA's optical system**, its single components and how these are connected with each other. While **blue lines** are indicating **open laser beams**, **orange** and **yellow lines** stand for **light-guiding** and **non-light-guiding optical fibers**, respectively. The **green lines** are **electrical cables** which are used to send commands from the software control to the single components and/or receive data from those elements. The **red line** also refers to an **electrical cable** which provides a communication interface between the AURORA system and JUNO's trigger.*

As illustrated in figure 6.3, the optical system is using a *laser diode* to generate a continuous wave (cw) laser beam (blue line), operating at a wavelength of around 430 nm and a maximum intensity of 50 mW [130]. According to the emission spectrum of bis-MSB (see figure 4.7), thus, the diode covers the most important wavelength region of the scintillation light. The intensity level of 50 mW corresponds to a number of photons per time interval which is more than enough for the transparency measurement. The first component the beam passes is an *iris shutter*. Its main purpose is to block the laser light in case of an emergency. Here, the diaphragm can be controlled by the local computer and JUNO's trigger system. This ensures that in case of a malfunction or an occurring supernova, the beam can be immediately blocked, terminating the whole measurement. Afterwards, the beam is coupled into a fiber via a *coupling unit*, which basically consists of an aspheric

lens focusing the light onto the fiber's core. The *fiber itself is Y-shaped*, hence, it has one inlet and two outlets. Here, the coupled light is distributed to both outlets with a ratio of 1:1. On the one hand 50% of the incident light intensity is guided to a *reference system* to monitor the laser's power. This is important, as the PMTs in the CD must not exposed to high illumination rates. The reference system consists of a photodiode that converts the light into an electrical signal. Subsequently, an amplifier amplifies the signal strength before it is sent to an ADC. The readings of the ADC are recorded by the PC. On the other hand 50% of the incident light intensity is still available for the transparency measurement. Firstly, the cw laser is decoupled from the Y-fiber, cut into small pulses via an *optical chopper* (blue dashed line) and after that again coupled into another optical fiber. The signal of a cw laser would be recognized by the PMTs as an increase in their dark count rate. As a consequence, it would be difficult so separate the actual signal from the background. For a pulsed laser with a sufficiently narrow pulse width, however, the signal-to-noise ratio can be improved and successfully separated from the background. Hence, by using the optical chopper, data acquisition becomes much more efficient. In addition, in case the safety precautions fail and the laser beam still illuminates the detector interior during a supernova event, most of the recorded data will be still useful for the supernova analysis. In a pulsed mode, the laser beam is blocked most of the time anyway. Secondly, the light beam is guided through an *attenuator*, which is able to reduce the beam intensity by up to four orders of magnitude. This is important, as the PMTs' lifetime will be significantly reduced if they are exposed to excessively high light intensities. Afterwards, the laser light is passed on the *fiber switch module*. This module has one inlet and twelve outlets. With the computer it is possible to control through which outlet the laser beam exits the device. Therefore, it is convincingly simple to redirect the laser light without any mechanical adjustments. Each outlet is connected to a *100 m long fiber*, which guides the laser light into the CD to a *fiber termination holder* (for more details see section 6.3). These holders (twelve in total) are mounted on the SSLS being distributed over the whole northern hemisphere. Here, the laser light decouples from the fiber, traversing a *GRIN lens* which collimates the laser beam. While ordinary lenses are not able to sufficiently collimate light underwater, GRIN lenses exhibit a gradient-index profile which permits collimation despites rather similar refractive indices between the lenses' material and the surrounding water. The following sections will present each of these optical components, discussing their specifications and performance measurements in more detail.

6.2.1 Laser Source

A light source is mandatory in order to be able to perform a transparency measurement. In this case a laser diode[3] (LD) from the Austrian company *Roithner LaserTechnik* is used operating at a wavelength of $\lambda = 430\,\text{nm}$ [130].

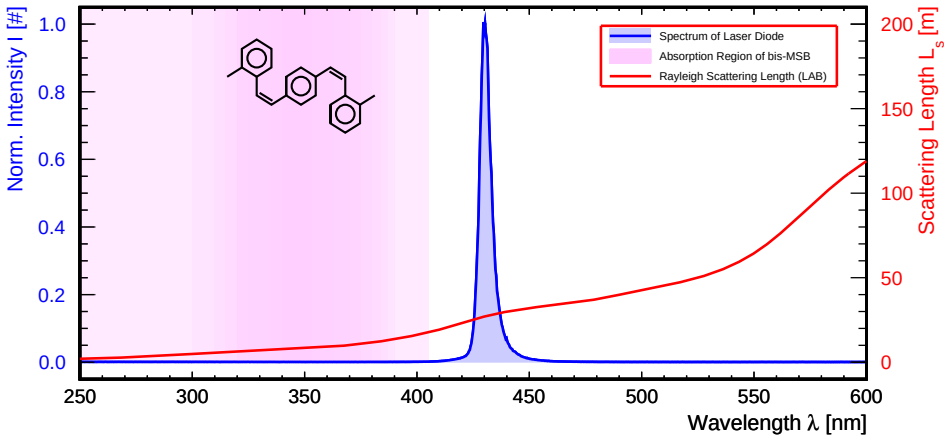

Fig. 6.4 Emission spectrum of the laser diode

*The graph presents the **emission spectrum** (blue) of the used LD. In addition, the **absorption spectrum of bis-MSB** (pink) and **LAB's Rayleigh scattering length** (red) are shown, too. While the **absorption spectrum of bis-MSB** relies on an actual **measurement** [26], the values for the **Rayleigh scattering length of LAB** are extracted from JUNO's **simulation framework** `offline` and only indicate an approximate data distribution [147].*

Figure 6.4 presents the diode's emission spectrum[4]. For the LD an operation wavelength of 430 nm was chosen. The measured peak lies at $\lambda = 431.1 \pm 0.8\,\text{nm}$ with a spectral width of $\sigma = 4.4 \pm 0.6\,\text{nm}$. On the one hand this wavelength lies within the emission region of bis-MSB. Thus, the diode covers the most important spectral region of the scintillation light. Furthermore, at a wavelength of 430 nm the energy of the emitted photons is already below the lower edge of the absorption spectrum of bis-MSB, and, therefore, losses due to absorption processes should be rather rare. In general, the scintillator is characterized by a long attenuation length, as the Rayleigh scattering length (natural limit of the LS transparency) is already close to 30 m in this region. If nevertheless absorption occurred, *e.g.* due to aging effects which might introduce new absorption bands in this wavelength region, AURORA would have a good chance to identify this degradation (for more details see section 4.4).

[3] Roithner LaserTechnik: RLT430-50CMG, InGaN quantum structure, $\lambda = 430\,\text{nm}$, $P = 50\,\text{mW}$, single transverse mode, 5.6 mm TO56 package without PD.
[4] Measured with the USB2000 spectrometer from Ocean Optics.

In addition to its emission spectrum, the linearity and longterm stability of the LD was measured with a power meter. As the output will be constantly monitored during the transparency measurements, these properties are not of major concern. However, the performance tests have shown that the power of the LD is linearly increasing with the applied current. Furthermore, within an hour of measurement the intensity of the diode varied at their maximum output by $\frac{\sigma}{\mu} \approx 0.1\%$. Here, σ stands for the standard deviation of recorded intensity values and μ for the calculated mean. Consequently, the diode's performance is sufficiently stable.

6.2.2 Collimation Lenses

As laser diodes are normally characterized by huge aperture angles (see section 5.1), the resulting light beam has to be collimated right from the beginning. On the one hand unnecessary intensity losses can be avoided because the cross section of the beam does not increase beyond a width further optical components still could handle (*e.g.* acceptance angle of fiber). On the other hand the coupling itself becomes much easier when dealing with already collimated light. In AURORA's case two collimation lenses are used. Firstly, a small aspheric lens[5] is directly mounted on the LD mount[6]. In addition, a second aspheric lens[7] is used to further collimate the light beam being attached to the mount via a cage system.

[5] Thorlabs: C230TMD-A, aspheric lens with focal length $f = 4.51$ mm, numerical aperture $NA = 0.55$, optimized for a wavelength region $350 \leq \lambda \leq 700$ nm.
[6] Thorlabs: LTC100-A, Laser/TEC Driver Kit.
[7] Thorlabs: C220TMD-A, aspheric lens with focal length $f = 11.00$ mm, numerical aperture $NA = 0.25$, optimized for a wavelength region $350 \leq \lambda \leq 700$ nm.

6.2.3 Iris Shutter

The same cage system is used to integrate the iris shutter[8] into the AURORA system. It can be remotely controlled and has reaction times of around 10 ms. The main purpose of the diaphragm is to block the laser light in case of an emergency – *e.g.* too high laser intensities because of a malfunction or in case of an occurring supernova. As the light blocking abilities of the iris are crucial, a performance test was conducted. Here, the light intensity behind the closed iris was measured with a power meter[9] while the laser was turned on and off. Figure 6.5 shows the results.

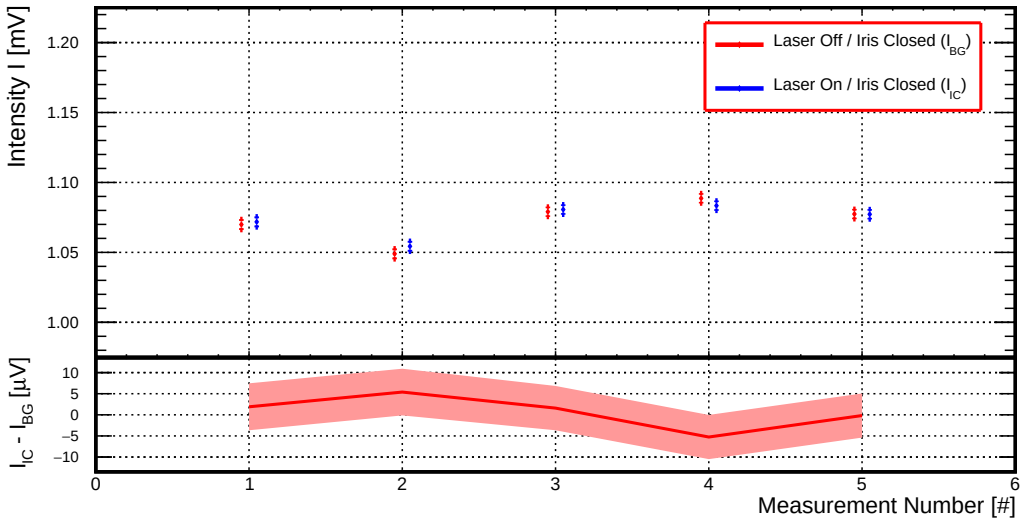

Fig. 6.5 Iris shutter performance measurement

The graph illustrates ***the performance measurement*** *of the* ***iris shutter****. While the* ***upper graph*** *shows the* ***absolute intensity values*** *during the measurement with the LD turned on and off, the* ***lower graph*** *presents the* ***difference of these values****. Here, the* ***red band*** *indicates the* ***uncertainty of the calculated values****.*

Five measurements were conducted. In each run no significant difference between the LD being turned off and on could be observed. Here, within their uncertainty range the values are the same. Thus, the iris shutter sufficiently blocks the laser light and is suitable for its purpose.

6.2.4 Coupling Unit

The laser light from the LD has to be coupled into a fiber. Here, a coupling unit is used which primarily consists of an aspheric lens directly attached to a SMA

[8] Thorlabs: SHB05T, PTFE coated blades, reaction time $t_r \approx 10$ ms.
[9] Thorlabs: S130C, slim photodiode sensor, optimized for a wavelength region $400 \leq \lambda \leq 1100$ nm, applicable power from 500 pW to 500 mW.

connector. The collimator[10] is installed on a post via a kinematic mount[11]. The holder can be adjusted in x- and y-direction. In addition, the mount is tiltable as well. This ensures an optimal adjustment in order to couple as much light as possible into the Y-fiber.

6.2.5 Y-Fiber

In order to be able to monitor the laser beam intensity, a constant and well known fraction of the light has to be separated from the main beam and continuously measured. For this purpose a Y-shaped fiber[12] with one inlet and two outlets is used splitting up the beam by a ratio of 1:1.

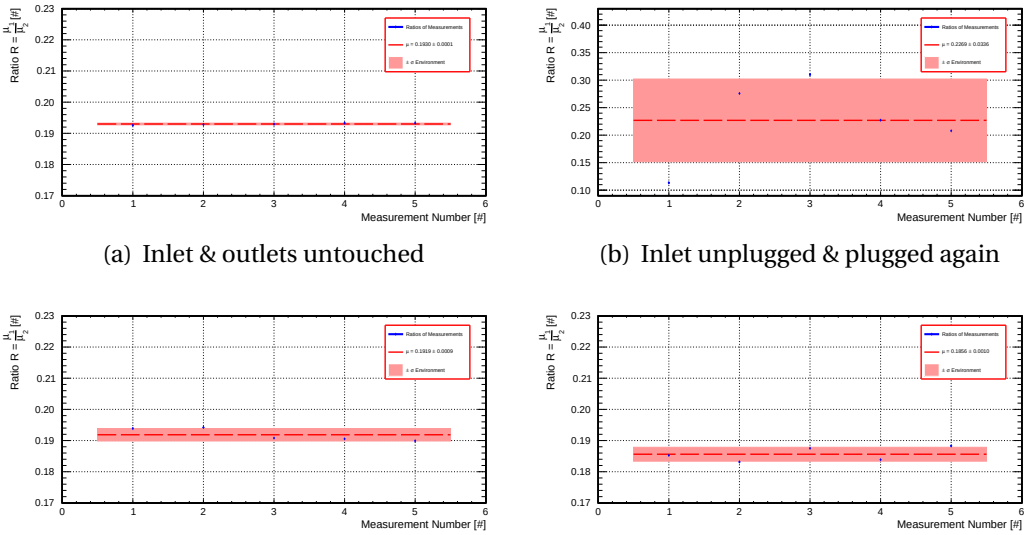

(a) Inlet & outlets untouched

(b) Inlet unplugged & plugged again

(c) Outlet 1 unplugged & plugged again

(d) Outlet 2 unplugged & plugged again

Fig. 6.6 Performance test of Y-fiber

*The graphs show the **results of the Y-fiber performance test**. Here, the **intensity ratio between both outlets** is measured with two photodiodes five times under four different circumstances. While figure 6.6(a) presents the results for the **inlet and both outlets being untouched**, figure 6.6(b) shows how the ratio differs if the **inlet is unplugged and plugged again** between each measurement. Figures 6.6(c) and 6.6(d) present the results in case **outlet 1 and outlet 2 are unplugged and plugged again**, respectively.*

It is obvious that the fiber does not split up the intensity of the beam by a ratio of 1:1. On the contrary, the intensity of the second outlet seems to be (at least) four

[10] Thorlabs: F671SMA-405, numerical aperture $NA = 0.60$, design wavelength $\lambda = 405\,\text{nm}$, focal length $f = 4.02\,\text{mm}$.

[11] Thorlabs: KM100, kinematic mount for tip and tilt adjustments.

[12] StellarNet Inc: F-600-Y-UV-SR, Y-shaped optical fiber with SMA connectors, core diameter 600 μm, optimized for a wavelength region $200 \leq \lambda \leq 2100\,\text{nm}$.

to five times higher than the intensity of the first one. However, the splitting ratio itself is of minor concern as long the ratio is stable and well known. Figure 6.6(a) clearly states that the ratio does not change if the inlet and both outlets are not touched, moved or unplugged and plugged again. Here, the ratio only differs by 0.05% from measurement to measurement. Unfortunately, after the calibration measurements (determination of the exact ratio after the system has been installed in the underground lab) one outlet has to be unplugged from one photodiode (the photodiode at the other outlet is used for the reference system and stays attached) and connected to the subsequent component of the AURORA system. In this case, the AURORA system has to deal with an uncertainty of the intensity ratio similar to the results of figure 6.6(c) and 6.6(d). With ratio fluctuations of 0.47% and 0.54%, those are very similar and still sufficiently small. When in the end the final beam intensity is calculated which comes out at the fiber's termination (GRIN lens), a conservative estimate for the uncertainty of the beam's intensity of 0.6% (regarding the Y-fiber) should be taken into account.

6.2.6 Reference Beam System

The reference beam system is used to monitor the actual laser beam intensity. For that purpose a photodiode[13] is connected to one of the Y-fiber's outlets transforming the optical signal into an electrical one. An amplifier[14] is amplifying the photodiode signal, so it can be analyzed by an ADC[15].

Firstly, the photodiode had to be calibrated in order to be able to convert its output (measured in V) back into an optical intensity (measured in W). For this calibration measurement, AURORA's laser light was coupled into the already discussed Y-fiber, monitoring its intensity by both the photodiode and a power meter. This was done for various intensity levels, so a relation between the ADC output and the actual beam intensity could be determined. Figure 6.7(a) shows the results of this calibration measurement.

Secondly, a control measurement was performed in order to check if the intensity values determined with the ADC fit the intensity levels directly measured with the power meter. Here, the laser light was again coupled into the Y-fiber and simultaneously monitored by both the photodiode and the powermeter. Afterwards, the

[13] Thorlabs: SM05PD1A, applicable for wavelength $350 \leq \lambda \leq 1100\,\text{nm}$, active area $A = 13\,\text{mm}^2$.
[14] Thorlabs: AMP120, transimpedance amplifier, DC to 1 kHz.
[15] Weeder Technologies: WTAIN-M, programmable analog input device, 20 bit ADC, sample rate is 60 sps, accuracy is $\pm\left(0.05\% + 20\mu\text{V}\right)$.

calibration curve was used to convert the ADC readings into an optical intensity. The results of this control measurement are presented in figure 6.7(b).

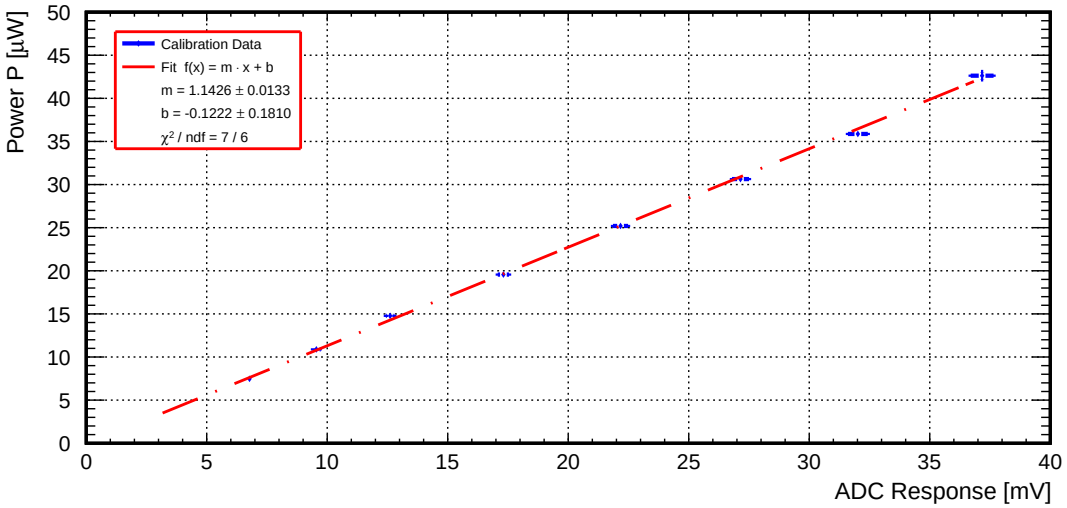

(a) Calibration measurement of photodiode + amplifier + ADC

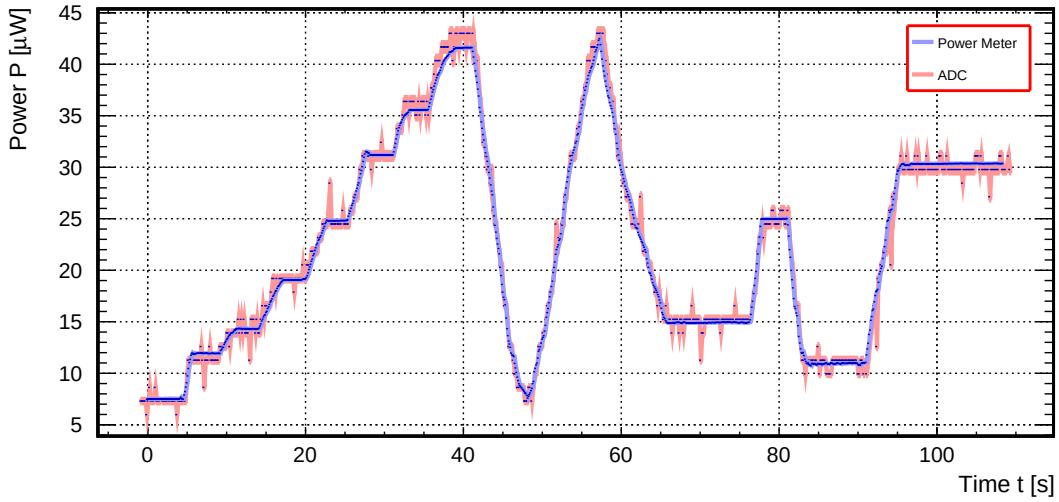

(b) Control measurement of photodiode + amplifier + ADC

Fig. 6.7 Calibration and control measurement of photodiode + amplifier + ADC

*In figure 6.7(a) the results of the **photodiode calibration measurement** are presented while figure 6.7(b) shows the results of the **control measurement**.*

As it can be seen in figure 6.7(a), the output of the photodiode-amplifier-ADC chain is proportional to the readings of the power meter. Thus, the following linear function can be used to convert the chain's results ADC_{out} into a proper beam intensity I_b.

$$I_b = m \cdot ADC_{out} + b \tag{6.2}$$

Here, m refers to the slope of the linear function while b stands for its intercept. According to the calibration measurement, the slope and intercept have a value of $m = 1.1426 \pm 0.0133\,\mu\mathrm{W\,mV^{-1}}$ and $b = -0.1222 \pm 0.1810\,\mu\mathrm{W}$, respectively. The reduced χ^2 value indicates that the linear function accurately describes the data distribution. Figure 6.7(b) confirms that the conversion between the ADC output and actual intensity values sufficiently works. Here, the directly recorded values of the power meter fit the converted values of the ADC quite well. However, figure 6.7(b) shows in addition that the ADC signal exhibits small and randomly distributed spikes. As a consequence, when later on the laser beam intensity is monitored by using the photodiode, a mean calculated out of a few actual recorded intensity values (in a predetermined, short time range) should describe the current intensity value even more accurate.

Regarding the conversion of the ADC output into a beam intensity, the uncertainty of I_b can be calculated via the Gaussian error propagation satisfying equation (6.3):

$$\Delta I_b = \sqrt{(ADC_{out} \cdot \Delta m)^2 + (m \cdot \Delta ADC_{out})^2 + (\Delta b)^2} \tag{6.3}$$

Taking the ADC accuracy and the errors of the fit parameters into account, the uncertainty of the calculated beam intensity (only regarding the signal conversion) is given by the following formula:

$$\Delta I_b = \sqrt{(ADC_{out} \cdot 0.0133)^2 + (1.1426 \cdot (0.0005 ADC_{out} + 0.02))^2 + (0.1810)^2} \tag{6.4}$$

Here, the units of the voltage and intensity are given in mV and μW. If the incident laser light exhibited an intensity of 500 μW, the ADC output would range around 220 mV (1:1 split at the Y-fiber). The absolute uncertainty of the beam intensity would be in this case $\Delta I_b = \pm 2.9\,\mu$W, which translates into a relative uncertainty of approximately 1.2%. Here, the first term under the square root (slope of linear fit) dominates the uncertainty of the beam intensity.

6.2.7 Optical Bridge With Chopper

Like the inlet, the second outlet of the Y-fiber is equipped with a collimator[16] of the same type. Thus, the beam decouples from the fiber traversing around 5 cm

[16] Thorlabs: F671SMA-405, numerical aperture $NA = 0.60$, design wavelength $\lambda = 405\,$nm, focal length $f = 4.02\,$mm.

of free space before it is coupled into a fiber again, using a third collimator[17]. In contrast to the other collimators, this one exhibits an FC/PC connector instead of a SMA standard. The optical performance, however, remains the same. Both collimators are fixed by kinematic mounts[18] in order to ensure an accurate adjustment of the collimators minimizing the intensity loss as good as possible. In total, this optical bridge is associated with an intensity loss of $\Lambda_{ob} = 1.5 \pm 0.3$ dB [151]. To be more accurate, it is recommended to determine again the attenuation of the optical bridge after the installation of the AURORA system has been completed. Unfortunately, already minor changes in the collimators' adjustment can lead to significantly different attenuation values.

The main reason to integrate an optical bridge into the AURORA system is the use of a chopper. Its purpose is to frequently block the laser light in order to transform the cw operating mode into a pulsed one. Later on, this makes it easier to disentangle AURORA's signals from the overall background (on average 30 kHz [165]). Here, instead of a supposedly rising background level, the PMTs will see more events in a short, well-defined time window. The optical chopper[19] itself consists of a motor which rotates two chopper wheels. These two blades[20] have both two slots with an overall *duty cycle* of 50%. By rotating those blades relatively to each other the final slot width can be adjusted. Besides the chopper frequency, the slot width determines the final pulse width of the laser beam.

During the transparency measurements a pulse width of 10μs is preferable. Assuming an operation frequency of $f = 200$ Hz, this would lead to a duty cycle of only 0.2%. As a consequence, most of the time the laser beam would be blocked, and, therefore, the CD would not see any laser light. On the one hand this small duty cycle allows all photons to reach their final destination[21] before the subsequent light pulse enters the detector. In addition, but of minor significance due to rather small fall times, the chosen duty cycle gives the overall electronics enough relaxation time. On the other hand, if the duty cycle is around 0.2%, 99.8% of AURORA's measurement duration the JUNO detector will not be blinded still being able to record other

[17] Thorlabs: F671FC-405, numerical aperture $NA = 0.60$, design wavelength $\lambda = 405$ nm, focal length $f = 4.02$ mm.
[18] Thorlabs: KM100, kinematic mount for tip and tilt adjustments.
[19] Edmund Optics: 34-424, maximum frequency $f = 200$ Hz.
[20] Edmund Optics: 56-066, chopper blade with two slots, duty cycle of 50%.
[21] Assuming a travel distance of 40.0 m and a velocity of $\frac{2}{3}c_0$, the propagation of the photons only take around 0.2μs. If a tolerance for forward and backward scattering is taken into account, the maximum travel time should be around 1μs.

events – *e.g.* an occurring supernova. Hence, even if the safety measures[22] failed and the AURORA system continued with its transparency measurements, most of the parallelly collected data would be still usable for an analysis.

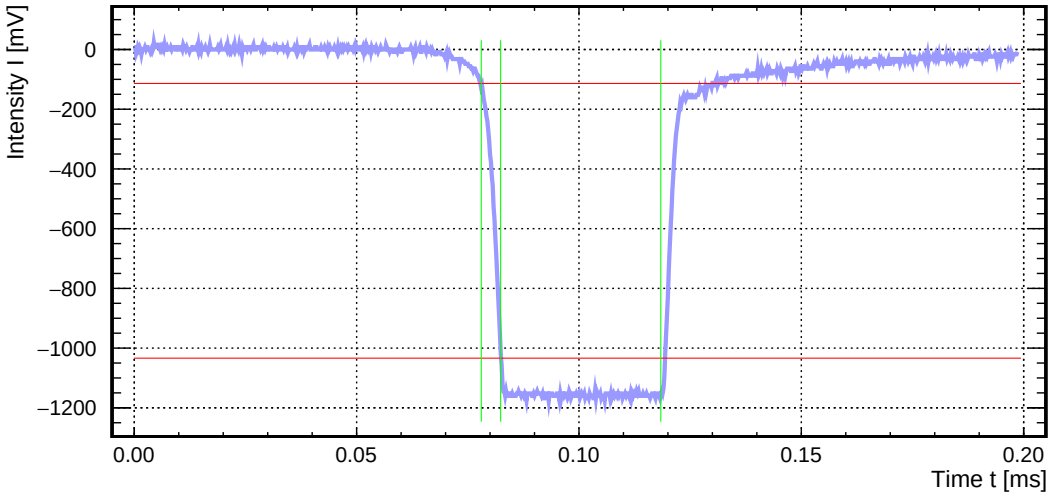

(a) Frequency $f = 160\,\text{Hz}$, slot width $w = 1.2\,\text{mm}$

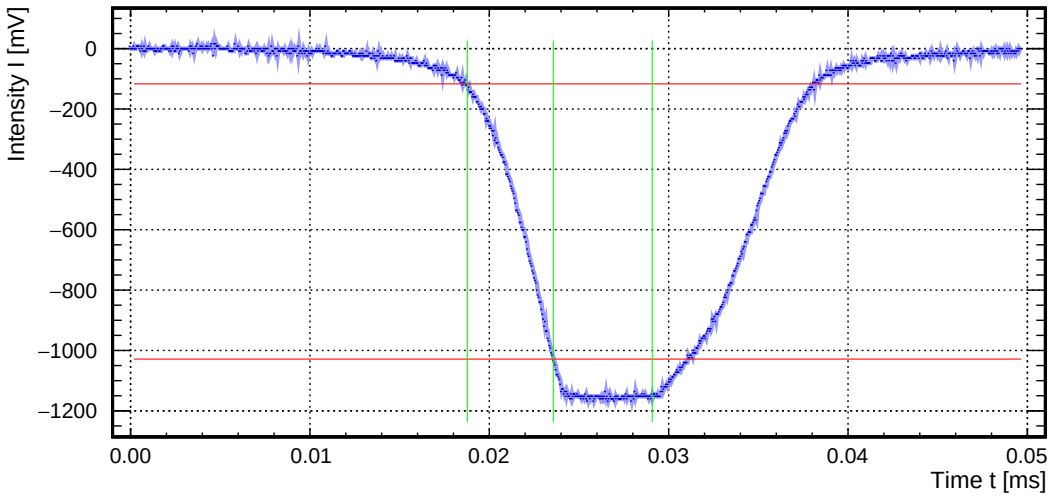

(b) Frequency $f = 160\,\text{Hz}$, slot width $w = 0.3\,\text{mm}$

Fig. 6.8 Chopper performance measurement

The figure shows two ***laser pulses for different chopper settings****. While in figure 6.8(a) the frequency is set to* $f = 160$ *Hz and the slot width to* $w = 1.2$ *mm, in figure 6.8(b)* $f = 160$ *Hz and* $w = 0.3$ *mm. The* ***lower and upper horizontal, red lines indicate 10% and 90% of the total pulse depth****, respectively. The vertical,* ***green line on the left*** *marks the* ***start of the pulse*** *while the* ***second one in the middle*** *highlights the* ***end of the pulse rise time****. Finally, the vertical,* ***green line on the right*** *marks the* ***end of the laser pulse****.*

[22] JUNO trigger sends command to close the iris shutter to abort the transparency measurement.

Figure 6.8 shows two recorded laser pulses for different settings after the beam passed the chopper. Here, the photodiode and the amplifier of AURORA's reference beam system were used to transform the optical signal into an electrical one. An oscilloscope[23] was used to record the pulses. For larger slot widths the pulse looks rather rectangular (see figure 6.8(a)). However, due to rising and falling times of around 4 μs and 6 μs, respectively, the used amplifier deforms these pulses, which is recognizable for shorter pulse widths (see figure 6.8(b)). In both graphs of figure 6.8 the actual start and end of the pulses (width) are marked by the vertical lines on the left and right, respectively. For a setting of $f = 160$ Hz and a slot width of $w = 0.3$ mm, a pulse width of approximately 10μs is achievable. If the frequency is increased to 200 Hz, even smaller pulse widths are realizable. However, assuming a pulse width of 10 μs, the contained amount of photons in one pulse is only $1 \cdot 10^{-5}$ of the overall incident intensity.

After the installation in the underground lab, it is recommended to check the final pulse width for a given chopper frequency and slot width. Here, the chopper provides a TTL-standard trigger signal with steep flanks and a width which is similar to the optical pulse width. Using a standard oscilloscope, this trigger signal is accurate enough to be used for the calibration of the chopper.

6.2.8 Attenuator

For AURORA's transparency measurements, it is important to have the possibility to modify the laser beam intensity remotely in order to adjust a suitable brightness level. On the one hand enough statistics should be collected in a moderate period of time. On the other hand the laser beam intensity must not exceed a brightness level which already could represent a potential danger to the PMTs. This task is performed by the attenuator[24] which was bought from the company *Oz Optics*.

The working principle is rather simple. Laser light which is already coupled into a fiber is guided through the inlet to a neutral density filter. This filter possesses a gradually changing optical transparency. Here, the light is decoupled from the fiber and traverses the density filter perpendicular to its gradient before it is again coupled into another fiber. Depending on the attenuator's settings, a micro motor changes the position of the filter along its gradient direction and, therefore, also the

[23] Tektronix: DPO5104B, digital oscilloscope.

[24] Oz Optics: DA-100-3S-430-50/125-QM-40, calibrated for a wavelength λ of 430 nm, equipped with 50/125 multimode fibers, numerical aperture is $NA = 0.12$, maximal return loss of 40 dB, accuracy of around 0.01 dB.

adjusted attenuation. The laser light with the diminished intensity is then guided via the fiber to the outlet of the device.

The attenuation can be expressed by the common logarithm of the quotient of the resulting intensity I and incident intensity I_0 satisfying equation (6.5):

$$\Lambda = -10 \cdot \log_{10}\left(\frac{I}{I_0}\right) \tag{6.5}$$

With the pre-logarithmic factor -10 the resulting attenuation is given in decibels (dB) and will be of positive sign. Thus, the higher the number, the higher the actual attenuation.

A characterization measurement was carried out using AURORA's LD and a power meter. First, I_0 was measured at the attenuator's outlet for a set attenuation of $\Lambda_s = 0.00$ dB. Then, in 2 dB steps, the attenuation was increased and the resulting intensity I again measured with the power meter. Doing that for the whole attenuation range from 0.00 dB up to 40.00 dB, formula (6.5) was used to calculate the measured attenuation Λ_t for each resulting intensity. Figure 6.9 shows the results of two measuring cycles and data provided by the company.

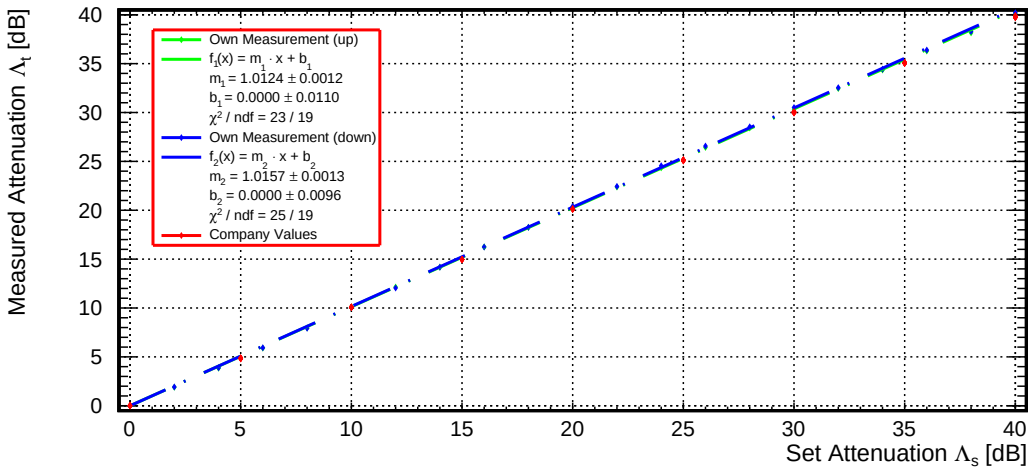

Fig. 6.9 Characterization measurement of the attenuator device

*Shown is the **characterization measurement** of the **attenuator**. Here, the **measured attenuation** is plotted against the **set attenuation**. While the **green data** shows a measuring cycle where the **intensity was reduced step-by-step**, the **blue data** illustrates a measuring cycle where the **intensity was gradually increased**. The **red data** shows the results of a **performance test carried out by the company** itself.*

A linear function $f(x) = m \cdot x + b$ is fitted to both performed measurements in order to find a relation between the set and measured attenuation. Here, the slope parameter m had an initial value of 1.0 and could be freely selected while the intercept parameter b had an initial value of 0.0 and the boundary condition to be only of positive sign. In both cases the reduced χ^2 value is close to 1 which indicates that the data distribution is adequately described by a linear function. For both measurements the intercept has a value of $b = 0.00 \pm 0.01$ dB. The slopes are slightly different and reach a value of $m_1 = 1.012 \pm 0.001$ and $m_2 = 1.016 \pm 0.001$. In order to satisfy both measuring cycles, an average slope of $m = 1.014 \pm 0.003$ is taken, covering the whole range for both measurements. Consequently, the following relation between the set attenuation Λ_s and the actual true attenuation Λ_t is given by equation (6.6). The Gaussian error propagation was used in order to derive an error for Λ_t.

$$\Lambda_t = m \cdot \Lambda_s + b \qquad \Delta\Lambda_t = \sqrt{(\Lambda_s \cdot \Delta m)^2 + (m \cdot \Delta\Lambda_s)^2 + (\Delta b)^2}$$

With the given values for the fit parameters and the device's accuracy the final relation translates into the following expression:

$$\Lambda_t = 1.014 \cdot \Lambda_s \qquad \Delta\Lambda_t = \sqrt{(\Lambda_s \cdot 0.003)^2 + (1.014 \cdot 0.01)^2 + (0.01)^2} \tag{6.6}$$

For the actual LS transparency measurement performed by AURORA, Λ_t will be used to calculate the correct attenuation of the laser beams. Here, $\Delta\Lambda_t$ will be considered as one of the uncertainties regarding the beam intensity of the laser system. In general, a small fraction of the beam intensity is lost during the coupling between an optical fiber and another component – like the inlet of the attenuator. However, due to the optimization to our needs (design wavelength of $\lambda = 430$ nm, fiber's core of 50 μm, $NA = 0.12$), no additional *intrinsic intensity loss* could be observed. Otherwise the fit parameter b would not be equal to zero. This is consistent with the company measurements, as these results claim that the intrinsic intensity loss is 0.00 dB as well [137, 138]. For a set attenuation $\Lambda_s = 40.00 \pm 0.01$ dB, the resulting attenuation will be $\Lambda_t = 40.56 \pm 0.12$ dB. As a consequence, the maximum relative uncertainty ranges around 0.3%, which is rather precise.

6.2.9 Fiber Switch Module

After the laser light passed the attenuator, it is guided via a 1 m long optical fiber to the *fiber switch module*. It has one inlet and twelve outlets. The main purpose of this device is to select one of the twelve 100 m long optical fibers through which the laser

light enters the CD. There are several properties which have to be carefully studied. On the one hand the channels must not communicate with each other. Thus, if the laser light is guided through a specific channel, the neighboring channels must not see any light. This ensures that during the transparency measurements light cannot enter the detector through one of the other channels, being background for the actual measurement. In addition, the mechanical system which changes the light path inside the module should be characterized by a high reliability. Hence, the attenuation of a specific channel must not change after the channel number has been switched several times. Finally, the attenuation value of each channel has to be recorded in order to be able to calculate the final beam intensity at the fiber termination inside the CD.

During the characterization measurements no channel-channel communication could be observed. As a consequence, no self-introduced background is expected. The reliability measurements have shown that all channels are characterized by a stable performance. Figure 6.10 presents the result of the reliability measurement of channel one.

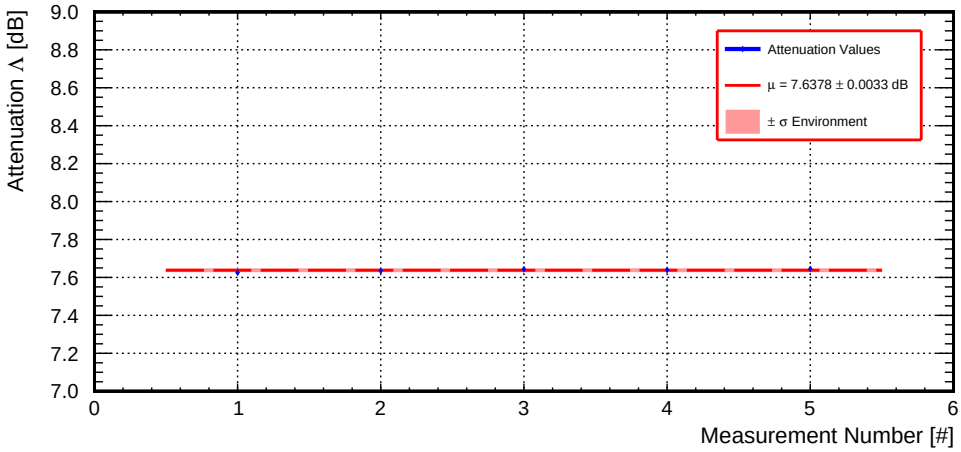

Fig. 6.10 Reliability measurement of channel one

*The graph shows the **result of the reliability measurement of channel one**. Here, the **attenuation** of the channel was **measured five times**. Between each run the channel number was switched to another channel and then switched back to the original setting. The **red line** indicates the **calculated mean** while the **red band** refers to the **1σ uncertainty environment**.*

Here, the fluctuation[25] is around 0.04%. The other channels exhibit a similar accuracy. These values are sufficiently stable for the calculation of the final beam intensity. Figure 6.11 presents the attenuation values of all twelve channels. While

[25] Fluctuation is estimated by calculating the quotient resulting from σ divided by μ.

the blue markers refer to another attenuation measurement campaign performed before the reliability test, the red markers show the calculated mean of the reliability measurement for each channel.

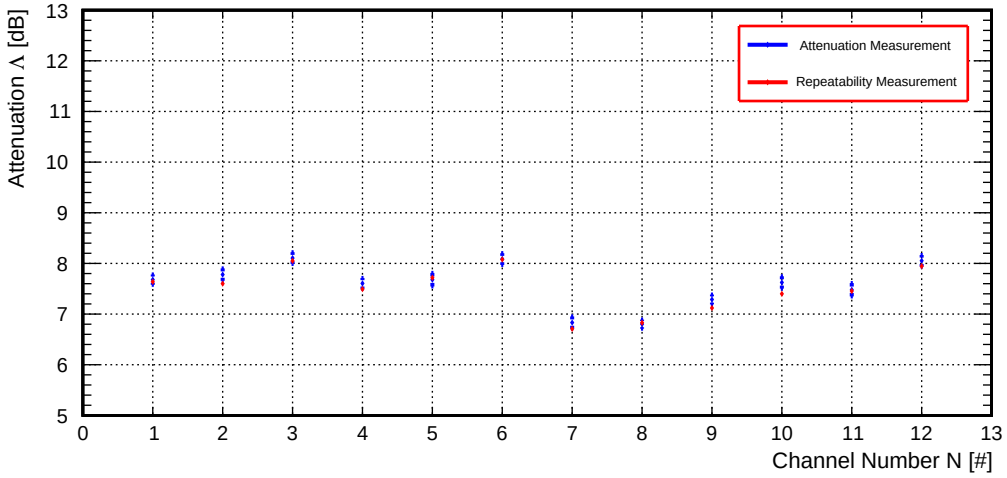

Fig. 6.11 Attenuation of all twelve fiber switch channels

*The graph presents the measured **attenuation value of each channel**. The **blue markers** show the **results of a single measurement** while the **red markers refer to the calculated mean values of the reliability performance test**.*

From figure 6.11 it can be derived that the optical fibers exhibit different attenuation values. Hence, when the final intensity of the laser beam is calculated, these differences should be taken into account.

6.2.10 100 m Optical Fiber

The 100 m long fibers[26] bought from the company *Leoni Fiber Optics* are equipped with FC/PC connectors at both ends and posses a nylon jacket. One end is directly connected to the fiber switch module, guiding the laser light from the TT bridge into the central detector to the fiber termination holder (see section 6.3). The most important property of the optical fibers is their transparency. Usually, glass fibers are characterized by low transparency values in the blue wavelength region. As a consequence, it was not easy to find a company which provides cables of this length with a sufficiently low attenuation. Figure 6.12 presents the attenuation values of all twelve optical fibers. Here, the blue markers refer to the measurements conducted in the lab while the red markers show the results of measurements which were conducted by the Leoni company itself. As it can be seen, most of the results of the

[26] Leoni Fiber Optics: KFCP-XXXV2100M A-V(ZN)Y 1S50/125UVAN, 100 m long optical fiber, multimode, designed for $\lambda = 430$ nm.

self-conducted measurements agree with the results of the company Leoni Fiber Optics. According to the self-conducted measurements, seven out of twelve cables exhibit an attenuation of $\Lambda \leq 8$ dB. However, the rest of them exceeds this value. Four of them have an attenuation of $\Lambda > 10$ dB. One of these four fibers even exceeds this limit with $\Lambda > 14$ dB.

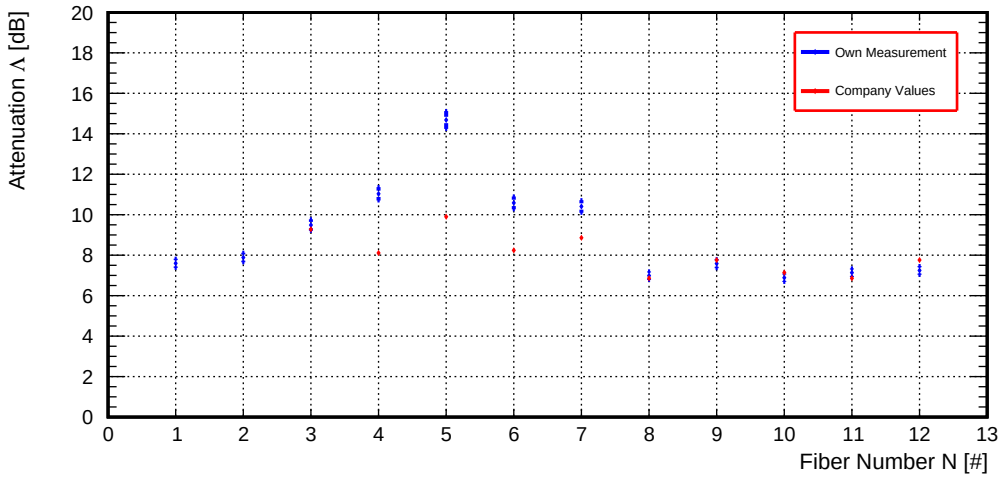

Fig. 6.12 Optical transparency measurement of the optical fibers

*The graph illustrates the **transparency measurement** for the **twelve 100 m long optical fibers** from Leoni. While the **blue data** shows the **attenuation measurements conducted in the lab**, the **red data** shows the **attenuation values** determined by the **Leoni company** itself.*

Even though these values are large, the laser intensity is still high enough to provide the necessary light for the transparency measurement. However, for the calculation of the final beam intensity, it is mandatory to know which of the 100 m long fibers is connected to which channel of the fiber switch module.

6.2.11 1 m Fiber With GRIN Lens

In the central detector, the 100 m fibers are connected via FC/PC mating sleeves with another type of optical fibers. These fibers[27] are only 1 m long and have GRIN lenses[28] directly mounted on their other end. Here, the laser is decoupled from the fibers. The GRIN[29] lens is extremely fragile, therefore, a screw[30] with a POM[31] tip is used to fix the lens at the fiber termination holder. A PO shrinking tube covers the

[27] CeramOptec: customized solution, silica glass fiber, core diameter $\varnothing = 50\,\mu$m, cladding 125 μm, acrylate jacket 250 μm.
[28] GRINTECH: GT-LFRL-180-025-20-CC, design wavelength $\lambda = 670$ nm.
[29] Gradient refractive index.
[30] MiSUMi: CBPPS3-10, hexagon socket M3 screw, length $L = 10$ mm, with POM tip.
[31] Polyoxymethylene.

1 m fibers to protect them against mechanical stress. The lens' main purpose is to collimate the laser beam underwater. As water has a higher refractive index then air, this is normally rather challenging. However, the GRIN lens exhibits a gradient profile regarding its refractive index in order to collimate the traversing rays already inside the lens' volume (for more details see section 5.3). Therefore, GRIN lenses are suitable for underwater collimation operations.

There are two properties which are of major concern for the AURORA system. On the one hand it is important to know how much light is lost when propagating through the 1 m fiber and the GRIN lens. These values must be taken into account when the final beam intensity is calculated. On the other hand the cone angle α^* (double aperture angle α) of each GRIN lens should be measured. It helps to understand how many PMTs are directly illuminated by the laser beams. Furthermore, it clarifies if a pinhole structure for a further reduction of the cone angle is necessary. Later on for the analysis, a collimated beam is preferable for the analysis algorithm to disentangle the optical lengths L, L_s and L_a from each other (for more details see chapter 7).

The attenuation of the 1 m fibers equipped with the GRIN lenses are in comparison to the channels of the fiber switch module and the twelve 100 m fibers negligible small. In the lab no significant intensity loss could be observed. However, for a conservative estimate an attenuation of $\Lambda = 0.04$ dB (provided by CeramOptec [124]) is considered for all twelve fiber-lens combinations.

As the refractive index value of water is higher than the value of air, the aperture angle of the laser beam is supposed to be smaller underwater. Thus, for an accurate measurement the aperture angle should be determined in a set-up which is submerged in water. Two pictures of the assembled set-up are shown in figure 6.13. For the measurement, laser light was guided through the GRIN lenses which were fixed to a mount structure. The whole construction was placed in an aquarium filled with distilled water. At a constant distance outside the aquarium the beam profiler (CCD camera) was located. In contrast to that, the distance between the GRIN lens and the aquarium glass was varied. At each distance the beam profile of the laser spot was recorded. In appendix A, a set-up scheme and a detailed derivation of the relevant formula can be found. In order to calculate the aperture angle, the recorded beam profile is cut through the spot's center into two slices – a horizontal and a vertical one (see appendix B). Afterwards, the full width at half maximum (FWHM) of both Gaussian profiles is determined. The horizontal and vertical beam

width can be transformed into a horizontal and vertical underwater aperture angle by using the following formula:

$$s = 2 \cdot \left[D_w \tan\alpha + D_g \tan\left(\sin^{-1}\left(\frac{n_w}{n_g}\sin\alpha\right)\right) + D_a \tan\left(\sin^{-1}\left(\frac{n_W}{n_a}\sin\alpha\right)\right)\right] \tag{6.7}$$

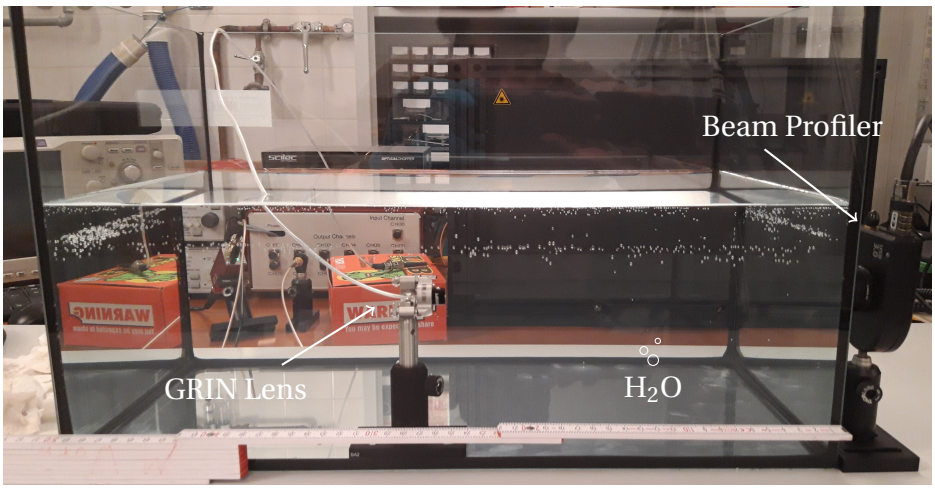

(a) Side view of the set-up

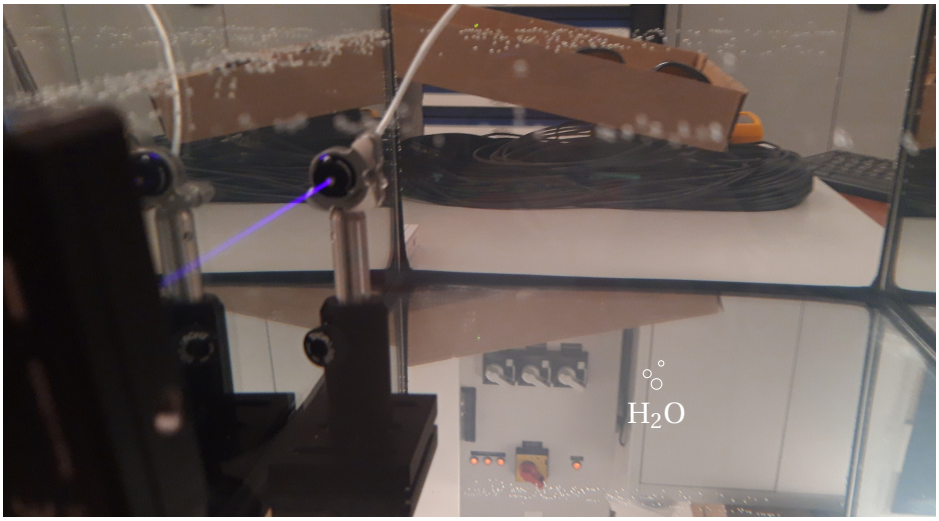

(b) Front view of the set-up

Fig. 6.13 Set-up of the aperture angle measurement

The figure presents ***two pictures of the set-up*** *which was assembled in order to* ***measure the aperture angle of the GRIN lenses*** *underwater. While figure 6.13(a) shows the* ***set-up from the side****, figure 6.13(b) visualizes the* ***front view of the assembly****. Here, it is possible to observe how the* ***blue laser light decouples from the GRIN lens****.*

Here, s is the spot width while α refers to the aperture angle. The parameters n_w, n_g and n_q stand for the refractive indices of water, glass and air, respectively, and D_w, D_g and D_a corresponds to the beam path lengths in the same media.

Equation (6.7) is rather complex. In order to avoid the attempt to transpose this equation (direct calculation of the aperture angle α and, therefore, of the cone angle α^*), the α value is varied until the result of s matches the measured slot width.

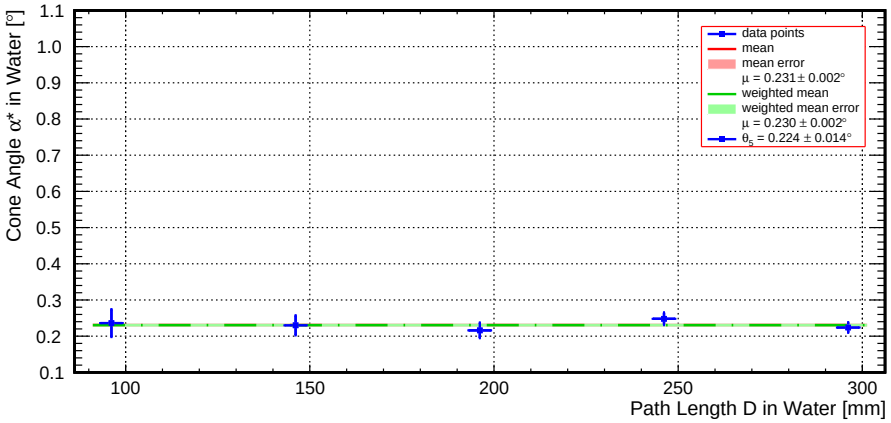

(a) Horizontal slice

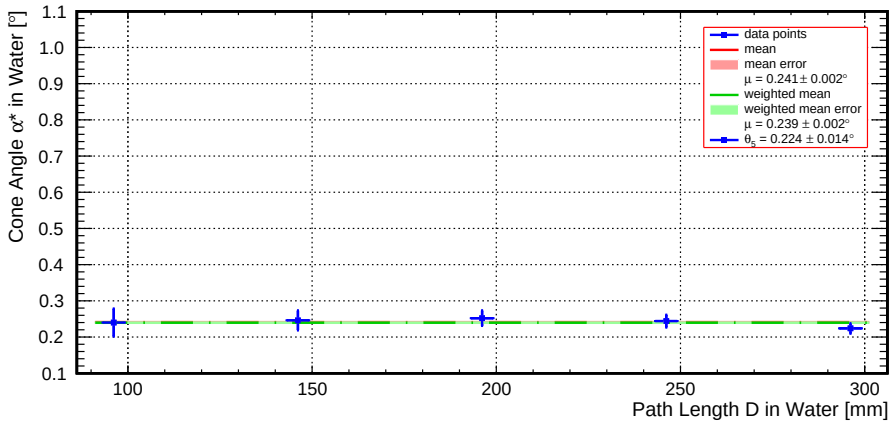

(b) Vertical slice

Fig. 6.14 Cone angle measurement of one of the GRIN lenses

*The figure shows the **results of the cone angle measurement** of one of the GRIN lenses. While the **blue markers** refer to the **calculated aperture angles** for a given path length D in the distilled water, the **red and green lines** stand for **mean values**. For the calculation of the **red mean** value all data points had the **same weight**. In contrast to that, for the calculation of the **green mean** value the data point's **values were weighted by the path length** D **in water**.*

Figure 6.14 shows the results of such a measurement. Here, the resulting cone angle α^* is plotted against the beam path D_w for the horizontal and vertical slice. For this

GRIN lens, a cone angle (FWHM) of $\alpha^* \sim 0.23°$ and $\alpha^* \sim 0.24°$ for the horizontal and vertical slice can be determined. These are already rather small cone angles. If only the value for the longest path length in water is considered, the final cone angle for both slices is $\alpha^* = 0.22 \pm 0.01°$. The conducted measurement was performed for all GRIN lenses. An overview of all results is presented in figure 6.15.

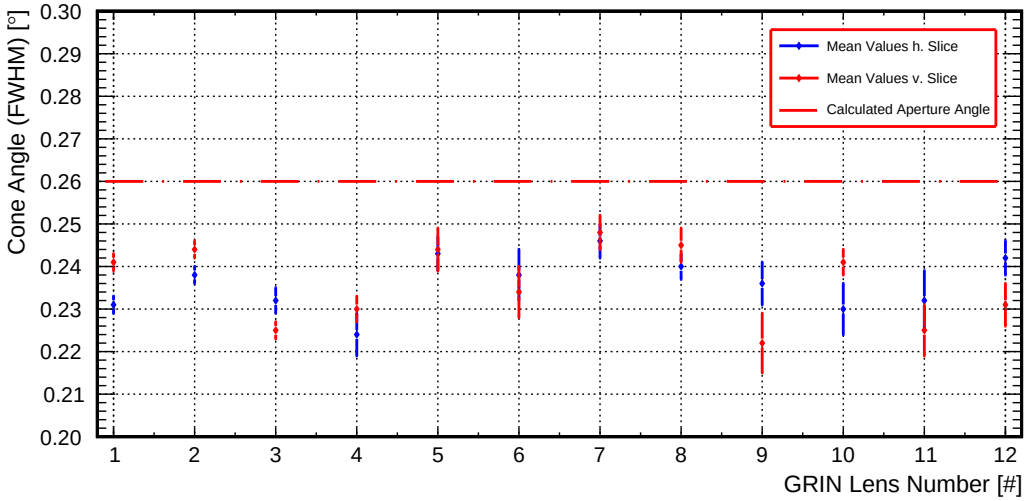

Fig. 6.15 Cone angles of all twelve GRIN lenses

*The graph presents the **results of the cone angle measurements for all twelve GRIN lenses**. Here, the aperture angle is given for the **vertical and horizontal** beam width colored **red and blue**, respectively. In addition, the **dashed, red line** shows the cone angle which is **predicted by the theory of GRIN optics**.*

Here, the mean values without weights are plotted together. They all scatter around a value of roughly $\alpha^* \approx 0.24°$. In addition, the cone angle predicted by the theory (for more details see section 5.3) is indicted by the dashed, red line. Even though the theory value is close to the results of the conducted measurements, it is still too high. This could have different reasons. For the calculation of the theory value the gradient constant g_0 of the GRIN lens plays an important role. This value was extracted from a graph which shows the chromatic aberration of the GRIN lenses (see appendix B). As this data is not based on an actual measurement but follows from a dispersion model [119], there might be already some kind of systematics included, which shift the aperture angle to higher values. Another reason could be a hidden systematical uncertainty in the conducted measurement, which shifts the results to lower values.

In order to evaluate if the measured cone angle of approximately $\alpha^* = 0.25°$ is already sufficient, laser beams of various cone angles were simulated with the

official JUNO simulation framework `offline` to check on the resulting hit map patterns in the PMT array. Figure 6.16 presents the results of this study.

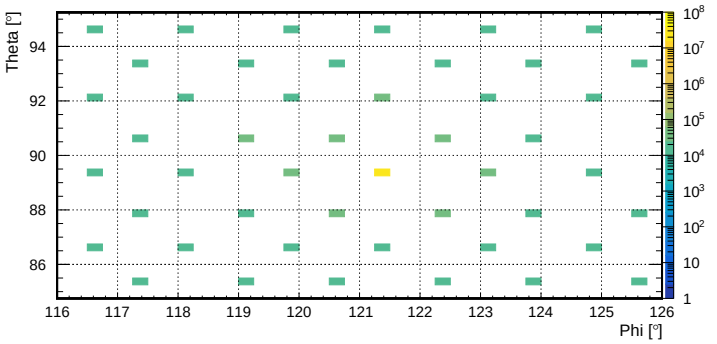

(a) $\alpha^* = 0.00°$, direct hit

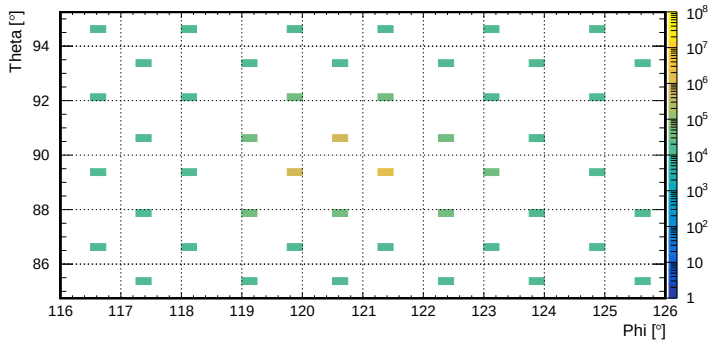

(b) $\alpha^* = 0.00°$, targeted small PMT slot

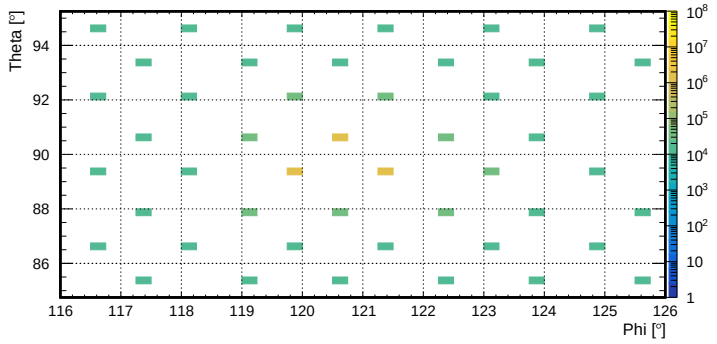

(c) $\alpha^* = 0.25°$, targeted small PMT slot

Fig. 6.16 Hit map pattern for various beam properties and alignments

The figure presents ***three different hit map patterns*** *of a small area of JUNO's PMT array. Here, the shown area corresponds to the location which is targeted by one of AURORA's laser beams. In figure 6.16(a) the* ***cone angle is zero*** *and a* ***large PMT is directly hit****. In figure 6.16(b) the* ***cone angle is zero*** *as well. However, here an unoccupied* ***slot of a small PMT is targeted****. Figure 6.16(c) presents the hit map pattern for a laser beam with a* ***cone angle*** $\alpha^* = 0.25°$ *(FWHM) which targets again a* ***slot of a small PMT****.*

Here, the laser beams have a Gaussian intensity profile and the declared cone angles. As a consequence, for a non-zero cone angle the beam intensity is dropped down to 50% of the maximum intensity under an angle of $\frac{\alpha^*}{2}$ (between optical axis and marginal ray). From figure 6.16(a) it can be derived that the recorded hit number is rather high if a PMT is directly hit by the beam[32]. However, if this beam with a zero cone angle is tilted until its maximum targets a slot of a small PMT, the recorded amount of events of the nearest PMTs drops down by around two orders of magnitude. Therefore, the hit map pattern significantly changes. However, for a laser beam with a cone angle of $\alpha^* = 0.25$ which targets the same slot of a small PMT, the hit map pattern does not change anymore. Here, the recorded number of hits is just slightly increased. This behavior can be explained by the Gaussian intensity profile. Even though the spatial photon distribution becomes broader with an increasing cone angle, most of the photons still strike the slot of the small PMT. The hits in the neighboring PMTs are primarily caused by scattered photons. Consequently, a further reduction of the cone angle will not significantly change the situation because here the scattering processes inside the LS volume dominate the spatial distribution of the beam. As a result, a pinhole for the GRIN lenses would not have any effect on the final cone angle of the beam. Therefore, the construction of a pinhole was not realized.

[32] In total, one billion photons were simulated.

6.2.12 Recapitulation Of All Intensity Losses

This section summarizes all discussed intensity losses for a beam which is operating within normal parameters.

Component	Attenuation [dB]	Uncertainty [dB]
Y-fiber	3.01	±0.02
Reference beam system	0.00	±0.05
Optical bridge	1.5	±0.3
Optical chopper	50.0	±0.5
Attenuator	0.00 to 40.00	±0.01 to ±0.12
Fiber switch module	7.6378	±0.0033
100 m fibers	7.89	±0.24
1 m fibers with GRIN lenses	0.04	±0.00

Table 6.1 Attenuation values of AURORA's optical components

*This table lists **typical attenuation** values of **AURORA's optical components**.*

Here, an incident intensity of $500.0 \pm 0.1\,\mu$W is assumed. Furthermore, the Y-fiber exhibits here a split ratio of 1:1. The optical chopper is assumed to cut the laser beam into pulses with a width of 10 μs. As a consequence, the amount of photons has to drop automatically by five orders of magnitude (treated as an attenuation). For the fiber switch module the attenuation value of the first channel is listed as its performance is located in the middle range. Similar argument holds for the 100 m fiber. Here, the value of fiber two was chosen. Unfortunately, no uncertainty for the attenuation value of the 1 m fibers is known. Thus, the listed value is assumed to exhibit no uncertainty at all. As the other listed attenuation values are much higher, this does not significantly affect the final result.

If the attenuator device is set to 0.00 dB, the final intensity of the laser will be reduced by 70.08 ± 0.63 dB, resulting in roughly $106.0 \pm 14.3 \cdot 10^6$ photons per pulse. The relative uncertainty of the final intensity is here 13.5%. With an attenuator set to 40.0 dB, the final attenuation will be 110.08 ± 0.64 dB. In this case a 10μs pulse would contain approximately $10.6 \pm 1.4 \cdot 10^3$ photons. Thus, the relative uncertainty is here 13.2%.

6.3 AURORA's Electro-Mechanical System

The following section presents the electro-mechanical system of AURORA. If necessary, this subsystem is used to adjust the laser beam direction during the transparency measurements. On the one hand the beam direction could be altered in case the beam's path is blocked by an obstacle[33]. On the other hand the laser spot can be moved to an unoccupied slot of a small PMT[34]. In this case the transparency measurements can be conducted at higher beam intensities without posing a threat to the nearby PMTs (see section 6.2.11). Besides the reduced risk to shorten the lifetime of directly illuminated PMTs, the signal-to-noise ratio can be improved as well. Figure 6.17 illustrates the accumulated number of recorded PE hits for the entire PMT array for 200 million[35] simulated photons in case an unoccupied slot of a small PMT is targeted. For the simulation, the attenuation and scattering length[36] of the LS were set to $L = 20.0\,\text{m}$ and $L_s = 30.0\,\text{m}$, respectively. In this case the absorption length is $L_s = 60.0\,\text{m}$.

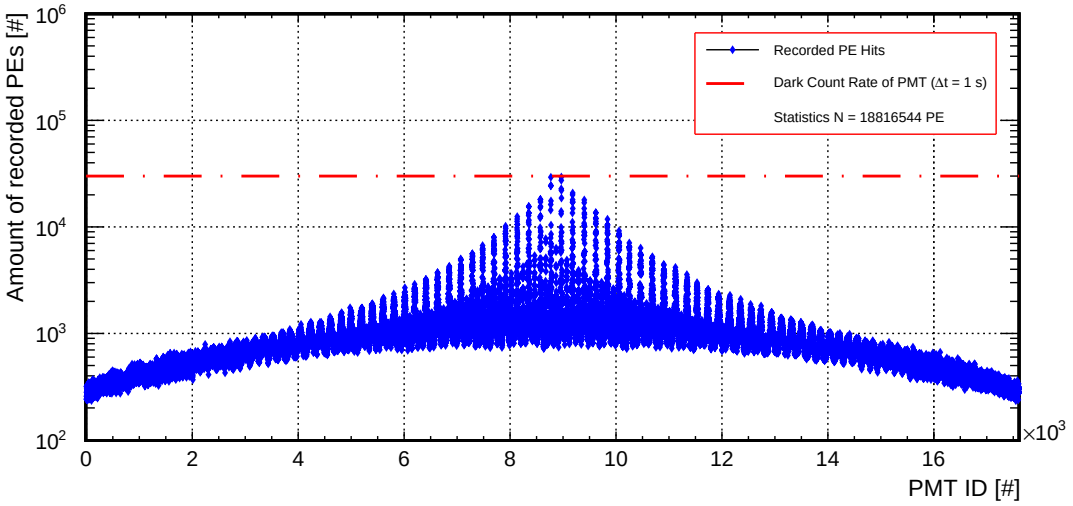

Fig. 6.17 PE hit distribution of an 1 s measurement

The graph presents the ***amount of PE hits*** *of an* ***1 s measurement for each PMT*** *for the* ***whole PMT array****. Here, it was assumed that the* ***laser beam is pulsed*** *with a* ***pulse width of 10 µs****, an* ***operation frequency of 200 Hz*** *and exactly* ***one million photons per pulse****. In addition, the* ***dashed, red line*** *indicates the* ***average dark count rate of a large PMT****. JUNO's simulation framework* `offline` *was used to produce the plot.*

[33] Like a connecting bar or an acrylic node.
[34] A 3" PMT.
[35] According to AURORA's performance, this is the amount of photons which is inserted into the JUNO detector in one second if the cw laser beam is cut into 10 µs pulses with one million photons per pulse and an operation frequency of 200 Hz.
[36] At a wavelength of $\lambda = 430\,\text{nm}$.

Here, the recorded PE hit numbers are plotted against the PMT ID numbers. The data only includes the readings of the large PMTs[37]. Thus, the ID number ranges between 0 and 17612. The data distribution is rather symmetric. While the wings of the distribution refer to the readings of peripheral PMTs, the maximum in the center corresponds to the PMTs close to the insertion and exit point of the laser beam. Taking a closer look, it seems that in the center two different distributions are layered on top of each other[38]. The distribution with the higher count rates originates from the hemisphere where the laser spot strikes the PMT array. The distribution with the lower hit numbers corresponds to the insertion point hemisphere[39]. In principle, the recorded PE hits of this hemisphere originate from photons which were reflected at the acrylic sphere or backward scattered inside the water layer, the acrylic vessel or the LS volume.

It can be seen that the PMTs, which recorded the highest statistics, exhibit just enough counts to reach the dark count rate limit (red, dashed line). This clearly indicates that an amount of one million photons per pulse combined with an operation frequency of 200 Hz does not pose a threat to the PMT array, as a signal strength similar to the dark count rate is manageable for a PMT. With a pulse width of 10 μs, the signal-to-noise ratio is still fine. Even for a dark count rate of 100 kHz, the expected amount of background events in such a short time window would be on average just 1. Consequently, even for the PMTs with the lowest statistics (left or right wing), the signal-to-noise ratio is already higher than 1:1 (for the comparison the PE hit numbers have to be divided by 200 while the dark count rate has to be divided by 10^5). For the PMTs close to the laser spot[40], the signal-to-noise ratio is on average 150:1. The readings for the PMTs close to the insertion point exhibit still a signal-to-noise ratio of roughly 50:1. This is sufficiently high enough as well. Thus, an operation frequency of 200 Hz, a pulse width of 10 μs and an intensity of one million photons per pulse meet all requirements for a smooth operation and an unproblematic data acquisition. However, from subsection 6.2.11 it can be concluded that for a directly illuminated PMT[41] the recorded PE numbers are at least two orders of magnitude higher than the shown maximum in figure 6.17. With more than 15000 PE hits in a time period of only 10μs for the whole measurement time, these settings could already shorten the lifetime of a directly targeted PMT. As a consequence, to reach convenient signal-to-noise ratios on the one hand

[37] Both 20" PMT types – MCP and Dynode.
[38] PMT ID number range from 4000 to 14000.
[39] Similar results can be found in chapter 7. *E.g.* compare figure 6.17 with figure 7.1.
[40] Exit point hemisphere.
[41] Gaussian maximum hits PMT cathode.

without exceeding the maximally tolerable amount[42] of PE hits on the other hand, the AURORA system is equipped with tiltable laser beams. Figure 6.18 lists all corresponding components of the electro-mechanical system and shows how they are connected with each other to realize this useful feature.

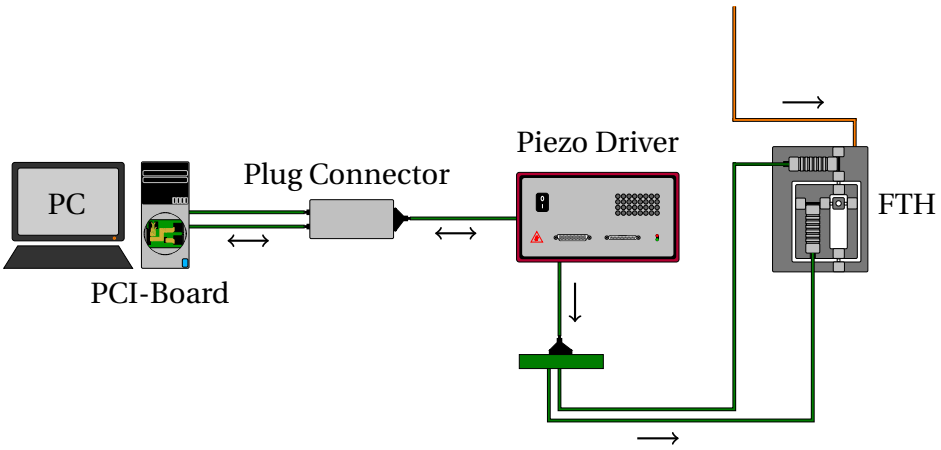

Fig. 6.18 Scheme of the electro-mechanical system

*The scheme illustrates **AURORA's electro-mechanical subsystem**. On the right the **FTH** is drawn which is able to tilt the end of the optical fiber (colored orange) and, therefore, can change the beam direction. The actuators of the FTH are **piezoelectric crystals** which receive their power from a **piezo driver** shown in the center right. This device is basically an amplifier being connected via a **plug connector** in the center left with a **PCI-board** on the left. The board itself is integrated in a **PC** and provides the necessary analog signals for the piezo driver.*

According to figure 6.18, there are three cables[43] which terminate at the FTH[44]. On the one hand there is one 1 m long optical fiber with a GRIN lens at its end where the laser is decoupled from. Here, the GRIN lens is fixed via a screw with a POM tip to the center of the FTH. The 1 m long optical fiber is connected to a 100 m long optical fiber which guides the laser light from the fiber switch module to the FTH (for more details read the previous subsection 6.2). On the other hand there are two *1 m long electrical cables* which are connected to the *piezoelectric crystals* of the FTH. These two 1 m long cables are connected to two *100 m long*

[42] PMT's response is linear up to around 1000 PEs. Signals in the order of 5000 PEs (*e.g.* muons) are still manageable. However, already in these cases the photons should not reach the PMT cathode at the same time [117, 154]. Intensities above this limit might be problematic for the DAQ or even dangerous for the PMT lifetime.

[43] Both the 100 m long electrical cables from AXON and the 100 m long optical fibers from Leoni are threaded through metallic bellows. For the sake of simplicity, these bellows were not included in figure 6.18.

[44] In total, there are twelve FTH components distributed over the whole northern hemisphere of the central detector (SSLS).

electrical cables which connect the FTH's actuators with their power source. This power source is an amplifier designated as *piezo driver* which amplifies the analog signals of a *PCI-board*. The board is integrated in a local computer. As the amplifier has a standard DB37 female connector as its input interface, the PCI-board's cables with their dozens of wires had to be rearranged in order to satisfy the amplifier's specifications. This rearrangement is organized inside the *plug connector*. Starting at the FTH and then going backwards through the electro-mechanical system, each component will be discussed in more detail in the following sections.

6.3.1 Fiber Termination Holder

As already mentioned, the main purpose of the electro-mechanical system is the realization of tiltable laser beams. The component which tilts the termination of the optical fiber is the FTH itself. Figure 6.19 shows both a picture of the constructed prototype and a 3D model[45] designed in SOLIDWORKS.

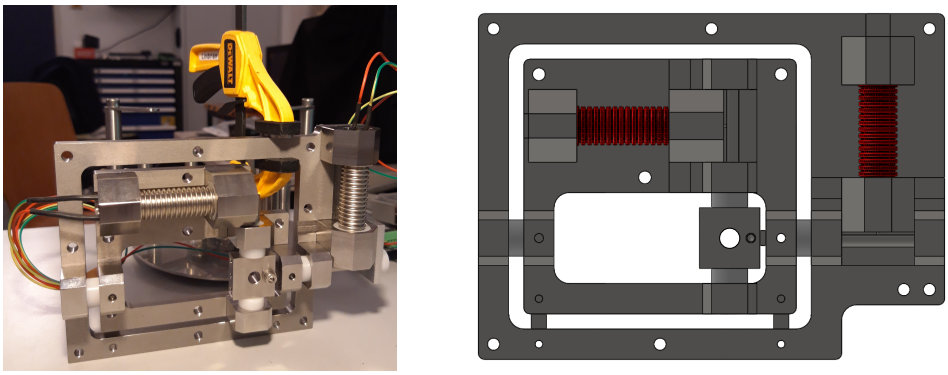

(a) Picture of FTH prototype (b) 3D model of FTH

Fig. 6.19 Design of the fiber termination holder

*The figure shows the **design of the FTH**. While figure 6.19(a) presents a **picture of the first fully functional prototype**, figure 6.19(b) illustrates a **3D model of the FTH** designed with **SOLIDWORKS**, highlighting in red the piezoelectric crystals.*

Highlighted in red in figure 6.19(b), the actuators of the FTH are the most important parts in order to tilt the laser beams. The working principle of the FTH component is shown in more detail in figure 6.20. Primarily, the linear expansion/contraction of a piezoelectric element is translated into a rotary motion. Piezoelectric actuators

[45] The design and construction phase of the FTH took some time and involved several people. While a first draft was designed with the help of Rainer Othegraven, the final version was created with a lot of help of Johannes Jakobi, Lukas Schmidt and Matthias Eck. Especially Johannes improved the design by adding a lot of useful features.

have the advantage that they do not generate strong magnetic fields which could influence the performance of the closely located PMTs (for more details about actuators see section 5.2; magnetic field measurements are presented in the subsequent section). Unfortunately, the typical mechanical stroke of such actuators is in the order of several tens of micrometers. Consequently, the FTH has to be accurately designed in order to be able to translate each micrometer of the stroke into a rotary motion.

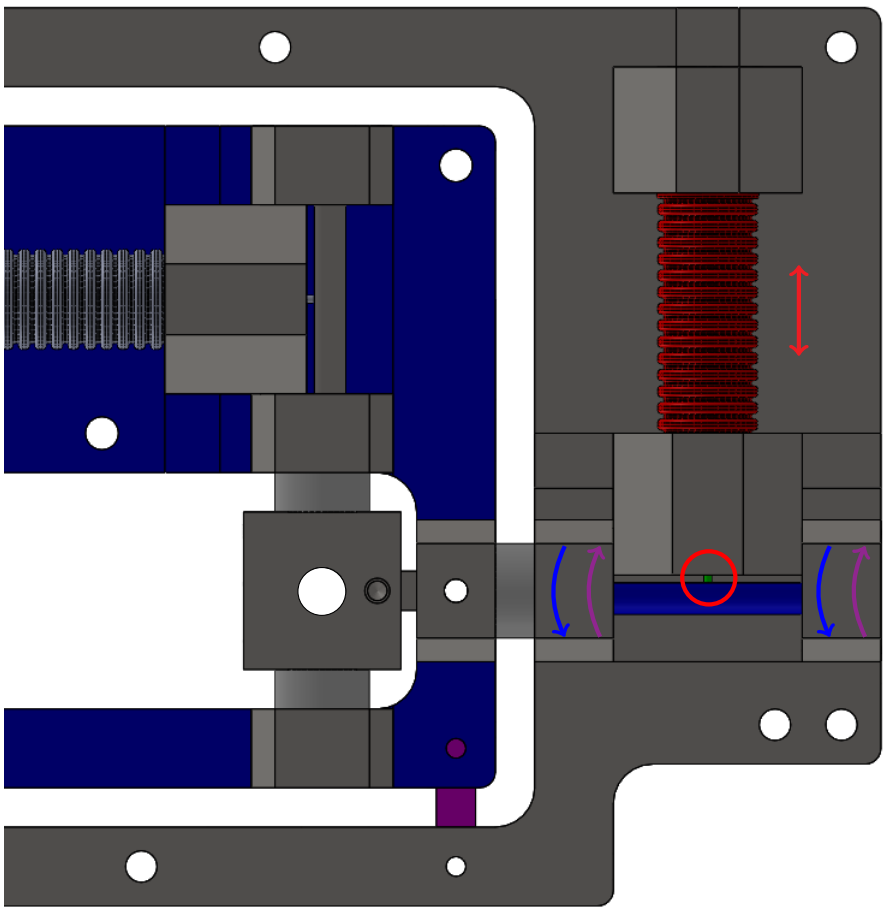

Fig. 6.20 FTH – working principle

*The figure presents the **working principle of the FTH**. Besides the **piezoelectric crystal** being **colored red**, a **pin colored green** and **indicated by the red circle**, and the **rotation axis** with the **corresponding middle plate colored blue** are drawn as well. In addition, the **plate which is providing the restoring forces** in order to let the FTH return into its zero position after the tilt movement is **highlighted in violet**. The **red arrow** indicates the **expansion/contraction direction** of the actuators if the voltage is altered. The **blue and violet arrows** are showing the **rotary motion of the blue plate** if the voltage of the piezoelectric crystal is increased or reduced, respectively.*

Here, the piezoelectric crystal will expand if a voltage is applied. While expanding, the actuator pushes a pin (green component indicated by the red circle in figure 6.20) against a rotation axis. This rotation axis is connected to a plate, which will rotate as well if the pin pushes against it (blue parts in figure 6.20). According to figure 6.20, the upper (lower) part of the blue plate will rotate out of (in) the image plane if the piezoelectric crystal is expanding. To return to its zero position, additional plates (violet part in figure 6.20) are installed which provide the necessary restoring forces. The same mechanism is used to tilt the center plate but in a perpendicular direction. The second piezoelectric crystal is needed for that.

In order to ensure that AURORA's beams can be moved to an unoccupied slot of a small PMT, the minimum displacement of the laser spot along the SSLS structure should cover a length similar to the diameter of a large PMT, so 20" or 50 cm in θ- and ϕ-direction. This requirement translates into a tilt angle $\alpha \simeq 1°$, assuming a beam path of around 40 m. The piezoelectric crystals are able to provide a stroke of $\Lambda = 48\,\mu$m. As a result, a rotation of around 1° can be realized if the lever arm of force of the FTH is approximately 2.75 mm long (see appendix A for more details regarding this calculation). This is why the pin's contact is located 2.5 mm away from the center of the rotation axis. A narrow pin is used to transfer the crystal's force because in this case the contact point is always clearly defined. Ball bearings made of stainless steel (type 1.4301) are used to fix the two rotation axes of the FTH. On the one hand this ensures an easy and smooth rotary motion. On the other hand the stainless steel frame of the bearings does not significantly deform. As a consequence, most of the piezo's mechanical stroke is translated into rotary motion rather than used to linearly displace the rotation axes themselves.

As the FTH will be mounted on the SSLS, it will be surrounded by water for the whole operation time of JUNO. Therefore, all assembled materials should exhibit a sufficient resistance against corrosion. This is why the metal parts of the FTH are made of stainless steel. The standard stainless steel (type 1.4301) is already suitable for an environment like distilled, ultrapure water. However, to be sure that the FTH does not corrode over the years, the stainless steel alloy of type 1.4404 with an improved resistance against corrosion is used for most of AURORA's parts. Here, the addition of molybdenum causes the higher resistance against corrosion. Around 2% of the alloy (stainless steel type 1.4404) is molybdenum. The exact chemical composition of the standard stainless steel 1.4301 and the stainless steel types 1.4401/1.4404 are listed in table 6.2. The alloy 1.4401 is presented as well because this stainless steel type will be used for the SSLS of the CD. Except for a

small difference in the carbon content, the stainless steel types 1.4401 and 1.4404 are the same. The lower carbon content further reduces the steel's tendency to oxidize.

Elements	Stainless Steel - Material Number			
	1.4301	1.4401	1.4404	
C	≤ 0.070	≤ 0.070	≤ 0.030	0.023
Si	≤ 1.000	≤ 1.000	≤ 1.000	0.410
Mn	≤ 2.000	≤ 2.000	≤ 2.000	1.800
P	≤ 0.050	≤ 0.045	≤ 0.045	0.038
N	-	≤ 0.100	≤ 0.110	0.083
S	≤ 0.020	0.015 - 0.030	0.015 - 0.030	0.022
Cr	17.500 - 19.500	16.500 - 18.500	16.500 - 18.500	17.020
Mo	-	2.000 - 2.500	2.000 - 2.500	2.020
Ni	8.000 - 10.500	10.000 - 13.000	10.000 - 13.000	10.020

Table 6.2 Chemical composition of stainless steel types [100, 127, 131, 133]

*Listed are the **chemical compositions** of three different alloys - the **standard stainless steel 1.4301**, the **stainless steel 1.4401** which is **used in the JUNO experiment for the SSLS** and the almost **similar stainless steel 1.4404** which will be **used for AURORA's components**. The last column is divided into two subcolumns. While the left one lists the **standard values for the chemical composition**, the right one presents the **measurement results of an alloy sample** from the **THRESS company**, which will provide the stainless steel for AURORA.*

However, the FTH prototype (see figure 6.19(a)) is made of stainless steel 1.4301. The mechanical properties of 1.4301 should hardly differ from 1.4404, thus, the prototype is expected to behave like the final twelve FTH devices. The prototype's performance was tested in air and later on underwater[46]. In order to evaluate the performance of the FTH, laser light is guided through a 1 m long optical fiber with a GRIN lens mounted on its end. This lens is fixed to the central plate of the FTH. A CCD camera is monitoring the position of the laser spot at a distance of only 1 cm while not more than 140 V are applied to the piezoelectric crystals via the piezo driver. Figure 6.21 presents the results of the underwater performance measurement. Firstly, taking into account that each pixel of the CCD camera covers an area of $5.5 \times 5.5\,\mu m^2$ and the distance between light source and detector is just 1 cm, the maximum tilt angle for the horizontal and vertical displacement is 1.0° and

[46] Unfortunately, it was not possible to include performance measurements of the final FTH components in this thesis because these devices are getting produced by the time this thesis will be handed in.

1.1°, respectively. Thus, the FTH prototype meets the requirement. Secondly, the four blue markers at the top left show that the zero position varies from run to run. In contrast to that, if a voltage is applied to the actuators and the FTH is inclined, the uncertainty of the spot's position becomes insignificantly small. It is most likely that the larger uncertainty of the zero position is a result of the retaining forces which normally fix the spot's position and are here at their minimum. It can be concluded that, except for the zero position, the FTH's performance is characterized by a high repeatability. This could be helpful for the adjustment of the laser beam direction during the transparency measurements. Once an unoccupied slot of a small PMT is targeted, the corresponding voltage levels of the piezoelectric crystals can be used for subsequent measurements as well. Thirdly, the laser spot's displacement for one direction is not entirely disentangled from the other direction. Otherwise the angle ζ should be exactly 90.0° instead of the measured 81.2°. However, this does not diminish the FTH functionality, as the area the laser spot covers remains the same. In addition, further measurements have shown that for both directions the resulting tilt angle is proportional to the applied voltage.

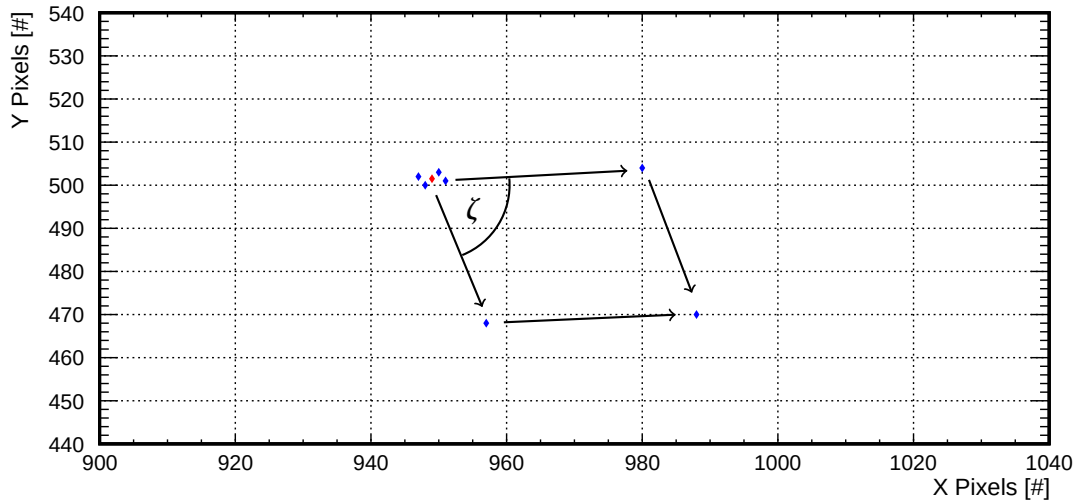

Fig. 6.21 FTH – performance measurement

*The figure presents the **FTH prototype's underwater performance measurement**. Here, each **blue marker** refers to the **position of the laser spot's center** for a specific voltage being applied to the piezoelectric crystals. The **red marker** is the **calculated mean**, taking all four blue marker's position at the top left into account. Here, the **voltage level of both piezos is set to zero**. The **other blue markers** indicate the **laser spot's position** of a tilted beam if the **maximum possible voltage is applied** to one or both actuators.*

All in all, the performance of the FTH meets the requirements. If necessary, the laser spot can be moved along the detectors inner surface in order to target a small PMT slot or bypass an obstacle like a node of the support structure.

6.3.2 Piezoelectric Crystals

As the piezoelectric crystals[47] are the key components of the FTH, this section will focus on their characteristics and performance. AURORA's actuators are made of lead zirconium titanate, which is a common piezoelectric ceramic (for more details see section 5.2). This kind of material is extremely vulnerable to water, and, therefore, it is associated with a reduction in its durability when it is exposed even to low humidity. In order to provide piezoelectric elements for underwater applications, the manufacturer *CeramTec* produces actuators in a stainless steel casing, which are hermetically sealed. The bought customized solution is a cylindrical actuator with a diameter $\varnothing = 13\,\text{mm}$, a length $L = 43\,\text{mm}$, a maximum blocking force of $F = 1300\,\text{N}$, a maximum applicable voltage of $V_{max} = 140\,\text{V}$ and a maximum resulting stroke of $\Delta L_{max} = 48\,\mu\text{m}$ [20]. According to [79], the actuator's casing is made of the two stainless steel alloys – 1.4305 and 1.4571. Their exact chemical composition is listed in the following table.

Elements	Stainless Steel - Material Number	
	1.4305	1.4571
C	≤ 0.100	≤ 0.080
Si	≤ 1.000	≤ 1.000
Mn	≤ 2.000	≤ 2.000
P	≤ 0.045	≤ 0.045
N	≤ 0.100	-
S	0.015 - 0.350	0.015 - 0.030
Cr	17.000 - 19.000	16.500 - 18.500
Mo	-	2.000 - 2.500
Ni	8.000 - 10.000	10.500 - 13.500
Ti	-	0.400 - 0.700
Cu	≤ 1.000	-

Table 6.3 Used stainless steel types for the actuators [79, 132, 136]

*The table lists the **chemical composition** of the **two stainless steel alloys** which are used for the **piezoelectric crystal's stainless steel casing**.*

While the top and bottom plate are made of stainless steel 1.4305, the bellow structure of the shell surface is made of the second alloy – stainless steel 1.4571. The first alloy exhibits a resistance against corrosion which is similar to the standard

[47] CeramTec: Hermetically sealed piezo-ceramic actuator, customized solution.

stainless steel 1.4301. In contrast to that, the bellow part of the piezo-ceramic, which is actually exposed to water, has a resistance against corrosion which is similar to the stainless steel types 1.4401 and 1.4404 [136]. All in all, the chemical and electro-mechanical properties of the sealed actuator indicate that this ceramic is suitable for AURORA's purpose. However, as the piezoelectric crystals will be located close to the PMTs, it was mandatory to check if they generate an external magnetic field, which could influence the PMT's performance. Hence, the magnetic flux density of an operating piezoelectric crystal was measured. The tests were performed at the highest applicable voltage values.

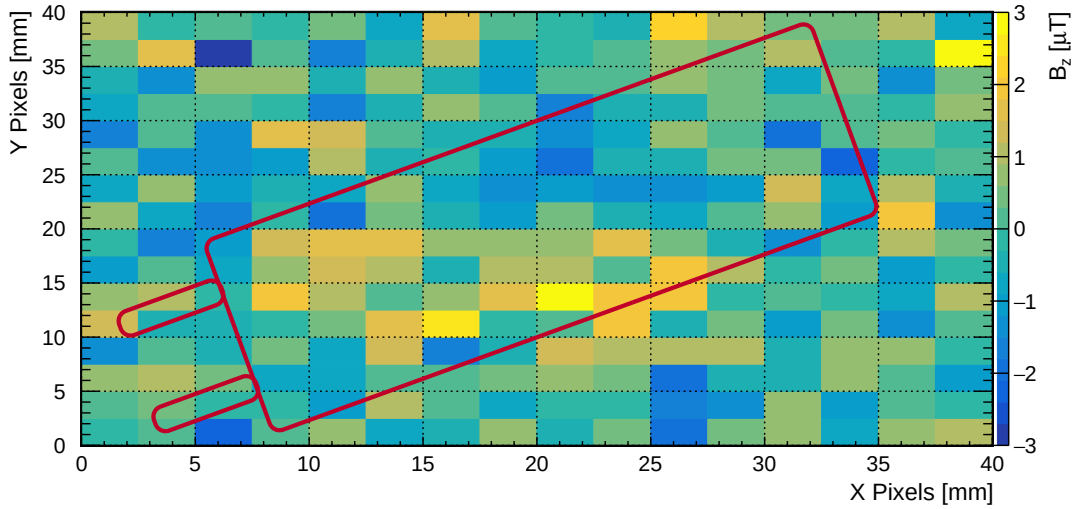

Fig. 6.22 Piezoelectric crystal's B-field – Hall probe

*The histogram presents the **result** of the first **magnetic flux density measurement**, which was performed with a* 16×16 ***hall probe array**. Here, each pixel refers to a single hall probe. While the **color code** stands for the **strength of the** B_z **component** of the B-field, the **red frame** indicates the **position and orientation of the piezoelectric crystal**.*

Figure 6.22 shows nothing but statistical fluctuations and noise. Consequently, if there is an external B-field, its signal is too weak to be recorded by this device. With a sensitivity of around 10 μT this result did not ensure that the actuator did not exceed the maximally allowed limit of 5 μT (10% of the Earth's magnetic field in Central Europe; limit was set by the JUNO collaboration [156]). Thus, the external field was measured a second time with a Foerster probe. This probe does not have a sensor array, therefore, it cannot provide the same spatial resolution as the previous used hall probe. However, the Foerster probe is characterized by a much higher sensitivity recognizing magnetic flux densities down to 0.1 nT. The sensor was attached to different positions of the piezoelectric crystal's casing. Neither at the top/bottom nor at the shell surface the magnetic flux density generated by

the actuator exceeded a value of 10 nT (see figure 6.23). As a consequence, the piezo-ceramic meets the requirements regarding the maximally allowed magnetic flux density.

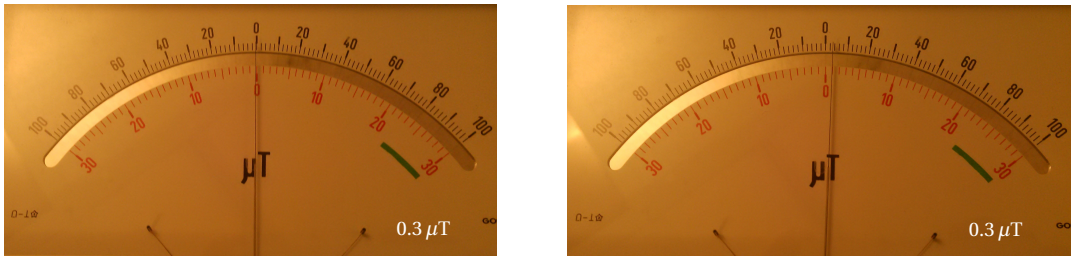

(a) Deactivated piezoelectric crystal (b) Activated piezoelectric crystal

Fig. 6.23 Piezoelectric crystal's B-field – Foerster probe

*The pictures show the **analog display of the Foerster probe**. While figure 6.23(a) presents the **display before 140 V were applied to the piezoelectric crystal**, figure 6.23(b) shows the moment when the **actuator was activated** and the floating current was at its maximum. The settings refer to the **red scale** during the measurement. Here, the 30 at the **scale's end stands for 0.3 µT**.*

In addition, the piezoelectric crystals were checked whether they expand by approximately 50 μm if a voltage of 140 V is applied. Here, a standard digital caliper with an accuracy of ± 5 μm was used. Each actuator passed the performance test.

6.3.3 100 m Electrical Cable

The voltage which is applied to the piezoelectric crystals is provided by the amplifier. As the amplifier is located on the TT bridge, there are around 100 m long electrical cables which connect the actuators with the amplifier. To be more precise, a 1 m long cable is directly attached to the pins of the piezo-ceramic and sealed with an epoxy resin. The other end of the cable is equipped with a waterproof connector. After the FTH is mounted on the SSLS, these 1 m long cables will be connected with the 100 m long cables which are equipped with the same type of waterproof connector. It is the *AXON* company which produced these cables[48] – the same company which also produces the cables for the small PMTs. Figure 6.24 illustrates the schematic cross section of an acquired AXON cable. The center of the AXON cable consists of a twisted pair of conductors. Here, stranded wires made of tin plated copper are used. The resistance of the cable is $R = 11.79\,\Omega$ per 100 m. Extruded FEP was used as an insulator. In addition to the two cores, 2×4 water blocking yarns are added to the

[48] AXON cables: 1 m and 100 m long cables with an HDPE jacket, waterproof connectors and self-sealing powder, customized solution.

cable's center in order to ensure that the cable exhibits a sufficiently round shape. This is important for a homogeneous distribution of the water blocking powder on the shield braid's surface. The shield braid is also made of plated copper and covers the whole cable's center. Serving as a safety measure, the water blocking powder becomes an extremely viscous liquid when it has contact with water curing after only a few seconds. This ensures that the electrical cable can seal itself in case the jacket material is damaged. An HDPE jacket is extruded on the shield resulting in a cable with a final diameter of $\varnothing = 2.95\,\text{mm}$ [134].

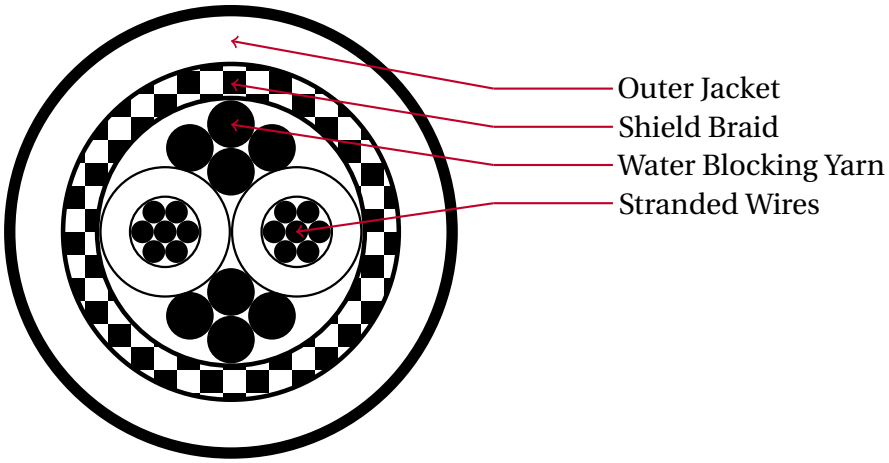

Fig. 6.24 AXON cable's cross section

*The figure illustrates the **cross section** of the **electrical cables** which are provided by the **AXON company**. The scheme is oriented towards reference [134].*

To ensure that the connectors of the AXON cables are waterproof and can withstand an overpressure[49] of around 5 bar, the AXON company tested the waterproofness of their cables. For that purpose, ten cables with a male connector were plugged into ten other cables with a female connector and submerged in a tank filled with water. After that, the vessel was pressurized with an overpressure of 8 bar for exactly one hour. Subsequently, the cables were visually checked for leakages or any other damages. In addition, the insulator's resistance was measured as well. Here, the resistance should not be smaller than 500 MΩ per 250 Vdc for 0.5 s. According to [144], the connectors, and with them the AXON cables themselves, passed the underwater tests. It can be concluded that the cables meet the requirements for longterm operations underwater.

[49] Maximum pressure inside the CD of JUNO.

6.3.4 Piezoelectric Crystal Driver

The piezoelectric crystals need for their maximum mechanical stroke a voltage of 140 V. Unfortunately, the PCI-board inside the computer can only provide voltages up to 10 V. Thus, the analog voltage signals from the PCI-board have to be amplified. This is done by the so called piezo driver[50]. Figures 6.25 and 6.26 show the input and output interface of the amplifier, presenting which pin refers to which channel and what kind of signal is applied.

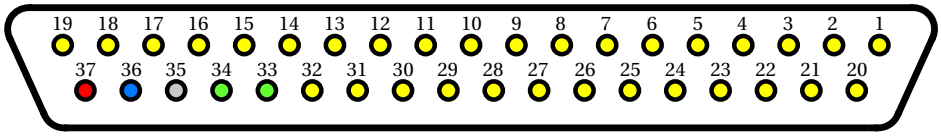

Fig. 6.25 Pin assignment of the amplifier input interface

*The figure shows the **pin assignment of the amplifier input interface**. Here, the **yellow and green pins** indicate channels of type **ANALOG and GROUND**, respectively. In addition, the **gray pin** is of type **NC** (not connected) while the **blue and red pin** is of type **DIGITAL**.*

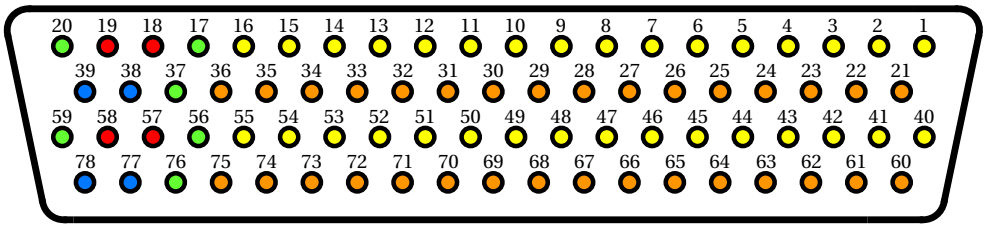

Fig. 6.26 Pin assignment of the amplifier output interface

*The figure shows the **pin assignment of the amplifier output interface**. Here, the **yellow and orange pins** indicate channels with **positive and negative analog outputs**. The **green pins** refer to outputs of **type GROUND**. In addition, the **red and blue pins** stand for **positive and negative high voltage signals** (for driving benders).*

Each analog signal at the input interface is amplified by a factor of 20. Here, the amplifier can handle both positive and negative voltage levels. The peak current of the output channels does not exceed 75 mA. Figure 6.27 exemplarily presents the amplifier's performance measurement. The results of the other channels look rather similar (see graphs in appendix B). In all cases the input voltage is successively amplified by a factor of 20. The recorded discrepancies are in the order of 0.1%. In addition, during the performance tests of the FTH no vibration of the piezoelectric

[50] Scientific Instruments: PD32-140/140, 32 channel amplifier.

crystals could be observed. As a consequence, the voltage levels of the amplifier are obviously stable enough. Thus, the piezo driver is suitable to control the actuators of the FTH components.

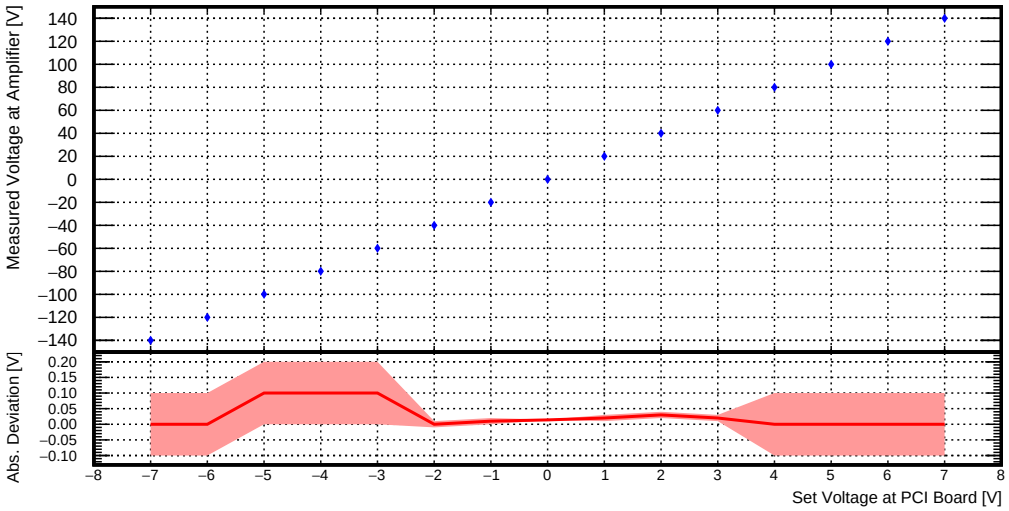

Fig. 6.27 Performance of the first analog channel of the amplifier

*Shown is the **performance measurement of the amplifier's first channel**. Due to the small differences between the set voltage (times an amplification factor of 20) and measured voltage at the amplifier channel, the graph is divided into two subgraphs. The **upper graph** shows the **measured voltages plotted against the set voltages** while the **lower graph** shows the **absolute deviation between the set voltage (times 20) and the measured voltage**. The light **red band** indicates the **uncertainty range of the measurement**.*

6.3.5 PCI-Board And Plug Connector

The actual source of the analog signals which are amplified by the piezo driver in order to control the actuators of the FTH is the PCI-board[51], being installed in a local computer. The PCI-board exhibits 32 analog channels which can provide a signal of ±10 V. In addition, the analog output device also has 8 digital channels with a logical voltage level of +5 V [128]. The output channels are accessible via two connectors. The first one provides the analog channels 1-8 and digital channels 1-8 while the second output interface is connected to the analog channels 9-32. As the PCI-board has two connectors, two cables are required to get full access to the board's features. Here, the two cables[52] were offered by the same company. Unfortunately, the piezo driver interface has a different standard requiring one

[51] National Instruments: PCI-6723, analog output device with 32 analog and 8 digital channels.
[52] National Instruments: SHC68-NT-S, PCI-board cable, 2 m long, second end without termination.

DB37 connector instead of two SHC68-NT-S connectors (see pin assignment in the previous section). Consequently, the wires of the two cables had to be rearranged and organized in one DB37 connector. This is done in AURORA's plug connector. Figure 6.28 shows the self-constructed adapter.

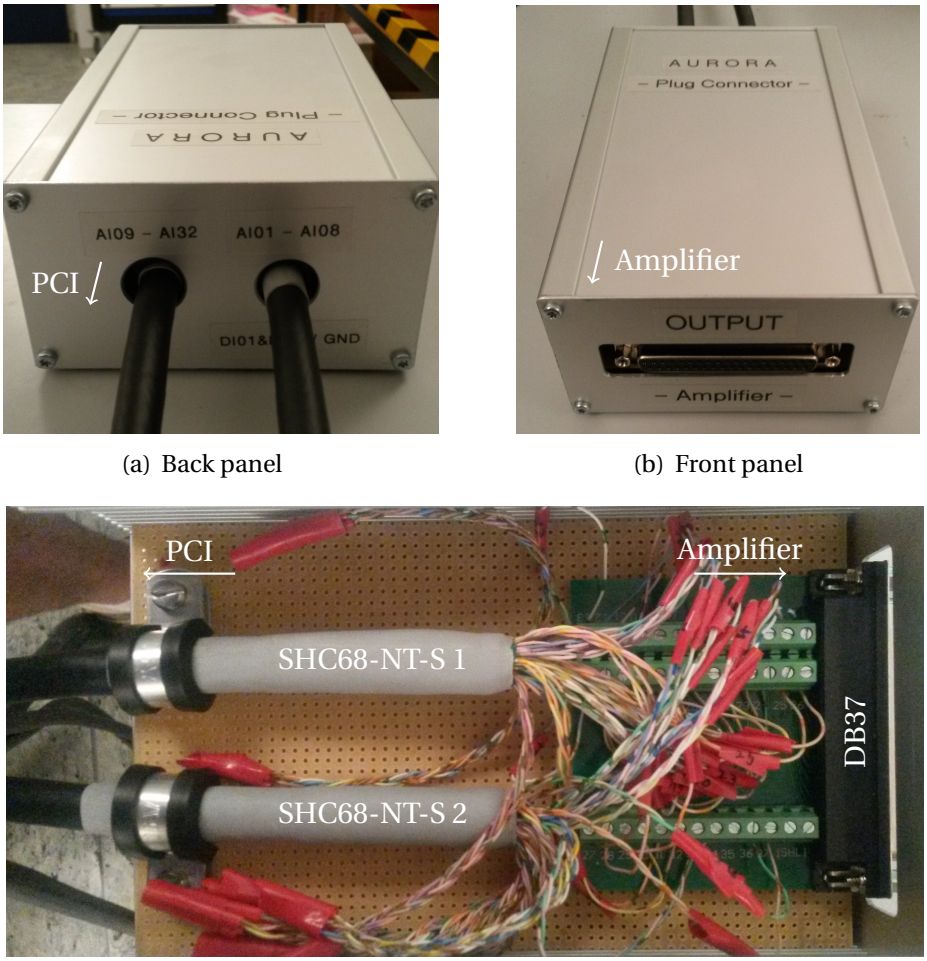

(a) Back panel

(b) Front panel

(c) Interior view

Fig. 6.28 AURORA's Plug Connetcor

*The three pictures show the **self-constructed adapter** in order to **connect the PCI-board with the piezo driver**. While figure 6.28(a) and 6.28(b) show the **back and front panel** of the plug connector, figure 6.28(c) presents the **interior** of the adapter.*

The two SHC68-NT-S cables provide in total 136 insulated copper wires while the DB37 connector just needs 37 wires[53] to be connected with. Thus, most of the wires do not have to be connected, and, therefore, they are insulated by red insulation tape (see figure 6.28(c)). In order to reduce the mechanical stress on the two SHC68-NT-S cables, they are fixed by clamps. Even though the cable routing inside the

[53] 32 analog channels, 2 digital channels, 2 ground channels and one not connected channel.

adapter looks slightly chaotic, the pin numbers of the DB37 connector and the corresponding wires of the SHC68-NT-S cables are sorted by the wire's color and listed in table 6.4.

Pin No.	Wire Color	Type		Pin No.	Wire Color	Type
1	**white-blue**	ANALOG		20	**violet-tan**	ANALOG
2	**white-yellow**	ANALOG		21	**white-yellow**	ANALOG
3	**violet-tan**	ANALOG		22	**yellow-tan**	ANALOG
4	**white-pink**	ANALOG		23	**blue-tan**	ANALOG
5	**white-gray**	ANALOG		24	**green-tan**	ANALOG
6	**white-tan**	ANALOG		25	**orange-tan**	ANALOG
7	**white-green**	ANALOG		26	**pink-tan**	ANALOG
8	**pink-blue**	ANALOG		27	**tan-brown**	ANALOG
9	**pink-gray**	ANALOG		28	**yellow-pink**	ANALOG
10	**pink-violet**	ANALOG		29	**orange-pink**	ANALOG
11	**pink-green**	ANALOG		30	**yellow-orange**	ANALOG
12	**pink-blue**	ANALOG		31	**orange-green**	ANALOG
13	**white-green**	ANALOG		32	**orange-blue**	ANALOG
14	**white-brown**	ANALOG		33	**pink-green**	GROUND
15	**white-tan**	ANALOG		34	**green-pink**	GROUND
16	**white-violet**	ANALOG		35		NC
17	**white-gray**	ANALOG		36	**green-tan**	DIGITAL
18	**white-pink**	ANALOG		37	**orange-tan**	DIGITAL
19	**white-orange**	ANALOG		-	-	-

Table 6.4 Cabling of the self-constructed plug connector

*The table above shows which wires of the two bought SHC68-NT-S cables are used for the **self-designed plug connector**. The wire color refers to the color code of the used wire. There are **32 channels (1-32) of type ANALOG** and **two channels (36-37) of type DIGITAL**. While the analog channels can provide any voltage between -10 V and +10 V, the digital channels only provide a logical signal of 0 V or +5 V. In addition, the plug connector has **two channels of type GROUND** which define the 0 V level, and **one channel of type NC** which stands for not connected.*

As it can be seen in figure 6.29, in comparison to the input interface of the amplifier (see figure 6.25) the pin assignment of the plug connector is mirrored in order to ensure a perfect match between those two interfaces. Similar to the amplifier, each channel of the PCI-board, also including all eight digital channels, were checked for their functionality. As an example, figure 6.30 shows the results of the first analog and digital channel.

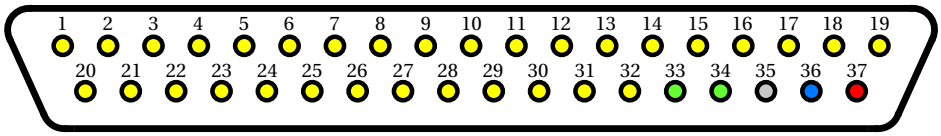

Fig. 6.29 Pin assignment of the self-designed plug connector

*The illustration above shows the **pin assignment of the self-designed plug connector**. The **pins with the numbers from 1 to 32** (yellow) are transmitting the **analog signals** of the PCI-board. Here, the voltage can vary between -10 V and +10 V. The **pins 33 and 34** are of **type GROUND** (green) and define the 0 V level of the plug connector. While **pin 35** is **not connected** (gray), **pins 36 and 37** are of **type DIGITAL** and can provide logical signals with 0 V or 5 V levels. Via **pin 36** (blue), a **channel-wide disable command** can be provided. With **pin 37** (red), the **LED of the overload indicator** can be activated.*

As the amplifier already works perfectly fine, it is obvious that the PCI-board has to operate within normal parameters as well. However, for the sake of completeness, the measurements of the first analog and digital channel are presented here nevertheless. The results of the other channels are rather similar (see appendix B). All in all, AURORA's electro-mechanical system is in good shape and fully functional.

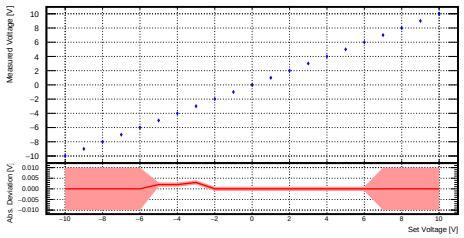

(a) Analog channel 01

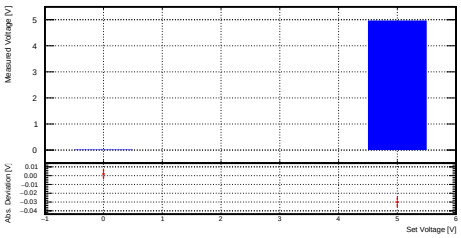

(b) Digital channel 01

Fig. 6.30 Performance measurements of the PCI-board

*Shown are the **performance measurement** of the **first analog and digital channel of the PCI-board**. The **upper graphs** show the **measured voltages** while the **lower graphs** show the **absolute deviation between the measured and the expected voltages**.*

6.4 AURORA's Installation

While the previous sections of this chapter focused on the design of the AURORA system itself, this section will present its installation location, the CD interface, the cabling's threading and the overall integration procedure.

6.4.1 Installation Location

The AURORA system has two different installation locations – the TT bridge and the SSLS of the CD. Figure 6.31 shows a technical drawing of the underground lab. Here, important areas, regarding installation and storage, are highlighted in red.

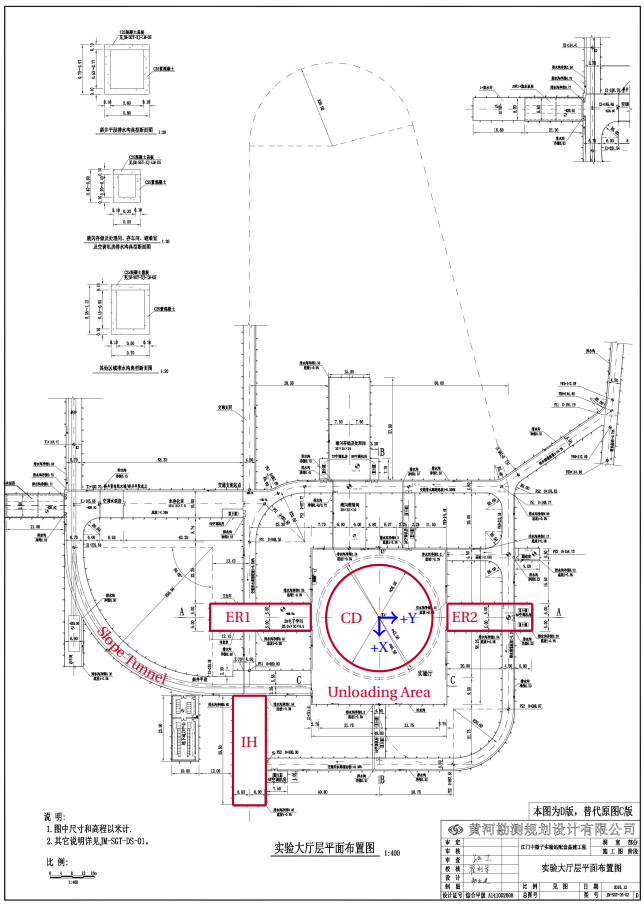

Fig. 6.31 Technical drawing of the underground laboratory [84]

The figure shows a technical drawing of the ***underground laboratory****. Besides the two* ***electronics rooms*** *ER1 & ER2 and the* ***CD****, the* ***slope tunnel****, the* ***unloading area*** *and the* ***installation hall*** *(IH) are highlighted in red as well.*

AURORA's CD components, the FTH and all related parts like the piezoelectric crystals and the GRIN lenses, will be installed in the PMT array. Here, each FTH will

occupy a slot of a small PMT. Furthermore, the electrical cables from AXON and the optical fibers from Leoni will be threaded through metallic bellows and guided along the SSLS and the water pool's wall, connecting their termination at the FTH with their electrical power and light source, respectively. Due to the similarities with the installation of the small PMTs, the original plan foresaw that AURORA's non-CD components should be stored in one of the electronics rooms (see figure 6.31). However, in one of the racks on the TT bridge was still enough free space to store the remaining components. As a consequence, all non-CD devices will be directly located on top of the CD in a rack on the TT bridge. This has two advantages. On the one hand AURORA's cabling can be organized much easier, as the optical fibers and the electrical cables do not have to be laid through the whole underground laboratory. On the other hand this *shortcut* minimizes the danger for the cabling of being damaged. The twelve different FTH components are distributed over the whole northern hemisphere of the detector. Figure 6.32 illustrates the installation locations of the FTH devices on the SSLS.

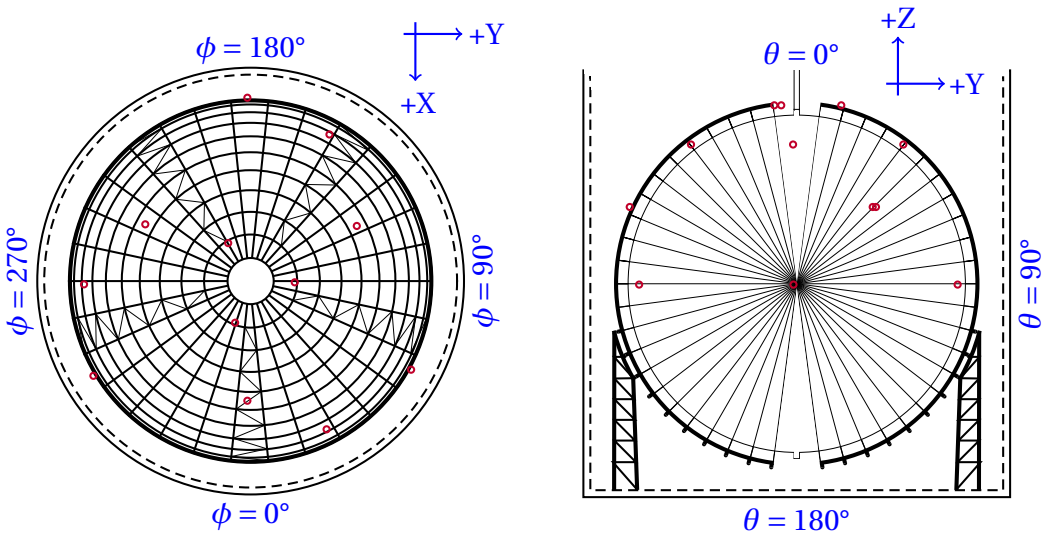

(a) Top view (b) Side view

Fig. 6.32 Installation location of AURORA's CD components

*The drawing shows the **installation location of the fiber termination holders at the SSLS** indicated by the **red circles**. While figure 6.32(a) illustrates the view onto the CD from the top, figure 6.32(b) shows the CD from the side. The **blue numbers** refer to the orientation of the chosen **coordinate system**.*

The presented top view in figure 6.32(a) explicitly illustrates that three FTH devices are always installed at one specific polar angle θ while the azimuth angles ϕ between these three components differs by 120°. These pairs of three FTH components are

installed at four different polar angles. The exact coordinates are listed in table 6.5. Here, the FTH locations are given in both Cartesian and spherical coordinates.

FTH No.	Cartesian Coordinates			Spherical Coordinates		
	X [mm]	Y [mm]	Z [mm]	R [mm]	ϕ [°]	θ [°]
1^{st}	139	4677	18811	19384	88.3	14.0
2^{nd}	-5843	11226	14682	19384	117.5	40.8
3^{rd}	-15516	8335	8094	19384	151.8	65.3
4^{th}	-19380	-361	-96	19384	181.1	90.3
5^{th}	-4029	2380	18811	19384	210.6	14.0
6^{th}	-5996	-11146	14682	19384	241.7	40.8
7^{th}	360	-17610	8094	19384	271.2	65.3
8^{th}	10003	-16603	-96	19384	301.1	90.3
9^{th}	4387	-1629	18811	19384	339.6	14.0
10^{th}	12651	-366	14682	19384	358.3	40.8
11^{th}	15683	8016	8094	19384	27.1	65.3
12^{th}	9377	16965	-96	19384	61.1	90.3

Table 6.5 Installation location of AURORA's CD components

This tables lists the exact ***location of the fiber termination holders*** *at the SSLS in both* ***Cartesian*** *and* ***spherical*** *coordinates.*

The pairs of the three FTH devices offer the advantage that in case of a malfunction (damage during installation or general failure) there are still two modules which can perform a transparency measurement under the same polar angle. In addition, if an obstacle influences the path of one beam, two other beams will be able to take over. Furthermore, this concept offers the opportunity to compare the results and cross check the collected data. If the findings significantly differ from each other, this could be a hint for unknown effects which might influence the data taking in general. Even though toy MC studies have shown that the expected temperature gradient[54] of two degrees Celsius [161] inside the CD will not be recognizable by AURORA, also here a cross check between different polar angles might help to reveal hidden effects which might influence the photon propagation inside the CD and, therefore, influence data taking and later on event reconstruction algorithms.

[54] In general, a temperature gradient inside the LS volume causes also a refractive index gradient. Similar to rays inside a GRIN lens (see section 5.3) AURORA's beams will be bent under these circumstances.

6.4.2 Interface Design

The interface between the FTH components and the SSLS structure of the CD is rather simple and only consists of three connecting bars and springs. Figure 6.33 illustrates the design of the mechanical interface in more detail.

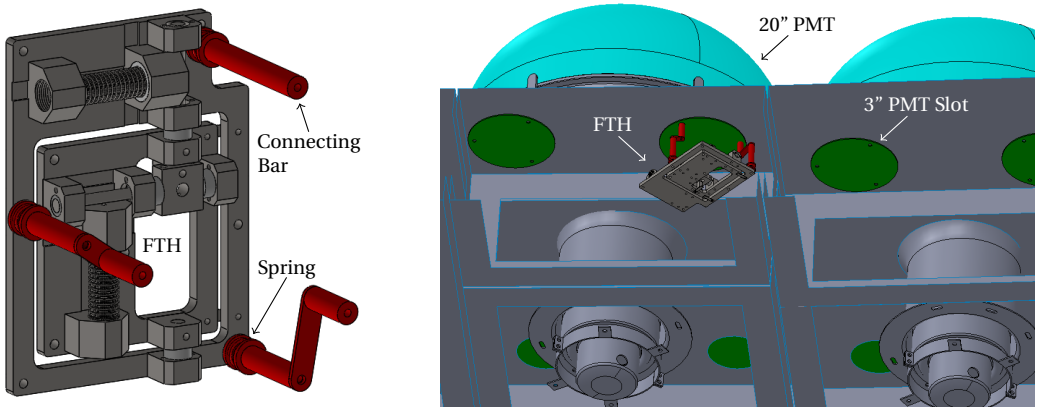

(a) Interface (b) Integration onto SSLS structure

Fig. 6.33 AURORA's interface with the SSLS

*The figure presents **AURORA's interface with the SSLS of the CD**. While figure 6.33(a) shows the **connecting parts of the interface** in more detail (**highlighted in red**), figure 6.33(b) illustrates the **integration of the FTH onto the SSLS** structure.*

Indicated in red, figure 6.33(a) shows the connecting parts of the AURORA interface. Those are three bars which are arranged in a circle around the position of the GRIN lens holder in the center of the FTH. This ensures that the laser beam is also centered relatively to the holder tube of the 3” PMTs (green plates in figure 6.33(b); not occupied by small PMT) through which the laser beam will enter the inner volume of the CD. Furthermore, two of the three bars are shaped like cranks. With this feature, it is possible to compensate an occurring misalignment of the FTH by slewing the termination along the opening of the small PMT holder. In case the laser beam already enters the holder of the small PMT at the center of the opening but is somehow tilted and, thus, not parallel aligned to the holder tube, the inclination angle of the FTH can be altered as well. For that purpose each connecting part has a spring between the FTH and the bar. By tightening the screws which connect the bars with the FTH, the length of these springs are varied and with it the inclination angle. The other end of the bars are connected with the holders of the small PMTs. In figure 6.33(b) it is possible to see three holes in the holder structure of the small PMTs. Through these holes the connecting screws are threaded.

6.4.3 Threading Of 100 m Cables

Before the 100 m cables can be installed, they have to be threaded through metallic bellows in order to protect them against mechanical loads during the installation procedure. The threading itself will be done in China at the bellow company. However, in order to check if it is possible to thread two electrical cables from AXON and one optical fiber from Leoni through the bellow without damaging the fiber, some threading tests were already performed in Mainz. Figure 6.34 presents important details regarding the threading procedure.

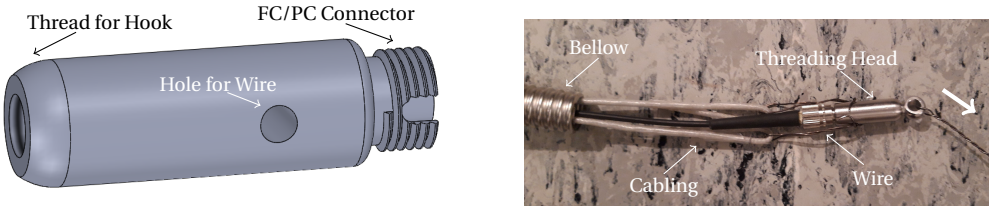

(a) Threading head (b) Threading process

Fig. 6.34 Threading of cabling

*The figure illustrates the **threading procedure of AURORA's cables**. While figure 6.34(a) presents the **threading head** which is used to thread the cables through the bellow, figure 6.34(b) shows the **threading process** itself during one of the threading tests.*

For the threading a so called *threading head* was designed and constructed (see figure 6.34(a)) in Mainz. Its main purpose is to simplify the threading on the one hand and reduce the danger for the optical fiber to be damaged during the procedure on the other hand. The tip of the threading head exhibits a thread. Here, a hook or a screw with a ring (see figure 6.34(b)) can be installed. This makes it easier to connect the treading head with the wire which will be used to thread the cables through the bellow. The other end of the threading head has a standard FC/PC connector. As a consequence, the optical fiber can be directly connected to the threading head. This minimizes the chances that the optical fiber is kinked during the threading. Furthermore, the threading head has a hole through which a second wire can be threaded. This wire is used to fix the two electrical cables from AXON. Figure 6.34(b) shows a picture from one of the threading tests. Here, the cable is pulled from left to right (thick, white arrow) via a wire. Besides the black optical fiber, the two white electrical cables can be seen as well. For the threading tests one 2 m long optical test fiber and two 2 m long electrical test cables from AXON were threaded through a 1.5 m long test bellow[55] 100 times. The fiber's attenuation Λ was measured before

[55] Standard bellow; $\varnothing$ = 14.7 mm. Thanks to Yangfu Wang who sent me this test bellow from China.

and after the threading. With $\Lambda_{before} = 0.25 \pm 0.04$ and $\Lambda_{after} = 0.23 \pm 0.04$, no significant change in its performance could be observed. Consequently, the threading tests have shown that the fiber can be successfully threaded through the bellow with the designed threading head.

Before the threading in China, a flange will be welded on one end of the bellow. Later on, this end will be located close to the FTH. Even though the electrical cables from AXON are waterproof, the flange presents a second safety measure in order to prevent water from entering.

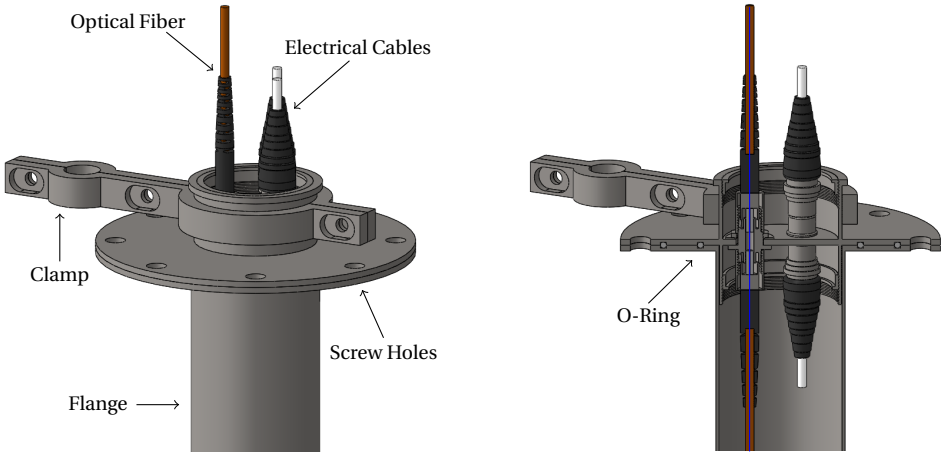

(a) Bellow flange – outside (b) Bellow flange – inside

Fig. 6.35 Bellow flange

*The figure presents the design of the **bellow flange** – figure 6.35(a) from **outside** and figure 6.35(b) from **inside**.*

As shown in figure 6.35, the flange is equipped with a clamp. This clamp will connect the bellow with the FTH interface (see figure 6.36). Two O-rings made of Teflon are used to seal the flange. In addition, similar to the pins of the piezoelectric crystals, an epoxy resin will be used to seal the cable feed-throughs.

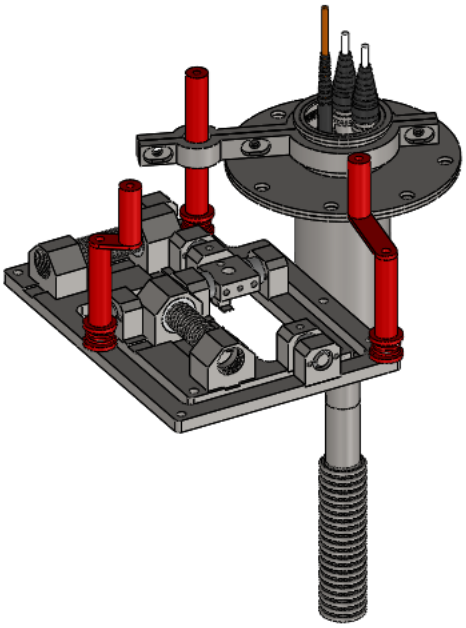

Fig. 6.36 Bellow & FTH interface

The figure presents the bellow and its connection with the FTH interface.

6.4.4 Integration Procedure

As already mentioned before, the non-CD components will be stored in a rack on the TT bridge. After these parts are assembled and calibrated, there are two further tasks to accomplish. On the one hand the FTH devices have to be mounted on the SSLS structure. On the other hand AURORA's electrical cables and optical fibers (inside the metallic bellows) have to be routed.

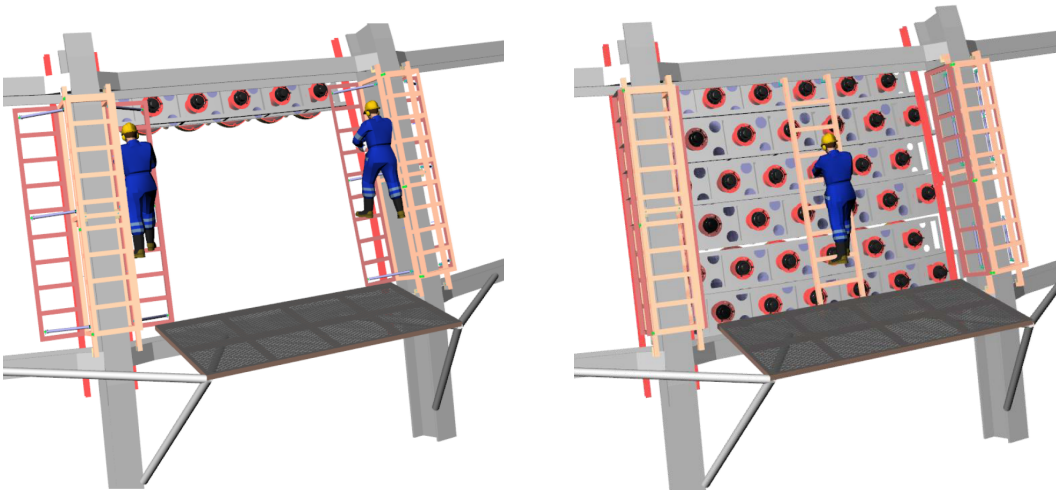

(a) FTH integration & alignment (b) Cable routing

Fig. 6.37 Installation of AURORA's CD components [77]

*The figure illustrates **two important steps of AURORA's installation**. While figure 6.37(a) presents the **integration procedure of a PMT module** equipped with five large PMTs, figure 6.37(b) shows the subsequent installation of the **cable routing**.*

During the installation phase five or six large PMTs are grouped together into one module (PMT row in figure 6.37(a)). This is done inside the installation hall (see figure 6.31). While the large PMTs are integrated, FTH components will be mounted on the holder structure of the small PMTs. During this step the beam direction of the FTH devices has to be aligned as adequate as possible before the whole module is transported to the CD and mounted on the SSLS structure. After the integration of the PMT modules, the bellows with the cables are routed (see figure 6.37(b)) connecting the 100 m cables with the 1 m long cables which are already fixed to the FTH (piezoelectric crystals and GRIN lens). The last integration step is the final performance test. On the one hand it is mandatory to check if the optical fiber was not damaged during the installation process. On the other hand, even though low-pass filters should successfully suppress the noise of the dirty ground, it is important to check if the electrical cables are in contact with the SSLS, as this could spoil the clean ground of the CD.

6.5 AURORA's Aging Tests

In the sections 6.1, 6.2 and 6.3, it was already presented that some parts of the AURORA system will be installed directly in the CD. Thus, they will be submerged in water and remain there for the whole operation time of JUNO. As these components cannot be replaced in case they are malfunctioning, their durability, resistance against corrosion and general aging behavior have to be investigated. Firstly, mechanical stress tests regarding the electrical cables from AXON will be shown in section 6.5.1 before section 6.5.2 focuses on the underwater persistence and resistance against corrosion of various components.

6.5.1 Mechanical Stress Tests

During the installation procedure AURORA's cables will be exposed to mechanical stress. For the optical fibers the bend radius should never be smaller than the minimum bend radius of 5 cm. In general, these optical fibers are made of silica glass, and, therefore, they are fragile. Consequently, these cables have to be handled with care. In contrast to that, the electrical cables are more robust. However, their mechanical resistance should be studied in order to know what kind of load they can withstand.

Firstly, an AXON cable was always repeatedly bent at the same position. Here, the minimal bend radius was approximately 1 cm. After 100 bend cycles, low voltage DC signals were sent through the bent cable while being submerged in a glass filled with distilled water. Parallel to that the same DC signal was sent through a reference cable which had not been bent at all (also submerged in water). Both signals were monitored with an oscilloscope. In case of a reduced performance or cable breakage, the DC level of the bent cable should change. In addition, the electric conductance of the distilled water was measured with a conductivity meter. This ensured that even micro-fractures in the cable's jacket could be immediately recognized, as fractions of the AXON cable's sealing powder (directly located under the jacket) would solve in water and, hence, increase its conductance. These work steps were repeated ten times until the AXON cable had been bent one thousand times in total. While figure 6.38 shows the bend procedure of the stress test, figure 6.39 presents the results of the study. There is a difference of 8 mV between the DC levels of the bent and unbent cable. This can be explained by different connectivities, as this property varies from cable to cable. However, for the stress test only changes relative to the start values are of importance. Here, it turns out that the performance of the

bent cable stayed constant during the whole stress test. Even after one thousand bend cycles the DC signal did not significantly change.

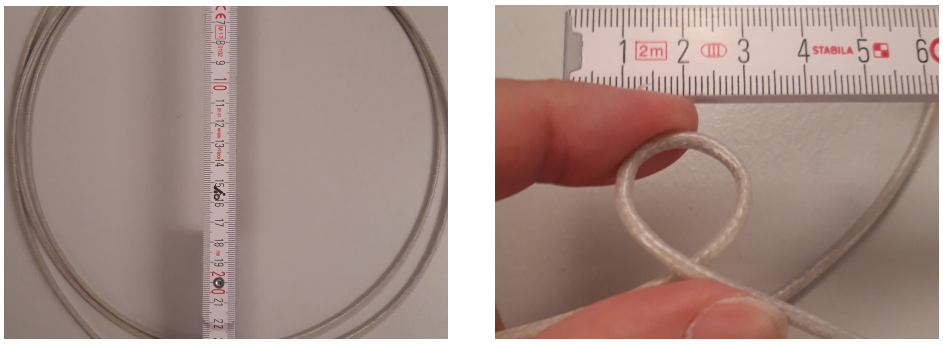

(a) AXON cable before bend procedure (b) AXON cable during bend procedure

Fig. 6.38 Bend stress test of the AXON cable

*The two pictures show **two stages of the bend stress test**. While figure 6.38(a) shows the electrical cable **before the stress test**, figure 6.38(b) illustrates the bent cable **during the procedure** with a **minimum bend radius** of around 1 cm.*

The conductance measurement only shows a small increase. This is not caused by micro-fractions and the sealing powder being dissolved in the water, as in this case a higher jump in the electric conductance would have been recorded. It can be explained by polar dust particles which are adsorbed by the cable's wet surface after putting it out of the glass.

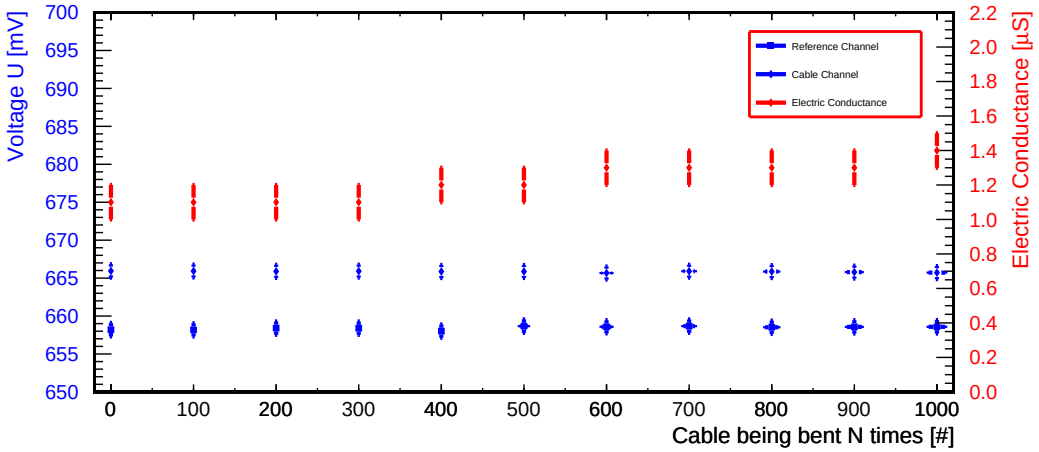

Fig. 6.39 Results of the bend stress test

*The graph shows the **results of the bend stress test**. Here, the **voltage levels** of the **bent and unbent cables** (first y-axis **colored blue**) and the **electric conductance** (second y-axis **colored red**) are plotted against the **number of bend cycles** (x-axis **colored black**).*

It can be concluded that excessive bending neither harms the HDPE jacket nor the copper core of the electrical cable.

Secondly, another AXON cable was repeatedly folded at the same position to estimate its mechanical resistance to this kind of load. After ten times of folding, a DC signal was sent through the folded and an untreated cable (serves as reference). In addition, the electric conductance test was performed (see paragraph above) to look for fractures in the cable's jacket. In total 60 folding cycles were performed.

(a) First folding cycle (b) After 60 folding cycles

Fig. 6.40 Folding stress test of the AXON cable

*Picture 6.40(a) shows the cable during its **first folding cycle** while picture 6.40(b) illustrates the **jacket's status after 60 folding cycles** have been completed.*

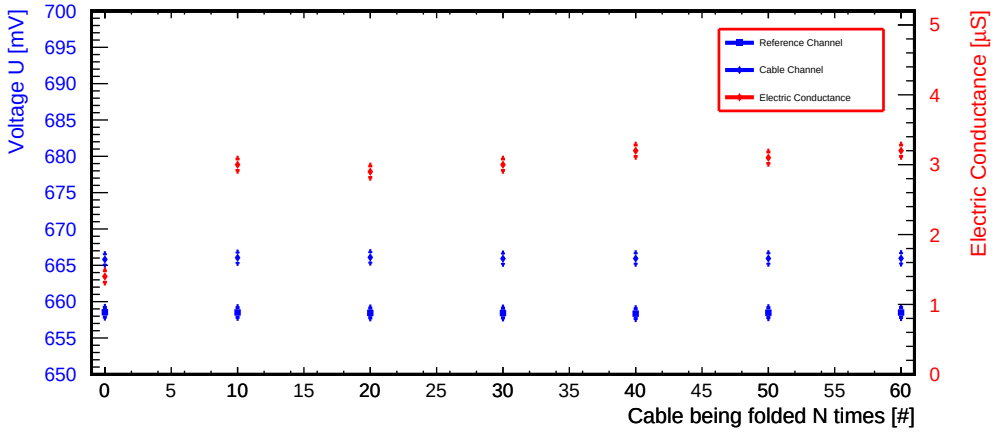

Fig. 6.41 Results of the folding stress test

*The graph presents the results of the folding stress test. Here, the **voltage levels** of the **treated and untreated cables** (first y-axis **colored blue**) and the **electric conductance** (second y-axis **colored red**) are plotted against the **number of folding cycles** (x-axis **colored black**).*

Figure 6.40 shows visual checks of the AXON cable during the folding stress test. Because of the extremely small bend radius, folding exposes the cable to higher mechanical loads than bending with a minimum bend radius of 1 cm does. As it can be seen in figure 6.40(b), at a certain point the jacket of the electrical cable was damaged. A clear crack could be observed after 20 folding cycles. Figure 6.40 shows the results of the folding stress test. The level of the DC test signal did not change. Thus, it can be concluded that the core of the folded cable was not seriously damaged during the stress test. However, the jump in the water's electric conductance shows that the jacket was harmed during the first ten folding cycles (not recognized during the visual check). In general, folding is more harmful than ordinary bending. Already a few kinks lead to cracks in the cable's jacket. Consequently, during the installation procedure also the electrical cables should be handled with care.

Thirdly, the self-sealing feature of an AXON cable was studied by cutting its jacket. Here, the dry cable's jacket was cut one time and then submerged in a glass filled with distilled water. Similar to the first two stress tests, a DC signal was sent through both the sample and a reference cable. In addition the water's electric conductance was measured. After that, the wet jacket of the AXON cable was cut a second time.

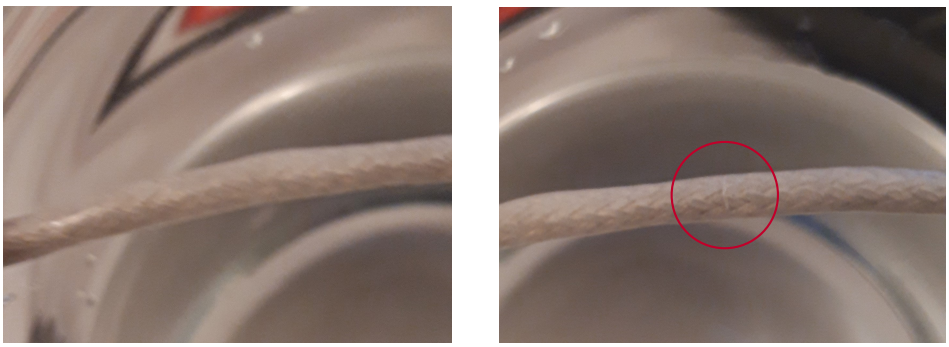

(a) Cable before its first cut (b) Cable after its first cut

Fig. 6.42 Cut stress test of the AXON cable

Picture 6.42(a) shows the cable's jacket ***before its first cut*** *while 6.42(b) presents the* ***jacket's status after the cable has been cut****. Here, the* ***cut position*** *is indicated by the* ***red circle****.*

Figure 6.42 shows two different stages of the cut stress test. After the cable was cut and submerged in the glass filled with water, a white layer was formed at the cut position sealing the leakage. Figure 6.43 presents the results of this third stress test. As it can be seen, the performance of the cable did not change after cutting the jacket of the cable. Here, the DC levels of both the sample and the reference cable stay stable. In contrast to that, a clear jump in the water's electric conductance can

be observed after the first cut. After the second cut the conductance level did not significantly change. This can be explained by the jacket's moisture, as the sealing powder needs contact with water in order to seal an occurring leakage. While after the first cut the cable was still dry and, therefore, the sealing mechanism did not promptly work (some powder was probably dissolved in water), the cable's jacket was already wet during the second cut and no further contaminants were added to the water volume.

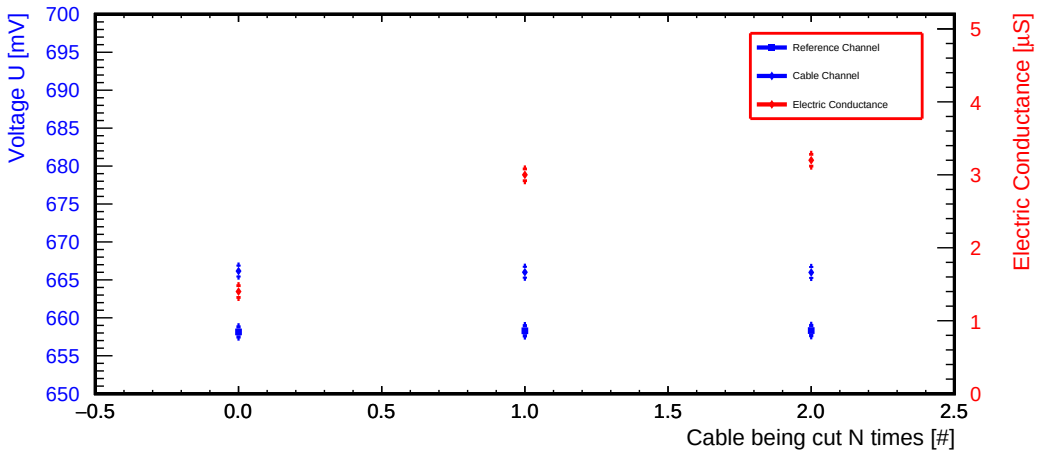

Fig. 6.43 Results of the cut stress test

The graph presents the results of the cut stress test. Here, the ***voltage levels*** *of the* ***treated and untreated cables*** *(first y-axis* ***colored blue****) and the* ***electric conductance*** *(second y-axis* ***colored red****) are plotted against the* ***number of folding cycles*** *(x-axis* ***colored black****).*

From this third stress test can be concluded that minor damages to the cable's jacket do not influence the performance of the cable. Furthermore, it could be demonstrated that the self-sealing mechanism of the AXON cable is working.

6.5.2 Accelerated Aging Underwater

As AURORA's CD components cannot be replaced during the operation time of JUNO, their resistance against corrosion and their general aging behavior in water should be investigated. In order to estimate if a material can survive the operation period underwater, it should be artificially aged under similar conditions. Following the *law of Arrhenius*, the velocity of a chemical reaction depends on the present temperature [59]. As a consequence, aging itself (caused by chemical reactions) can be accelerated by increasing the material's temperature, initiating thermal deterioration. AURORA's components are submerged in water, hence, the following aging tests were performed in water as well. To be more precise, AURORA's samples were

simmered in distilled water. For a period of eight weeks the samples were visually checked each week at the same day and approximately around the same time. In addition, the electric conductance of the water was measured. As most of the investigated polymers are normally produced via ionic polymerization [28, 55, 92], thermal deterioration will add ionic molecule fragments to the water which increases its electric conductance. A similar effect will lead to an increased electric conductance level if a metal component starts to corrode.

According to reference [109], for most of the polymers and plastics the following formula sufficiently describes the accelerated aging. As water is an excellent oxidizer, the same formula is used as an conservative lower limit for the accelerated aging (regarding corrosion) of metal components.

$$t_{aged} = t_{sim} \cdot 2^{\frac{T_s - T_0}{10°C}} \tag{6.8}$$

Here, t_{sim} stands for the time a sample is simmered in distilled water while t_{aged} represents the corresponding accelerated age. The parameters T_0 refers to the temperature of the standardized conditions under which the sample would have normally aged – *e.g.* 20°C. T_s is the actual simmering temperature, which was set to 80°C. Hence, after eight weeks an artificial aging of around 10.7 a is realized.

Firstly, the aging test of the AXON cable is presented. Figure 6.44 shows the cable's jacket before and after the eight weeks of simmering. The visual check did not reveal any deterioration of the HDPE material, as the surface became neither rough nor brittle. The HDPE's color did not change as well.

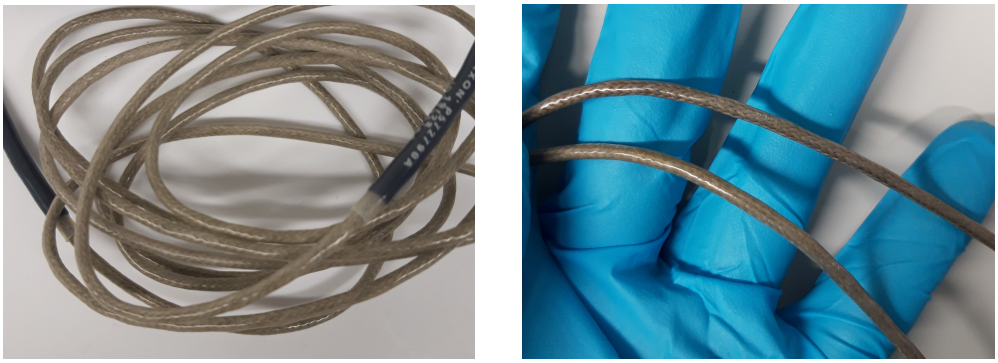

(a) Before simmering started (b) After eight weeks of simmering

Fig. 6.44 Aging test of the AXON cable

Picture 6.44(a) shows the cable's ***jacket before the aging test started*** *while picture 6.44(b) presents the result of the* ***visual check after the aging test was completed****.*

After each week the performance of the AXON cable was evaluated. Similar to the mechanical stress tests, a low voltage DC signal was sent through the sample cable and an untreated cable as reference. The recorded voltage levels and the electric conductance values of the water in which the AXON cable was simmered are shown in figure 6.45.

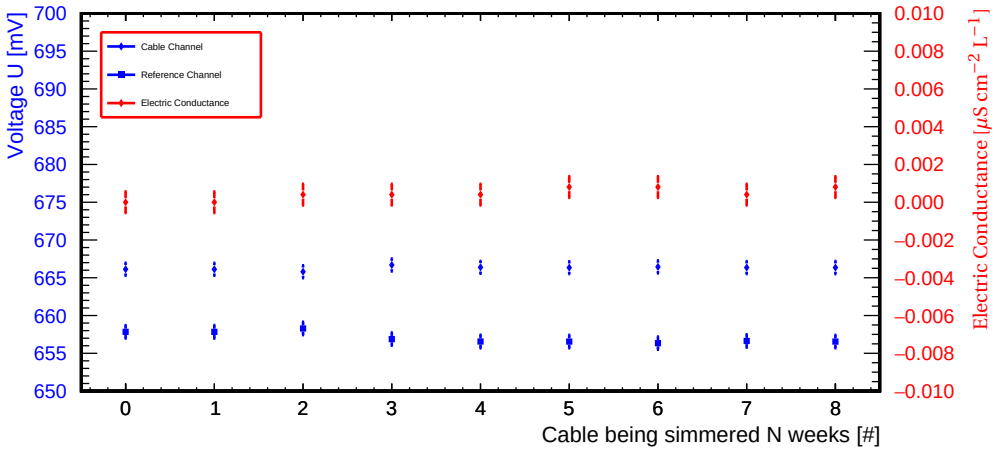

Fig. 6.45 Results of the aging test of the AXON cable

The graph presents the results of the aging test. Here, the ***voltage levels*** *of a* ***simmered and untreated cable*** *(first y-axis* ***colored blue****) and the* ***electric conductance of the water*** *(second y-axis* ***colored red****) are plotted against the* ***number of weeks the sample cable had been simmered*** *(x-axis* ***colored black****).*

Both the voltage values and the electric conductance[56] level are rather constant. For an HDPE sample, a more or less stable electric conductance level is not surprising because HDPE is produced via radical polymerization. Therefore, primarily no ionic additives were expected. However, taking the results of the visual check into account, it can be concluded that the AXON cable's performance did not significantly change. Consequently, the AXON cable passed the aging test.

Secondly, the aging test of the optical fiber from Leoni is presented. Here, only changes in the nylon jacket were of primary concern, as the silica glass (core of fiber) is not expected to change its properties underwater over time. In contrast to that, nylon is known to be slightly hygroscopic. Hence, it was not clear if the material might be harmed in case of a long-term exposure to water. Figure 6.46 presents the results of the visual check which was conducted during the aging test.

[56] For the aging tests the electric conductance was normalized to the water volume (L) and the component's surface (cm^2) in order to be able to compare these values among the different samples.

In general, the material and surface properties of the nylon jacket did not change. The nylon became neither rough nor brittle. Also the color did not change.

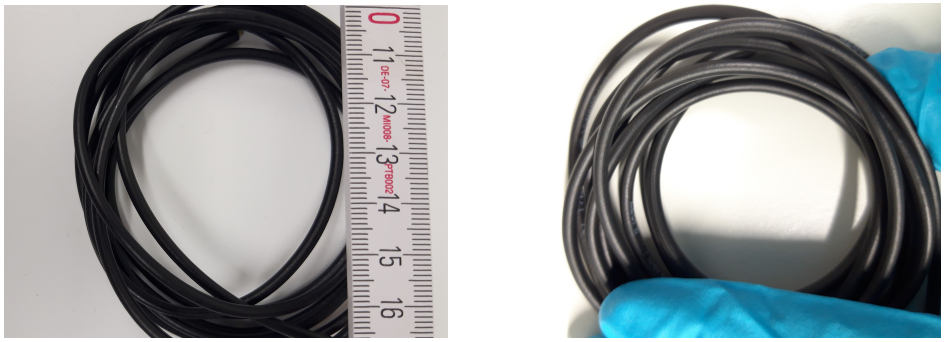

(a) Before simmering started (b) After eight weeks of simmering

Fig. 6.46 Aging test of the Leoni fiber

*Picture 6.46(a) shows the fiber's **jacket before the aging test started** while picture 6.46(b) presents the result of the **visual check after the aging test was completed**.*

The results of the actual aging test are shown in figure 6.47. While the thickness of the fiber did not significantly change (hygroscopic effect seems to be negligible), the electric conductance increased a lot. As nylon is produced via ionic polymerization, this polymer adds ionic molecule fragments to the water volume when its structure is cracked during the aging. As a consequence, the electric conductance is quickly increasing.

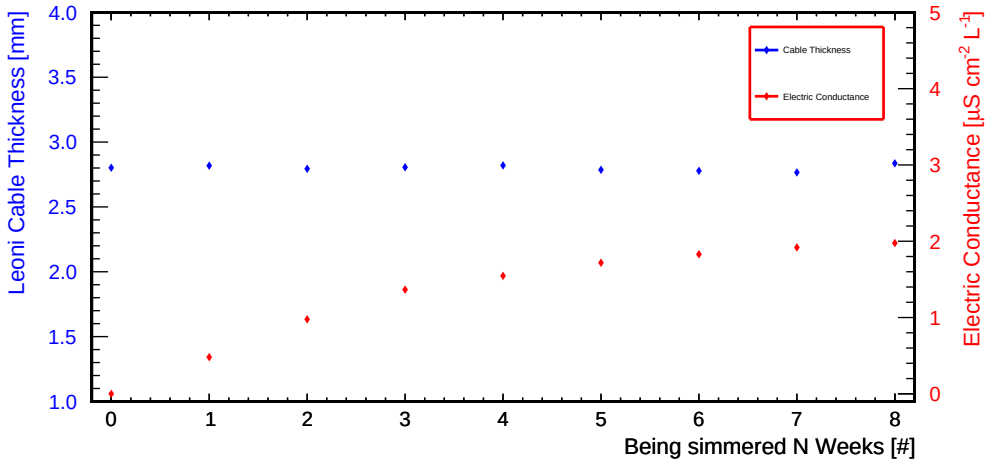

Fig. 6.47 Results of the aging test of the Leoni fiber

*The graph presents the results of the aging test. Here, the **fiber's thickness** (first y-axis **colored blue**) and the **electric conductance of the water** (second y-axis **colored red**) are plotted against the **number of weeks the fiber had been simmered** (x-axis **colored black**).*

Even though the electric conductance level increased a lot over the eight weeks of simmering, the visual check and the measurement regarding the fiber's thickness did not show any sign of degradation. Hence, also the optical fiber from Leoni Fiber Optics passed the aging test.

Thirdly, the aging test of the POM screw is presented. As the screws are made of stainless steel 1.4301 (standard) and not 1.4401 or 1.4404, it was not completely sure if the screws started to corrode. In addition, the behavior of the POM tip underwater was not known as well. Figure 6.48 shows the results of the visual check.

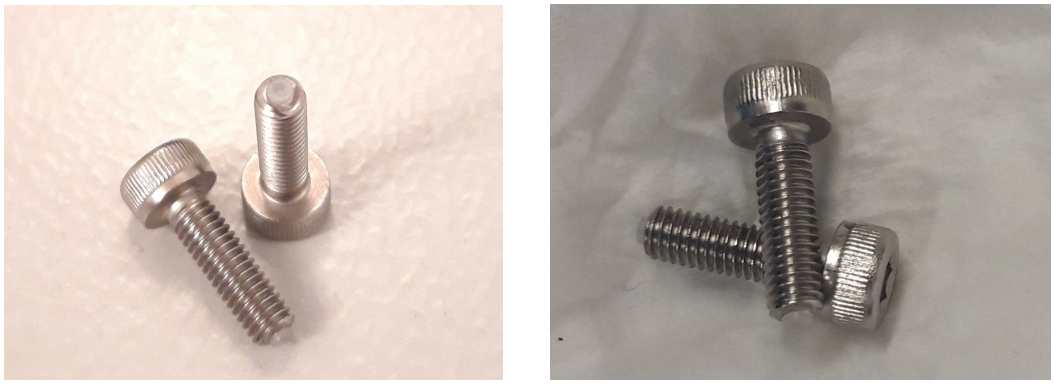

(a) Before simmering started (b) After eight weeks of simmering

Fig. 6.48 Aging test of the POM screw

*Picture 6.48(a) shows the **screws before the aging test started** while picture 6.48(b) presents the result of the **visual check after the aging test was completed**.*

The visual check did not reveal any degradation. The POM tip became neither rough nor brittle. Also the color did not change. As a consequence, it seems that the POM withstood the accelerated aging of around 10.7 a. In addition, also the stainless steel remained unchanged and did not show any sign of corrosion. Figure 6.49 shows the results of the actual aging measurement. Here, it can be seen that the electric conductance was slowly increasing during the eight weeks of simmering. This is probably a result of the visual check, as for that purpose the screws were put out of the glass. Ionic impurities can be easily adsorbed by the wet surface of the screw. When the screws were again submerged in the water glass, these impurities dissolved in the water resulting in slightly increasing its electric conductance. However, in comparison to the optical fiber of Leoni, the electric conductance values range on a much lower level. Consequently, the measurement confirms the results of the visual check. Therefore, also the POM screws passed the aging test.

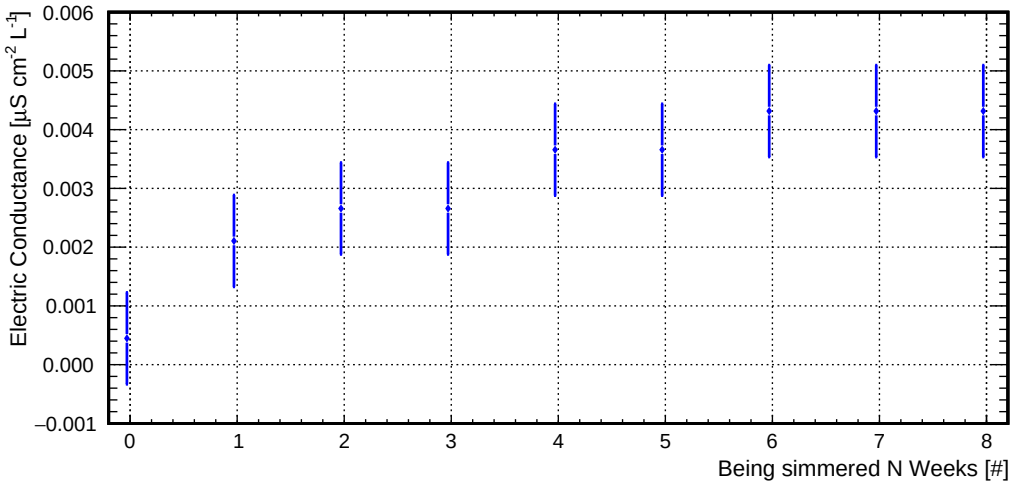

Fig. 6.49 Results of the aging test of the POM screw

*The graph presents the results of the aging test. Here, the **electric conductance of the water** is plotted against the **number of weeks the screw had been simmered**.*

Fourthly, the aging test of the PO shrinking tube is presented. Similar to POM, the behavior of PO underwater, especially for a period comparable to JUNO's operation time, was not known.

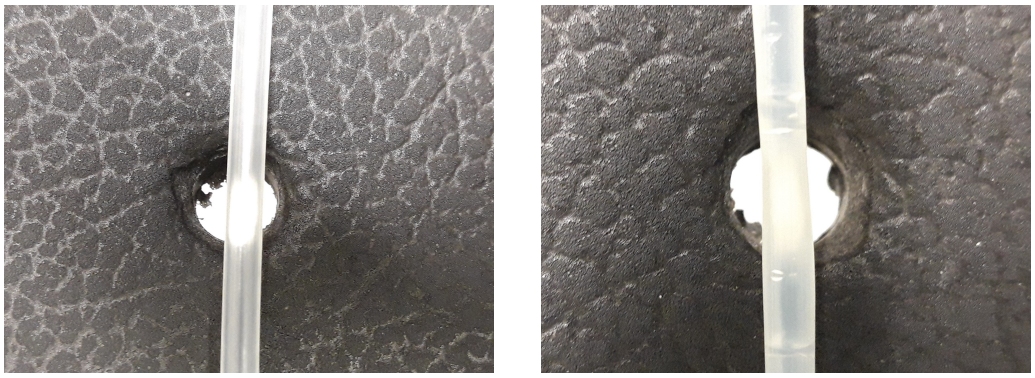

(a) Before simmering started (b) After eight weeks of simmering

Fig. 6.50 Aging test of the PO shrinking tube

*Picture 6.50(a) shows the **PO shrinking tube before the aging test started** while picture 6.50(b) presents the result of the **visual check after the aging test had been completed**.*

In comparison to the other components, the visual check of the PO shrinking tube was less promising. Here, the color changed and during the 8 weeks of simmering a slight yellowness appeared. Normally, this is a sign for a chemical reaction – most likely thermal deterioration. However, the PO tube's surface became neither rough nor brittle. In contrast to that, the PO kept its flexibility. Thus, the color change

can be regarded as insignificant. Figure 6.51 presents the results of the actual aging measurement. The graph shows a continuously increasing electric conductance. In comparison to the optical fiber from Leoni, the PO values are still one order of magnitude smaller. In addition, PO is also produced by ionic polymerization. Consequently, even lower deterioration rates could already explain a moderate increase of the electric conductance. This confirms the result of the visual check regarding the color change. However, as the tube kept its flexibility and did not show any sign of being close to falling apart, the PO tube passed the aging test as well.

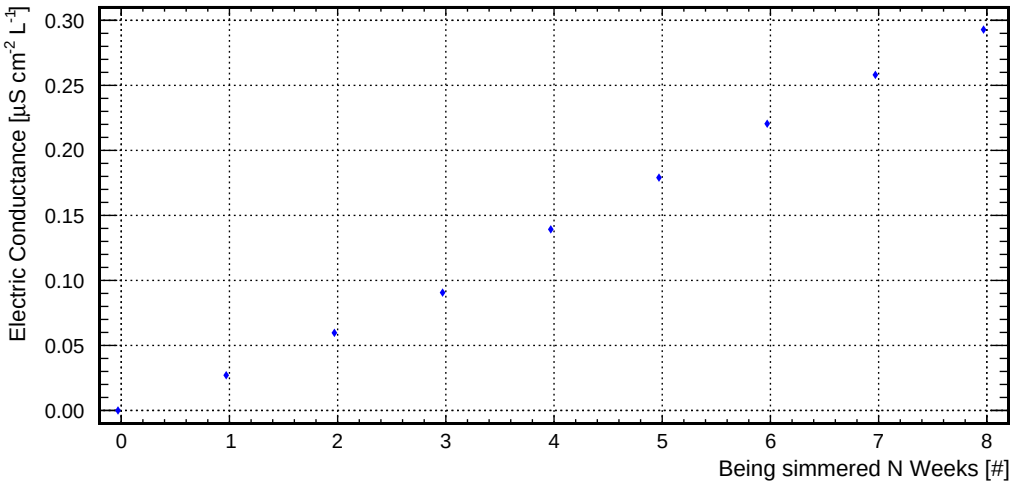

Fig. 6.51 Results of the aging test of the PO shrinking tube

The graph presents the results of the aging test. Here, the ***electric conductance of the water*** *is plotted against the* ***number of weeks the PO shrinking tube had been simmered****.*

Even though some of the studied components have shown small indications of thermal deterioration, all tested parts of the AURORA system passed the aging test. Neither the metal components started to corrode nor the used polymers became rough and brittle. They sufficiently kept their performance. As a consequence, all parts of the AURORA system which will be submerged in the CD's water layer are, therefore, expected to survive the whole operation time.

6.6 AURORA's Radioactive Background Contribution

The following section presents AURORA's contribution to the overall radioactive background. Here, the radioactive budget was either measured or conservatively estimated. These studies are important, as each radioactive decay diminishes the signal-to-noise ratio or even mimic neutrino interactions inside the LS volume.

6.6.1 Stainless Steel Of FTH And Interface

The FTH and its interface to the CD will be made of stainless steel. With its installation location close to the PMTs and, thus, close to the acrylic sphere, radioactive radiation could initiate electron cascades inside the PMTs which lead to an diminished signal-to-noise ratio. In addition, γ rays could enter the acrylic sphere, delocalize shell electrons of LS molecules and fake neutrino events by irradiating scintillation light. Consequently, the radioactivity of the bought stainless steel had to be studied. Table 6.6 lists the results of a gamma spectroscopy screening.

Isotope	Activity [Bq/kg]
^{232}Th	-
^{228}Ac	< 0.09
^{208}Tl	< 0.08
^{238}U	-
^{226}Ra	< 0.70
^{214}Bi	< 0.06
^{235}U	< 0.10
^{40}K	< 0.50
^{60}Co	< 0.01
^{137}Cs	< 0.01

Table 6.6 Gamma spectroscopy results of a THRESS stainless steel sample [111]

*Shown is the result of a **gamma spectroscopy of a stainless steel sample** sent from the **company THRESS**, which will provide the alloy for AURORA's components. Due to the **high radio-purity**, only upper limits (90% C.L.) are listed. For the measurement, 20 stainless steel cylinders with a diameter of 2 cm and a height of 3 cm were used. The total mass was 1.5 kg. The analysis was performed by our Italian colleague Monica Sisti[57], using an HPGe detector.*

[57] Monica Sisti, Dipartimento di Fisica G.Occhialini, Università Milano-Bicocca, Piazza della Scienza 3, 20126 Milano, Italy.

In order to estimate the ^{222}Rn pollution originating from the THRESS stainless steel, the specific activity values of the uranium series[58] isotopes should be carefully checked. Those are the isotopes ^{226}Ra and ^{214}Bi. On the one hand only upper limits are listed, and, therefore, the true radioactivity for the two isotopes will be less. On the other hand ^{226}Ra and ^{214}Bi are in a secular equilibrium. Consequently, the specific activity levels should be similar. Taking these aspects into account, the specific activity of ^{214}Bi presents a more adequate estimate for the radon activity of the stainless steel sample. Here, the upper limit is 60 mBq kg^{-1}. In the end, around 12 kg of stainless steel will be used to construct all components of the AURORA system which will be located inside the central detector. This leads to the upper limit of an overall radon activity of around 720 mBq. Assuming that the whole radon content emanates from the stainless steel[59] and distributes homogeneously inside the water volume of the central detector, the upper limit for the radon pollution contribution is around 21 μBq m^{-3}. Considering the contribution of around 10 mBq m^{-3} [163] from the rest of the stainless steel support structure, AURORA's contribution is negligible.

6.6.2 Piezoelectric Crystals

In principle the piezoelectric crystals are part of the FTH as well. However, because of the more complex chemical composition they will be separately discussed in the following section.

According to [20], the piezoelectric material of the crystals is made of lead zirconium titanate (PZT). Hence, this compound primarily contains lead, zirconium, titanium, oxygen and silicone isotopes. Table 6.7 lists all naturally occurring isotopes. In addition, their relative abundances are presented as well. While the non-radioactive isotopes are marked as stable, the radioactive isotopes exhibit additional information like the half life time $t_{1/2}$, the possible decay channels, the related Q-value and the resulting daughter nuclei. Fortunately, most of the listed isotopes are stable, thus, they do not contribute to the radioactive background inside the CD. However, there are three different radioactive isotopes whose decay chains have to be carefully studied. Firstly, ^{96}Zr occurs with a relative abundance of only 2.80%. This zirconium isotope undergoes a double β decay (see figure 6.52) which is characterized by an extremely high half life time of $t_{1/2} = 24 \cdot 10^{18}$ a. Taking into account that the weight of a single piezoelectric crystal is less than 20 g and the abundance and activity of

[58] Also called radium or uranium-radium series.
[59] Reasonable assumption, as the radon emanation rate for untreated stainless steel ranges around (0.36 ± 0.04) mBq m^{-1} [169].

^{96}Zr in this material is rather low, the radioactive contribution of this isotope pose no threat. Furthermore, the daughter nucleus ^{96}Mo is stable. Consequently, no further radioactive decays occur.

Isotope	Abundance [%]	Half Life $t_{1/2}$	Decay	Q-Value [MeV]	Product
^{16}O	99.76	stable			
^{17}O	0.04	stable			
^{18}O	0.20	stable			
^{28}Si	92.23	stable			
^{29}Si	4.67	stable			
^{30}Si	3.10	stable			
^{46}Ti	8.00	stable			
^{47}Ti	7.30	stable			
^{48}Ti	73.80	stable			
^{49}Ti	5.50	stable			
^{50}Ti	5.40	stable			
^{90}Zr	51.45	stable			
^{91}Zr	11.22	stable			
^{92}Zr	17.15	stable			
^{94}Zr	17.38	stable			
^{96}Zr	2.80	$24 \cdot 10^{18}$ a	$\beta^-\beta^-$	3.350	^{96}Mo
^{204}Pb	1.40	$1.4 \cdot 10^{17}$ a	α	2.186	^{200}Hg
^{206}Pb	24.10	stable			
^{207}Pb	22.10	stable			
^{208}Pb	52.40	stable			
^{210}Pb	trace	22.3 a	α	3.720	^{206}Hg
			β^-	0.064	^{210}Bi

Table 6.7 Piezo crystal's radiochemical composition [140]

*The table lists all **isotopes** which might be **present in a typical PZT compound**. In addition to the **relative abundances**, details like the **half life time** $t_{1/2}$, occurring **decay channels**, Q-**values** and resulting **daughter nuclei** (if isotope is radioactive) are mentioned as well.*

Secondly, ^{204}Pb occurs with a relative abundance of 1.40%. This lead isotope undergoes an α decay (see figure 6.53) which is characterized by a long half life time of $t_{1/2} = 1.4 \cdot 10^{17}$ a. Regarding the abundance and the activity of this isotope, ^{204}Pb does not contribute much to the overall radioactive background as well. The daugh-

ter nucleus is ^{200}Hg and also stable. As a consequence, the radioactive chain comes already to an end here.

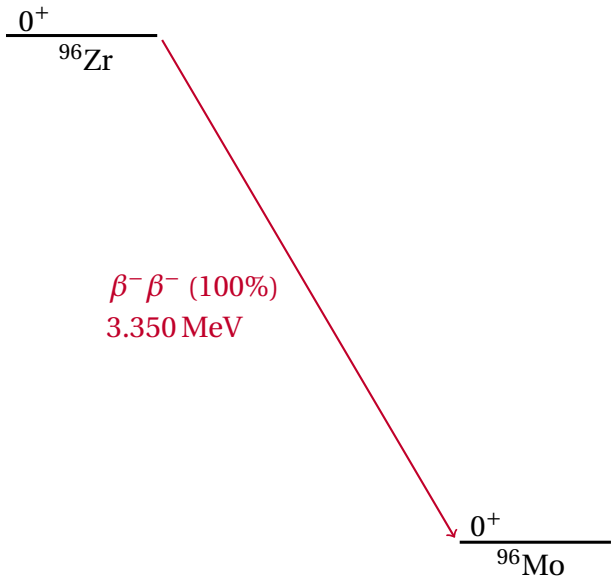

Fig. 6.52 Decay scheme of ^{96}Zr

*The scheme illustrates the decay scheme of the isotope ^{96}Zr. Here, the **only possible decay mode** is a transition from ^{96}Zr to ^{96}Mo via a **double beta decay**. The **Q-value** of this decay mode is 3.350 MeV and represents the **maximally possible kinetic energy** of the emitted β-particles [141].*

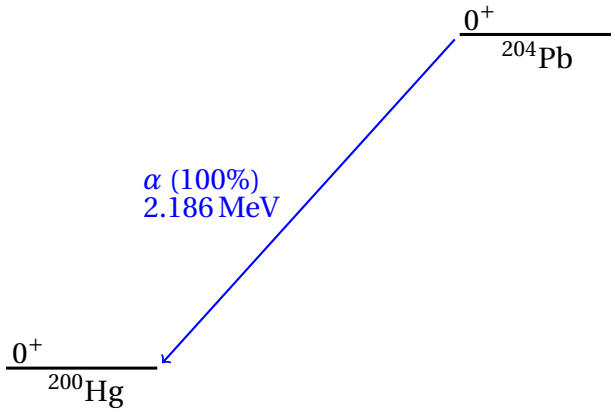

Fig. 6.53 Decay scheme of ^{204}Pb

*Shown is the decay scheme of the isotope ^{204}Pb. Here, the **transition** is moderated by an α **decay** with a Q-value of 2.186 MeV [142].*

Finally, ^{210}Pb which is just a trace element. This lead isotope can undergo both α and β decays characterized by a moderate half life time $t_{1/2} = 22.3$ a. As both daughter

nuclei are again unstable, the decay scheme is more complex in comparison to ^{96}Zr and ^{204}Pb. Figure 6.54 presents all possible decay channels until the stable isotope ^{206}Pb is reached.

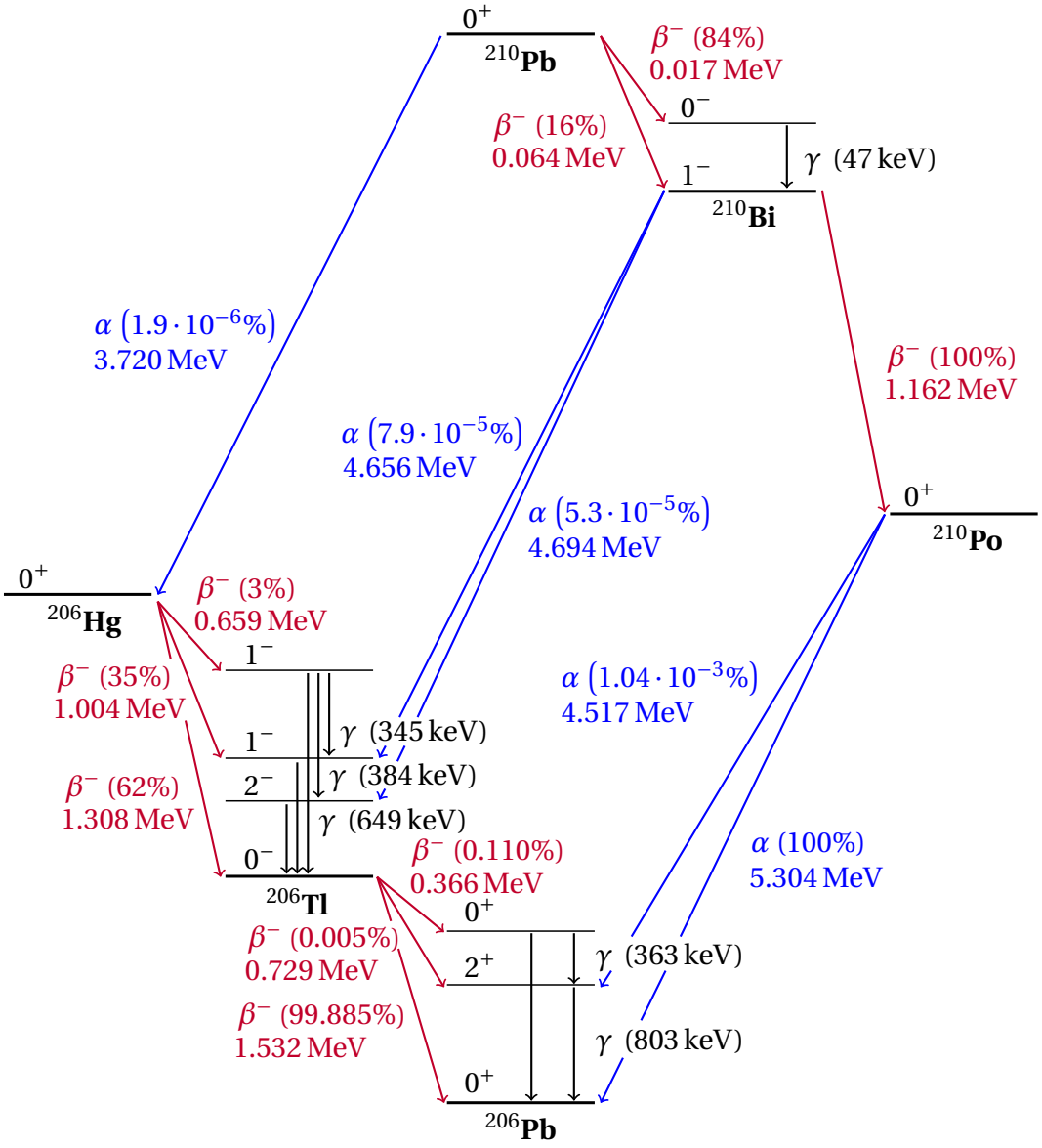

Fig. 6.54 Decay scheme of ^{210}Pb

*Illustrated is the decay scheme of the isotope ^{210}Pb. Here, the **blue** and **red colors** refer to α and β **decays**, respectively. While the blue energy values define the actual energy of the emitted α-particles, the red energy values only represent the maximally possible energy of the released β-particles. Excited states which are involved in the decay chain are also displayed in the scheme. The **transitions between excited and ground state** and the **released γ energies** are indicated by the **black arrows and energy values**, respectively [143].*

Even though the relative abundance is rather small and the isotope only exhibits a moderate half life time, the successive decays should be carefully checked to evaluate if the ^{210}Pb content might pose a threat to the radio-purity of the JUNO detector.

From the decay schemes shown in figures 6.52, 6.53 and 6.54 it follows that the energy of the emitted α-, β- and γ-particles does not exceed 5.304 MeV, 3.350 MeV and 1.166 MeV, respectively. While for those energies α- and β-particles have a maximal range of 0.5 cm and 2.0 cm [73] before they are completely absorbed by the surrounding absorber material[60] between piezoelectric crystals and acrylic sphere, γ radiation in principle is just diminished in its intensity and could still excite liquid scintillator molecules behind the acrylic sphere. The intensity loss for a narrow γ beam in a medium can be described by an exponential decay law satisfying the following equation:

$$I(x) = I_0 \cdot e^{-\mu \cdot x} \tag{6.9}$$

Here, I_0 stands for the initial intensity of the γ source[61], μ is the linear attenuation coefficient and depends on the medium properties, x is the path length inside the absorber medium and $I(x)$ is the beam intensity after traveling the distance x inside the absorber medium.

With a linear attenuation coefficient of $\mu = 0.0706\,\mathrm{cm}^{-1}$ [72] for a 1 MeV γ-particle in water, the intensity of the most severe γ source will be already reduced down to $7.4 \cdot 10^{-5}$% after 2 m in water. Here, it was assumed that the value for μ is a constant and does not depend on the particle's energy. In fact, the value for μ will increase with a decreasing particle energy [71], resulting in even faster intensity losses. In addition, the γ-particles have to cross the stainless steel hull of the piezoelectric crystals on the one hand and to traverse the acrylic sphere on the other hand in order to reach the liquid scintillator. Consequently, the intensity of the γ radiation will be further reduced. As already mentioned, ^{210}Pb is a trace element and a single piezoelectric crystal weights less than 20 g. Taking all these aspects into account, the contribution of the ceramic material of the piezoelectric crystals to the overall background rates is negligible.

[60] 2 m of distilled water.
[61] Intensity of the γ beam.

6.6.3 Radon Emanation From AXON Cables

The AURORA system is making use of 24 AXON cables in order to provide the necessary voltage for the piezoelectric crystals, which are integrated in the FTH. These coaxial cables are 100 m [134] long and with the high density polyethylene (HDPE) jacket around 3 mm [134] thick. The weight of the cables is around 14 g m^{-1} [134]. Consequently, one cable has a mass of around 1.4 kg. Taking into account that 24 cables are used, the total mass is 33.6 kg. At IHEP an HDPE sample was screened. The results show a ^{238}U content of around (8.06 ± 3.23) ppb [164] which translates into a specific activity[62] of around (100 ± 40) mBq kg^{-1}. With a total mass of 33.6 kg this leads to an overall activity of (3.36 ± 1.34) Bq. If we assume that the radon and uranium isotopes are in a secular equilibrium, the radon and uranium activity should be the same. With the attempt to do a conservative estimate, full radon emanation is assumed. The cables are covered by bellows and have no direct contact to JUNO's water pool. However, in a worst case scenario (leakage) a homogeneous and complete distribution of radon inside the 35 kt water pool [49] filled with ultrapure water is assumed. In this case AURORA's AXON cables only contribute around 0.096 mBq m^{-3} to the overall radioactive background, which is three orders of magnitude below JUNO's radon pollution limit for water of 200 mBq m^{-3} [163]. Consequently, AURORA's electrical cables do not pose a threat to JUNO's radiopurity requirements.

6.6.4 Radon Emanation From Optical Fibers

In addition to the 24 AXON cables, twelve optical fibers from the company Leonie Fiber Optics are used in order to guide the laser light from the TT bridge into the central detector. These silica glass fibers are also 100 m [64] long and equipped with a nylon jacket, which is around 4 mm [64] thick. The weight of one fiber was determined to be around 6.8 g m^{-1}, which translates into a total mass of around 8.2 kg including all twelve cables. A survey conducted by the Borexino collaboration investigated the ^{238}U contamination levels of several nylon samples in order to find a suitable nylon manufacturer for their nylon balloon. For industrial nylon an average uranium content of around 1 ppb [30, 104] could be determined. This would translate into a specific activity of around 12 mBq kg^{-1} for uranium. Repeating the assumptions and calculation steps presented in section 6.6.3, the radon contri-

[62] An additional screening of an AXON cable revealed a specific activity for ^{238}U of around 50 mBq kg^{-1} [158]. In order to get a more conservative estimate of the radon emanation, the IHEP result is used for the following calculation steps.

bution of the optical fibers is around 0.003 mBq m^{-3}, which is even five orders of magnitude below JUNO's radon pollution limit for water and, therefore, negligible.

6.6.5 Epoxy Resin

An epoxy resin will be used in order to insulate the pins of the piezoelectric crystals after they have been connected to the electrical cable from AXON. In addition, the same epoxy resin will be used to seal the feed-through at the flanges of the bellows (see section 6.4). Even though epoxy resins are a useful tool to sufficiently insulate and seal a huge variety of components, they are also characterized by higher rates of radioactivity. As a consequence, their contribution to JUNO's radioactive background has to be carefully studied. AURORA's epoxy resin[63] is bought from the *MasterBond* company. In total, around 0.5 kg of the resin is needed to seal all critical parts of the AURORA system. Assuming that the contribution of the resin should be smaller than one thousandth of the maximum radon pollution limit of 200 mBq m^{-3}, the specific activity of the resin should not exceed 14 Bq kg^{-1}. This is a moderate value. However, by the time this thesis will be handed in, a screening is ongoing being performed by our colleagues in Munich. If the test results show that the specific activity exceeds the calculated limit, another epoxy resin will be used.

[63] MasterBond: EP30-4, optically clear, two component epoxy for bonding, sealing, coating and casting.

6.7 AURORA's Software Control

In the previous sections each detail of AURORA has been presented. As this calibration system consists of several components, it makes sense to provide a software control which allows the communication with all these devices rather than trying to control all parts manually. In addition, this offers the opportunity to operate the system via remote access. In contrast to the detector control system (DCS) of JUNO, AURORA's software is written in `LabVIEW`[64] and not in `EPICS`[65]. This is the reason why the current software control cannot actively communicate with the DCS. Instead, only a passive communication (see section 6.7.1) is available. Even though the software control already provides all features which are necessary to perform the foreseen transparency measurements, a future version which implements an `EPICS` interface in order to establish a two-way-communication is desirable. However, in the scope of this thesis the integration of AURORA's software control into JUNO's DCS was not possible. As a consequence, section 6.7.1 will focus on the current software control version while section 6.7.2 deals with possible future features which will ensure an active communication with JUNO's DCS on the one hand and an easier handling during AURORA's transparency measurements on the other hand.

6.7.1 Current Features

The features of the current version are illustrated in figure 6.55, which presents the GUI of AURORA's software control. Firstly, on the left the figure shows the fiber termination holder array. Here, the voltage levels of each piezoelectric crystal can be adjusted. In order to alter the laser beam direction inside the CD, an FTH component has two piezoelectric crystals. That is why two of them are always grouped together. By increasing the voltage levels, the FTH will tilt the holder of the GRIN lens and, therefore, change the direction of the laser beam. For safety precautions, the software does not allow to exceed a maximum voltage of 140 V, as higher voltages are not tolerated by the piezoelectric crystals. However, if for any other reason an overload at the piezo driver (amplifier) occurs, the green control lamp *OVERLOAD* lights up. In this case all voltage levels can be immediately set to zero by pushing the red *DISABLE CHs* button. Secondly, in the center the GUI shows the control panel for the laser beam array. Here, the fiber can be chosen through which the laser light enters the CD. A green control lamp indicates which channel is currently activated. Thirdly, on the top right the figure presents the control of the optical chopper. Here, the chopper frequency can be set by entering an exact value

[64] `LabVIEW` 2014 for Windows.
[65] **E**xperimental **P**hysics and **I**ndustrial **C**ontrol **S**ystem.

in the display (white box) or by touching the indicator bar below. Fourthly, on the center right the GUI has its control panel for the attenuator. Similar to the optical chopper, its attenuation can be set either by entering an exact value in the display or by touching the indicator bar. Fifthly, directly under the attenuator's control panel a blue button *IRIS* is shown which controls the iris beam shutter. An indicator lights up if the diaphragm is open. In case of a malfunction, too high laser intensities or events like a supernova, JUNO's trigger system can send a command to the iris closing the diaphragm (passive communication). Sixthly, on the bottom right the GUI has a monitor window which displays the readings of the reference systems and, therefore, the actual intensity of the laser beam. These values are also written to a file. In addition, the corresponding time stamps are recorded as well. The whole measurement can be started and ended via the green *START* and red *STOP* button.

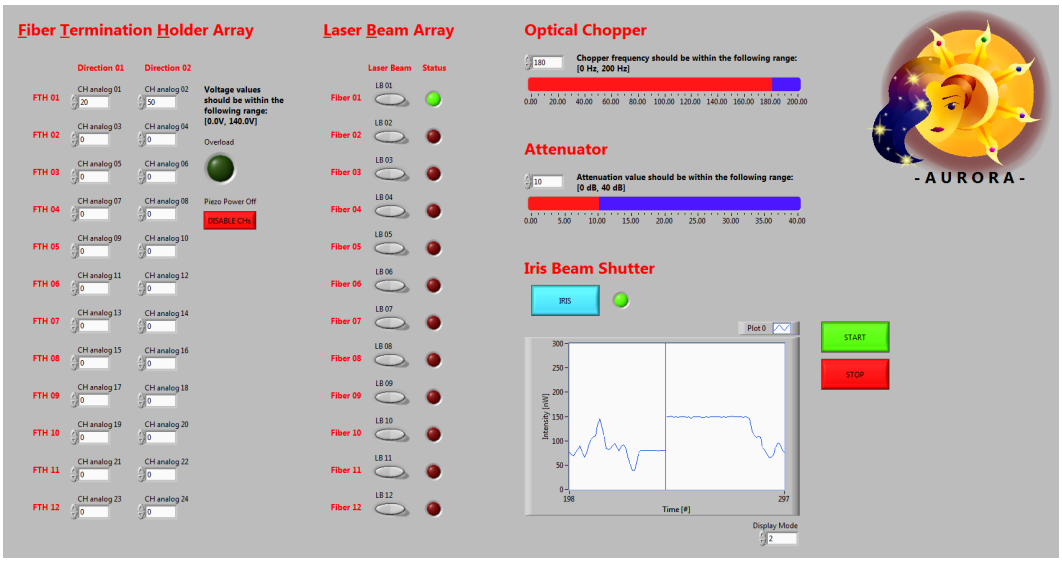

Fig. 6.55 GUI of software control

*The figure presents the **graphical user interface of the AURORA system**. The GUI includes control panel for the **piezoelectric crystals** inside the **fiber termination holders** (left), the **fiber switch module** (center), the **optical chopper** (top right), the **attenuator** (centered right) and an **intensity monitor** (bottom right).*

6.7.2 Outlook

Even though the current software is already able to control the whole AURORA system and perform a complete transparency measurement, an upgrade from a `LabVIEW`-based to an `EPICS`-based software control will offer additional attractive features. One advantage would be that AURORA can be controlled by the DCS and

not only by AURORA's local computer. This would make transparency measurements much easier, as those can be performed from everywhere by everyone. In addition, the direct communication with the DCS could also simplify the adjustment of the beam direction. While up to now the exact location of the laser spot has to be extracted from a hit map pattern (number of recorded PEs in relation to PMT coordinates) by hand, an `EPICS`-based software control can receive these numbers from JUNO's DCS and calculate the laser spot location by weighting the PMT coordinates with the detected amount of PEs. In this case a feedback loop can be used to alter the voltage levels of the piezoelectric crystals until the number of detected PE hits is approximately the same for the neighboring PMTs around the laser spot. A first study has shown that with this approach the location of the laser spot can be determined in θ- and ϕ-direction with an accuracy of around $\pm 0.2°$ which translates into an uncertainty of approximately $\pm 6.8\,\text{cm}$. As the small PMTs have a diameter of $\varnothing = 7.6\,\text{cm}$, this accuracy is hardly ideal. However, it is good enough to guide the laser spot into a free slot of a small PMT.

Chapter 7

A U R O R A – Sensitivity Study

As already discussed in the previous chapters, AURORA is a valuable tool to measure and monitor the optical transparency of the LS inside the JUNO detector. While chapter 6 presents the conceptual design of the developed laser system, characterizing the performance of each single component in detail, this chapter focuses on the analysis strategy regarding the determination of the LS transparency and the related uncertainties. These studies were carried out with the official JUNO simulation framework called `offline`[1]. Firstly, section 7.1 deals with AURORA's general approach on how to determine the attenuation length L and the scattering length L_s of JUNO's LS and, therefore, its transparency. Secondly, section 7.2 evaluates the statistical uncertainty for typical measurement durations. Finally, section 7.3 investigates AURORA's limiting systematics.

7.1 General Approach

The general analysis approach is based on the fact that the propagation of photons in the scintillator medium depends on the optical lengths L, L_a and L_s of the LS (see section 4.4). While in experiments the quantities L and L_s can be measured directly, L_a is subsequently calculated via equation (4.5). Their actual values determine the probability for photons to be scattered off molecules under a certain angle, to be entirely absorbed or to traverse the detector volume unhindered. The recorded PMT hit map pattern is a direct result of all these individual processes. Taking this into account, the following analysis procedure compares PE distribution data from a lookup table (LUT) with the results of an actual measurement. For the comparison a log-likelihood function is used to find the true values for L and L_s. The PE data of the LUT were generated with the `offline` framework, simulating collimated and

[1] `Offline` Version `J19v1r1-Pre4`.

mono-energetic laser beams[2] which are traversing the detector's center. In the end, the actual measurement will be conducted with the AURORA system. However, the data set for the sensitivity study was also created with the `offline` simulation.

Figure 7.1 shows such a PE distribution for an attenuation length $L = 20.0\,\text{m}$ and a scattering length $L_s = 30.0\,\text{m}$.

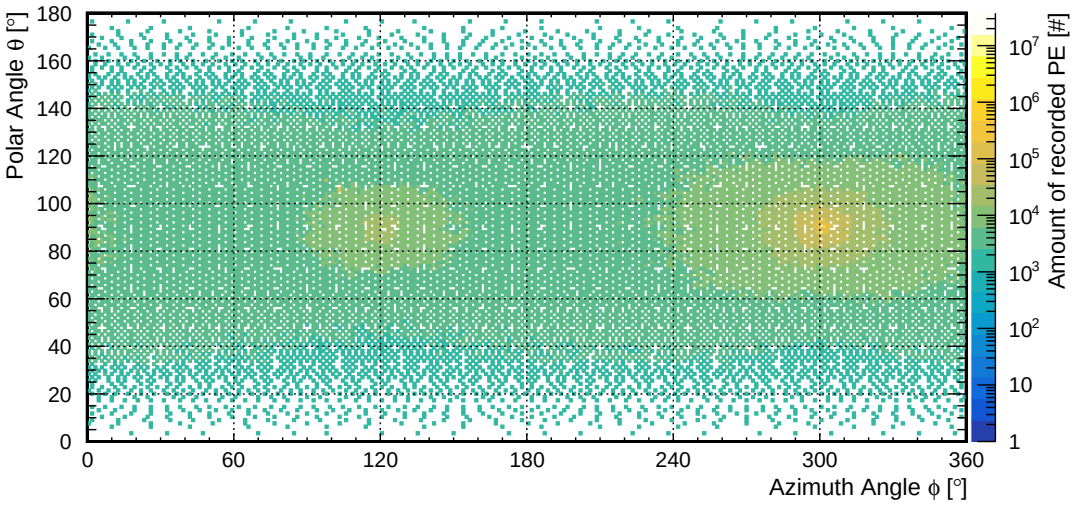

Fig. 7.1 PMT hit map - equivalent of a 5 s measurement

*The histogram shows the **hit map pattern** of **JUNO's PMT array**. Here, the inner surface of the detector is given by the **azimuth angle** ϕ (x-axis) and the **polar angle** θ (y-axis). The **color code** indicates the **amount of detected PEs** of each PMT. The simulated laser beam enters the detector volume at $\phi \approx 300\,°$ and strikes the PMT array on the other side of the detector at $\phi \approx 120\,°$. Exactly **one billion photons were simulated**, which is the **equivalent of a five second measurement**, assuming a pulsed laser with an **operation frequency of 200 Hz**, a **pulse width of 10** μ**s** and an **intensity of one million photons per pulse**.*

The figure presents the PE distribution of a centered laser beam with its insertion location at $\theta = 90.3°$ and $\phi = 301.1°$ (8^{th} FTH position, see table 6.5). As it can be seen, the graph exhibits two maxima – one at the entry point and the second one where the laser beam hits the PMT array on the opposite side of the detector's inner surface. The maximum at the exit point is the result of direct illumination by the laser beam. In addition, this maximum is broadened by the forward scattering component of Rayleigh scattering[3]. The maximum at the insertion location is a superposition of reflected photons at the transition layers water-acrylic and acrylic-LS on the one hand and backward scattered photons originating from the LS volume

[2] Wavelength has a value of $\lambda = 430\,\text{nm}$.
[3] Dominant scattering process for photons with a wavelength $\lambda = 430\,\text{nm}$, assuming a perfectly cleaned and purified LS.

on the other hand. As already discussed in section 4.4, Rayleigh scattering exhibits an amplitude for backward scattering which is as large as the amplitude for forward scattering. This is the reason why the maximum at the insertion point is strongly pronounced.

In order to simplify the 2D distribution in figure 7.1 for the subsequent analysis, the detected amount of PEs are plotted against the orthodromic distance along the detector's spherical surface between a reference point and the actual hit. For the sake of simplicity, the maximum at the insertion point is chosen as the reference point. This step in the procedure ensures that the PE distributions can be compared with each other independent of the insertion location of the laser beam[4]. Also worth mentioning here is the fact that due to the symmetry[5] of the photon distribution, the transformation of the 2D histogram into a 1D histogram is associated with a minimum loss of information. Figure 7.2 shows the resulting 1D PE distribution.

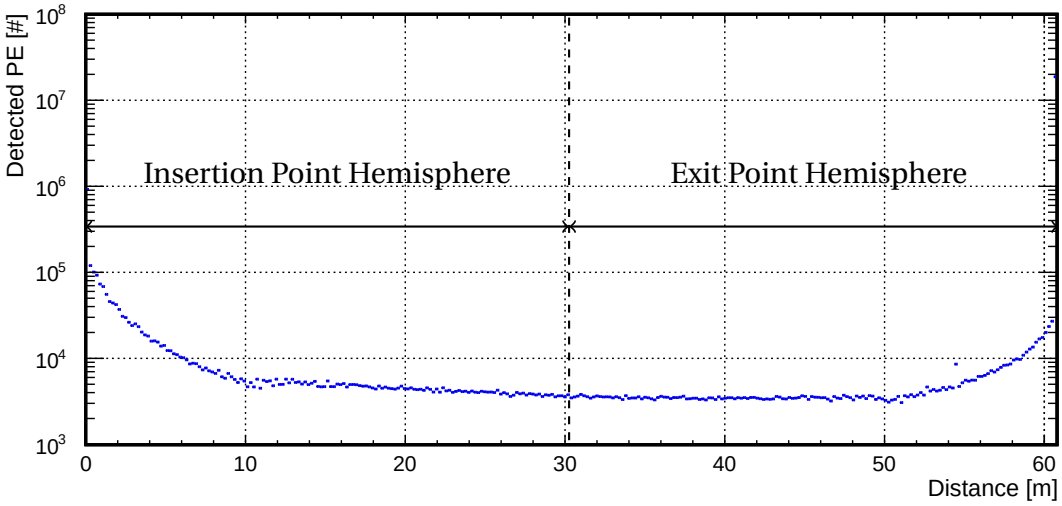

Fig. 7.2 Detected amount of PE along orthodromic distance

*The histogram shows the **amount of detected PE** corresponding to the **orthodromic distance along the detector's inner surface** between laser insertion point and actual hit. Here, all recorded events integrated over the whole surface are included. While the distance of **0.0 m refers to the location where the laser is decoupled from the fiber**, the distance of around **60.8 m is related to the location directly opposite to the insertion point** on the other side of the detector's inner surface.*

Similar to figure 7.1 this histogram also exhibits two maxima. The first maximum is located at a distance of 0.0 m because its location is defined as the reference point.

[4] AURORA will provide twelve different laser beams with insertion points distributed all over the detector's northern hemisphere (see section 6.4).
[5] Laser beam points to the detector's center.

The second maximum is located at 60.8 m on the opposite side of the detector due to the centered alignment of the laser beam. Choosing a logarithmic scale for the y-axis, the data distribution of the insertion point hemisphere has three different regions with nearly linear slopes. Consequently, the PE distribution of the insertion point hemisphere can be approximated with an exponential decay law with three different decay constants. Even though the data exhibits this exponential distribution, the PE amount is faintly fluctuating around this trend. Due to the logarithmic scale, this kind of behavior is easier to observe in the region above 8.0 m. In principle this is just a binning artifact. Here, each bin contains the hits of PMTs which lie on a circle around the maximum of the insertion point with an inner radius r_i and an outer radius $r_{i+1} = r_i + 0.2\,\text{m}$. Depending on the exact location of the chosen reference point and the relative distance of each PMT to this reference point, some circles contain an above-average count of photon hits. To get rid of this artifact, the bin width in figure 7.2 could be increased. This would lead to a smoother data distribution. Alternatively, it is also possible to fit the data distribution in order achieve a smoothening. For the analysis the second approach was chosen using the following fit function f_{fit} to describe the data distribution within the insertion point hemisphere.

$$f_{fit}(x) = c_1 \cdot \exp\left(-\frac{x}{\tau_1}\right) + c_2 \cdot \exp\left(-\frac{x}{\tau_2}\right) + c_3 \cdot \exp\left(-\frac{x}{\tau_3}\right) \tag{7.1}$$

Equation (7.1) is an exponential, three-component decay law. Here, the parameters c_1, c_2 and c_3 are related to the axis intercept of the three different linear parts of the logarithmic representation while the parameters τ_1, τ_2 and τ_3 determine their slopes.

Figure 7.3 illustrates how the data distribution in a histogram like figure 7.2 changes if the parameters L and L_s are varied. In case of a fixed scattering length L_s and a varied attenuation length L (see figure 7.3(a)) the recorded amount of PE events near the insertion point is virtually the same for all L values while at the equator the PE number clearly increases with the attenuation length. Due to the fixed L_s value, the probability for a photon to alter its propagation direction is constant for all combinations of L. However, a variation of the attenuation length L implies a variation of the absorption length L_a and, therefore, the probability for a photon to be absorbed during its way through the detector volume is changed as well. The larger the distance a photon has to cover, the stronger the influence of those absorption effects. As a consequence, the difference between the fit curves continuously

increases with a growing path length. In principle, a lower L value corresponds to smaller τ_i and c_3 values.

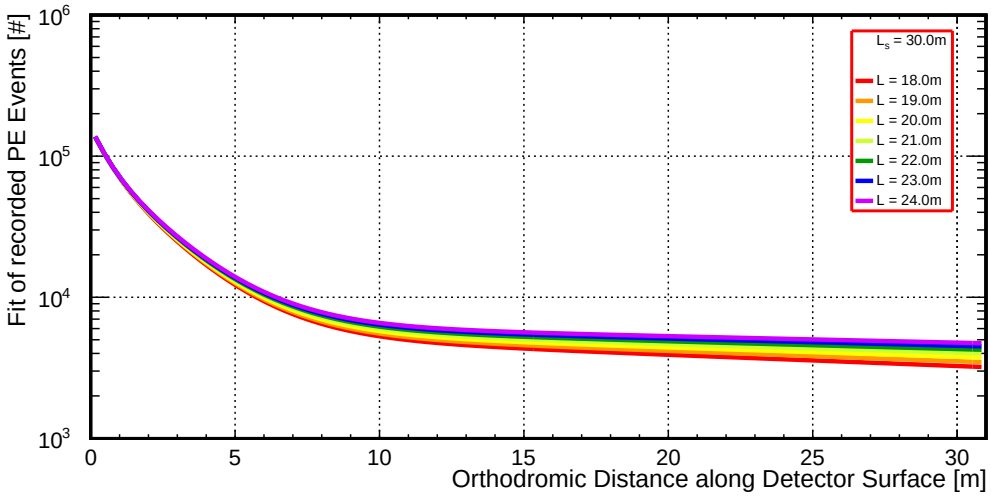

(a) Influence of L on the photon distribution

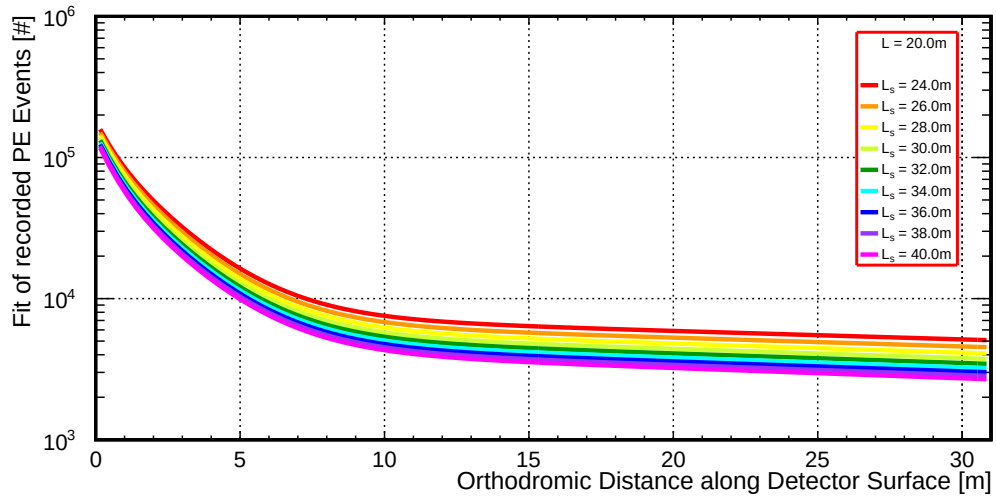

(b) Influence of L_s on the photon distribution

Fig. 7.3 Influence of L and L_s on the photon distribution

*The graphs show the **influence of the optical lengths** L **and** L_s **on the photon distribution** inside the JUNO detector. Here, **data distributions** like the one illustrated in figure 7.2 **were fitted and subsequently listed** in these plots for **different value combinations**. In figure 7.3(a), the value for the **scattering length is fixed** and the **attenuation length is varied**. On the contrary, figure 7.3(b) presents the fit results for a **fixed attenuation length** and a **varied scattering length**.*

In case of a fixed attenuation length L and a varying scattering length L_s (see figure 7.3(b)), the overall amount of PE is changed and the fit curves are just vertically

shifted. It looks like this effect would be smaller for shorter distances. In fact, this is just caused by the logarithmic scale. A shorter scattering length leads to more photons which are scattered to the peripheral PMTs. Consequently, more PE events are recorded in all PMTs except for those directly illuminated by the laser beams. That is why the τ_i parameters are barely influenced while the c_i factors of the fit functions are increasing with a decreasing scattering length.

The generated LUT considers and contains all 6 fit parameters for the two simulated optical lengths L and L_s and the resulting third length L_a. In addition, another photon distribution is created with the `offline` framework, hereafter just designated as *sample*, which provides analyzable data (in the end provided by AURORA) and will be fitted as well. It is assumed that the PE hits of a PMT are Poisson distributed satisfying the following formula:

$$P_\mu(k) = \frac{\mu^k}{k!} e^{-\mu} \tag{7.2}$$

Here, $P_\mu(k)$ stands for the probability to record k PE hits in a PMT if on average μ events are expected.

If the PE hits of a single PMT are Poisson distributed, the occurrence of PE events in a single bin of figure 7.2 satisfies the Poisson statistics as well. As a consequence, the following log-likelihood function can be used to compare the fit curve's value of the sample with the fit curves' values of the LUT bin-by-bin. Here, for each bin i the LUT values and the sample values are identified with the expected count number μ and the actual hit number k, respectively.

$$\chi^2 = -2 \sum_i^n \ln\left[P_\mu(k)\right]_i \tag{7.3}$$

Using equation (7.3), the result of the log-likelihood can be transformed into a χ^2 value. Figure 7.4 presents the results for the final χ^2 for the comparison of the sample with all entries of the LUT. The attenuation length L is varied between 15.0 m and 25.0 m with a 0.5 m binning. The scattering length L_s is varied between 20.0 m and 40.0 m and also has a 0.5 m binning. In the center of the histogram close to the striven values of $L \approx 20.0$ m and $L_s \approx 30.0$ m a finer binning is chosen. Here, within the region of 19.5 m $< L <$ 20.5 m and 29.5 m $< L_s <$ 30.5 m the bin width is reduced to 0.1 m. In addition, the absorption length L_a is varied between 40.0 m and 120.0 m. Value pairs of L and L_s with a corresponding absorption length L_a which does not

lie in this region are not considered in the analysis. This is why figure 7.4 does not exhibit any entries in the upper left and lower right corner. The color code specifies the χ^2 value of the bin. Each bin contains the difference $\Delta\chi^2$ between the original result χ^2 and the histogram's minimum χ^2_{min}. While the green diamond indicates the location of the sample's input parameters (Monte Carlo truth), here $L = 20.0\,\text{m}$ and $L_s = 30.0\,\text{m}$, the red spade shows the location of the minimal χ^2 value and, therefore, the location of the determined values for L and L_s of the sample file (reconstructed values). The red line specifies the 1σ uncertainty area.

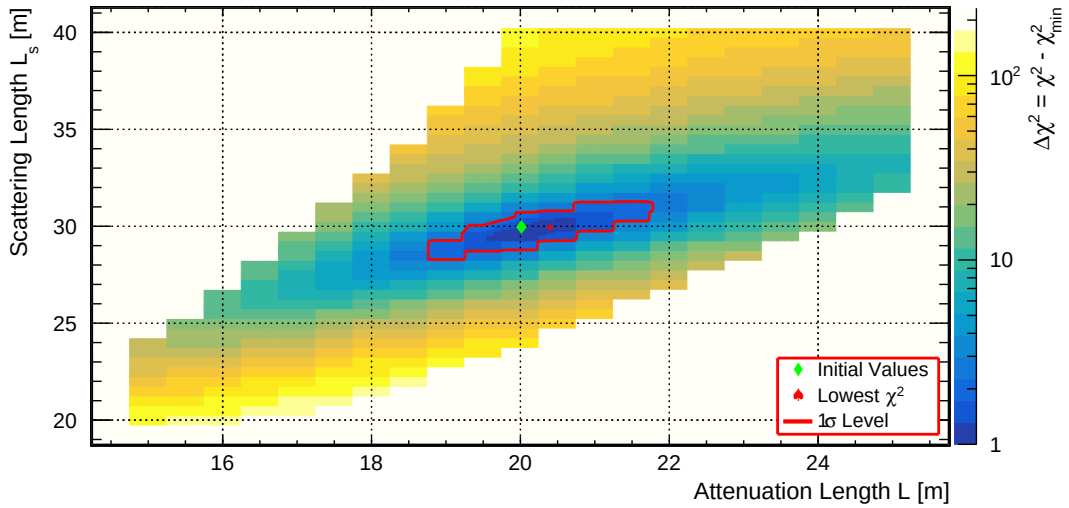

Fig. 7.4 The χ^2 distribution of the (L, L_s) parameter space

The histogram presents the χ^2 ***distribution*** *which results from a* ***log-likelihood function****. Here, the* ***photon distributions of an LUT for various*** *(L, L_s)* ***value combinations*** *are compared with a* ***sample file's photon distribution of one specific*** *(L, L_s)* ***value pair****. While the* ***green diamond*** *symbol refers to the* ***sample file's location*** *within the chosen parameter space, the* ***red spade*** *symbol corresponds to the* ***location with the lowest χ^2 value****. The* ***red line*** *indicates the 1σ* ***environment****.*

As it can be seen in figure 7.4, the Monte Carlo truth (green diamond) lies within the 1σ uncertainty area of the reconstructed LS transparency value with the corresponding L and L_s value (red spade). The relatively large size of the 1σ uncertainty area can be explained by the low statistics of the used sample file, as only one million photons were simulated instead of one billion. The general analysis approach foresees a freely selectable factor which scales the total amount of recorded PE events in the LUT statistics. This factor is varied during the minimization of the log-likelihood in order to compensate an occurring discrepancy in the photon statistics between the LUT and the sample file[6]. A detailed discussion of such systematic errors can

[6] This is important because the laser intensity and, therefore, the injected amount of photons will be only known up to a certain level of accuracy.

be found in section 7.3. A sample file with low statistics and the corresponding χ^2 distribution chart are presented here because, in this case, the 1σ area is still large enough to be recognized. With statistics comparable to the LUT the 1σ region is already shrinking to a size where it is hidden behind the red spade symbol. In principle, occurring systematic errors can be identified by a displacement of the red spade, so that the green diamond does not lie in the 1σ uncertainty region anymore.

In order to determine the statistical uncertainty of the reconstructed values for L and L_s, the χ^2 distribution of figure 7.4 can be vertically and horizontally sliced through the position of the red spade. The results are two χ^2 parabolas – one with a varying attenuation length L and a fixed scattering length L_s (see figure 7.5), and the other one with a varying scattering length L_s and a fixed attenuation length L (see figure 7.6). The χ^2 distribution in figure 7.4 depends on two independent parameters – L and L_s. As a consequence, the 1σ uncertainty and, hence, the statistical fluctuation of both quantities is determined by a limit $\chi^2_{1\sigma}$ which lies 2.3 units above the histogram's minimum χ^2_0.

The χ^2 distribution in figures 7.5 and 7.6 can be described by the following quadratic equation:

$$f_{fit}(x) = \begin{cases} a_1 (x-b)^2 + c & \text{for } x < b \\ a_2 (x-b)^2 + c & \text{for } x \geq b \end{cases} \tag{7.4}$$

Here, both parabola branches share the same vertex $V(b|c)$ but exhibit different curvatures determined by the parameters a_1 and a_2. This is important in order to satisfy the asymmetric shape of the data distribution.

From figure 7.5 follows that the reconstructed value for the attenuation length is $L = 20.29^{+1.32}_{-1.11}$ m. Here, the lower uncertainty is smaller because of the stronger curvature of the left parabola branch. The same procedure is repeated for the scattering length in order to determine the value and the corresponding uncertainties of L_s. Similar to the previous step, equation (7.4) is used to describe the data distribution in figure 7.6. From this graph follows a scattering length of about $L_s = 29.98^{+1.28}_{-1.00}$ m.

The discussed approach is used in the following sections to determine the statistical uncertainty of L and L_s on the one hand and the dominant systematic uncertainties of those optical lengths on the other hand.

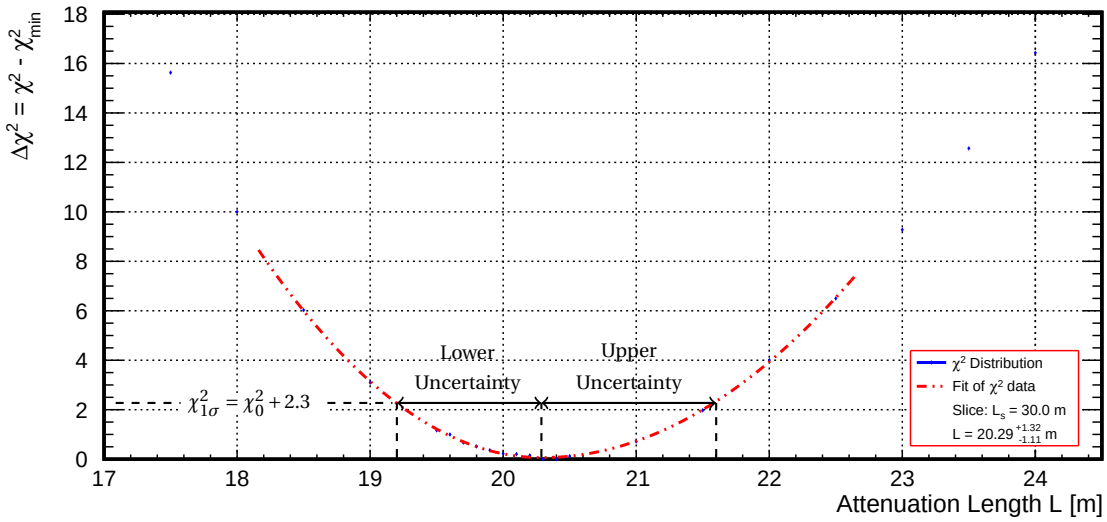

Fig. 7.5 The χ^2 parabola with L as free parameter

The graph shows the χ^2 ***parabola*** *which follows from figure 7.4 if the* ***histogram is horizontally sliced*** *through its minimum (red spade). In addition, the* ***asymmetric*** 1σ ***uncertainty range*** *is drawn as well. The resulting* ***lower and upper uncertainty values*** *are used to quantify the* ***statistical uncertainty*** *of the parameter L. While the χ^2* ***data*** *is represented by the* ***blue markers****, the* ***fit curve*** *is indicated by the* ***dashed, red line****.*

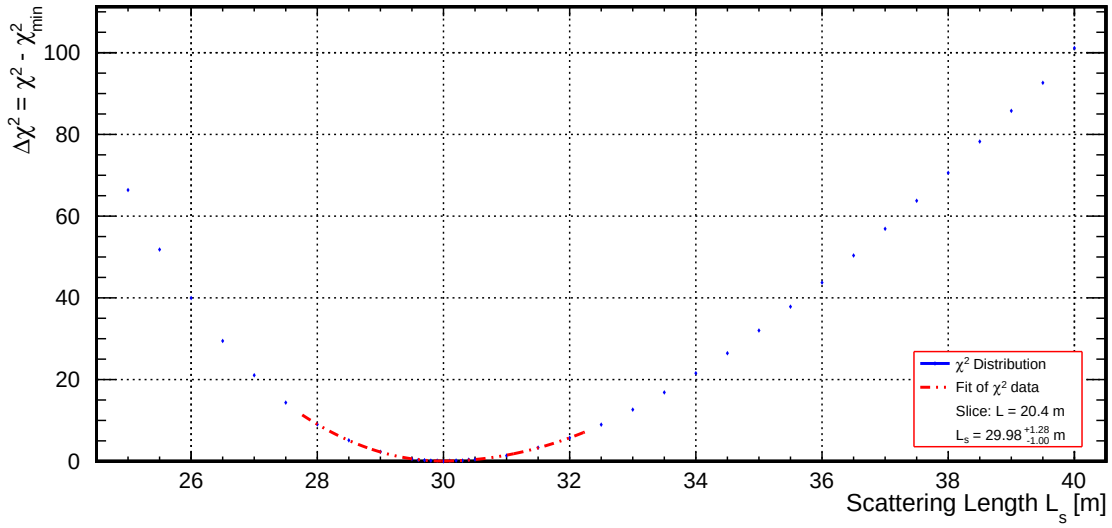

Fig. 7.6 The χ^2 parabola with L_s as free parameter

The graph shows the χ^2 ***parabola*** *which follows from figure 7.4 if the* ***histogram is vertically sliced*** *through its minimum (red spade). While the χ^2* ***data*** *is represented by the* ***blue markers****, the* ***fit curve*** *is indicated by the* ***dashed, red line****.*

7.2 AURORA's Statistical Uncertainty

In the following section the statistical uncertainty of a typical 5 s measurement[7] is investigated. For this purpose the LUT data is compared with a sample file which was generated by simulating one billion photons and, therefore, contains an equal amount of recorded PE events. Similar to the properties of the laser beams which were simulated during the generation of the LUT data, the simulated laser beam of the sample file is mono-energetic ($\lambda = 430\,\text{nm}$), centered and perfectly collimated. As discussed in section 7.1, for the comparison between the sample file and each LUT entry a χ^2 value is calculated. Figure 7.7 shows the results of the log-likelihood function. The following histogram has the same parameter space, range of values for the optical lengths L and L_s and binning like figure 7.4.

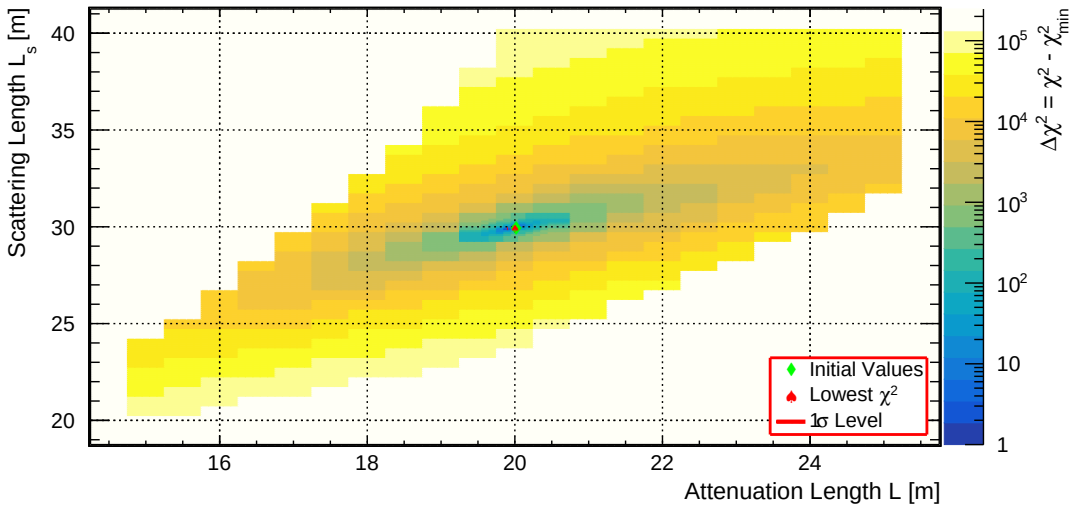

Fig. 7.7 The χ^2 distribution – pure statistical uncertainty

The histogram shows the χ^2 ***distribution*** *from a* ***comparison between the LUT data*** *and a* ***sample file with a mono-energetic, centered and perfectly collimated laser beam****. Here, just the* ***seed for the simulated photons was changed*** *in order to investigate the* ***statistical uncertainty*** *of the analysis approach. Similar to each LUT entry, exactly* ***one billion photons*** *were simulated for the sample file.*

In contrast to figure 7.4, the locations of the Monte Carlo truth and the χ^2_{min} value are here the same. This indicates that regarding the statistical uncertainty the analysis approach is working very well. Furthermore, it can be seen that the χ^2 values are rising fast when moving away from the bin with the lowest χ^2 value – significantly faster than in figure 7.4. As a consequence, the L and L_s parabolas (see

[7] Assuming a pulsed laser with a frequency $f = 200\,\text{Hz}$, a pulse width of $\Delta t = 10\,\mu\text{s}$ and one million photons per pulse. See section 6.3 for more details regarding the chosen beam performance.

figures 7.8(a) and 7.8(b)) are steeper and, accordingly, the resulting statistical uncertainty is smaller. For a five second measurement, the 1σ uncertainty region is so small that it cannot be resolved anymore being hidden behind the red spade symbol.

In order to derive a value for L and L_s with the corresponding 1σ uncertainties, the χ^2 parabolas for both parameters are plotted and subsequently fitted by using a fit function similar to equation (7.4). The resulting limits can be interpreted as the overall statistical uncertainty[8] of the L and L_s values (see section 7.1).

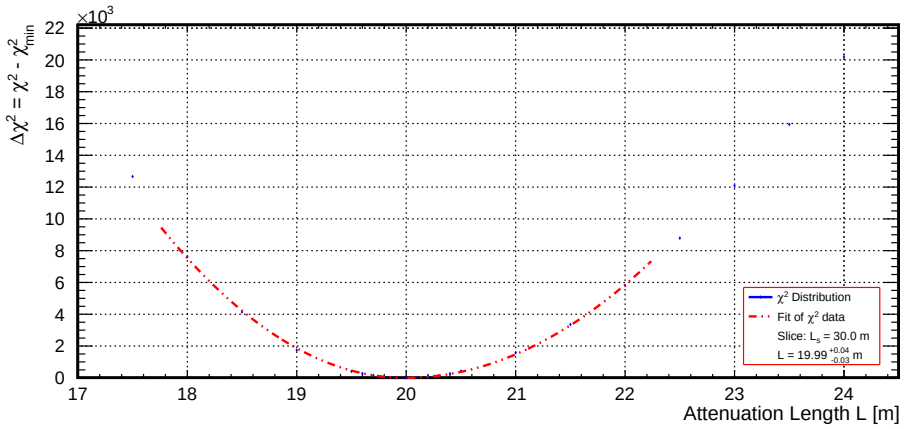

(a) χ^2 parabola – L as the free parameter

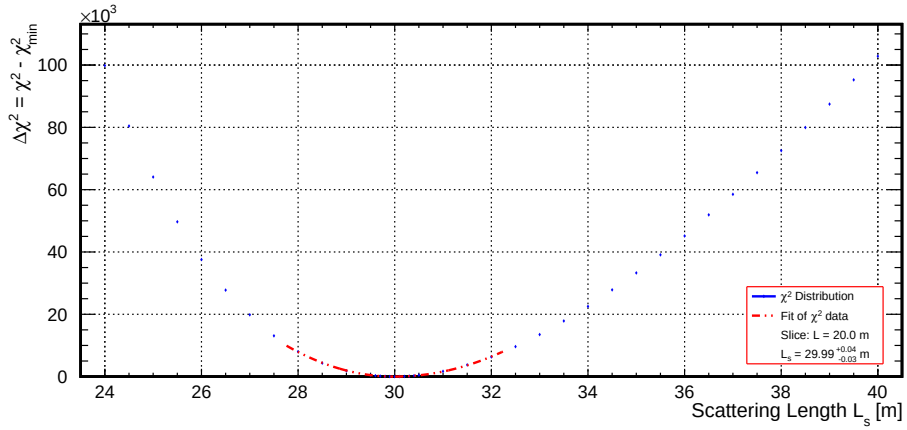

(b) χ^2 parabola – L_s as the free parameter

Fig. 7.8 L and L_s parabola – pure statistical uncertainty

*The two **histograms show the** χ^2 **parabolas** which follow from figure 7.7 if the **distribution is horizontally and vertically sliced** through its minimum.*

While for the attenuation length a value of $L = 19.99^{+0.04}_{-0.03}$ m can be deduced, the scattering length is $L_s = 29.99^{+0.04}_{-0.03}$ m. In addition, the Monte Carlo truth (initial

[8] Assuming a typical five seconds measurement.

parameters) of the sample file lies within the 1σ uncertainty range of the reconstructed values for the optical lengths L and L_s. This demonstrates the functionality of the analysis algorithm. Furthermore, with an amount of one billion photons the statistical uncertainties of the results of L and L_s are already in the single-digit centimeter range. Finally, these results prove that this approach can be used to resolve both the attenuation length L and the scattering length L_s at the same time with an unprecedented statistical accuracy. The following graph shows how the statistical uncertainty develops if the photon statistics is further increased.

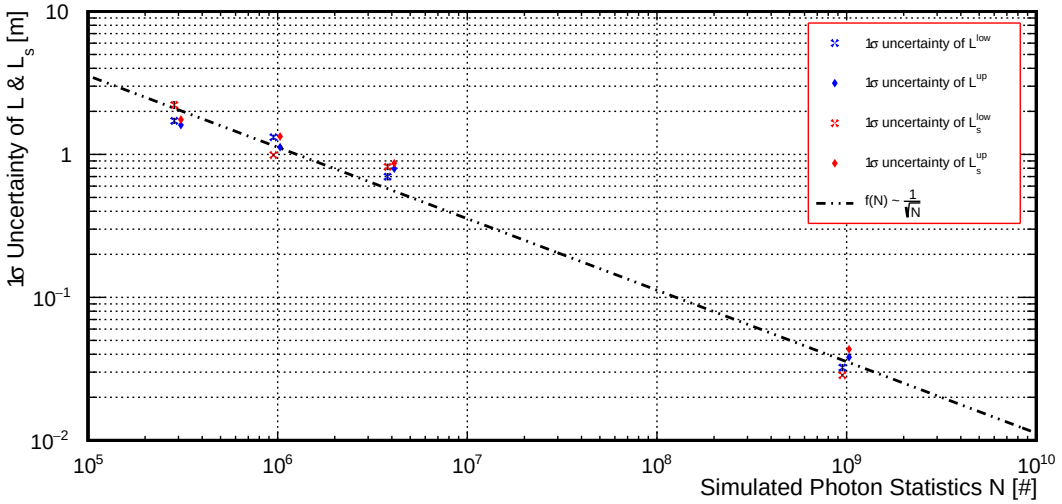

Fig. 7.9 Improvement of statistical uncertainty

*The graph illustrates the **statistical uncertainty** of the **optical lengths** L (blue markers) and L_s (red markers) for **various statistics N** – with $N_1 = 3 \cdot 10^5$, $N_2 = 1 \cdot 10^6$, $N_3 = 4 \cdot 10^6$ and $N_4 = 1 \cdot 10^9$. While the **cross markers refer to the lower uncertainties**, the **diamond markers stand for the upper ones**. For the sake of clarity, the two marker types are horizontally shifted to each other. The **black line** indicates the **expected trend** for statistical uncertainties.*

From figure 7.9 it can be concluded that an increase of the photon statistics by a factor of ten would lead to an absolute statistical uncertainty of around 1 cm. Assuming an attenuation length $L = 20.0$ m and a scattering length $L_s = 30.0$ m, the relative statistical uncertainty would already enter a precision regime smaller than 0.1%. In order to achieve such a precision, a measurement time of at least 50 s is needed, assuming a pulsed laser beam with a frequency $f = 200$ Hz, a pulse width of $\Delta t = 10\,\mu$s and 1 million photons per pulse (for beam performance see section 6.3). A duration of around one minute for one measurement seems to be practicable. Thus, considering all twelve laser beams, a complete measurement circle could be performed in less than 15 minutes. In addition, the graph clearly states that the fit method for determining the L and L_s uncertainties is working, as the results for the statistical uncertainties satisfy the expected $1/\sqrt{N}$ behavior.

7.3 AURORA's Systematic Uncertainties

This section will focus on the systematic uncertainties of the developed laser system. On the one hand there are several systematics which are related to the beam performance, concerning the beam intensity, alignment, aperture angle and spectrum. On the other hand there are systematics regarding the CD. Here, the transparency of the surrounding water and acrylic sphere can influence AURORA's performance. In addition, the target mass' temperature affects the recorded data. The following subsections will discuss each of those systematics in more detail and evaluate the magnitude of their influence on AURORA's accuracy.

7.3.1 Uncertainty Of The Beam Intensity

The first investigated systematics concerns the laser beam intensity. As already presented in chapter 6, the luminosity of the laser beam is continuously monitored. Nevertheless, the transparency of each component and, therefore, the amount of photons which are entering the central detector, is only known to a certain precision. Consequently, it is important to know how the analysis approach is influenced if a wrong laser beam intensity is assumed. For this kind of systematics, the LUT entries are compared with several sample files of various photon statistics. While for the creation of each LUT entry one billion photons were simulated, the photon statistics of the sample files ranges between one million and ten billion. For the sample files, the attenuation and scattering length were always set to 20.0 m and 30.0 m, respectively.

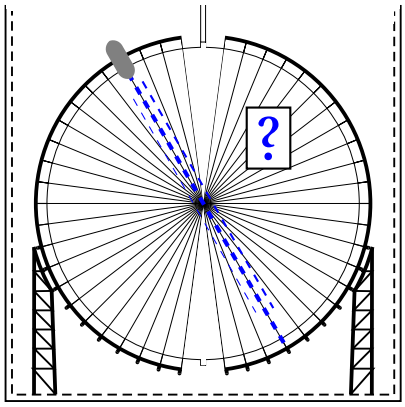

Fig. 7.10 Laser beam intensity

Following the description in section 7.1, each generated sample file is compared with all LUT entries using equation (7.3). During the minimization, the fit function which describes the data distribution of the LUT entry is scaled by a freely selectable parameter in order to compensate the mismatch between the photon statistics. Figure 7.11 presents the results of this study. The Monte Carlo truth lies for both parameters, L and L_s, within the uncertainty region of almost all data points. While for a sample file statistics of $N > 0.5 \cdot 10^9$ the reconstructed values for L and L_s do

not strongly fluctuate around the Monte Carlo truth, the discrepancy increases with a decreasing photon statistics for $N \leq 0.5 \cdot 10^9$. For these data points ten different runs with the same photon statistics were performed. Afterwards, the average value for the optical lengths and the corresponding 1σ uncertainties were calculated in order to estimate the statistical uncertainty of the stronger fluctuating data points even more accurately.

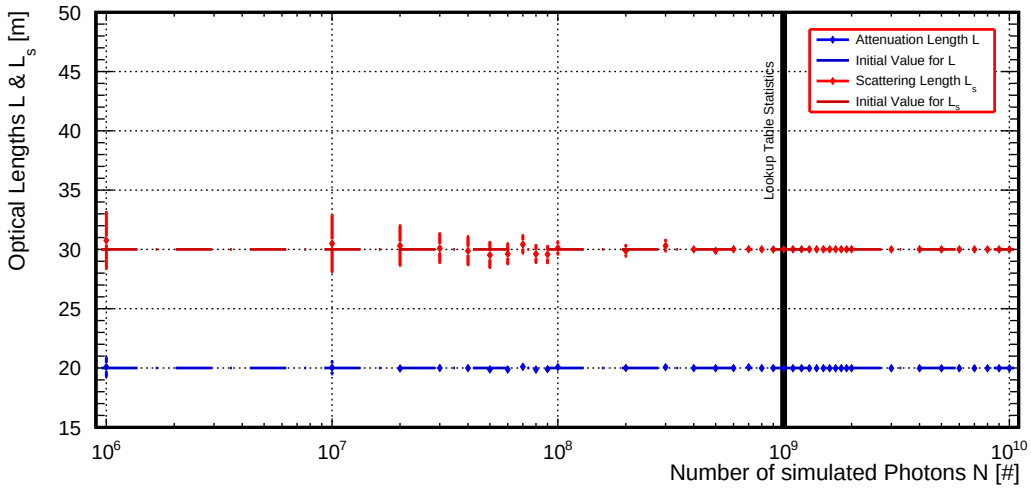

Fig. 7.11 Various photon statistics and their influence on L and L_s

The graph shows how a ***wrongly assumed beam intensity influences the results for the attenuation length*** *L* ***and scattering length*** L_s*. While for the* ***LUT entries always one billion photons*** *were simulated (black line), the* ***photon statistics of the sample files varies from one million to ten billion simulated photons****. The results for the* ***attenuation and scattering length*** *are colored* ***blue and red****, respectively. According to that color code, the* ***dashed lines*** *refer to the* ***Monte Carlo truth*** *values of L and* L_s*.*

For the attenuation length the statistical uncertainty does not increase as fast as for the scattering length. In addition, the average values of L match the Monte Carlo truth very well even for a photon statistics which are three orders of magnitude smaller than the used photon statistics for the LUT entries. This can be explained by figure 7.3(a). Here, it was already pointed out that the attenuation length primarily influences the decay constants τ_i of the fit functions. Those parameters are robust against intensity fluctuations and do not change. As a consequence, even for significantly differing photon statistics the correct value for the attenuation length L can be reconstructed. In contrast to that, the scattering length L_s exhibits a larger variance around the Monte Carlo truth. This is reflected by both the discrepancy between average value and Monte Carlo truth and the statistical uncertainty of the individual data point. Similar to the attenuation length L, the behavior for L_s can

be explained by figure 7.3(b). It can be concluded that the scattering length L_s has a predominant impact on the c_i parameters of the fit function. As these factors are changing if the intensity of the laser beam is varied, the expected uncertainty of L_s has automatically to increase. In order to estimate a systematic uncertainty of L and L_s regarding a beam intensity that is only known up to a certain accuracy, the region of interest in figure 7.11 has to be carefully examined.

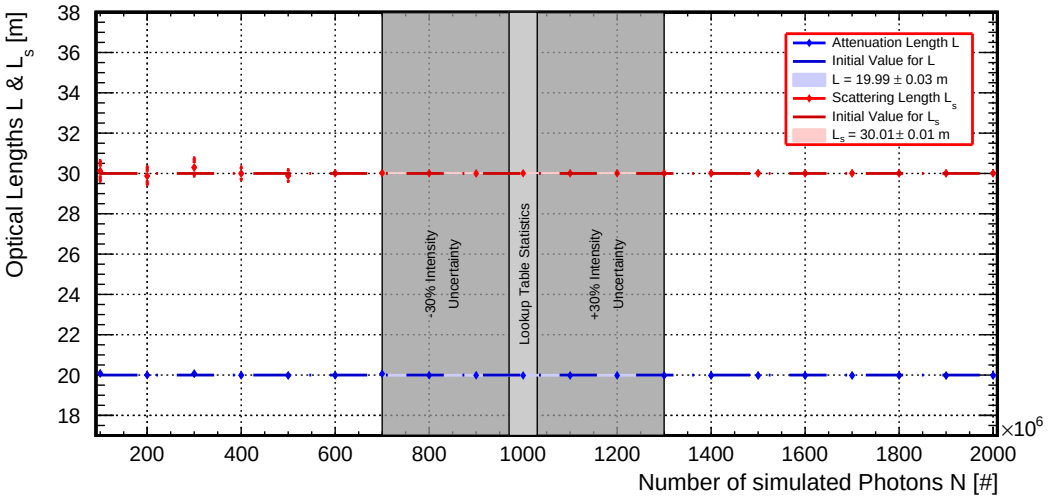

Fig. 7.12 Various photon statistics – region of interest

The graph illustrates a magnified part of figure 7.11. Here, the ***region of interest*** *is presented in more detail. The* ***photon statistics ranges between 100 million and 2000 million simulated photons****. Similar to figure 7.11 the LUT statistics, the results for L and the results for L_s are colored gray, blue and red, respectively. In addition, a* ***conservatively estimated uncertainty of the beam intensity*** *(colored dark gray) of 30% is shown as well.*

Figure 7.12 illustrates the region of interest of figure 7.11 with an additional uncertainty range regarding the beam intensity. Here, a conservative estimate[9] of 30% was assumed. The fluctuation of the reconstructed L and L_s values in this intensity interval can be used to determine the corresponding systematic uncertainty. Here, the RMS of the data points within the intensity uncertainty range of ±30% defines the final uncertainty of L and L_s. For the attenuation length L and the scattering length L_s a systematic uncertainty of ±3 cm and ±1 cm can be determined. Taking into account that the statistical uncertainty for a typical 5 s measurement is for both optical length around ±4 cm, these values are upper limits. As a consequence, the systematic uncertainty caused by a wrongly assumed beam intensity could be even smaller.

[9] According to the previous chapter, the uncertainty of the beam intensity will be less than 14%.

7.3.2 Uncertainty Of The Beam Alignment

The second systematics is about the laser beam alignment. In section 7.1, it was shown that the photon distribution is used to determine the optical lengths L and L_s. Up to now, only the ideal case of a perfectly centered beam was taken into account. However, in reality this might be not the case. As discussed in section 6.4, the FTH components will be integrated in a PMT array subunit before this element is mounted on the supporting stainless steel structure. As a consequence, the laser beam might be misaligned after the installation. Furthermore, after the filling procedure, the beam path could be altered due to the changed refraction indices. In addition, due to the starting buoyancy of all submerged components, the laser beam might change its trajectory relatively to the PMTs after the filling. On the other hand, even if the beam alignment is accurate and the laser beam points to the detector's center, obstacles like a connection bar or an acrylic node might force the operator to re-adjust the beam direction resulting in an off-centered beam. This would be also necessary if a PMT were directly hit by the laser beam while operating at higher intensities to collect more statistics in a shorter time period. In all these scenarios the photon distribution will differ from the ideal case. Theoretically, this could influence the analysis approach changing the results of L and L_s. Consequently, the impact of a tilted laser beam on the analysis has to be carefully studied. For the study several sample files were created. Here, for all samples the attenuation and scattering length were chosen to be 20.0 m and 30.0 m, respectively. In addition, the laser beam was tilted by an angle θ, which ranges between 0° and 10°. According to the installation procedure, not occupied slots of small PMTs will be used to access the inner volume of the CD and to inject the laser light. Due to the length of the sPMT's holder tubes and the distance between FTH and sPMT holder, the maximally realizable tilt angle is around $\theta = 7°$. At higher tilt angles, the laser beam hits the holder tube and gets deflected or even blocked (mechanical limit). Nevertheless, this study also includes larger tilt angles because the whole PMT array subunit could be misaligned as well. This might increase the overall tilt angle θ. Following the analysis approach presented in section 7.1, values for the attenuation length

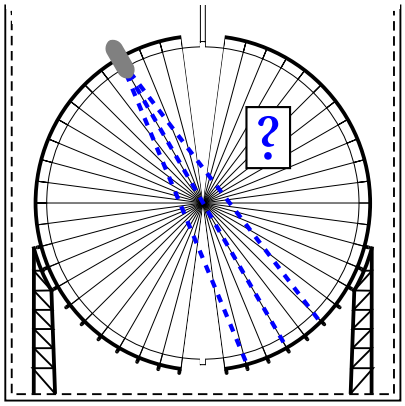

Fig. 7.13 Laser beam alignment

L and scattering length L_s were determined. Figure 7.14 shows the results of the conducted study. Both graphs show a similar behavior. While for tilt angles $\theta \leq 4°$ the Monte Carlo truth lies still within the statistical uncertainty range of the results for L and L_s, the reconstructed optical lengths are significantly shifted to higher values for tilt angles $\theta > 4°$.

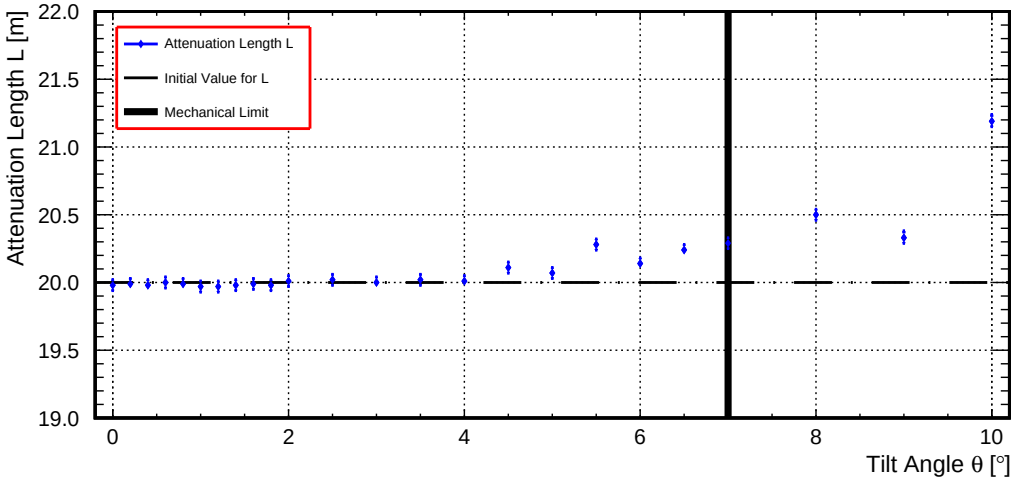

(a) L depending on the tilt angle θ

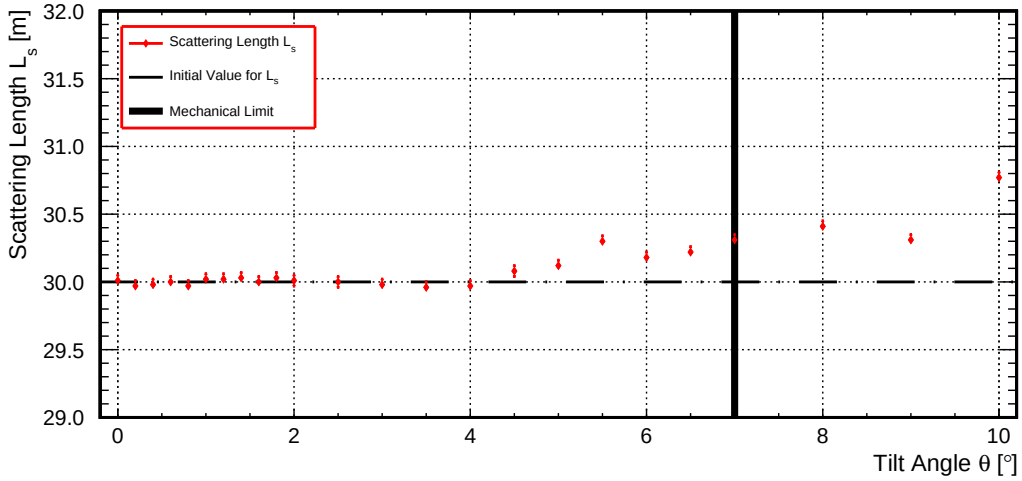

(b) L_s depending on the tilt angle θ

Fig. 7.14 L and L_s and their tilt angle dependency

The graphs 7.14(a) and 7.14(b) present the ***tilt angle dependency of the attenuation and scattering length****, respectively. While the values for the* ***Monte Carlo truth*** *are indicated by the* ***thin, black and dashed lines****, the position of the* ***upper limit for the tilt angle*** *(mechanically caused by sPMT holder) is highlighted by the* ***thick, black and solid lines*** *at* $\theta = 7°$.

This tendency is a result of the asymmetric distribution of the PE events recorded along the detector surface. Figure 7.15 compares hit map patterns of different tilt angles.

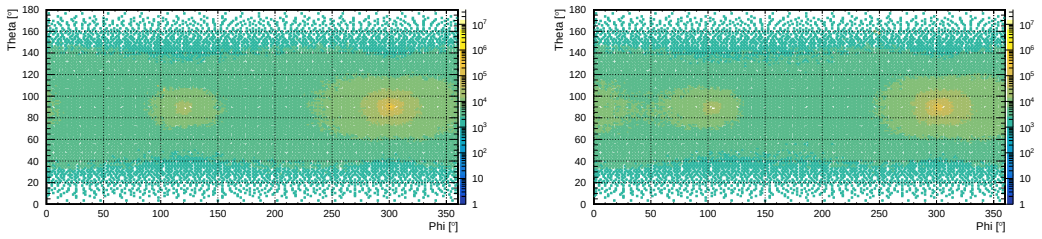

(a) Tilt angle $\theta = 0°$ (b) Tilt angle $\theta = 9°$

Fig. 7.15 Hit map patterns for various tilt angles θ

*The histograms present **hit map patterns for various tilt angles** θ. While figure 7.15(a) shows the **PE distribution for a centered laser beam**, figure 7.15(b) illustrates the **hit map pattern of an off-centered beam** with a tilt angle of* $\theta = 9\,°$.

Here, the comparison demonstrates how the amount of recorded PE events is increasing in the equator area if the laser beam is tilted. As a consequence, when transforming the 2D hit map pattern into a 1D representation, the data distribution becomes flatter for higher tilt angles. Figure 7.16 shows the resulting fit functions which describe the 1D representations of the two histograms shown in figure 7.15.

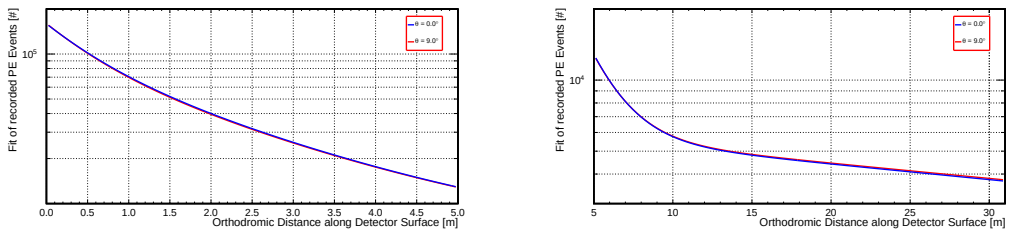

(a) Distance ranging from 0.0 m to 5.0 m (b) Distance ranging from 5.0 m to 31.0 m

Fig. 7.16 Fit functions of photon distributions for various tilt angles θ

*The two graphs show the **fit functions** which result **from the photon distributions** presented in figure 7.15(a) and 7.15(b) for different distance ranges.*

Figure 7.16(a) emphasizes that for distances between 0.0 m and 5.0 m the recorded amount of PEs is smaller for higher tilt angles. Nevertheless the recorded PE amount close to the insertion point remains unchanged. In contrast to that, the overall amount of recorded PE events is higher whithin the distance range of 5.0 m to 31.0 m for higher tilt angles. As a consequence, except for τ_1 the decay constants

are increasing with the tilt angle. This is why the analysis approach shows the tendency to reconstruct higher values for the attenuation length L if the laser beam is off-centered. In addition, the higher values for c_2 and c_3 lead to higher values for the reconstructed scattering length L_s.

In principle, figure 7.14 could be used to quantify the systematic uncertainty of a tilted laser beam. However, in order to ensure that the shown shifts are really based on systematic effects, values for L and L_s were reconstructed in nine different runs for 5 tilt angles. While the graphs of the individual runs can be found in appendix B, the final results are shown in the following figure.

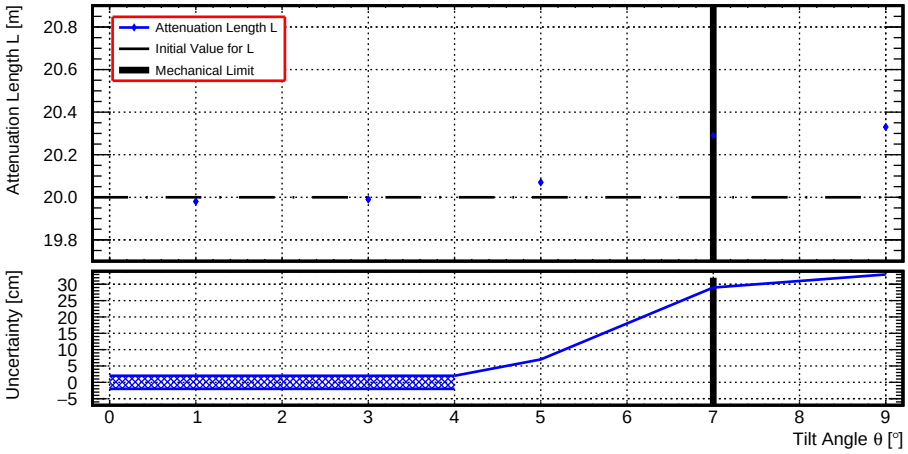

(a) Systematic uncertainty of the attenuation length L

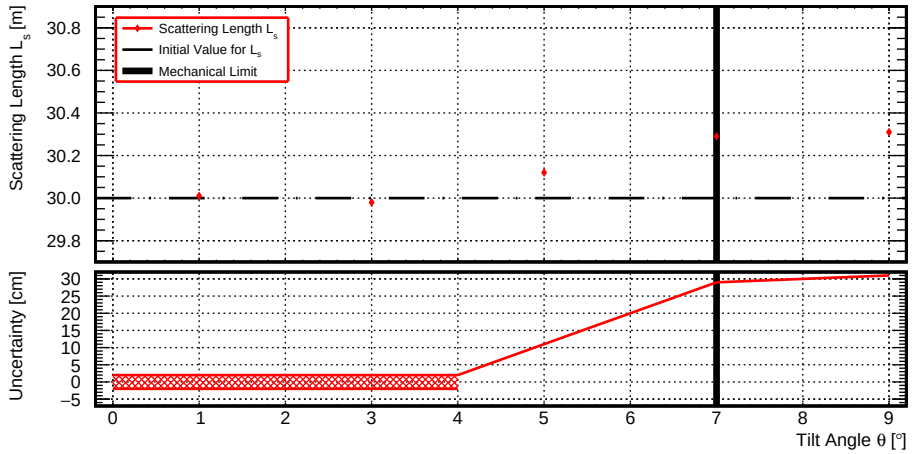

(b) Systematic uncertainty of the scattering length L_s

Fig. 7.17 Systematic uncertainty of L and L_s depending on the tilt angle θ

*Presented are the **shifts of** L **and** L_s for five different tilt angles. In addition, both graphs show the **derived systematic uncertainty** depending on θ.*

The statistical uncertainties in figures 7.17(a) and 7.17(b) are in the order of 1 cm. As a consequence, the error bars are hidden behind the markers. Similar to figure 7.14, the shifts for L and L_s are insignificant for tilt angles $\theta \leq 4°$. Due to an average statistical uncertainty of around ± 4 cm when performing a 5 s measurement, the systematic uncertainties in this range are conservatively estimated to be ± 4 cm. For $\theta > 4°$ the shift becomes significant. Here, only a shift to higher values is realized. Consequently, the systematic uncertainty is always of positive sign.

In general, during the installation a misalignment of $\theta > 4°$ should be recognizable. Here, the laser beam will be adjusted in a way that its spot hits the center of the entry and exit aperture of the small PMT holder tube. With a tube length of $L = 26.0$ cm the spot has to be off-center by more than 1.8 cm in order to realize a tilt angle of $\theta > 4°$. This is easy to observe and, therefore, avoidable. Thus, a systematic uncertainty of ± 4 cm regarding the laser beam alignment seems to be a realistic estimate for both L and L_s. As the statistical uncertainty for the used photon statistics ranges in the same order of magnitude, the ± 4 cm uncertainty for both optical length is again just an upper limit.

7.3.3 Uncertainty Of The Beam Aperture Angle

The third systematic uncertainty is related to the aperture angle of the laser beam. Although the aperture angles of all GRIN lenses were measured with high precision (see section 6.2.11), even small differences in the photon distribution (recorded PE events at the whole verge of the detector) might influence the results of L and L_s. To be more precisely, as for the analysis only the photon statistics of the insertion point hemisphere is used, changes in this area are of great importance. Hence, the impact of the aperture angle uncertainty of the reconstructed L and L_s values has to be studied. For this purpose several sample files with different aperture angles (half of the cone angle) were generated. The beam profile exhibits a Gaussian intensity distribution whereas its width (FWHM) ranges between zero and one degree. For all sample files the Monte Carlo truths of the attenuation length and scattering length were chosen to be 20.0 m and 30.0 m, respectively.

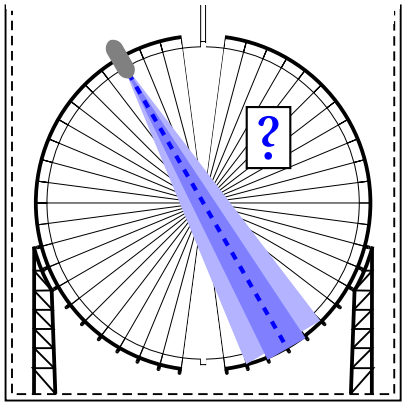

Fig. 7.18 Laser beam aperture angle

Figure 7.19 presents the results of the study. For the attenuation length L as well as for the scattering length L_s, the Monte Carlo truth lies within the uncertainty range of all data points. Here, the errors of the data points are with an average value of ± 4 cm too small and hidden behind the markers. No effect on the reconstructed values of the optical lengths can be observed. This outcome is surprising as an increased aperture angle should correspond to higher PE statistics in the peripheral PMTs. As a result, the fitted curves of the PE hit distribution should exhibit higher τ_i and c_i values which normally is associated with an upwards shift of the reconstructed L values and a downwards shift of the reconstructed L_s values. Even though a slight tendency seems to be recognizable, the magnitude of this effect is still insignificantly small. For a conservative estimate, an uncertainty of the aperture angle of $\Delta\alpha = \pm 0.05°$ was assumed, although the measured uncertainty of the average aperture angle for the GRIN lens is less than $\Delta\alpha = \pm 0.01°$ (see section 6.2.11). For both the attenuation length L and the scattering length L_s the fluctuation of the reconstructed values is ± 1 cm. These numbers are just upper limits as the results are still dominated by the statistical uncertainty and no clear systematics can be

observed. In order to find out why the results of the attenuation and scattering length are not affected by an increasing aperture angle of the simulated laser beam, the hit map patterns of the generated sample files were further investigated.

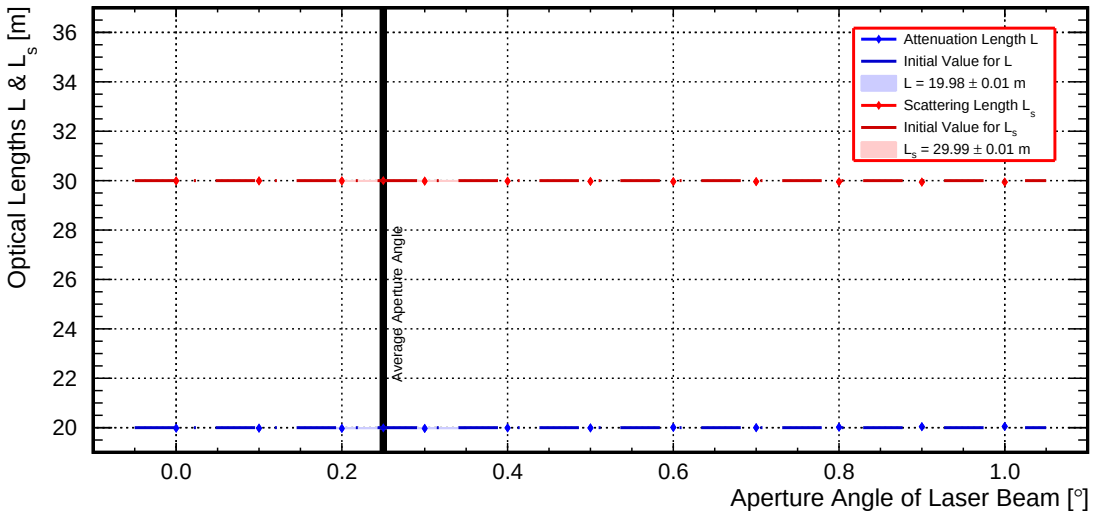

Fig. 7.19 The aperture angle and its influence on L and L_s

*The graph shows the **results of the systematics study** regarding the **aperture angle of the laser beam**. Here, the aperture angle was **varied between** $\alpha = 0.00°$ **and** $\alpha = 1.00°$. On average, the **aperture angle** of the laser beam was **determined to be** $\alpha = 0.25 \pm 0.01°$ (**black line**). While the **blue data points** refer to the reconstructed **attenuation length values**, the **red data points** stand for the determined **scattering length values**. The **colored, dashed lines** indicate the **Monte Carlo truth values**.*

Figure 7.20 visualizes the different PE distributions. While figure 7.20(a) exhibits an aperture angle of $\alpha = 0.00°$, the aperture angles are subsequently increased by 0.20° until figure 7.20(f), which shows the hit map pattern for an aperture angle of $\alpha = 1.00°$. In all six cases, the laser beam enters the detector on the right side ($\phi \approx 300°$) and strikes the PMT array on the left side ($\phi \approx 120°$) of the histogram. Taking all distributions into account, it becomes clear why the aperture angle of the laser beam does not affect the results of the attenuation length L and scattering length L_s – at least not for the investigated range between zero and one degree. The PE distribution of the insertion point hemisphere does not significantly change. And for the analysis only the PE statistics of this hemisphere is used. On the contrary, the intensity maximum of the exit point hemisphere is broader and, therefore, more pronounced for larger aperture angles. As a consequence, the systematic uncertainty would be larger if the PE distribution of the exit point hemisphere were used for the determination of the optical length L and L_s. In order to proof that the PE statistics does not significantly change on the hemisphere of the insertion

point, the entries of figure 7.20(f) are divided by the entries of figure 7.20(a). If the recorded event rate in this area does not change, the ratios should be around one.

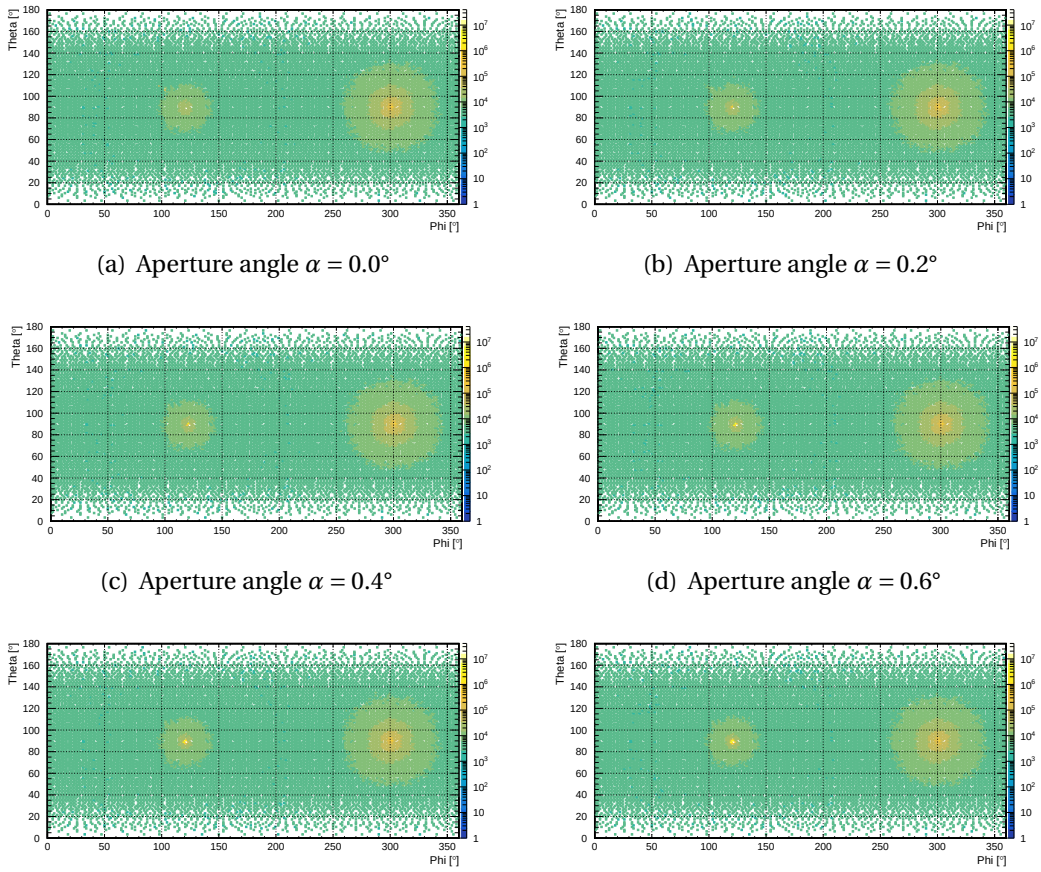

(a) Aperture angle $\alpha = 0.0°$

(b) Aperture angle $\alpha = 0.2°$

(c) Aperture angle $\alpha = 0.4°$

(d) Aperture angle $\alpha = 0.6°$

(e) Aperture angle $\alpha = 0.8°$

(f) Aperture angle $\alpha = 1.0°$

Fig. 7.20 PE hit map patterns for various aperture angles

*The graphs presents the **recorded PE hit map patterns for various aperture angles**. In all figures the **laser beam enters** the detector at an **azimuth angle** $\phi \approx 300°$ and points to the opposite side. The **attenuation and scattering length** is **20.0 m and 30.0 m**, respectively. Exact **one billion photons were simulated** for each sample file.*

For an estimate regarding the statistical uncertainties, the entries of figure 7.20(a) were divided by a second histogram with an aperture angle of $\alpha = 0.00°$. Here, only the seed of the simulated photons was changed. Figure 7.21 presents the results of this cross check. In figure 7.21(a), the ratio between two histograms with an aperture angle $\alpha = 0.00°$ is plotted. The bins' content close to the insertion and exit point is close to one. Here, due to the higher event rate, the statistical uncertainty is around $\pm 1\%$. For the peripheral PMTs the statistical uncertainty is increased and, therefore, the bin values scatter wider around the mean value of one. Figure 7.21(b) illustrates the ratio between two histograms with $\alpha = 0.00°$ and $\alpha = 1.00°$. The only difference

to figure 7.21(a) can be observed in the area of the exit point. Here, the recorded event rate is much higher (yellow spot) for an aperture angle $\alpha = 1.00°$. In contrast to that, the entries of the insertion point hemisphere are still scattered around a mean value of one. Hence, the uncertainty of the laser beam's aperture angle of the results for L and L_s plays a minor role in the presented analysis approach.

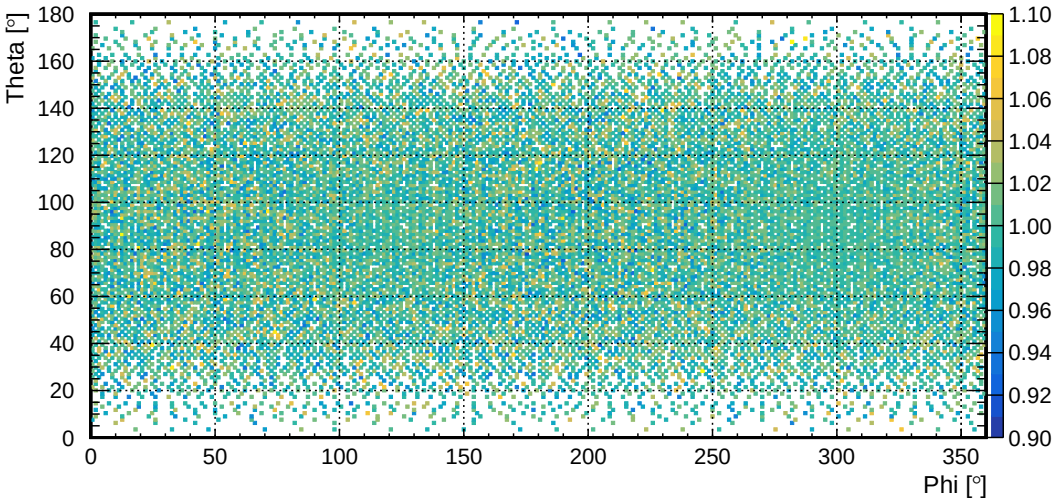

(a) Aperture angle $\alpha = 0.0°$

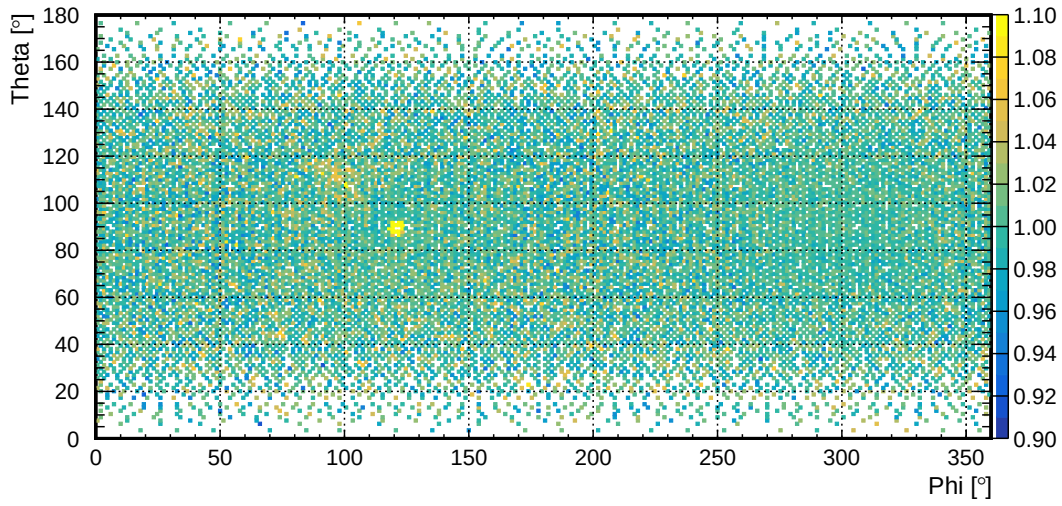

(b) Aperture angle $\alpha = 1.0°$

Fig. 7.21 Ratios of hit map patterns for different aperture angles

*The graphs show the **ratios of PE hit map patterns** for the whole verge of the detector. Figure 7.21(a) presents the **ratios between two histograms with an aperture angle** $\alpha = 0.0°$. Here, **different seeds** were used for both sample files. Figure 7.21(b) illustrates the **ratio of PE hit map patterns** between a histogram with an **aperture angle** $\alpha = 0.0°$ **and** $\alpha = 1.0°$.*

7.3.4 Uncertainty Of The Laser Spectrum

The fourth systematic uncertainty concerns the spectral distribution of the light produced by the laser diode. Here, the optical lengths L, L_a and L_s directly depend on the photon's wavelength. However, for the wavelength region of interest[10] the values for the absorption length do not significantly vary, and with $L_a \approx 77.0\,\text{m}$ the absorption length can be assumed to be constant. Therefore, the wavelength dependency of the attenuation length L is primarily given by the behavior of the scattering length L_s. Furthermore, the scattering length in this wavelength region is predominantly determined by the Rayleigh scattering length which exhibits the typical λ^4 behavior (see section 4.4). There are two different systematic sources which might have an impact on the spectral distribution of the diode. On the one hand the location of the emission peak depends on the diode's temperature [130]. As a consequence, the wavelength distribution of the emitted light might fluctuate according to the temperature variations of the environment. Even though the temperature of the diode is stabilized with fluctuations less than ±0.1°C, for a conservative estimate the expected temperature variations inside the experimental hall are considered for this study. Here, the temperature might vary from 20°C to 22°C ($T = 21 \pm 1$°C) [161]. On the other hand the peak's position itself has an uncertainty of $\lambda = 431.1 \pm 0.8\,\text{nm}$ (see section 6.2.1). As the produced light is not mono-energetic but exhibits a narrow spectral profile (see section 6.2.1), an effective wavelength λ_{eff} for the whole spectral distribution can be calculated using equation (7.5). The uncertainty of this effective wavelength will be equal to the uncertainty of the peak's location. With the λ^4 dependency, equation (7.5) can also be used to calculate a resulting effective Rayleigh scattering length $L_{Ray,eff}$.

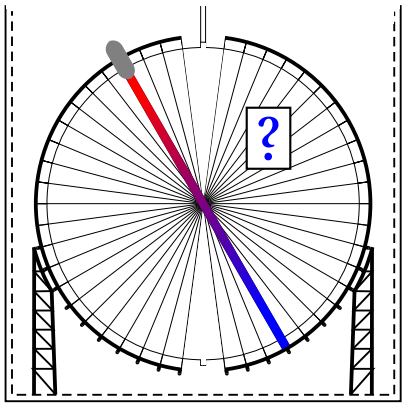

Fig. 7.22 Laser beam spectrum

$$\lambda_{eff} = \frac{\int_{\lambda_1}^{\lambda_2} I(\lambda) \cdot \lambda \, \mathrm{d}\lambda}{\int_{\lambda_1}^{\lambda_2} I(\lambda) \, \mathrm{d}\lambda} \quad \text{and} \quad L_{Ray,eff} = \frac{\int_{\lambda_1}^{\lambda_2} I(\lambda) \cdot L_{Ray} \mathrm{d}\lambda}{\int_{\lambda_1}^{\lambda_2} I(\lambda) \, \mathrm{d}\lambda} \tag{7.5}$$

Here, $I(\lambda)$ stands for the diode's intensity at a wavelength λ. The parameters λ_1 and λ_2 are integration limits with values of 350.0 nm and 510.0 nm, respectively. Slightly

[10] From 420.0 nm to 440.0 nm.

varying these integration limits had no impact on the results, as they are located in a spectral region where the diode emits no light.

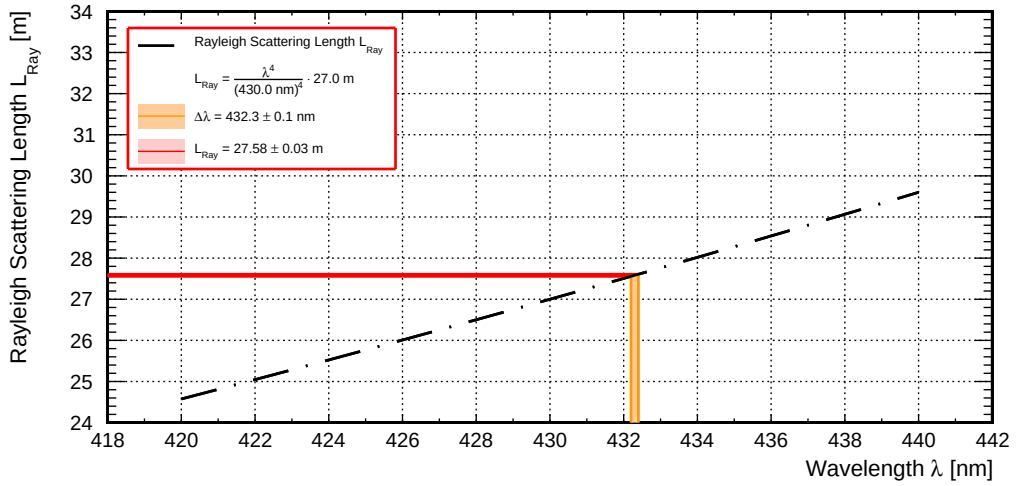

(a) Influence of the diode's temperature on L_{Ray}

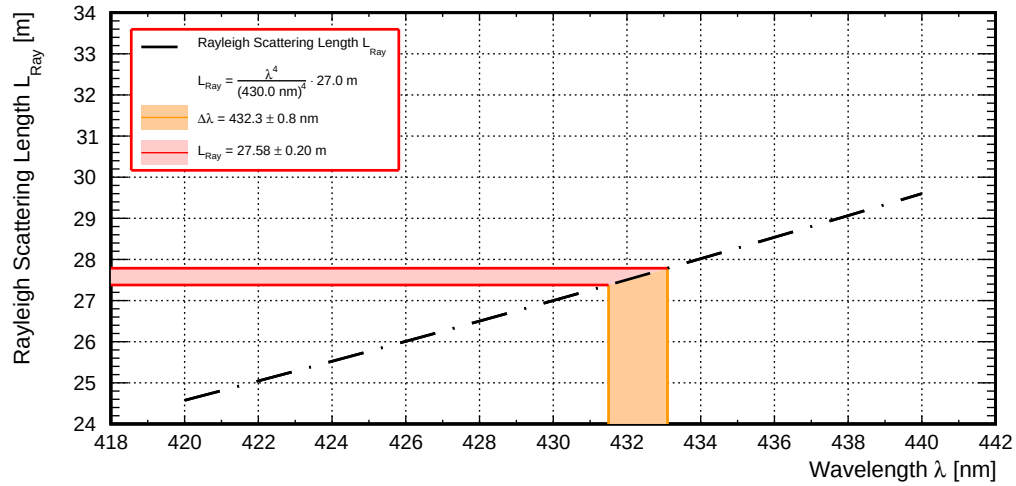

(b) Influence of the diode's spectral distribution on L_{Ray}

Fig. 7.23 Systematic uncertainty of L_{Ray} depending on laser spectrum

*The graphs show the **wavelength dependency** of L_{Ray} which is indicated by the **dashed, black line**. While figure 7.23(a) illustrates the uncertainty of the resulting L_{Ray} caused by a **fluctuating peak position** due to a varying diode temperature, figure 7.23(b) presents the uncertainty of L_{Ray} caused by the **uncertainty of the spectral peak position of the diode's emission profile**. In both cases the uncertainty region for the **wavelength and the Rayleigh scattering length** are colored **orange and red**, respectively.*

According to the emission profile of the laser diode, an effective wavelength of $\lambda_{eff} = 432.3 \pm 0.8\,\text{nm}$ could be calculated. For this study the typical λ^4 dependency was used to describe the behavior for the Rayleigh scattering length. Here, the

L_{Ray} value was set to 27.0 m at a wavelength $\lambda = 430$ nm. From reference [130] it is known that the position of the diode's emission peak varies by 0.1 nm per degree Celsius. Figure 7.23(a) shows the influence on the Rayleigh scattering length for the given temperature variation inside the experimental hall. The impact on L_{Ray} with a resulting uncertainty of ±3 cm seems to be rather small. For the attenuation length L an uncertainty of ±1 cm is expected if an absorption length of $L_a = 77.0$ m is assumed (see the corresponding graph in appendix B). In contrast to that, figure 7.23(b) illustrates the influence of the uncertainty of the emission peak's location itself. Here, the uncertainty of $\lambda = 432.3 \pm 0.8$ nm translates into an uncertainty of $\Delta L_{Ray} = \pm 0.20$ m. For L an uncertainty of $\Delta L = \pm 0.11$ m can be determined (see graph in appendix B).

In comparison to the other investigated systematics, the uncertainty of the spectral distribution of the laser diode shows the largest uncertainties of L_{Ray} and, therefore, of L_s and L as well. However, this uncertainty has only to be taken into account if an absolute measurement for the transparency of the LS is performed. For a relative measurement which compares the development of the LS transparency over time, this systematic contribution does not have to be taken into account, as it always influences the LS transparency in the same way.

7.3.5 Uncertainty Of The Water Transparency

The fifth systematic uncertainty is related to the transparency of the water inside the CD. As already shown in chapter 3, the acrylic sphere of the CD is submerged in water. According to the installation location of the FTH components, the laser beams of the AURORA system have to traverse this water buffer layer twice. The first time directly takes place after the light is decoupled from the fiber (GRIN lens). Here, the beam points to the detector center and has to overcome a distance of around 1.7 m. The photons have to propagate through water a second time when they leave the acrylic vessel again and strike the PMT array. Depending on their propagation direction relatively to the acrylic surface, a minimal distance of at least 1.7 m has to be covered. All in all, the photons have to travel through not less than 3.4 m of water. With an absorption length of around $L_a = 26.5 \pm 2.7$ m [87, 147], the water transparency is expected to be tolerably high. However, the influence of a minimal path length of 3.4 m in water might be not negligible anymore. In addition, with an uncertainty of approximately 10%, the given transparency values are only known to a certain point of accuracy. As a consequence, the impact of a wrongly assumed water transparency on the reconstructed values for L and L_s of the LS has to be investigated.

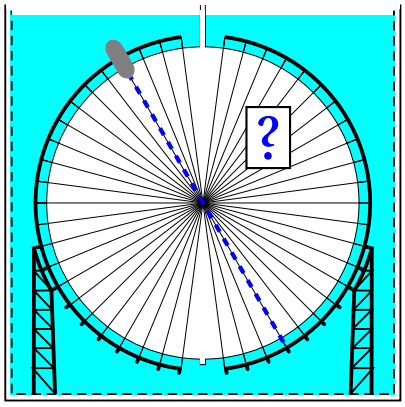

Fig. 7.24 Water transparency

In order to study this systematics several sample files with different water transparency values were created. For the attenuation and scattering length of the LS the standard Monte Carlo truth values of $L = 20.0$ m and $L_s = 30.0$ m were chosen. Afterwards, the analysis approach presented in section 7.1 was used to reconstruct the LS transparency. Figure 7.25 shows the results of the conducted study. With a statistical uncertainty of around ±4 cm, the error bars of the data points are very small. As a consequence, they are hidden behind the markers. The attenuation length does not show any large influence. Thus, the Monte Carlo truth always lies within the statistical uncertainty of each data point. However, a slightly larger variance can be identified in the region with an absorption length L_a <22.0 m. Above this value the water's transparency is already sufficiently high and only a moderate

fraction of traversing photons gets still absorbed. The scattering length shows a similar behavior. Nevertheless, for an absorption length of $L_a < 22.0\,\text{m}$, the Monte Carlo truth does not lie within the statistical uncertainty of each data point. The reconstructed values of the scattering length show a tendency to higher values.

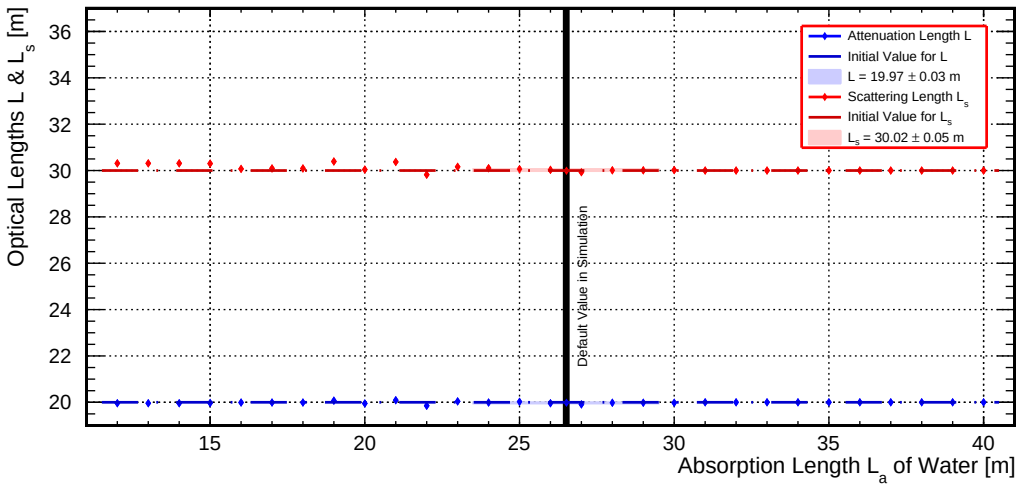

Fig. 7.25 Water transparency and its influence on L and L_s

*The graph shows the **results of the systematics study** regarding the **water transparency** inside the CD. Here, the value for the **absorption length** L_a **of water** was **varied between 12.0 m and 40.0 m**. The default value in the simulation is set to be 26.5 m (black bar). While the **blue data points** refer to the reconstructed **attenuation length** values, the **red data points** stand for the determined **scattering length** values. The **colored, dashed lines indicate the Monte Carlo truth** values.*

These results can be explained by the fact that the water transparency only influences the amount of photons which are entering the LS volume in the first place, and the amount of photons which are detected by the PMTs in the second place. The photon distribution itself will not change. Consequently, the decay constants τ_i of the data distribution describing fit functions are not influenced. Those parameters are basically determining the reconstructed values for the LS's attenuation length. In contrast to that, the absorption length of water primarily has an impact on the c_i parameters of the fit functions and, therefore, on the reconstructed values of the scattering length (see figure 7.3).

The measured absorption length L_a of water has an uncertainty of around 10% [87]. Hence, the 1σ fluctuation of the reconstructed values for L and L_s within a range between 24 m and 29 m can be used to derive a value for the systematic uncertainty regarding the water transparency. For the attenuation and scattering length a systematic uncertainty of ±3 cm and ±5 cm can be concluded.

7.3.6 Uncertainty Of The Acrylic Transparency

The sixth systematic uncertainty concerns the transparency of the acrylic sphere. Similar to the water buffer layer, AURORA's laser beams will have to traverse this medium twice during their propagation through the detector. This takes place for the first time when the photons are entering the LS volume. On their way out they travel through the acrylic vessel a second time. Even though the acrylic sheets have a thickness of only 12 cm, the absorption length of the acrylic is with $L_a = 4.0\,\text{m}$ [123, 147] already very small. As a consequence, small changes in the acrylic transparency might influence the results of the reconstructed values for the attenuation length L and scattering length L_s of the LS. In order to estimate the magnitude of this systematic uncertainty, the impact of the acrylic transparency on L and L_s has to be investigated.

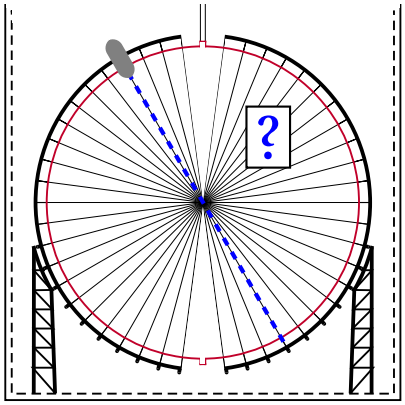

Fig. 7.26 Acrylic transparency

Similarly to the previous section, several sample files with different absorption length values for the acrylic were generated. Regarding the length, there is a variation from 2.0 m to 5.0 m. Subsequently, the previously described analysis approach of section 7.1 was used to determine the optical lengths L and L_s of the LS for each sample file. Figure 7.27 presents the results of the conducted study.

According to figure 7.27, the acrylic transparency exhibits a stronger influence on the results of the scattering length L_s than on the results of the attenuation length L. Below an absorption length $L_a = 3.6\,\text{m}$ the Monte Carlo truth does not lie within the statistical uncertainties of the reconstructed L_s values anymore. Instead, a continuously growing shift to higher reconstructed values can be observed when decreasing the acrylic transparency. For absorption length values above the default value of 4.0 m, a slight tendency to L_s values can be identified which are smaller than the Monte Carlo truth (0.3% effect). Furthermore, the Monte Carlo truth does not lie within the statistical uncertainty range of the L_s value for $L_a = 5.0\,\text{m}$ anymore. In comparison to that, the impact on the reconstructed attenuation length values becomes much smaller. Here, except for absorption length values $L_a < 2.4\,\text{m}$, the

Monte Carlo truth lies within the statistical uncertainty range of all other data points. For an absorption length $L_a < 2.4$ m, a shift of maximal 2.5% to values higher than the Monte Carlo truth can be observed.

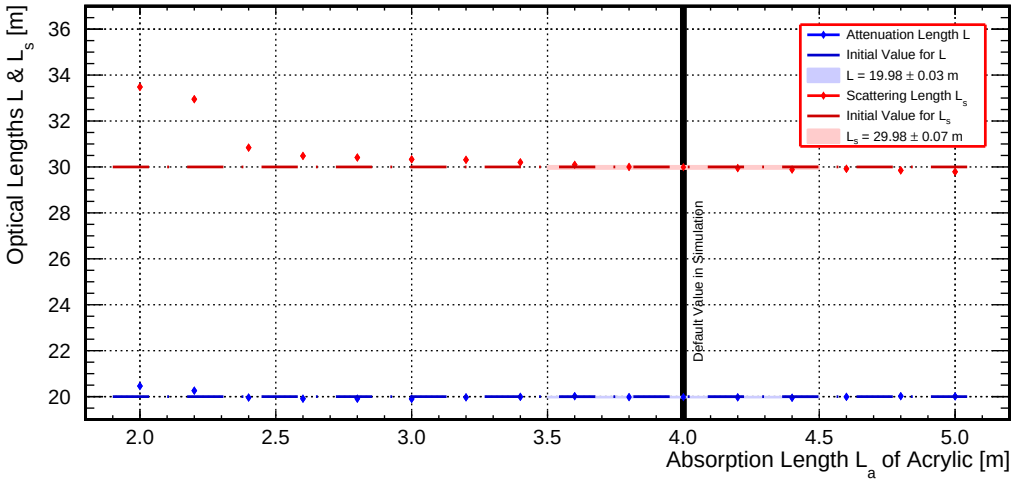

Fig. 7.27 Acrylic transparency and its influence on L and L_s

The graph presents the results of the study which investigates the ***systematic uncertainty*** *of the* ***acrylic transparency****. For the study, the* ***absorption length of the acrylic was varied between 2.0 m and 5.0 m****. The* ***default value*** *in the simulation is set to be* ***4.0 m*** *(black bar). The reconstructed values for the* ***attenuation length and scattering length*** *are indicated by the* ***blue and red markers****, respectively. According to this color code, the* ***dashed lines*** *show the values of the* ***Monte Carlo truth****.*

Similarly to the study in the previous section, a variance for the acrylic transparency will predominantly influence the amount of photons which are entering the LS volume on the one hand and the amount of photons which are successfully detected by the PMTs on the other hand. The relative PE distribution of the hit map pattern will not be influenced significantly. As before, this is the reason why the τ_i values of the fit functions are underlying only minor changes when varying the acrylic transparency value. Thus, the attenuation length values also do not alter. However, for really small transparency values, the c_3 dependency of the attenuation length L leads to shifted L values. The acrylic transparency directly influences the total amount of recorded PE and, therefore, the c_i parameters of the fit functions. Hence, the impact on the scattering length L_s becomes larger.

With an uncertainty of 10% [123], the systematic uncertainty caused by the acrylic transparency is given by the L and L_s fluctuation in the range of 3.6 m to 4.4 m. Figure 7.27 shows that the systematic uncertainties of the attenuation and scattering length are ±3 cm and ±7 cm, respectively.

7.3.7 Uncertainty Of The Target Material's Temperature

The seventh systematic uncertainty is related to the temperature of the LS inside the acrylic vessel. Here, the average temperature will be around $T = 21 \pm 1°C$ [161]. Even though the temperature fluctuation is expected to be rather small with $\pm 1°C$, the influence on the LS transparency might not be negligible anymore. Hence, the temperature dependencies of the absorption length L_a and scattering length L_s of the LS, which is basically composed of LAB, have to be checked. The AURORA laser operates at a wavelength of $\lambda = 430\,\text{nm}$. In this wavelength region, Rayleigh scattering is the most dominant scattering process (see chapter 4). As a consequence, focussing on the temperature dependency determined by the Rayleigh scattering length L_{Ray} will be sufficient for a reasonable estimate of the L_s temperature dependency. As previously mentioned, the systematic uncertainties of the attenuation length L and scattering length L_s were studied. In order to present a standardized report, equation (4.5) was used to calculate the uncertainty of L with the results of L_a and L_{Ray}.

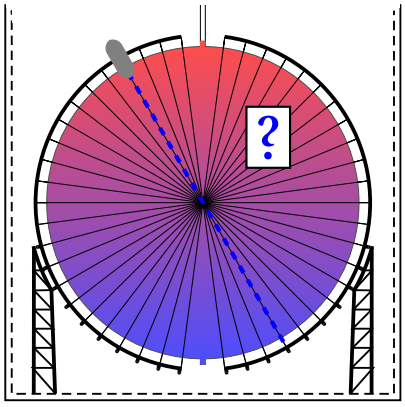

Fig. 7.28 LS temperature

According to the reference [166], the Rayleigh scattering length of condensed, isotropic liquids like LAB can be described by the following *Einstein-Smoluchowski-Cabannes* formula:

$$L_{Ray} = \left\{ \frac{8\pi^3}{3\lambda^4} \left[\frac{\left(n^2-1\right)\left(2n^2+0.8n\right)}{n^2+0.8n+1} \right]^2 \kappa_T k_B T \frac{6+3\delta}{6-7\delta} \right\}^{-1} \tag{7.6}$$

Here, π is just the mathematical constant, λ equals the wavelength of the photon with $\lambda = 430\,\text{nm}$ and k_T refers to the Boltzmann factor. All three parameters remain constant when varying the temperature. The parameter κ_T describes the isothermal compressibility of a liquid and generally exhibits a temperature dependency. However, due to the fact that the compressibility of a liquid does not dramatically alter for small temperature changes, this quantity is also treated as a constant with $\kappa_T = 7.743 \pm 0.035 \cdot 10^{-10}\,\text{Pa}^{-1}$ for LAB [166]. The factor δ stands for the depolarization ratio (see section 4.4) and was determined as $\delta = 0.31 \pm 0.04$ [166]. While T

refers to the liquid's temperature, n is the refractive index with $n = 1.49829 \pm 0.00026$ (for $\lambda = 430\,\text{nm}$) and exhibits a temperature dependency of less than 0.001 per degree Celsius [166]. With equation (7.6), the temperature dependency of L_{Ray} and, therefore, the temperature dependency of scattering length L_s can be determined. The absorption length L_a is assumed to scale with the density of a medium because the density determines the number of absorption centers in a given volume. Figure 7.29 presents the results of the conducted study.

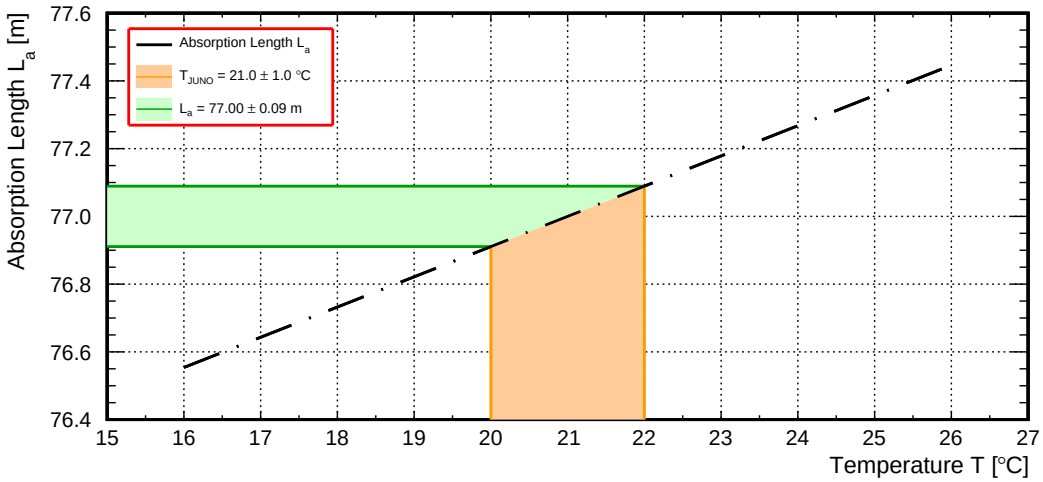

(a) Systematic uncertainty of the absorption length L_a

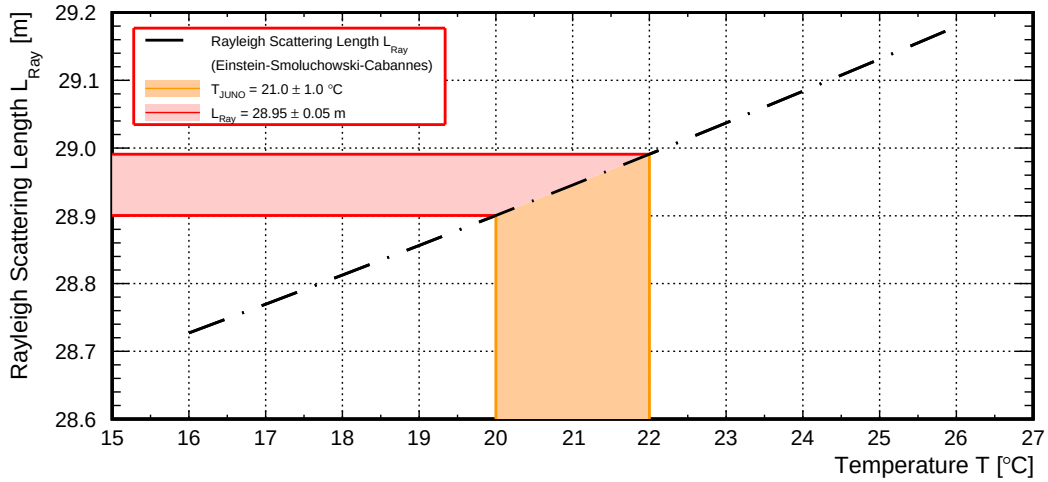

(b) Systematic uncertainty of the Rayleigh scattering length L_{Ray}

Fig. 7.29 Systematic uncertainty of L_a and L_{Ray} depending on the LS temperature

The two graphs visualize how the ***uncertainty of the LS temperature*** *(colored orange) translates into a* ***systematic uncertainty of the absorption length*** L_a *(colored green) and the* ***Rayleigh scattering length*** L_{Ray} *(colored red) of the LS. The* ***black, dashed lines*** *refer to the* ***theoretically predicted distribution*** *of* L_a *and* L_{Ray}*.*

Both graphs show a linear temperature dependency for L_a and L_{Ray} within the given temperature range. These translate into systematic uncertainties[11] of ±3 cm and ±5 cm for the attenuation length L and scattering length L_s, respectively.

[11] A toy Monte Carlo study showed that a gradient in the refractive index (caused by the temperature gradient) would lead to a displacement of the laser spot's position (bent beam trajectory) of less than 3 cm for a temperature gradient of 5°C. Therefore, this effect is deemed to be negligible.

7.3.8 Summary Of All Uncertainties

This section summarizes all studied uncertainties of the laser system AURORA. In addition, their determined values are listed in table 7.1 for a quick overview.

Uncertainty	Quantity	L	L_s
Statistical	-	$^{+4}_{-3}$ cm	$^{+4}_{-3}$ cm
Beam Intensity	$\Delta I = \pm 30\%$	< 3 cm	< 1 cm
Beam Alignment	$\theta < 4°$	< 4 cm	< 4 cm
Beam Aperture Angle*	$\Delta\alpha = \pm 0.05°$	< 1 cm	< 1 cm
Diode Temperature	$\Delta\mu = \pm 0.1$ nm	< 1 cm	< 3 cm
Emission Peak Position*	$\Delta\mu = \pm 0.8$ nm	± 11 cm	± 20 cm
Water Transparency	$\Delta L_a = \pm 10\%$	< 3 cm	± 5 cm
Acrylic Transparency	$\Delta L_a = \pm 10\%$	< 3 cm	± 7 cm
LS Temperature	$\Delta T = \pm 1°$C	< 3 cm	± 5 cm

Table 7.1 Summary of AURORA's uncertainties

*The table **lists all investigated statistical (red) and systematic (blue) uncertainties** of the developed laser system AURORA. While the **first column** lists the **names of the individual uncertainties**, the **second column** presents the **corresponding uncertainty ranges**. Here, the **uncertainties marked with the asterisk symbol *** always influence the optical lengths L and L_s in the same way and, therefore, **do not have to be considered when performing relative measurements** for L and L_s. The **third and fourth columns** present the **resulting uncertainties of the attenuation length** L **and the scattering length** L_s.*

The statistical uncertainty exhibits a typical $\sqrt{N}$ dependency for Poissonian processes with an absolute uncertainty of $^{+4}_{-3}$ cm for L and L_s for a measurement duration of 5 s. According to the $\sqrt{N}$ behavior, an absolute uncertainty value of around ± 1 cm for L and L_s can be achieved if the measurement time is increased to 50 s.

The systematic uncertainty which is related to the beam intensity was determined to be ± 3 cm and ± 1 cm for L and L_s, respectively. Here, a conservative estimate of 30% was used for the intensity uncertainty.

The beam alignment represents another systematic uncertainty. Here, both L and L_s exhibit an absolute uncertainty value of ± 4 cm. The tilt angle and, therefore, the misalignment was assumed to be $\theta < 4°$.

Another systematic uncertainty refers to the aperture angle of the laser beam. The conducted studies have shown that the reconstructed values of L and L_s are hardly affected by this parameter. This can be explained by the PE hit map patterns which show no significant changes in the considered PMT area for varying aperture angles of 0.0° to 1.0°. The uncertainty of L and L_s was estimated to be less than 1 cm.

A further systematic source arises from the spectral distribution of the laser beam. According to reference [130], the peak position should not change by more than 0.1 nm if the temperature fluctuations of the environment are not larger than ±1°C. The resulting uncertainty of a changing peak position was estimated to be less than 1 cm for the attenuation length L and less than 3 cm for the scattering length L_s. The overall uncertainty of the emission peak position leads to a systematic uncertainty of around ±11 cm and ±20 cm for L and L_s, respectively. Even though these uncertainties are large, they stay constant and, therefore, have only to be considered for absolute measurements.

The water transparency can influence the results of L and L_s as well. An uncertainty of the water transparency of 10% translates into a systematic uncertainty of ±3 cm and ±5 cm for L and L_s, respectively.

Similar to the water transparency, the acrylic transparency has an additional impact on the reconstructed L and L_s values. In this case, the transparency uncertainty of 10% translates into a systematic uncertainty of ±3 cm for L and ±7 cm for L_s.

According to [161], the temperature of the LS might fluctuate with an uncertainty range of ±1°C. This influences the LS transparency as well, resulting in a systematic uncertainty of ±3 cm and ±5 cm for L and L_s, respectively.

To determine the LS transparency, the PE hit map pattern of a measurement performed with AURORA is compared with several PE distributions of a lookup table that was generated with JUNO's official simulation framework `offline`. As a consequence, the Monte Carlo simulation is another source for a systematic uncertainty. Depending on the simulation's quality, this systematic effect might have a significant influence on the results for the optical lengths L, L_s and L_a. Unfortunately, without actual data from a measurement conducted with AURORA, it is difficult to quantify the impact of this systematic effect. However, on the one hand the Monte Carlo

simulation is already highly sophisticated providing an advanced optical model[12]. On the other hand the development of the Monte Carlo still continues and will lead to an ever more realistic simulation in the time to come. As a consequence, it is assumed that the contribution of the Monte Carlo to the overall systematic uncertainty is rather small being dominated by larger effects like the spectral distribution of the laser diode.

In case of an absolute measurement all listed uncertainties have to be considered. Here, the overall systematic uncertainty of L is ± 13 cm while the systematic uncertainty of L_s is ± 23 cm. For a relative measurement, systematic uncertainties do not have to be taken into account which always influence the results of L and L_s in the same way (aperture angle and spectral distribution). As a consequence, the overall systematic uncertainties of L and L_s reduce to ± 7 cm and ± 11 cm.

[12] A realistic model for the photon propagation inside the detector volume which includes optical processes like absorption, reemission and scattering of photons. In addition, wavelength dependencies and surface physics related processes like reflection and refraction are modeled as well.

Chapter 8

Conclusion And Outlook

One of the remaining secrets in neutrino physics is the question concerning whether the normal or inverted mass ordering is realized in nature. JUNO is one of the future experiments which will explore this sector in neutrino physics being currently built in South China. With a target mass of around 20 kt of LS, the spherical detector volume exhibits a diameter of 35.4 m. As a result, the JUNO detector is rather vast placing high demands on the LS transparency. Here, the attenuation length L must be at least 20 m at a wavelength of $\lambda = 430$ nm in order to meet the challenging requirement of a minimum energy resolution of 3% @ 1 MeV. Only with this resolution, JUNO will be able to reach a 3σ significance on the NMO within six years of data taking.

The laser calibration system AURORA that was developed in the course of this thesis will monitor the LS transparency to ensure that degradation in the target material, caused by accidental pollution incidents or general aging effects, is recognized as early as possible. Here, laser light is guided into the JUNO detector via an array of twelve different 100 m long fibers which can be individually controlled with an automated fiber switch. GRIN lenses are used to collimate the CD traversing laser beams underwater. A part of the light will be scattered or absorbed on its way through the detector center, leading to characteristic hit map patterns in the PMT array. A log-likelihood is then used to compare the results of the actual measurement with a MC-based lookup table (generated with JUNO's official simulation framework `offline`) to identify the true values of the attenuation length L and scattering length L_s and with these parameters the actual LS transparency.

In the first part of this thesis, the design, construction and performance of the AURORA components were presented. In general, AURORA can be divided into two different subsystems – the optical and the electro-mechanical system.
Firstly, I showed that the optical system creates light beams with well-defined properties, so that sufficient intensity is injected into the detector as adequately collimated, short laser pulses that do not pose a threat to the PMT array: Pulses of 10 μs duration containing one million photons will be injected at an operation frequency of 200 Hz. The overall uncertainty of the beam's intensity is less than 14% and the full aperture angle is less than 0.25°. Afterwards, I showed that the electro-mechanical system is able to adjust the laser beam direction by around 1° for both ϕ- and θ-direction. This provides the possibility to correct for a misalignment that might occur due to changes in geometry after the detector filling induced by buoyancy forces. Moreover, I presented the planned installation locations of the AURORA components as well as the design of the interface which connects the calibration system with the stainless steel latticed shell of the CD. Subsequently, I presented the results of the aging tests of AURORA's CD components. Each test indicated a sufficient durability for the corresponding material. Furthermore, I checked the contribution of AURORA's CD components to the overall radioactive background. None of the components significantly contribute to the maximally allowed budget. Finally, I presented a self-written `LabVIEW`-based software control which is fully functional and able to control all necessary hardware components in order to perform the transparency measurement.
In the scope of this thesis it was not yet possible to establish an `EPICS`-based two way communication between AURORA's software control and JUNO's detector control system. Besides the installation of the AURORA system, this is the only open task to be addressed in the next year. Otherwise, the AURORA system is completed and ready to be integrated into the JUNO detector.

The second part of this thesis focuses on AURORA's analysis approach, investigating the sensitivity as well as statistical and systematical uncertainties of the LS transparency parameters. I could show that AURORA is able to measure the attenuation length L and the scattering length L_s at the same time. For a 5 s run, I determined the statistical uncertainty of both the attenuation and scattering length to be $^{+0.04}_{-0.03}$ m. For a 50 s run, the statistical uncertainty is in the order of $\pm$0.01 m and, therefore, reaches already a relative uncertainty level of less than 0.1% assuming a value for $L = 20.0$ m and $L_s = 30.0$ m. In addition, I investigated several sources of systematic uncertainties. The uncertainties regarding the beam intensity, the beam alignment, the beam aperture angle and the diode's temperature were found to be negligibly

small. Moreover, the uncertainties of the water transparency, acrylic transparency and the LS temperature did not show any significant effect on the reconstructed value of the attenuation length L and only a minor effect on the scattering length L_s. The most dominant contribution to the overall systematic uncertainty comes from the spectral distribution of the laser and the related uncertainty of the effective wavelength of the laser light. I can conclude that the overall uncertainties of a conducted 5 s measurement for the attenuation L and scattering length L_s are $^{+0.04}_{-0.03}$ m (stat.) ± 0.13 m (sys.) and $^{+0.04}_{-0.03}$ m (stat.) ± 0.23 m (sys.), respectively. For a relative measurement that compares the development of the LS transparency over time, the systematic uncertainties regarding the aperture angle and the diode's spectral distribution do not have to be included, as those always influence the results of L and L_s in the same way. Consequently, the overall uncertainties of L and L_s reduce to $^{+0.04}_{-0.03}$ m (stat.) ± 0.07 m (sys.) and $^{+0.04}_{-0.03}$ m (stat.) ± 0.11 m (sys.), respectively. The dominant systematic uncertainty could be further reduced by replacing the current light source by one with an even more narrow spectral distribution.

Up to now, comparable transparency monitoring calibration systems in neutrino detectors aimed to measure predominantly the attenuation length. However, AURORA features the unique capability to determine both the attenuation and the scattering length of the target material at the same time with high precision. This offers a huge advantage compared to prior transparency monitoring systems, as the additional knowledge about the scattering length helps to understand how much light is really absorbed during its way through the detector directly influencing the energy resolution. Furthermore, the scattering length also has an impact on the spatial resolution. As a consequence, AURORA's output will provide a means to investigate the systematic uncertainty which arises from scattering inside the detector influencing event reconstruction algorithms. Finally, AURORA's output can be compared with the results of other calibration subsystems to cross-check the findings and to look for consistency.

Appendix A – Calculations

In the following appendix section the most important calculations and derived relations are presented in order to prove the correctness of various considerations which were made in this thesis.

Length Of The Lever Arm Of Force

This section refers to the length of the lever arm of force of the FTH in order to ensure a sufficiently large tilting angle of the laser beam.

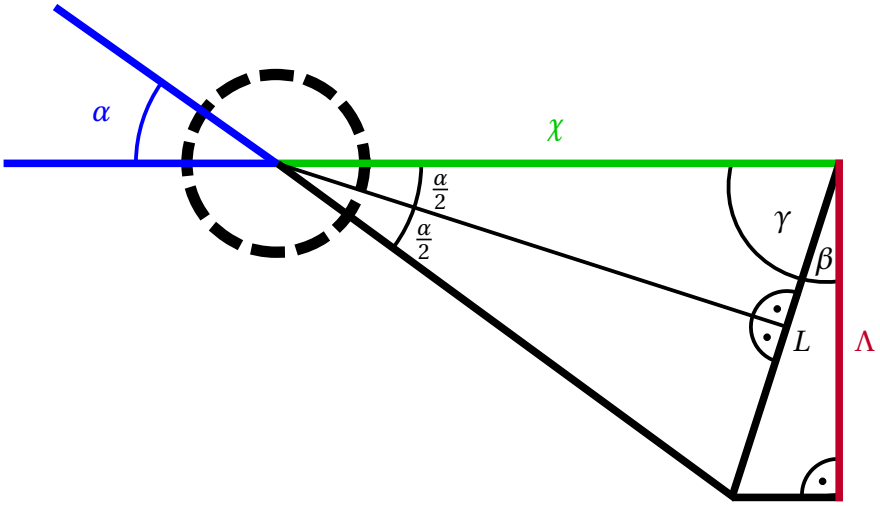

Fig. 1 Lever arm of force of the FTH

*The figure shows the **geometrical relation** between the **stroke** Λ of the piezoelectric crystal (**colored red**), the required length of the **lever arm of force** χ (**colored green**) of the FTH and the resulting **tilt angle** α (**colored blue**).*

The following calculation is valid for the rotational movement of the FTH in both directions, ϕ and θ, referring to a spherical coordinate system.

As shown in figure 1, it is possible to derive equation (1) to connect the length of the lever arm of force χ with the tilt angle α.

$$\sin\left(\frac{\alpha}{2}\right) = \frac{L/2}{\chi} \tag{1}$$

For the design of the fiber termination holder it is important to know how long the lever arm of force has to be to get a tilt angle of a desired size. In order to calculate χ, equation (1) has to be transposed leading to equation (2):

$$\chi = \frac{L}{2 \cdot \sin\left(\frac{\alpha}{2}\right)} \tag{2}$$

In addition to that, a relation between the length L and the stroke Λ of the piezoelectric crystal has to be found. From figure 1 equation (3) can be derived.

$$\cos\left(\beta\right) = \frac{\Lambda}{L} \tag{3}$$

Furthermore, the angle β should be replaced by an expression which only depends on the angle α. This relation between α and β can be derived from figure 1 as well.

$$\beta + \gamma = 90° \qquad \text{and} \qquad \frac{\alpha}{2} + \gamma = 90° \qquad \Rightarrow \qquad \beta = \frac{\alpha}{2}$$

Equation (3) can be rewritten resulting in formula (4).

$$\cos\left(\frac{\alpha}{2}\right) = \frac{\Lambda}{L} \tag{4}$$

Transposing equation (4) leads to formula (5).

$$L = \frac{\Lambda}{\cos\left(\frac{\alpha}{2}\right)} \tag{5}$$

If variable L in equation (2) is replaced by formula (5), an expression for the lever arm of force χ can be derived, only depending on the stroke Λ and the resulting tilt angle α.

$$\chi = \frac{\Lambda}{2 \cdot \sin\left(\frac{\alpha}{2}\right) \cdot \cos\left(\frac{\alpha}{2}\right)}$$

This expression can be simplified by using the following trigonometric relation taken from [29]:

$$\sin\left(2x\right) = 2\sin\left(x\right)\cos\left(x\right) \tag{6}$$

As a result, the final formula is the rather simple equation (7):

$$\chi = \frac{\Lambda}{\sin(\alpha)} \tag{7}$$

GRIN Lens Aperture Angle Measurement

The most important parameter of the GRIN lens is the aperture angle. Consequently, this property has to be accurately measured. Due to issues with waterproofness, the available beam profiler (CCD camera) is only working in air but not underwater. Thus, the following set-up, being illustrated in figure 2, was chosen to determine the GRIN lenses' aperture angle.

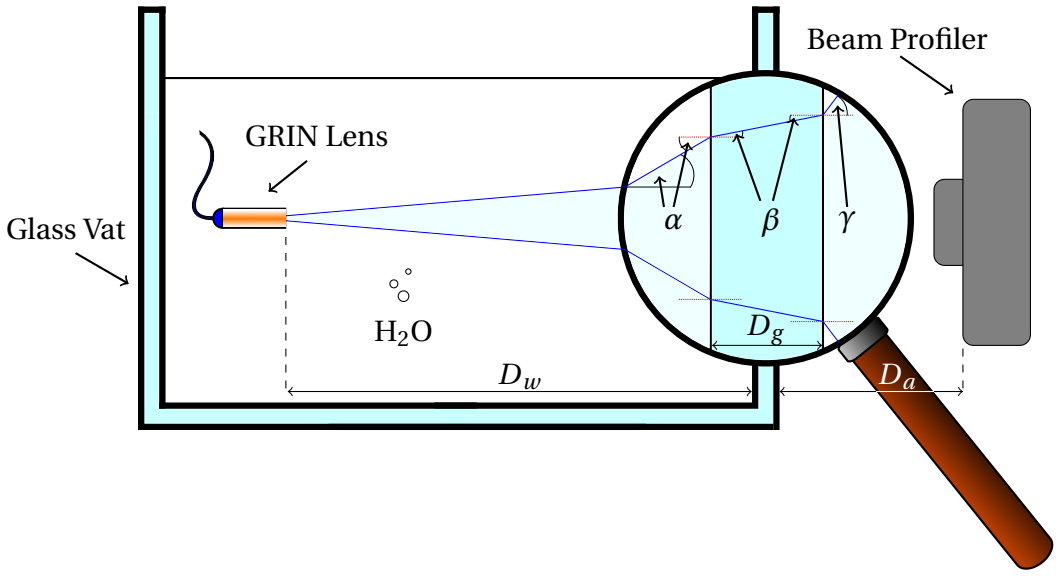

Fig. 2 Scheme of the aperture angle measurement set-up

*The figure illustrates the **experimental approach** to measure the **aperture angle of the GRIN lenses** underwater.*

Here, the laser light with a wavelength of $\lambda = 430\,\text{nm}$ is guided via an optical fiber to the GRIN lens. The laser light is decoupled from the GRIN lens and propagates through a glass vat filled with distilled water. The width of the laser spot is then measured outside the vat with the beam profiler for different path length D_w. The lengths D_g and D_a are not changed during the measurements. Because of refraction effects which occur at the transition surfaces between water & glass and glass & air, the aperture angle in air is different from the actual aperture angle in water.

In this section a relation between the aperture angle in water and the measured spot width in air is derived. Later on, this formula will be used to calculate the aperture angles only by knowing the distances D_w, D_g and D_a and the measured spot width s. The light beam propagation and the influence of the changing refractive indices are shown in figure 2 in more detail.

Following Snellius' law, α and the related beam angle in the glass vat β are satisfying equation (8).

$$n_w \cdot \sin(\alpha) = n_g \cdot \sin(\beta) \tag{8}$$

Here, n_w and n_g stand for the refractive indices of water and glass, respectively. Snellius' law is also valid for the relation between the beam angle β and the beam angle γ in air leading to equation (9).

$$n_g \cdot \sin(\beta) = n_a \cdot \sin(\gamma) \tag{9}$$

Here, n_a stands for the refractive index of air. Obviously, equation (8) and (9) can be set equal to each other resulting in the subsequent relation (10).

$$n_w \cdot \sin(\alpha) = n_a \cdot \sin(\gamma) \tag{10}$$

According to figure 2, the spot width s is given by three following vertical lengths satisfying trivial trigonometrical relations:

$$s = 2 \cdot \left[D_w \tan\alpha + D_g \tan\beta + D_a \tan\gamma \right] \tag{11}$$

Using equations (8) and (9), the beam angles β and γ can be replaced by the aperture angle α resulting in the final formula for the spot width s:

$$s = 2 \cdot \left[D_w \tan\alpha + D_g \tan\left(\sin^{-1}\left(\frac{n_w}{n_g} \sin\alpha \right) \right) + D_a \tan\left(\sin^{-1}\left(\frac{n_W}{n_a} \sin\alpha \right) \right) \right] \tag{12}$$

This formula is used in section 6.2.11 to calculate the aperture angle α and, therefore, the cone angle $\alpha^* = 2\alpha$. As equation (12) is difficult to transpose in order to directly calculate α, a series of values for α are inserted into equation (12) looking for the best matching spot width value. The same method is used to translate the uncertainty of s into an uncertainty of α.

Appendix B – Graphs

In the following appendix section the graphs are listed which could not be included in this thesis for space reasons and because of redundancy.

Characterization Of The PCI Board

Here, the graphs of the PCI board performance measurement are shown including all 32 analog and both digital channels.

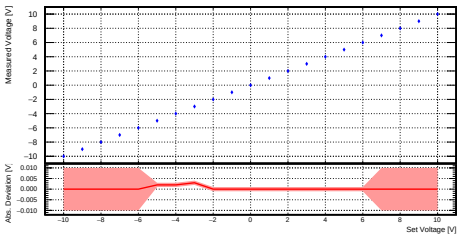

Analog channel 01

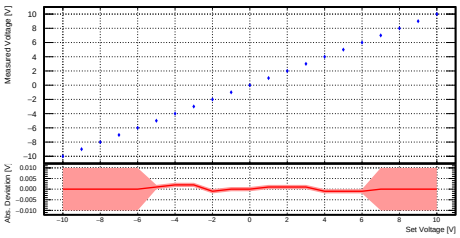

Analog channel 02

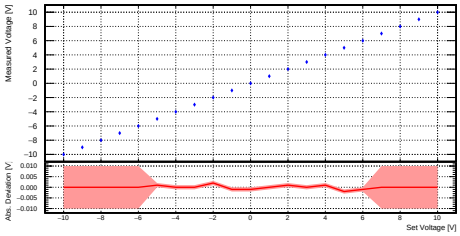

Analog channel 03

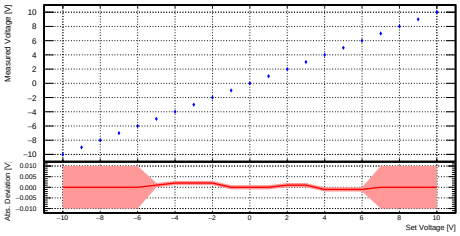

Analog channel 04

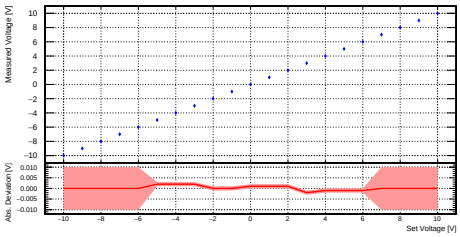

Analog channel 05

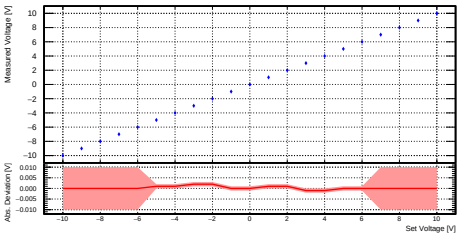

Analog channel 06

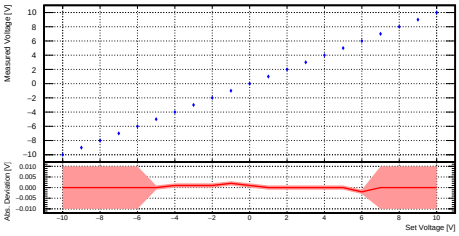

Analog channel 07

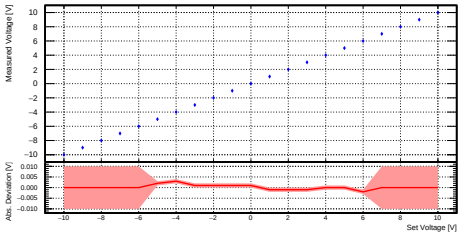

Analog channel 08

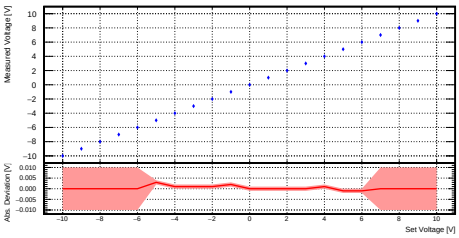

Analog channel 09

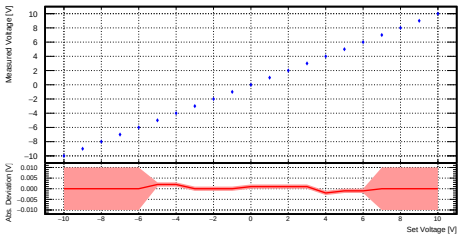

Analog channel 10

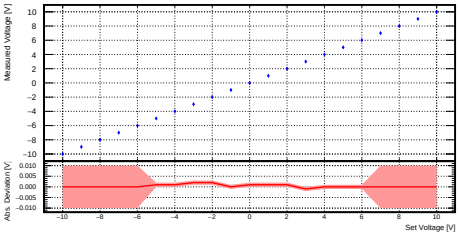

Analog channel 11

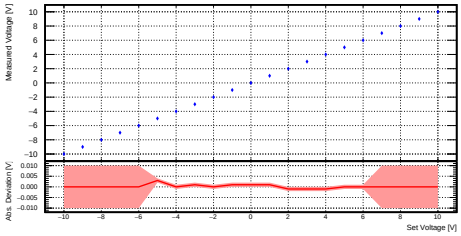

Analog channel 12

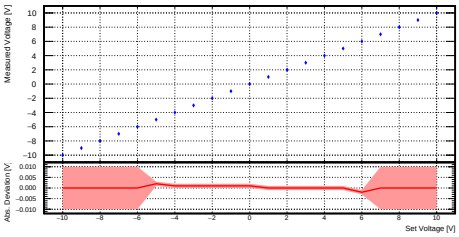

Analog channel 13

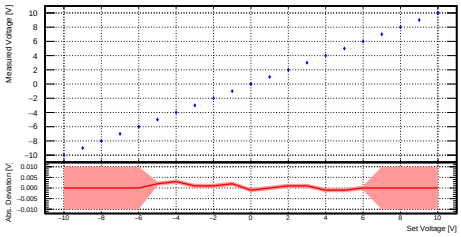

Analog channel 14

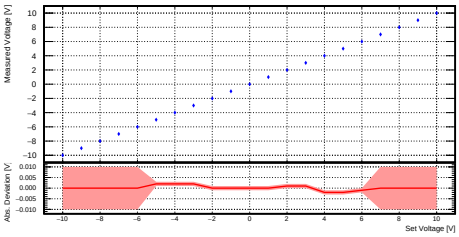

Analog channel 15

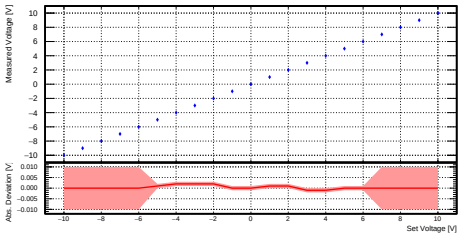

Analog channel 16

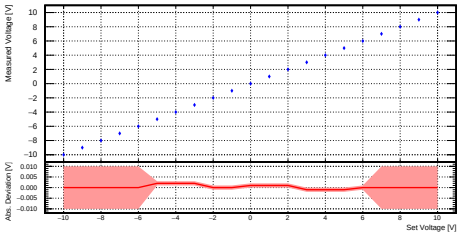

Analog channel 17

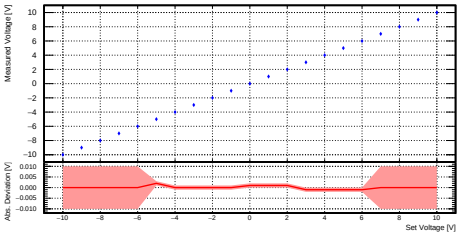

Analog channel 18

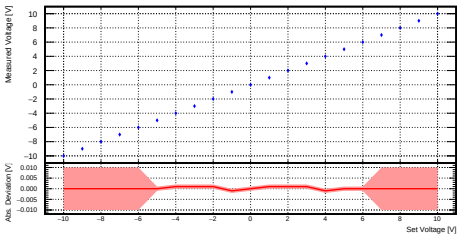

Analog channel 19

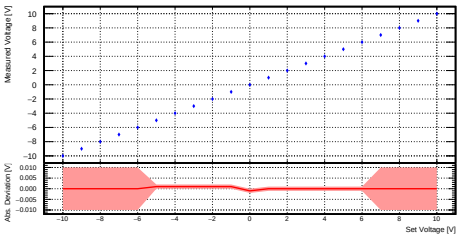

Analog channel 20

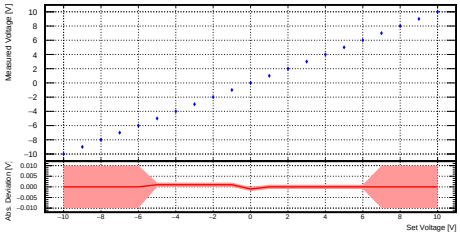

Analog channel 21

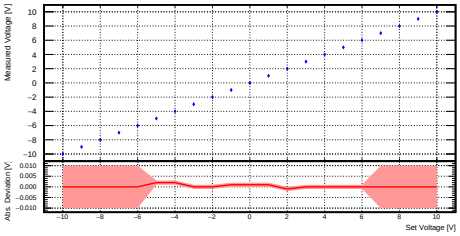

Analog channel 22

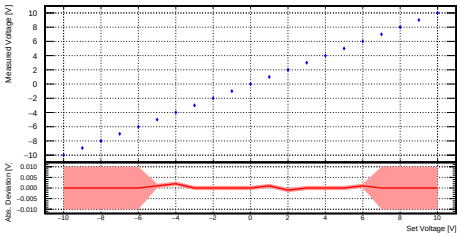

Analog channel 23

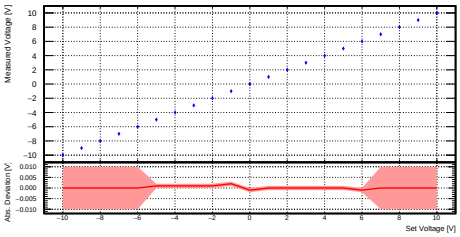

Analog channel 24

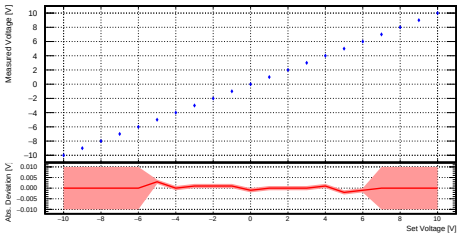

Analog channel 25

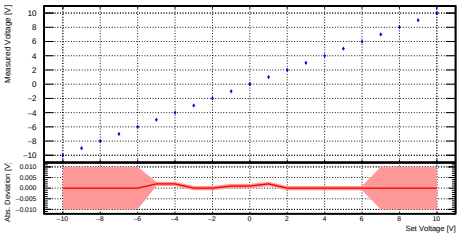

Analog channel 26

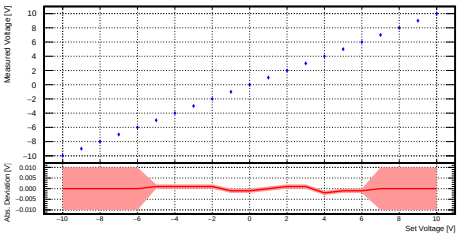

Analog channel 27

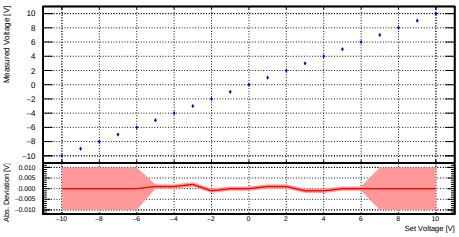

Analog channel 28

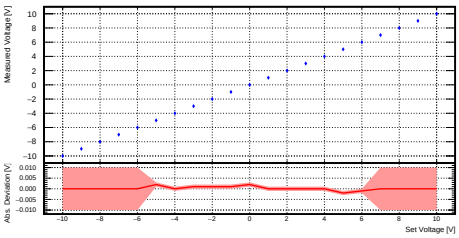

Analog channel 29

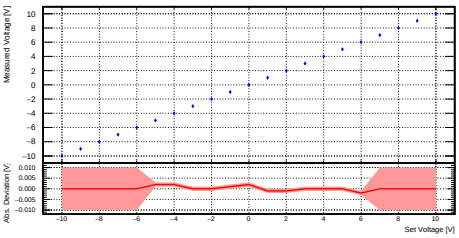

Analog channel 30

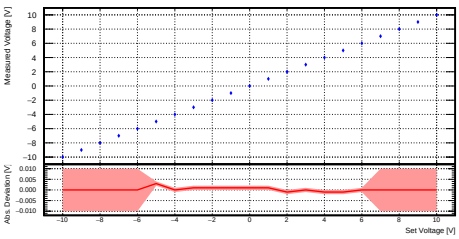

Analog channel 31

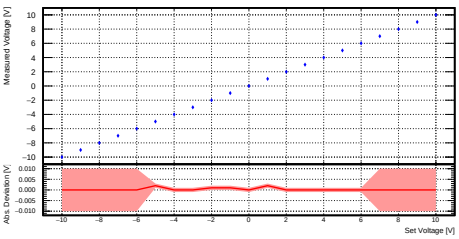

Analog channel 32

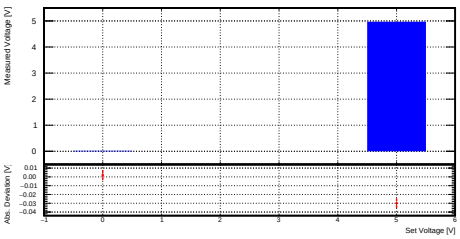

Digital channel 01

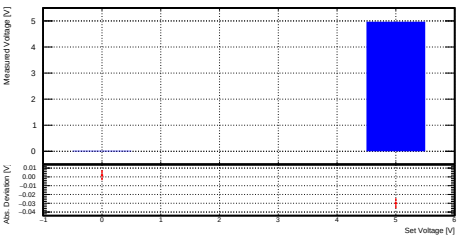

Digital channel 02

Characterization Of The Amplifier

Here, the graphs of the amplifier performance measurement are shown including all 32 analog and both digital channels.

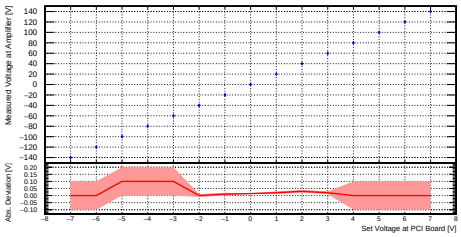

Analog channel 01

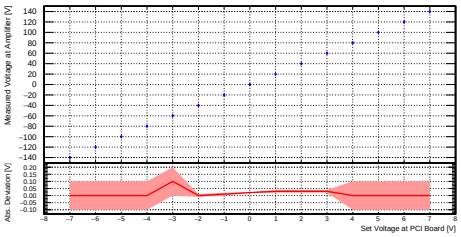

Analog channel 02

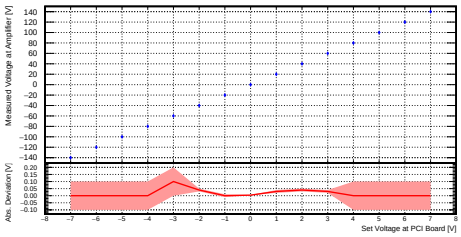

Analog channel 03

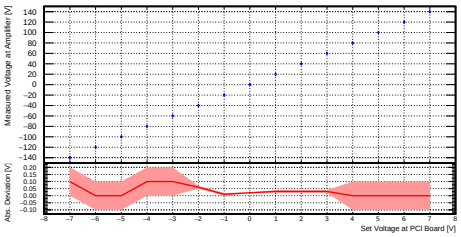

Analog channel 04

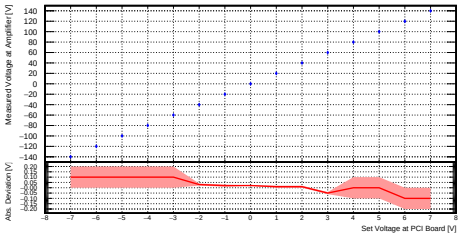

Analog channel 05

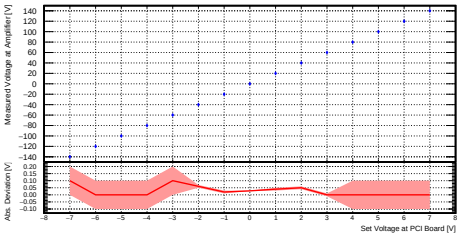

Analog channel 06

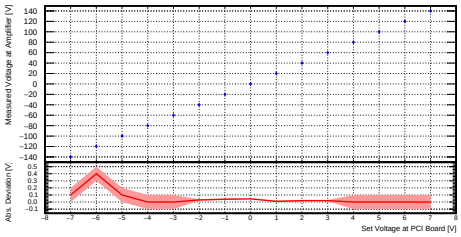

Analog channel 07

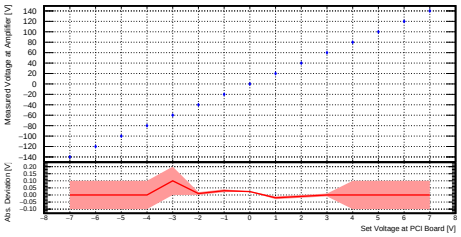

Analog channel 08

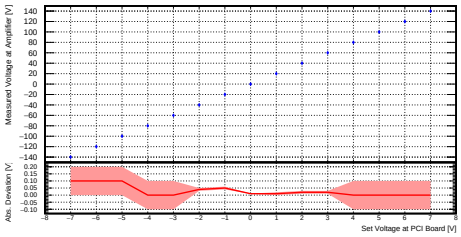

Analog channel 09

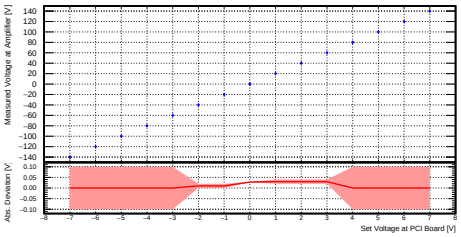

Analog channel 10

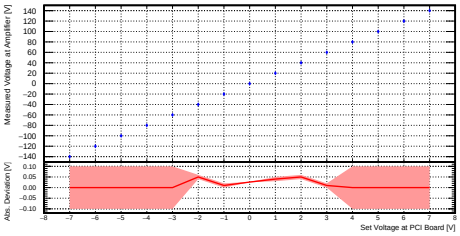

Analog channel 11

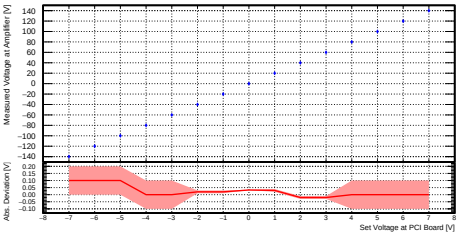

Analog channel 12

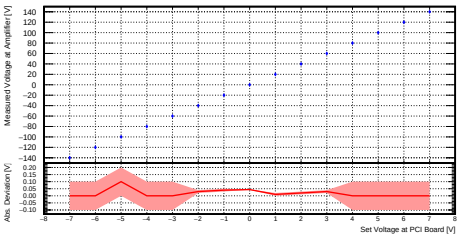

Analog channel 13

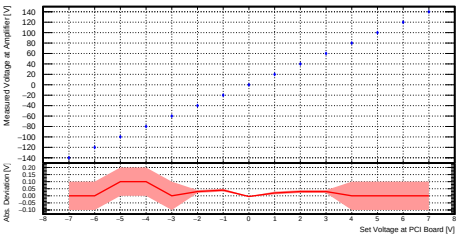

Analog channel 14

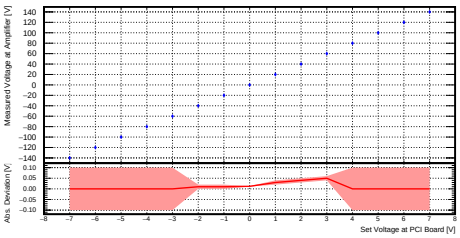

Analog channel 15

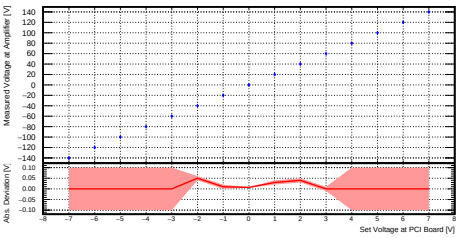

Analog channel 16

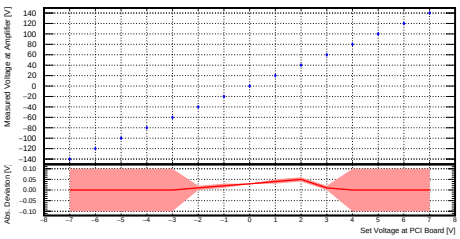

Analog channel 17

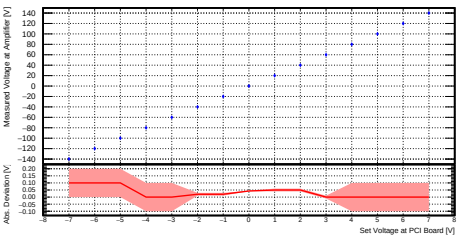

Analog channel 18

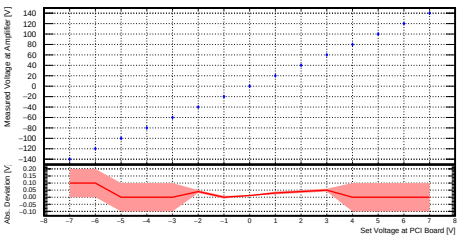

Analog channel 19

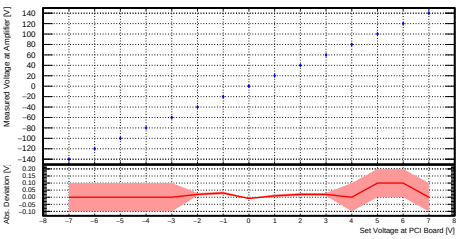

Analog channel 20

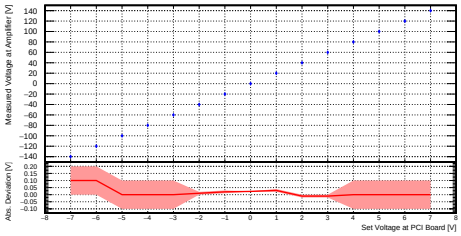

Analog channel 21

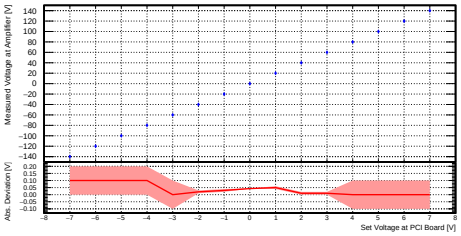

Analog channel 22

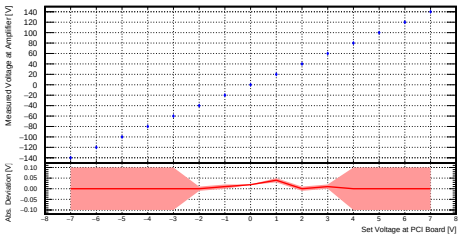

Analog channel 23

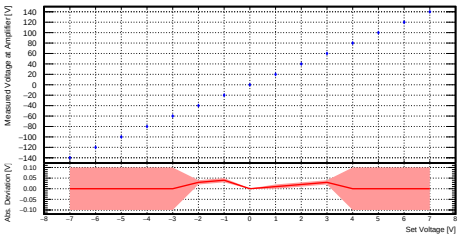

Analog channel 24

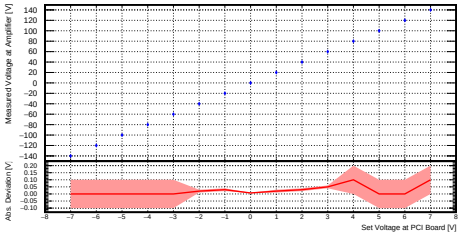

Analog channel 25

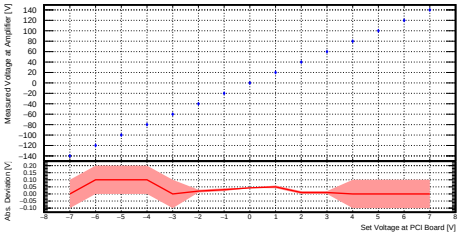

Analog channel 26

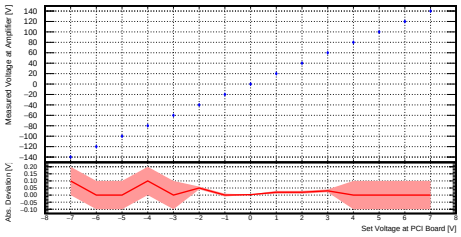

Analog channel 27

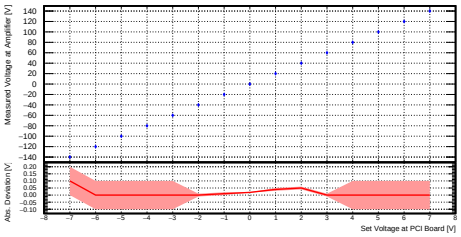

Analog channel 28

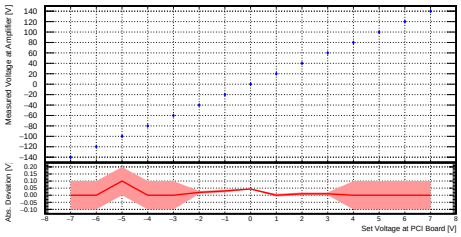

Analog channel 29

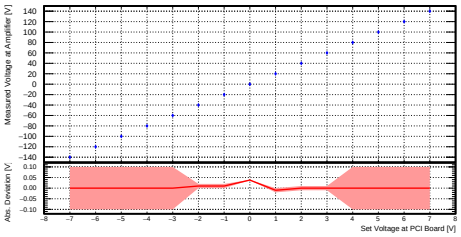

Analog channel 30

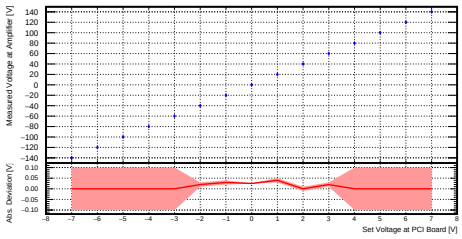

Analog channel 31

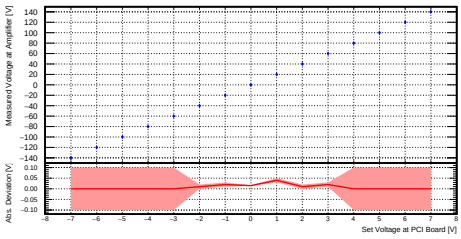

Analog channel 32

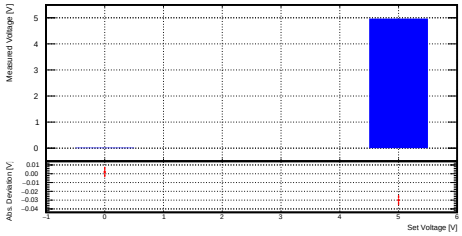

Digital channel 01

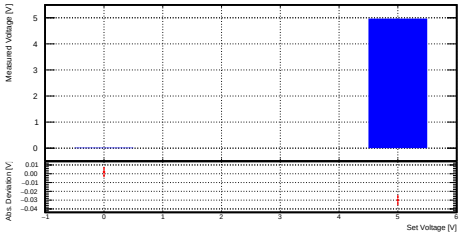

Digital channel 02

Systematic Uncertainty Of L & L_s – Tilted Laser Beam

Here, the graphs of the systematics study are shown regarding a tilted laser beam during the transparency measurements performed by AURORA.

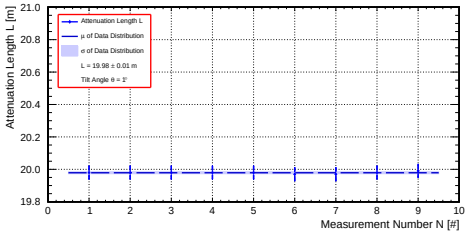

L shift for a tilt angle $\theta = 1°$

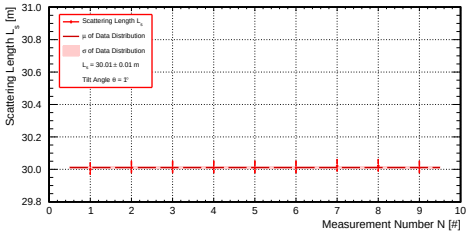

L_s shift for a tilt angle $\theta = 1°$

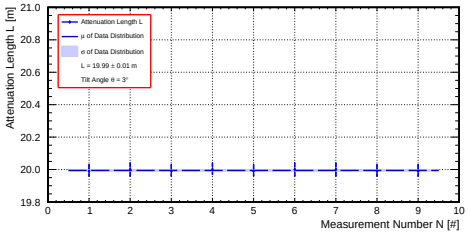

L shift for a tilt angle $\theta = 3°$

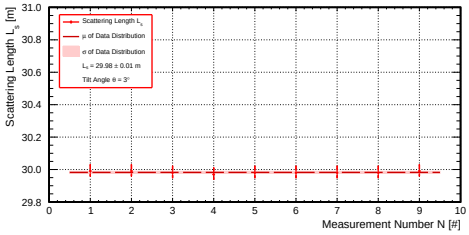

L_s shift for a tilt angle $\theta = 3°$

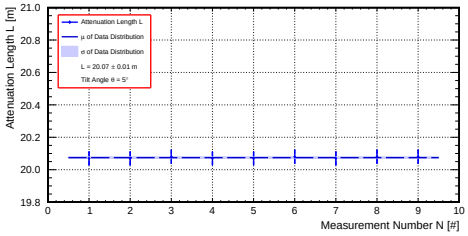

L shift for a tilt angle $\theta = 5°$

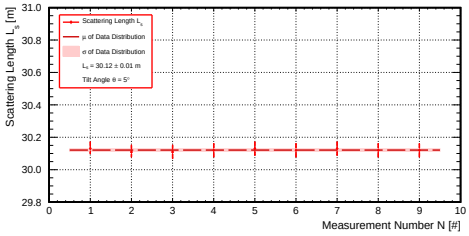

L_s shift for a tilt angle $\theta = 5°$

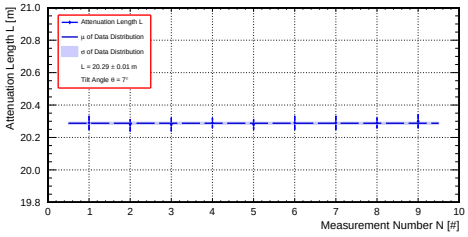

L shift for a tilt angle $\theta = 7°$

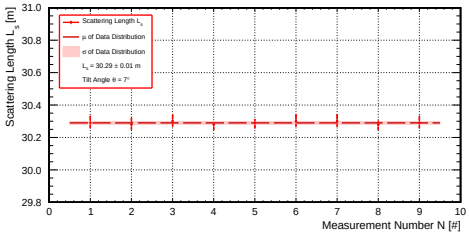

L_s shift for a tilt angle $\theta = 7°$

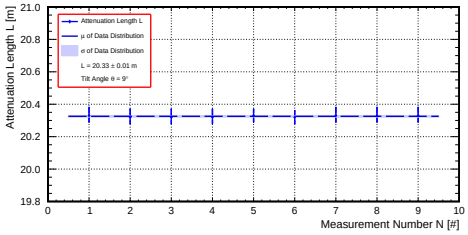

L shift for a tilt angle $\theta = 9°$

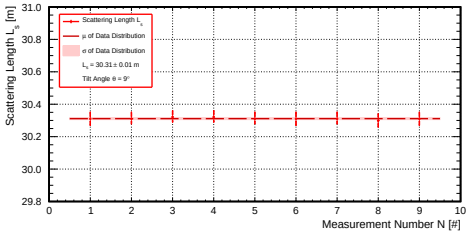

L_s shift for a tilt angle $\theta = 9°$

Systematic Uncertainty Of L – Laser Spectrum

Here, the graphs of the systematics study are shown regarding the spectral distribution of AURORA's laser diode.

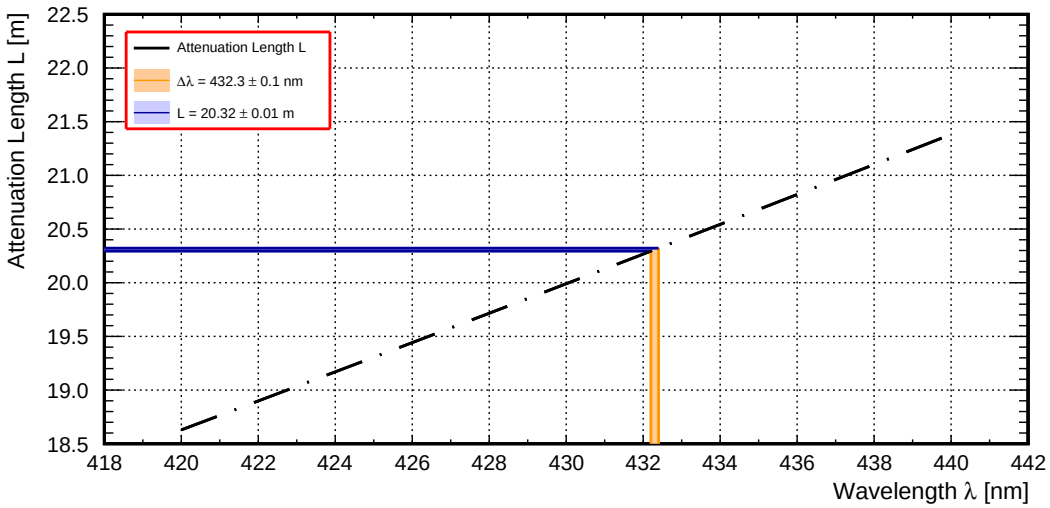

Influence of the diode's temperature on L

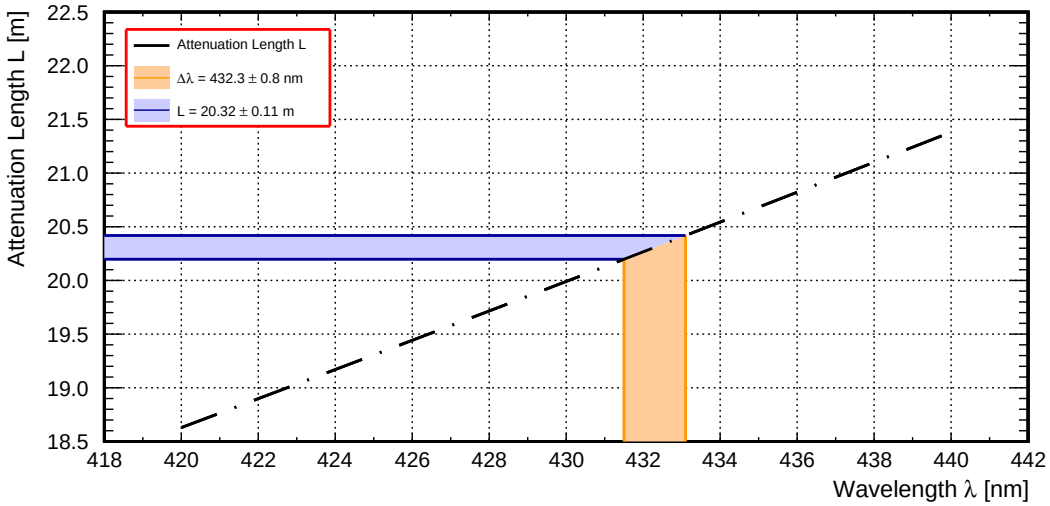

Influence of the diode's spectral distribution on L

GRIN Lens – Chromatic Aberration And g_0 Constant

The graph illustrates the wavelength dependency of the GRIN lens' chromatic aberration and gradient constant g_0. In addition, the gradient constant for a wavelength $\lambda = 430\,\text{nm}$ with a value of $g_0 = 0.096\,\text{mm}^{-1}$ is given as well. While the data of the chromatic aberration was extracted from reference [119], the distribution of the gradient constant was calculated with formulas from section 5.3.

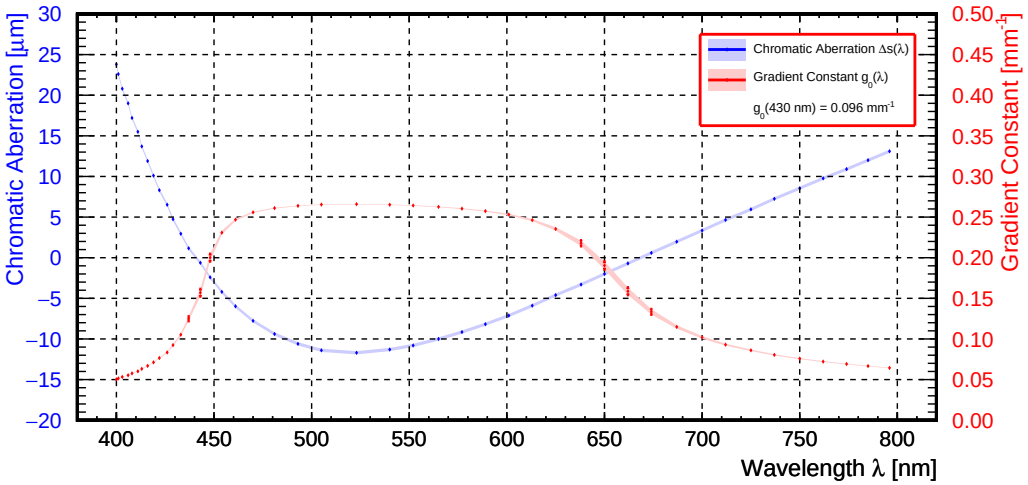

Wavelength dependency of chromatic aberration & gradient constant

GRIN Lens – Laser Beam Profile

The figure presents a typical beam profile of AURORA's laser beams. The figure on the top shows the cross section of the laser beam while the figures in the middle and at the bottom present the intensity distribution along a horizontal and vertical line through the spot's center.

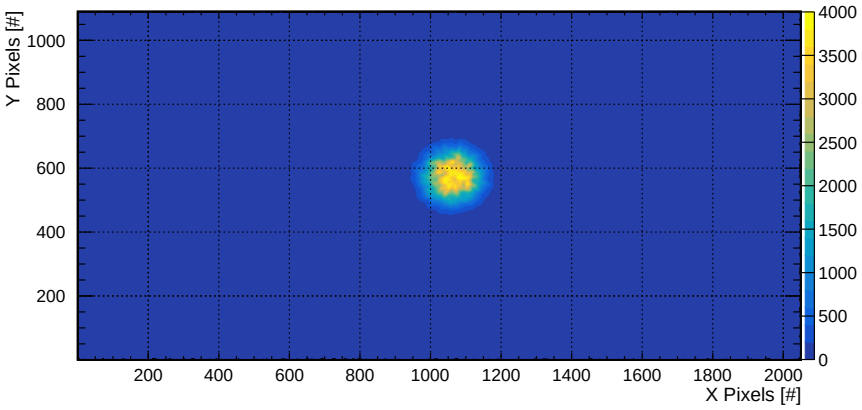

Cross section

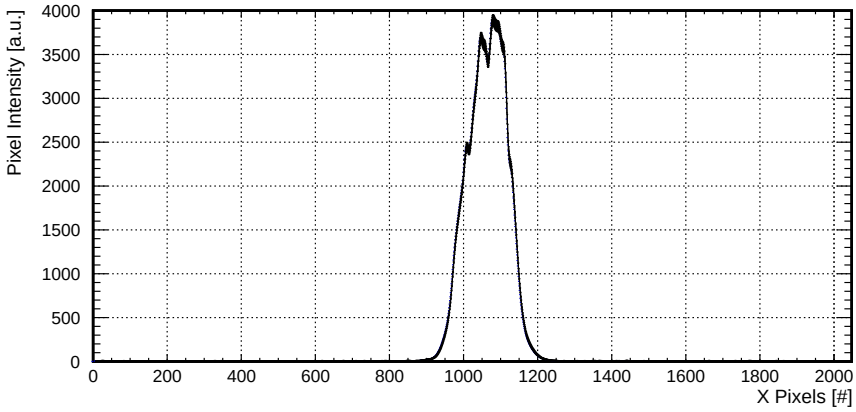

Horizontal Slice

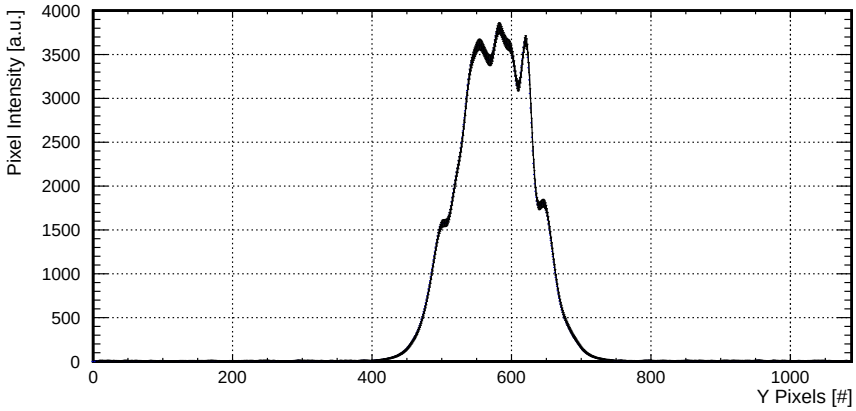

Vertical Slice

AURORA – Set-Up

This section shows a few pictures of the AURORA set-up. Here, the focus is on the non-CD components.

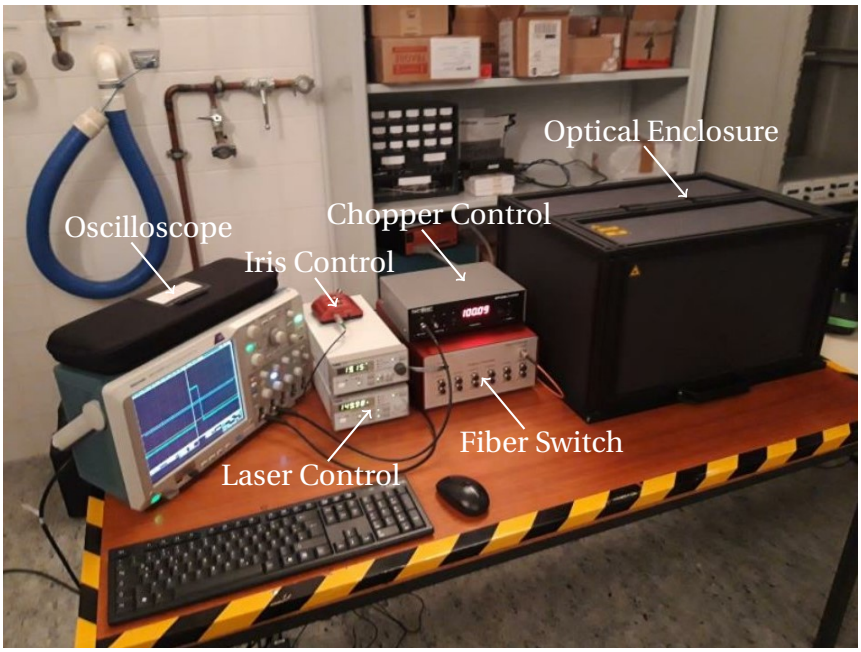

Non-CD components of the AURORA set-up

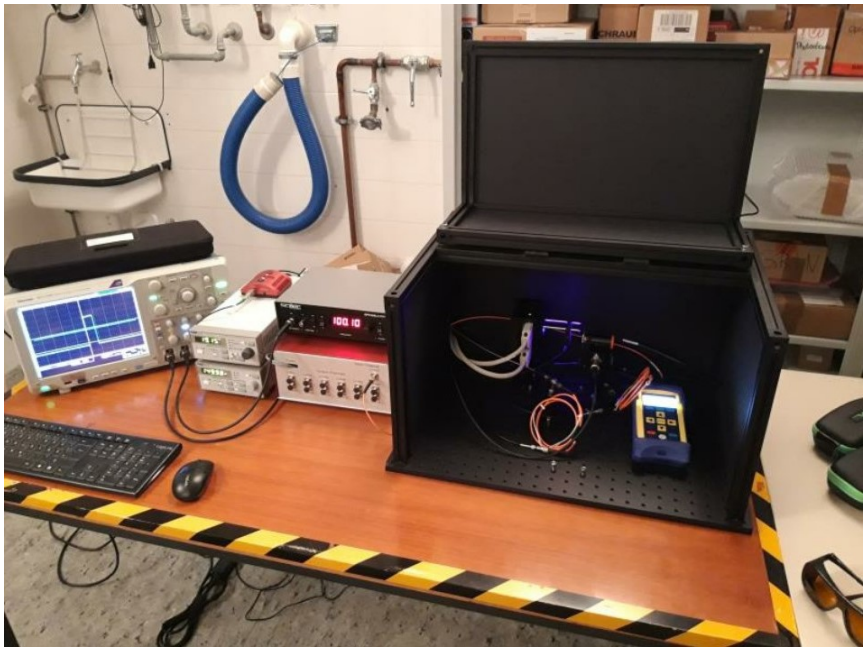

AURORA set-up with an opened optical enclosure

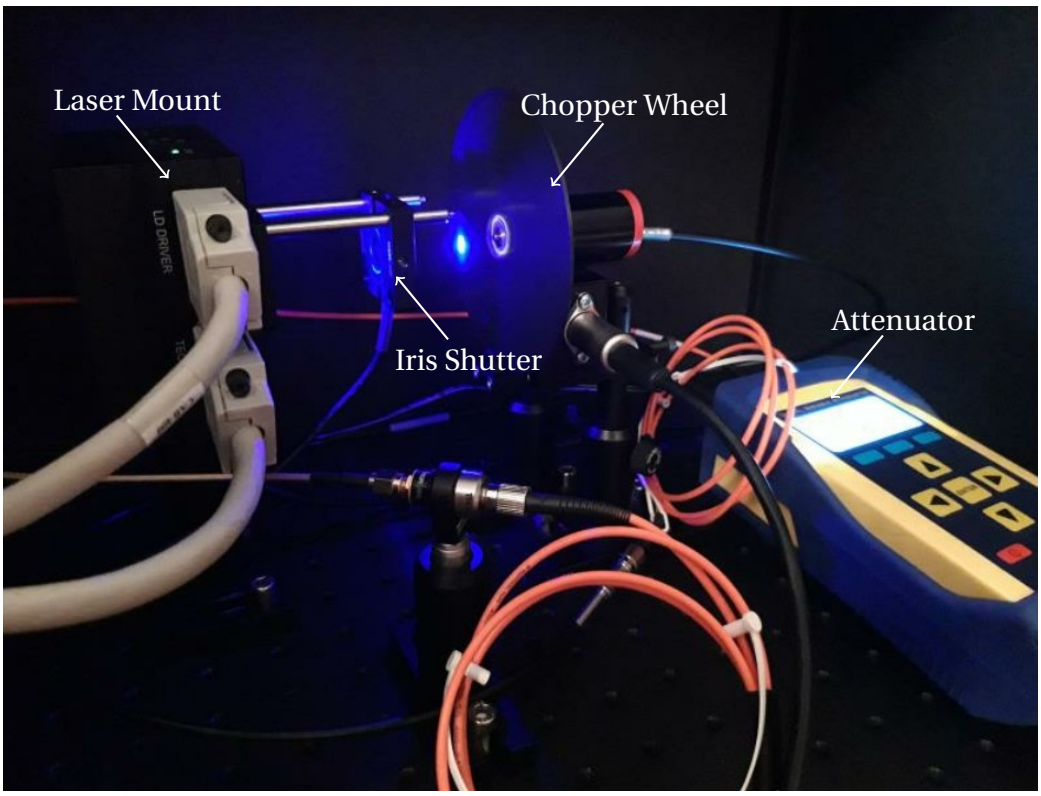

View on the inner life of the optical enclosure

Bibliography

[1] Aartsen, M. G. et al. (2014). Letter of Intent: The Precision IceCube Next Generation Upgrade (PINGU). arXiv:1401.2046 [physics.ins-det].

[2] Aartsen, M. G. et al. (2020a). Combined Sensitivity to the Neutrino Mass Ordering with JUNO, the IceCube Upgrade, and PINGU. *Phys. Rev. D*, 101:032006.

[3] Aartsen, M. G. et al. (2020b). Development of an Analysis to probe the Neutrino Mass Ordering with atmospheric Neutrinos using three Years of IceCube DeepCore Data. *The European Physical Journal C*, 80(1).

[4] Abazajian, K. et al. (2011). Cosmological and astrophysical Neutrino Mass Measurements. *Astroparticle Physics*, 35(4):177–184.

[5] Abe, K. et al. (2020). Constraint on the Matter-Antimatter Symmetry-Violating Phase in Neutrino Oscillations. *Nature*, 580(7803):339–344.

[6] Abi, B. et al. (2020a). Deep Underground Neutrino Experiment (DUNE), Far Detector Technical Design Report, Volume II DUNE Physics. arXiv:2002.03005 [hep-ex].

[7] Abi, B. et al. (2020b). Volume I. Introduction to DUNE. *JINST*, 15(08):T08008.

[8] Abusleme, A. et al. (2020). Optimization of the JUNO Liquid Scintillator Composition using a Daya Bay Antineutrino Detector. arXiv:2007.00314 [physics.ins-det].

[9] Acero, M. A. et al. (2019). First Measurement of Neutrino Oscillation Parameters using Neutrinos and Antineutrinos by NOvA. *Phys. Rev. Lett.*, 123:151803.

[10] Adam, T. et al. (2007). The OPERA Experiment Target Tracker. *Nuclear Instruments and Methods in Physics Research Section A: Accelerators, Spectrometers, Detectors and Associated Equipment*, 577(3):523–539.

[11] Agostini, M. et al. (2020). First Direct Experimental Evidence of CNO neutrinos. arXiv:2006.15115 [hep-ex].

[12] Aker, M. et al. (2019). Improved Upper Limit on the Neutrino Mass from a Direct Kinematic Method by KATRIN. *Phys. Rev. Lett.*, 123:221802.

[13] Akhmedov, E. K. (2011). Neutrino Oscillations: Theory and Phenomenology. *Nucl. Phys. Proc. Suppl.*, 221:19–25.

[14] Altmann, M. et al. (1998). *Proceedings of the Fourth SFB-375 Ringberg Workshop*. Sonderforschungsbereich 375, München. arXiv:9801320v1 [astro-ph].

[15] An, F. et al. (2016). Neutrino Physics with JUNO. *J. Phys.*, G43(3):030401.

[16] Ashtari Esfahani, A. et al. (2017). Project 8 Detector Upgrades for a Tritium Beta Decay Spectrum using Cyclotron Radiation. In *Proceedings, 27th International Conference on Neutrino Physics and Astrophysics (Neutrino 2016): London, United Kingdom, July 4-9, 2016*. arXiv:1703.05761 [physics.ins-det].

[17] Ashtari Esfahani, A. et al. (2019). Electron radiated Power in Cyclotron Radiation Emission Spectroscopy Experiments. *Phys. Rev.*, C99(5):055501.

[18] Bahcall, J. N., Murayama, H., and Pena-Garay, C. (2004). What Can We Learn from Neutrinoless Double Beta Decay Experiments? *Phys. Rev.*, D70:033012.

[19] Barger, V., Whisnant, K., Pakvasa, S., and Phillips, R. J. N. (1980). Matter Effects on Three-Neutrino Oscillations. *Phys. Rev. D*, 22:2718–2726.

[20] Beck, K. (2017). *SealActoren*. Email Exchange. Private Communication on the 13$^{\text{th}}$ of July 2017.

[21] Bergmann, L. (1937). *Schwingende Kristalle und ihre Anwendungen in der Hochfrequenz- und Ultraschalltechnik*. B. G. Teubner, Leipzig.

[22] Biller, S. D., Leming, E. J., and Paton, J. L. (2020). Slow Fluors for effective Separation of Cherenkov Light in Liquid Scintillators. *Nuclear Instruments and Methods in Physics Research Section A: Accelerators, Spectrometers, Detectors and Associated Equipment*, 972:164106.

[23] Birks, J. (1964). *The Theory and Practice of Scintillation Counting*. Macmillan, Frankfurt am Main, first edition.

[24] Bisping, D. (2010). *Wachstum und Charakterisierung von GaInNAs-basierenden Halbleiterstrukturen für Laseranwendungen in der optischen Telekommunikation*. PhD thesis, Julius-Maximilians-Universität, Fakultät für Physik & Astronomie, Würzburg.

[25] Bohren, C. and Huffman, D. R. (1998). *Absorption and Scattering of Light by Small Particles*. Wiley Science Paperback Series, Weinheim.

[26] Bonesini, M. et al. (2015). *Stokes-Shift engineered colloidal Quantum Dots as Wavelength Shifter for Detection of VUV Light in LAr and LXe Detectors*. European Physical Society Conference on High Energy Physics, https://indico.cern.ch/event/356420/contributions/1764078/attachments/1131644/1617612/Qdots.pdf. Visited on the 21$^{\text{st}}$ of July 2020.

[27] Born, M. (1943). *Optik – Ein Lehrbuch der elektromagnetischen Lichttheorie*. Springer, Berlin, third edition.

[28] Breitmaier, E. and Jung, G. (2014). *Organische Chemie, 7. vollst. Überarb. u. erw. Auflage 2012: Grundlagen,Verbindungsklassen, Reaktionen, Konzepte, Molekülstruktur, Naturstoffe, Syntheseplanung, Nachhaltigkeit*. DeL. Thieme.

[29] Bronstein, I. et al. (2006). *Taschenbuch der Mathematik*. Harri Deutsch Verlag, Frankfurt am Main, sixth edition.

[30] Cadonati, L. (2001). *The Borexino Solar Neutrino Experiment and its Scintillator Containment Vessel*. PhD thesis, Princeton University, Princeton.

[31] Cahn, R. N. et al. (2013). White Paper: Measuring the Neutrino Mass Hierarchy. In *Proceedings, 2013 Community Summer Study on the Future of U.S. Particle Physics: Snowmass on the Mississippi (CSS2013): Minneapolis, MN, USA, July 29-August 6, 2013*. arXiv:1307.5487 [hep-ex].

[32] Cao, D. et al. (2019a). Light Absorption Properties of the High Quality Linear Alkylbenzene for the JUNO Experiment. *Nucl. Instrum. Meth.*, A927:230–235.

[33] Cao, J. et al. (2019b). Towards the meV Limit of the effective Neutrino Mass in Neutrinoless Double-Beta Decays. arXiv:1908.08355 [hep-ph].

[34] Capozzi, F., Lisi, E., and Marrone, A. (2014). Neutrino Mass Hierarchy and Electron Neutrino Oscillation Parameters with one hundred thousand Reactor Events. *Phys. Rev. D*, 89:013001.

[35] Capozzi, F., Lisi, E., and Marrone, A. (2015). Neutrino Mass Hierarchy and Precision Physics with Medium-Baseline Reactors: Impact of Energy-Scale and Flux-Shape Uncertainties. *Phys. Rev. D*, 92:093011.

[36] Chadwick, J. (1914). Intensitätsverteilung im magnetischen Spectrum der β-Strahlen von Radium B + C. *Verhandl. Dtsc. Phys. Ges.*, 16:383.

[37] Chiu, S. H., Huang, C.-C., and Lai, K.-C. (2015). Signatures of the Neutrino Mass Hierarchy in Supernova Neutrinos. *PTEP*, 2015(6):063B01.

[38] Ciuffoli, E. et al. (2014). Advantages of Multiple Detectors for the Neutrino Mass Hierarchy Determination at Reactor Experiments. *Phys. Rev. D*, 89:073006.

[39] Daniels, G. et al. (2003). Resonance Energy Transfer: The Unified Theory Revisited. *The Journal of Chemical Physics*, 119:2264–2274.

[40] Dasgupta, B. et al. (2010). Neutrino Mass Hierarchy and Three-Flavor Spectral Splits of Supernova Neutrinos. *Physical Review D*, 81(9).

[41] De Salas, P. F. et al. (2018). Neutrino Mass Ordering from Oscillations and Beyond: 2018 Status and Future Prospects. *Frontiers in Astronomy and Space Sciences*, 5:36.

[42] Demtröder, W. (2008). *Experimentalphysik 2 – Elektrizität und Optik*. Springer, Heidelberg, seventh edition.

[43] Demtröder, W. (2016). *Experimentalphysik 3 – Atome, Moleküle und Festkörper*. Springer, Heidelberg, fifth edition.

[44] Demtröder, W. (2017). *Experimentalphysik 4 – Kern-, Teilchen- und Astrophysik*. Springer, Heidelberg, fifth edition.

[45] Dharmapalan, R. et al. (2012). Letter of Intent: A new Investigation of $\nu_\mu \rightarrow \nu_e$ Oscillations with improved Sensitivity in an enhanced MiniBooNE Experiment. arXiv:1210.2296 [hep-ex].

[46] Di Bari, P. (2019). Neutrino Masses, Leptogenesis and Dark Matter. In *Prospects in Neutrino Physics (NuPhys2018) London, United Kingdom, December 19-21, 2018*. arXiv:1904.11971 [hep-ph].

[47] Di Bari, P., Re Fiorentin, M., and Samanta, R. (2019). Representing Seesaw Neutrino Models and their Motion in Lepton Flavour Space. *JHEP*, 05:011.

[48] Diwan, M. V. et al. (2003). Very long Baseline Neutrino Oscillation Experiments for precise Measurements of Mixing Parameters and *CP* Violating Effects. *Phys. Rev. D*, 68:012002.

[49] Djurcic, Z. et al. (2015). JUNO Conceptual Design Report. arXiv:1508.07166v2 [physics.ins-det].

[50] Drexlin, G. et al. (2013). Current Direct Neutrino Mass Experiments. *Advances in High Energy Physics*, 2013.

[51] Duan, H., Fuller, G. M., and Qian, Y.-Z. (2010). Collective Neutrino Oscillations. *Annual Review of Nuclear and Particle Science*, 60(1):569–594.

[52] Esteban, I. et al. (2019). Global Analysis of Three-Flavour Neutrino Oscillations: Synergies and Tensions in the Determination of θ_{23}, δ_{CP}, and the Mass Ordering. *Journal of High Energy Physics*, 2019(1).

[53] Fang, D. and Li, C. (1999). Nonlinear electric-mechanical Behavior of a soft PZT-51 ferroelectric Ceramic. *Journal of Materials Science*, 34(16):4001–4010.

[54] Fermilab and U.S. Department of Energy, O. o. S. (2020). *Building an Inernational Flagship Neutrino Experiment – DUNE Fact Sheet*. Website, https://news.fnal.gov/wp-content/uploads/dune-fact-sheet.pdf. Visited on the 21st of June 2020.

[55] Fink, G. and Brintzinger, H.-H. (2006). Polymerization Reactions. In Chiusoli, G. P. and Maitlis, P. M., editors, *Metal-catalysis in Industrial Organic Processes*, pages 218–254. Royal Society of Chemistry, Cambridge.

[56] Forero, D. V., Hawkins, R., and Huber, P. (2017). The Benefits of a Near Detector for JUNO. arXiv:1710.07378 [hep-ph].

[57] Fukugita, M. and Yanagida, T. (1986). Barygenesis without Grand Unification. *Physics Letters B*, 174(1):45–47.

[58] Gando, A. et al. (2016). Search for Majorana Neutrinos near the inverted Mass Hierarchy Region with KamLAND-Zen. *Phys. Rev. Lett.*, 117(8):082503.

[59] Gillen, K. T. et al. (1997). Extrapolation of accelerated Aging Data – Arrhenius or Erroneous? *Trends in Polymer Science*, 5(8):250–257.

[60] Gispert, J. R. (2008). *Coordination Chemsitry*. Wiley-VCH, Weinheim, first edition.

[61] Gomez-Reino, C. et al. (2008). Design of GRIN optical Components for Coupling and Interconnects. *Laser & Photonics Reviews*, 2:203–215.

[62] Gomez-Reino, C., Perez, M. V., and Bao, C. (2002). *Gradient-Index Optics – Fundamentals and Applications*. Springer, Berlin, first edition.

[63] Gough, D. O. (2019). Anticipating the Sun's Heavy-Element Abundance. *Monthly Notices of the Royal Astronomical Society: Letters*, 485(1):L114–L115.

[64] Gropp, S. (2017). *100 m Optical Fibers for 50 mW Laser at a wavelength of 430 nm*. Leoni AG. Technical Drawing.

[65] Hackspacher, P. C. (2014). Studies of Light Quenching Effects in Liquid Scintillators and Parameter Determination of the Buffer and Veto Fluids of the Double Chooz Near Detector. Master's Thesis, Techn. Univ., München.

[66] Hackspacher, P. C. (2020a). *Differential Cross Section of various Scattering Processes*. Poster. Private Communication on the 11th of March 2020.

[67] Hackspacher, P. C. (2020b). *Scintillator Spectra*. Email Exchange. Private Communication on the 28th of July 2020.

[68] Hagiwara, K. et al. (2019). Gamma Ray Spectrum from Thermal Neutron Capture on Gadolinium-157. *PTEP*, 2019(2):023D01.

[69] Heng, Y. et al. (2018). *Standard Slides about Detector Design for Conferences*. JUNO DocDB, https://juno.ihep.ac.cn/cgi-bin/Dev_DocDB/ShowDocument?docid=1468. ID: 1468, v15.

[70] Hernandez Cabezudo, A., Parke, S. J., and Seo, S.-H. (2019). Constraint on the Solar Δm^2 Using 4000 Days of short Baseline Reactor Neutrino Data. *Phys. Rev. D*, 100:113008.

[71] Hubbel, J. H. (1969). *Photon Cross Sections, Attenuation Coefficients, and Energy Absorption Coefficients from 10 keV to 100 GeV*. NSRDS, Washington, DC.

[72] Hubbell, J. H. (2006). Review and History of Photon Cross Section Calculations. *Physics in Medicine and Biology*, 51(13):R245–R262.

[73] ICRU (2016). Report 90. *Journal of the International Commission on Radiation Units and Measurements*, 14(1):NP–NP.

[74] Igor Medintz, N. H. (2013). *FRET – Förster Resonance Energy Transfer, From Theory to Applications*. Wiley-VCH, Weinheim, first edition.

[75] Jang, S., Newton, M. D., and Silbey, R. J. (2004). Multichromophoric Förster Resonance Energy Transfer. *Phys. Rev. Lett.*, 92:218301.

[76] Jensen, C. (2000). *Controversy and Consensus: NuclearBetaDecay 1911-1934*. Birkhäuser Verlag, Berlin, first edition.

[77] Jing, X. (2018). *Installation of PMT Module*. JUNO DocDB, https://juno.ihep.ac.cn/cgi-bin/Dev_DocDB/ShowDocument?docid=3614. ID: 3614, v3.

[78] Kapon, E. (1999). *Semiconductor Lasers I: Fundamentals*. Optics and Photonics. Elsevier Science, London.

[79] Knoch, M. (2019). *Stainless Steel Components of hermetically sealed Piezoceramic Actuators*. Email Exchange. Private Communication on the 27th of November 2019.

[80] Konetschny, W. and Kummer, W. (1977). Nonconservation of total Lepton Number with Scalar Bosons. *Physics Letters B*, 70(4):433–435.

[81] Kurt, H. et al. (2017). Conformation-mediated Förster Resonance Energy Transfer (FRET) in blue-emitting Polyvinylpyrrolidone (PVP)-passivated Zinc Oxide (ZnO) Nanoparticles. *Journal of Colloid and Interface Science*, 488:348–355.

[82] Leo, D. W. R. (1994). *Techniques for Nuclear and Particle Physics Experiments*. Springer, Heidelberg, second edition.

[83] Lesgourgues, J. and Pastor, S. (2012). Neutrino Mass from Cosmology. *Adv. High Energy Phys.*, 2012:608515.

[84] Li, X. (2019). *Underground Facility Drawing*. JUNO EngDB, https://juno.ihep.ac.cn/cgi-bin/Eng_DocDB/ShowDocument?docid=5. ID: 5, v3.

[85] Liu, Q. et al. (2015). Rayleigh Scattering and Depolarization Ratio in Linear Alkylbenzene. *Nucl. Instrum. Meth.*, A795:284–287.

[86] Lombardi, P. et al. (2019). Distillation and Stripping Pilot Plants for the JUNO Neutrino Detector: Design, Operations and Reliability. *Nucl. Instrum. Meth.*, A925:6–17.

[87] Lu, H. (2020). *Water Transparency*. Email Exchange. Private Communication on the 4th of July 2020.

[88] Luo, W. et al. (2018). Quenching of Fluorescence for Linear Alkylbenzene. arXiv:1801.04432 [physics.ins-det].

[89] Lychkovskiy, O. V. (2009). Neutrino Oscillations: Deriving the Plane-Wave Approximation in the Wave-Packet Approach. *Physics of Atomic Nuclei*, 72(9):1557–1559.

[90] Marrodán Undagoitia, T. (2008). *Measurement of Light Emission in organic Liquid Scintillators and Studies towards the Search for Proton Decay in the future large-scale Detector LENA*. PhD thesis, Techn. Univ., München.

[91] Mason, W. P. (1950). *Piezoelectric Crystals and their Application to Ultrasonics*. D. Van Nostrand Company, Inc., New York.

[92] McIntyre, J. (2005). *Synthetic Fibres: Nylon, Polyester, Acrylic, Polyolefin*. Woodhead Publishing Limited series on fibres. Elsevier Science.

[93] Melz, T. (2002). *Entwicklung und Qualifikation modularer Satellitensysteme zur adaptiven Vibrationskompensation an mechanischen Kryokühlern*. PhD thesis, Techn. Univ., Darmstadt.

[94] Mena, O. and Parke, S. (2004). Unified Graphical Summary of Neutrino Mixing Parameters. *Phys. Rev. D*, 69:117301.

[95] Mikheyev, S. P. and Smirnov, A. Y. (1986). Resonant Amplification of ν Oscillations in Matter and Solar-Neutrino Spectroscopy. *Il Nuovo Cimento C*, 9(1):17–26.

[96] Mohapatra, R. et al. (2007). Theory of Neutrinos: A White Paper. *Rept. Prog. Phys.*, 70:1757–1867.

[97] Morrison, J. C. (2010a). Chapter 10 – Semiconductor Lasers. In Morrison, J. C., editor, *Modern Physics*, pages 235–269. Academic Press, Boston.

[98] Morrison, J. C. (2010b). Chapter 9 – Charge Carriers in Semiconductors. In Morrison, J. C., editor, *Modern Physics*, pages 223–234. Academic Press, Boston.

[99] Motz, H. T. (1956). Slow-Neutron Capture Gamma Rays from Sodium and Cadmium. *Phys. Rev.*, 104:1353–1364.

[100] Murthy, R. (2018). *Certificate of Stainless Steel Sample 1.4404 – 316L*. Julius Thress GmbH & Co. KG. Certificate.

[101] Nemchenok, I. B. et al. (2011). Liquid Scintillator based on Linear Alkylbenzene. *Physics of Particles and Nuclei Letters*, 8:129–135.

[102] Oberauer, L., Steiger, H. T. J., and Stock, M. R. (2020). *Fluorescence Decay-Time Spectroscopy of the JUNO Liquid Scintillator using Gamma Radiation and a Pulsed Neutron Beam*. JUNO DocDB, https://juno.ihep.ac.cn/cgi-bin/Dev_DocDB/ShowDocument?docid=5523. ID: 5523, v2.

[103] Oser, S. M. (2006). Neutrino Physics: A Selective Overview. In *21st Lake Louise Winter Institute: Fundamental Interactions*, pages 63–92. arXiv:0604021 [hep-ex].

[104] Pocar, A. (2005). Low Background Techniques for the Borexino Nylon Vessels. In Cleveland, B., Ford, R., and Chen, M., editors, *Topical Workshop on Low Radioactivity Techniques: LRT 2004.*, volume 785 of *American Institute of Physics Conference Series*, pages 153–162. arXiv:0503243 [physics.ins-det].

[105] Qian, X. and Vogel, P. (2015). Neutrino Mass Hierarchy. *Prog. Part. Nucl. Phys.*, 83:1–30.

[106] Ramond, P. (2019). Neutrinos and Particle Physics Models. In *Proceedings of the International Conference on History of the Neutrino: 1930-2018: Paris, France. September 5-7, 2018*. arXiv:1902.01741 [physics.hist-ph].

[107] Ranucci, G. (2017). Status and Prospects of the JUNO Experiment. *Journal of Physics: Conference Series*, 888:012022.

[108] Renk, K. F. (2012). *Basics of Laser Physics*. Springer, New York.

[109] Robert L. Feller (1994). *Accelerated Aging: Photochemical and thermal Aspects*. Getty Publications, Ann Arbor, Michigan, first edition.

[110] Rupitsch, S. J. (2019). *Piezoelectric Sensors and Actuators – Fundamentals and Applications*. Springer, Heidelberg, first edition.

[111] Sisti, M. (2019). *Analysis Results of an HPGe Gamma Spectroscopy*. Dipartimento di Fisica G. Occhialini, Università Milano-Bicocca. Certificate.

[112] Smirnov, A. Y. (2005). The MSW Effect and Matter Effects in Neutrino Oscillations. *Physica Scripta*, T121:57–64.

[113] Snell, A. H. and Pleasonton, F. (1955). Spectrometry of the Neutrino Recoils of Argon-37. *Phys. Rev.*, 100:1396–1403.

[114] Sommer, F. (2004). *Kurzwellige Diodenlaser auf der Basis der Gruppe III-Nitride*. PhD thesis, Albert-Ludwigs-Universität, Fakultät für Mathematik & Physik, Freiburg i. Br.

[115] Somoza, M. M. (2006). *Wikimedia Commons – the free Media Repository*. Website, https://commons.wikimedia.org/wiki/File:Franck-Condon-diagram.png. Visited on the 21st of May 2020; Search Items: Franck-Condon-Principle.

[116] Spießberger, S. (2012). *Compact Semiconductor-Based Laser Sources with Narrow Linewidth and High Output Power*. PhD thesis, Techn. Univ., Fakultät für Elektrotechnik & Informatik, Berlin.

[117] Steinmann, J. (2019). *Gepulster Laserstrahl*. Email Exchange. Private Communication on the 31st of January 2019.

[118] Strocchi, F. (1977). Spontaneous Symmetry Breaking in Local Gauge Quantum Field Theory: The Higgs Mechanism. *Commun. Math. Phys.*, 56:57.

[119] Stürmer, H. (2019). *GRIN Linsen & chromatische Aberration*. Email Exchange. Private Communication on the 7th of March 2019.

[120] Sun, H. (2015). *A practical Guide to handling Laser Diode Beams*. Springer, Heidelberg, first edition.

[121] Tanabashi, M. et al. (2018). Review of Particle Physics. *Phys. Rev. D*, 98:030001.

[122] Tanaka, T. et al. (2019). Gamma Ray Spectra from thermal Neutron Capture on Gadolinium-155 and Natural Gadolinium. arXiv:1907.00788 [nucl-ex].

[123] Tang, J. (2020). *Transparency of Acrylics*. Email Exchange. Private Communication on the 3rd of July 2020.

[124] Unknown (2003a). *Optran UV and Optran WF – Silica with Optional Buffers*. CeramOptec. Data Sheet.

[125] Unknown (2003b). *PD32 – 32 Channel Piezo Driver – Manual and Specifications*. SI Scientific Instruments GmbH. Manual.

[126] Unknown (2006a). *Acrylic Sheet – Forming Manual*. Altuglas International Arkema Inc. Manual.

[127] Unknown (2006b). *Stainless Steel 1.4404 – 316L*. Thyssenkrupp AG. Data Sheet.

[128] Unknown (2017a). *Device Specifications NI 6722/6723*. National Instruments. Data Sheet.

[129] Unknown (2017b). *Material Safety Data Sheet for Linear Alkylbenzene*. FAMICO Trading Limited. Data Sheet.

[130] Unknown (2017c). *RLT4xx-50CMG*. Roithner LaserTechnik GmbH. Data Sheet.

[131] Unknown (2017d). *Stainless Steel 1.4301 – 304*. Thyssenkrupp AG. Data Sheet.

[132] Unknown (2017e). *Stainless Steel 1.4305 – 303*. Thyssenkrupp AG. Data Sheet.

[133] Unknown (2017f). *Stainless Steel 1.4401 – 316*. Thyssenkrupp AG. Data Sheet.

[134] Unknown (2018a). *100 m Cables for Piezo Crystals*. AXON Cable S.A.S. Technical Drawing.

[135] Unknown (2018b). *GRIN Rod Lenses – Numerical Aperture 0.2*. GRINTECH GmbH. Data Sheet.

[136] Unknown (2018c). *Stainless Steel 1.4571 – 316Ti*. Thyssenkrupp AG. Data Sheet.

[137] Unknown (2019a). *Calibration Measurement of DA-100-3S-430-50/125-QM-40*. Oz Optics. Test Report.

[138] Unknown (2019b). *Digital Variable Attenuator – DA-100*. Oz Optics. Data Sheet.

[139] Unknown (2019c). *Google LLC*. Website, https://www.google.com/maps. Visited on the 9th of March 2019; Search Items: Jiangmen + China.

[140] Unknown (2019d). *IAEA - Nuclear Data Section; Live Chart of Nuclides*. Website, https://www-nds.iaea.orf/relnsd/vcharthtml/VCHARTHTML.html. Visited on the 28th of November 2019; Search Items: O, Si, Ti, Zr, Pb.

[141] Unknown (2019e). *IAEA - Nuclear Data Section; Live Chart of Nuclides*. Website, https://www-nds.iaea.orf/relnsd/vcharthtml/VCHARTHTML.html. Visited on the 13th of December 2019; Search Items: 96Zr.

[142] Unknown (2019f). *IAEA - Nuclear Data Section; Live Chart of Nuclides*. Website, https://www-nds.iaea.orf/relnsd/vcharthtml/VCHARTHTML.html. Visited on the 29th of November 2019; Search Items: 204Pb.

[143] Unknown (2019g). *IAEA - Nuclear Data Section; Live Chart of Nuclides*. Website, https://www-nds.iaea.orf/relnsd/vcharthtml/VCHARTHTML.html. Visited on the 4th of December 2019; Search Items: 210Pb, 210Bi, 210Po, 206Hg, 206Tl.

[144] Unknown (2019h). *Pressure Test on Harness Axon' P/N P572790A JUNO Project*. AXON Cable S.A.S. Test Report.

[145] Unknown (2020a). *Edmund Optics GmbH*. Website, https://www.edmundoptics.com. Visited on the 3rd of March 2020; Search Items: Fiber.

[146] Unknown (2020b). *Leoni AG*. Website, https://www.leoni-fiber-optics.com/en. Visited on the 3rd of March 2020; Search Items: Fiber.

[147] Unknown (2020c). *OpticalProperty.icc*. JUNO Collaboration: Simulation Framework `offline`. Data Sheet, `offline` version: `J19v1r1-Pre4`.

[148] Unknown (2020d). *Refractive Index Database; RefractiveIndex.INFO*. Website, https://refractiveindex.info. Visited on the 3rd of April 2020; Search Items: SCHOTT BK Borosilicate Crown BK7G18.

[149] Unknown (2020e). *Refractive Index Database; RefractiveIndex.INFO*. Website, https://refractiveindex.info. Visited on the 3rd of April 2020; Search Items: Water (H2O).

[150] Unknown (2020f). *Thorlabs GmbH*. Website, https://www.thorlabs.com. Visited on the 3rd of March 2020; Search Items: Fiber.

[151] Unknown (2020g). *Thorlabs GmbH*. Website, https://www.thorlabs.com. Visited on the 14th of October 2020; Search Item: Fiber Benches, FBP-A-FC.

[152] Wang, H. et al. (2017). Mass Hierarchy Sensitivity of medium Baseline Reactor Neutrino Experiments with Multiple Detectors. *Nucl. Phys.*, B918:245–256. arXiv:1602.04442 [physics.ins-det].

[153] Wang, Y. et al. (2014). Application of an Acrylic Vessel Supported by a Stainless-Steel Truss for the JUNO Central Detector. *Science China Technological Sciences*, 57(12):2523–2529.

[154] Wang, Z. (2016). *PMT-non-linearity*. JUNO DocDB, https://juno.ihep.ac.cn/cgi-bin/Dev_DocDB/ShowDocument?docid=1592. ID: 1592, v1.

[155] Wong, Y. Y. Y. (2011). Neutrino Mass in Cosmology: Status and Prospects. *Ann. Rev. Nucl. Part. Sci.*, 61:69–98.

[156] Wonsak, B. S. (2017). *PMTs & maximal verträgliches Magnetfeld?* Email Exchange. Private Communication on the 20th of March 2017.

[157] Wurm, M. (2017). Solar Neutrino Spectroscopy. *Phys. Rept.*, 685:1–52.

[158] Wurm, M. (2019). *Emanation Estimate for HDPE Cable*. Email Exchange. Private Communication on the 30th of July 2019.

[159] Wurm, M. (2020). *Liquid Scintillator Status Report*. JUNO DocDB, https://juno.ihep.ac.cn/cgi-bin/Dev_DocDB/ShowDocument?docid=5468. ID: 5468, v1.

[160] Wurm, M. et al. (2010). Optical Scattering Lengths in large Liquid-Scintillator Neutrino Detectors. *Rev. Sci. Instrum.*, 81:053301.

[161] Yang, X. (2020). *Calculation of Convection and Circulation of LS*. JUNO DocDB, https://juno.ihep.ac.cn/cgi-bin/Dev_DocDB/ShowDocument?docid=6096. ID: 6096, v1.

[162] Yen, Y.-R. (2019). Status of the KATRIN Neutrino Mass Experiment. In *8th Meeting on CPT and Lorentz Symmetry (CPT'19) Bloomington, Indiana, USA, May 12-16, 2019*. arXiv:1906.10168 [nucl-ex].

[163] Zhao, J. (2015). *Rn in Water*. JUNO DocDB, https://juno.ihep.ac.cn/cgi-bin/Dev_DocDB/ShowDocument?docid=1086. ID: 1086, v3.

[164] Zhao, J. (2019). *HDPE Screening*. JUNO Collaboration: Material Radioactvity Database. Data Sheet.

[165] Zhao, R. and Li, M. (2020). *Container PMT Testing Results Update*. JUNO DocDB, https://juno.ihep.ac.cn/cgi-bin/Dev_DocDB/ShowDocument?docid=6036. ID: 6036, v1.

[166] Zhou, X. et al. (2015). Rayleigh Scattering of Linear Alkylbenzene in large Liquid Scintillator Detectors. *Rev. Sci. Instrum.*, 86(7):073310.

[167] Zinth, W. and Zinth, U. (2018). *Optik: Lichtstrahlen – Wellen – Photonen*. De Gruyter Studium. De Gruyter.

[168] Zuber, K. (2011). *Neutrino Physics*. CRC Press, Boca Raton, second edition.

[169] Zuzel, G. and Simgen, H. (2009). High Sensitivity Radon Emanation Measurements. *Applied Radiation and Isotopes*, 67(5):889–893. 5th International Conference on Radionuclide Metrology – Low-Level Radioactivity Measurement Techniques ICRM-LLRMT'08.